



UNIVERSITY OF OXFORD

DOCTORAL THESIS

A Room Temperature Single Photon Source, Cavity Coupling of Single Solid-State Defects to Open-Access Microcavities

Author:

Sanmi ADEKANYE

Supervisor:

Prof. Jason SMITH

A thesis submitted in fulfillment of the requirements

for the degree of Doctor of Philosophy

Photonic Nanomaterials Group

Department of Materials

September 2019



"What is the fruit of these teachings? Only the most beautiful and proper harvest of the truly educated – tranquillity, fearlessness, and freedom. We should not trust the masses who say only the free can be educated, but rather the lovers of wisdom who say that only the educated are free. "

Epictetus, Discourses

Abstract

Room temperature solid-state emitters provide a promising source of single photons for use in quantum technologies. The emitters studied in this thesis are the nitrogen-vacancy (NV) centre in diamond, and defects in two-dimensional hexagonal boron nitride (hBN). In this thesis, I present investigations into the coupling of these defects to open-access microcavities at room temperature. The optical microcavity serves to confine the electric field down to mode volumes on the order of λ^3, increasing the spontaneous emission rate of these emitters and channelling this emission into well defined cavity modes. The general properties of both emitters will be presented, including examples of single photon emission, emission spectra, saturation behaviour and photo-stability. A few examples highlighting the long-term photo-stability of the NV centre under pulsed excitation will be displayed. This will highlight the suitability of the NV centre for a practical device. Following the preparation and characterisation of each emitter, single photon emission into the cavity modes is verified, reaching single photon purities greater than 97%. Enhancements in the spectral density of photons were observed for both the NV centre ($\sim 25\times$) and defect in hBN ($\sim 3\times$), along with decreases in the excited state lifetimes. While the NV centre provides a stable source of single photons, the cavity enhancement is limited by its broad emission spectrum. Defects in hBN present near-ideal optical properties in the absence of the cavity, and were expected to deliver superior results within the cavity. However, the poor photo-stability of these defects did not allow complete characterisation of the cavity coupled emission. FDTD simulations were combined with changes in the excited state lifetime to infer the quantum efficiency of these defects. The results of this thesis form the foundation for the realisation of a robust room temperature single photon source.

Acknowledgements

I would firstly like to thank the members of the Photonic Nanomaterials Group, past and present, for providing such a welcoming and productive working environment over the last four years. To Andrew, Ben, Brandon, Dean, Fred, Kiana, Laiyi, Larry, Lucas, Matt, Matteo, Shannon and Will, I have valued spending my time with all of you. Shazeaa Ishmael deserves individual praise for bringing the group together on birthdays, for market lunch and trips to the Royal Oak. The value of these occasions cannot be understated, and have always been a highlight of my time here. To Immy, Chen, Jack and Kaitlin, it has been a pleasure working directly with you all. You have all been brilliant students and your contributions to the group are invaluable. I wish you all the best in the future.

Particular thanks goes to the many Postdocs who have guided me along the way from a position of zero knowledge in this field. I am very grateful to Philip Dolan for taking the time to teach me the basics of confocal microscopy and giving me my first opportunity to get stuck into meaningful lab work. It was a shame when you left the group, but I am very much looking forward to working with you again at NPL. Further thanks goes to Sam Johnson, who has been an invaluable part of my experience at Oxford. Despite having such a large workload, you always took the time to engage with all aspects of my project, and your selflessness has inspired me to always be there for other members of the group. Aurélien Trichet deserves "*beaucoup de merci*" for dealing with my dubious articulation of the French language over the years. You have provided me with such an entertaining outlet even at the most stressful of times. My lengthy discussions on philosophy and science with Amit Dhawan have been a refreshing experience. Your precise and fundamental methods have softened my somewhat bullish approach to experimental science, making me a more well rounded scientist.

Outside the lab, there have been several people who have provided endless moments of laughter. I have thoroughly enjoyed being part of OUAFC and will always hold a place in my heart for the Broncos. It was an honour to lead the team, and our tenacious cup run to the BUCS final is amongst my proudest sporting achievements. The opportunity to coach the University of Oxford Blues at the World Elite University Football Tournament was an unexpected reward, and I am forever grateful for that experience. The Linacre/Corpus college football team provided me with my first sporting silverware, with numerous gritty performances leading to a Cuppers victory. I will forever apologise for my penalty in the shootout being saved. To Affie, Ajay, Haider, Jack, John and Timi, your friendship has made my final year the most memorable at university. Our fits of laughter, endless stories and top-shelf banter has kept me sane during the toughest moments. I am exceptionally grateful to Kerri Leigh-Bryant for being there for me during the most difficult stage of my education. It's not easy to share a partner with a thesis, but your patience and constant encouragement has allowed me to reach this point and I am deeply thankful to you.

Special thanks goes to my supervisor Professor Jason Smith. You have been the perfect mentor and offered brilliant scientific guidance throughout this project. I can not appreciate enough the opportunity you gave me to join the group and mould this project into my own. Finally, I would like to thank my family, Ajibola, Olaitan, Aanu and Glory Adekanye. I would not be here without you all. Thank you so much for supporting me throughout my education and always driving me to be the best I can be. *Oluwa ma tọju gbogbo wa*.

Publications

- *Robust, tunable, and high purity triggered single photon source at room temperature using a nitrogen-vacancy defect in diamond in an open microcavity*. P. R. Dolan, **S. Adekanye**, A. A. P. Trichet, S. Johnson, L. C. Flatten, Y. C. Chen, L. Weng, D. Hunger, H-C. Chang, S. Castelletto and J. M. Smith. *Optics Express*, 2018, **26**(6), 7056
- *Instabilities in nanodiamond single photon sources under prolonged pulsed excitation*. J. Aspinall, **S. Adekanye**, I. Brown, A. R. Dhawan and J. M. Smith. *Optical Materials Express* (Forthcoming), 2019
- *High-throughput detection and manipulation of single nitrogen-vacancy center's charge in nanodiamonds*. M. Sow, H. Steuer, **S. Adekanye**, L. Gines, S. Mandal, B. Gilboa, O. A. Williams, J. M. Smith, A. N. Kapanidis, *arXiv:1909.13297v1*, 2019
- *Open-access microcavity enhanced single photon emission from defects in two-dimensional hexagonal boron nitride*. **S. Adekanye**, T. T. Trang, I. Aharonovich and J. M. Smith. *Manuscript in preparation*

Conference Presentations

- *Towards a Triggered Single Photon Device; Open-Access Cavity Enhancement of Solid-state Emitters*, **Photon 18**, September 2018, Birmingham, United Kingdom
- *Cavity Enhanced Single Photon Emission of Single Defects in Solid-state Materials*, **Photonics West**, January 2018, San Francisco, California, USA
- *Room Temperature Single Photon Sources*, **Single Photon Single Spins II (SPSS II)**, August 2017, Troyes, France
- *Room Temperature Single Photon Sources*, **Department of Materials: University of Oxford**, February 2017, Oxford, University of Oxford

Contents

Abstract iii

Acknowledgements iv

Publications vi

List of Figures xi

List of Tables xvii

List of Abbreviations xix

Physical Constants xxi

List of Symbols xxiii

1 Introduction 1

1.1 Quantum Technologies . . . 1

1.2 Quantum Key Distribution . . . 2

1.3 Single Photon Sources . . . 3

1.3.1 Solid-State Emitters . . . 6

1.4 Optical Microcavities . . . 8

1.5 Thesis Outline . . . 10

2 Literature Review 13

2.1 Introduction . . . 13

2.2 Diamond-based Emitters . . . 14

2.2.1 Nitrogen-Vacancy Centre . . . 15

2.2.2 Silicon-Vacancy Centre . . . 18

2.3 Hexagonal Boron Nitride . . . 21

2.4 Optical Resonator Approaches 24
2.4.1 Photonic Crystal Cavities 26
2.4.2 Open-Access Microcavities 28
2.4.3 Micropillar Enhanced QD Source 34
2.5 Conclusion 36

3 Theoretical Background **39**
3.1 Introduction 39
3.2 Solid-State Emitters 40
3.2.1 Single Photon Emission 42
3.2.2 Saturation 44
3.3 Optical Resonators 45
3.3.1 The Gaussian Beam 48
3.3.2 The Hermite-Gaussian Beam 50
3.3.3 Distributed Bragg Reflectors 54
3.4 Cavity Quantum Electrodynamics 59
3.4.1 Free Space Emission 61
Optical density of states 61
Spontaneous Emission Rate 63
3.4.2 Cavity Coupled Emission 64
3.4.3 Bad Emitter Regime 66
3.5 Finite Difference Time Domain Simulations 68
3.5.1 Purcell Factor Analysis 71
3.6 Conclusion 75

4 Experimental Methods **77**
4.1 Introduction 77
4.2 FIB Milling and Mirror Coatings 78

4.3 Sample Fabrication . . . 82
4.3.1 Spin Coating . . . 82
4.3.2 NV Centres in Nanodiamond . . . 83
4.3.3 Hexagonal Boron Nitride Nanoflakes . . . 84
4.4 Confocal Microscope . . . 85
4.5 Hanbury-Brown Twiss and Lifetime Measurements . . . 88
4.5.1 Pulsed HBT Measurements . . . 90
4.6 Saturation Measurements . . . 92
4.7 Cavity Coupling Setup . . . 96
4.8 Conclusion . . . 103

5 Single Photon Characterisation of NV Centres in Nanodiamonds 105
5.1 Introduction . . . 105
5.2 Single Emitter Survey . . . 106
5.3 Properties of NV232 . . . 113
5.4 NV Centre Efficiency . . . 116
5.5 NV Centre Stability . . . 120
5.6 Conclusion . . . 130

6 NV Centre Cavity Coupling 133
6.1 Introduction . . . 133
6.2 Open Cavity Characterisation . . . 134
6.2.1 Summary . . . 140
6.3 NV232 Cavity Coupling . . . 140
6.3.1 Discussion . . . 144
FDTD Simulation . . . 146
6.4 NV25 Cavity Coupling . . . 151
6.5 NV-Cavity Single Photon Source Specifications . . . 158

6.6 Conclusion 160

7 Hexagonal Boron Nitride Single Photon Source **163**

7.1 Introduction 163

7.2 Single Emitter Survey 164

7.2.1 Sample 1 164

7.2.2 Sample 2 170

7.2.3 Sample 3 174

7.3 hBN40 Single Photon Source 176

7.3.1 hBN40 Half-space Characterisation 176

7.3.2 hBN40 Cavity Coupling 179

7.3.3 Discussion 181

7.4 Conclusion 183

8 Conclusions and Outlook **185**

Bibliography **191**

List of Figures

1.1 Example of the BB84 protocol for quantum key distribution. 2
1.2 Solid state emitters emitting single photons. 7
1.3 Schematic of the open-access microcavity. 9

2.1 Spectral maps of emitters in diamond 14
2.2 Crystal structure and room-temperature PL spectrum of the NV centre in diamond 16
2.3 Negative NV centre proportion and nanoablation rate vs laser fluence . . 17
2.4 Crystal structure and room-temperature PL spectrum of the SiV centre in diamond. 18
2.5 Blinking of SiV centres 19
2.6 Room-temperature PL spectrum and structure of the defect in hBN. 20
2.7 hBN PL properties with varying excitation wavelengths. 22
2.8 PL spectra of a typical emitter n hBN ar room ad cryogenic temperatures. . 23
2.9 NV centre light collection techniques 25
2.10 SEM images of a fabricated 2D and 1D photonic crystal cavities. 27
2.11 Schematic of the planar-hemispherical microcavity 29
2.12 NV centre coupling to fibre cavity 30
2.13 Rate model description of NV cavity coupling. 32
2.14 hBN defect coupling to open-access microcavity 33
2.15 InGaAs QD coupling to a micropillar cavity. 35

3.1 Franck-Condon configuration diagram 41
3.2 HBT theory of coherent light and true single photon emission 43
3.3 The Fabry-Perot optical resonator 46
3.4 Mode spectrum of the Fabry-Perot resonator. 48
3.5 The Gaussian beam. 49

3.6 Transverse electric field distribution of Hermite-Gauss modes. 51
3.7 Transverse mode spectrum. 52
3.8 Mode volumes for different radii of curvatures. 53
3.9 The bad emitter/good cavity regime 56
3.10 Transfer matrix simulations. 58
3.11 Free space optical density of states. 62
3.12 Density of states for free space and a cavity mode 65
3.13 The bad emitter/good cavity regime 67
3.14 FDTD simulation structures. 69
3.15 FDTD simulations of NV centre's lifetime in a nanodiamond. 70
3.16 Purcell factor spectra 72

4.1 Plinth substrate fabrication 78
4.2 FIB milling of hemispherical features and DBR deposition. 79
4.3 FIB processing of 300 μm plinth to reduce the lateral dimensions. 80
4.4 FIB marking of registration features on the planar mirror. 81
4.5 Spin coated distribution of fluorescent nanoparticles. 83
4.6 Schematic and details of the nanodiamonds used in this work. 84
4.7 hBN transfer process. 85
4.8 Schematic of the confocal microscope. 86
4.9 Confocal microscope resolution. 87
4.10 Hanbury-Brown Twiss interferometry. 89
4.11 Hanbury-Brown Twiss interferometry. 91
4.12 Saturation measurements under continuous wave and pulsed excitation. . 93
4.13 Schematic of defect dipoles and example polarisation measurement. . . . 95
4.14 Schematic of the confocal microscope. 97
4.15 PL images of background fluorescence before and after photo-bleaching. . 98
4.16 Mirror alignment process. 99

4.17 532 nm tranmission through the cavity. 100
4.18 Transmission of 8 and 16 pair DBRs. 101
4.19 Optimisation of the cavity coupled emission. 102

5.1 PL image of nanodiamonds. 106
5.2 Continuous wave HBT measurements. 107
5.3 Power dependent HBT measurement for a single NV centre. 108
5.4 Spectral survey of NV centres 110
5.5 CW saturation measurements. 111
5.6 Lifetime measurements of NV centres. 112
5.7 CW HBT and emission spectrum of NV232. 113
5.8 Pulsed HBT and lifetime measurements of NV232 114
5.9 CW and pulsed saturation measurements for NV232. 115
5.10 Histogram of single NV centre lifetimes from 50 nm and 100 nm nanodiamonds. 117
5.11 NV centre saturation behaviour under pulsed excitation. 118
5.12 NV7 photo-instability. 122
5.13 PL count traces of NV232 following long term exposure 123
5.14 CW saturation and lifetime measurement of NV232 following long term excitation. 124
5.15 CW saturation and lifetime measurement of NV18 following long term excitation. 125
5.16 Fluorescence intensity and lifetime of NV11 over 62.5 hrs of excitation. . . 126
5.17 Fluorescence intensity and lifetime of NV12 over 62.5 hrs of excitation. . . 127
5.18 Fluorescence intensity and lifetime of NV13 over 150 hrs of excitation. . . 128
5.19 Fluorescence intensity and lifetime of NV11 over 62.5 hrs of excitation. . . 129

6.1 Optical microscope and white light transmission 640 nm plinth 134

6.2 Single defect coupling to varying radii of curvature features. 135
6.3 Coupling of single defect to different RoC 8 μm features 137
6.4 Cavity length sweep of a $\beta = 8$ μm showing the fluorescence intensity and associated spectra. 138
6.5 PL images of a single emitter outside and inside the cavity. 139
6.6 PL image with mirror racing towards and away from objective. 141
6.7 Spectral profile and CW saturation measurement of half-space and cavity coupled emission for NV232. 142
6.8 Cavity single photon emission from NV232 under both CW and pulsed excitation. 143
6.9 Pulsed saturation and lifetime measurements for NV232 half-space and TEM_{00} emission. 144
6.10 FDTD simulation results for the Purcell factor as a function of wavelength 147
6.11 FDTD simulation of the intensity distribution of a 50 nm nanodiamond within the open access microcavity. 148
6.12 Characterisation of NV25 with the mirror facing the objective lens. 152
6.13 PL image of NV25 with the mirror facing towards and away from the objective lens. 153
6.14 Cavity sweeps and saturation measurements as a function of mode index. 154
6.15 TEM_{00} mode spectra and CW saturation curve for NV25. 156
6.16 Continuous wave and pulsed HBT measurements of NV5's TEM_{00} emission. 157
6.17 Pulsed saturation and TRPL measurements for NV25's half-space and TEM_{00} emission. 158

7.1 PL image of hBN defects before and after gentle photo-bleaching. 164
7.2 Continuous wave HBT measurements of hBN defects. 165
7.3 Spectral survey of defects in hBN. 166
7.4 Pulsed excitation measurements of hBN defects. 167

7.5 Count traces of hBN defects before and after pulsed excitation. 169
7.6 Webcam and PL image of the region where single hBN defects were found. 171
7.7 Emission spectra and HBT characterisation of hBN38 and hBN86. 172
7.8 Pulsed saturation measurements of filtered hBN defects. 173
7.9 Webcam and PL image of the region in Sample 3 where single hBN defects were found. 174
7.10 Emission spectra and HBT characterisation of six hBN defects in Sample 3. 175
7.11 Characterisation of hBN40 177
7.12 PL images of Sample 3 with the mirror facing towards and away from the objective lens. 178
7.13 PL spectra and HBT measurements for hBN40's half-space and cavity-coupled emission. 179

8.1 Schematics of the NV-cavity module. 188
8.2 Prototype single photon source device. 189

List of Tables

2.1 Summary of the achieved device specifications of solid-state single photon emitters. 37

5.1 Summary of various lifetimes describing the rate dynamics of single NV centres. 120

List of Abbreviations

CQED	**C**avity **Q**uantum **E**lectro**D**ynamics
CW	**C**ontinuous **W**ave
DBR	**D**istributed **B**ragg **R**eflector
FDTD	**F**inite **D**ifference **T**ime **D**omain
FWHM	**F**ull **W**idth **H**alf **M**aximum
hBN	**H**exagonal **B**oron **N**itride
HBT	**H**anbury **B**rown **T**wiss
NA	**N**umerical **A**perture
NV	**N**itrogen **V**acancy
PCC	**P**hotonic **C**rystal **C**avity
PL	**P**hoto**L**uminescence
PSB	**P**honon **S**ide **B**and
RoC	**R**adius of **C**urvature
RT	**R**oom **T**emperature
SEM	**S**canning **E**lectron **M**icroscopy
SiV	**S**ilicon **V**acancy
SNR	**S**ignal **N**oise **R**atio
TEM	**T**ransverse **E**lectro**M**agnetic
TRPL	**T**ime **R**esolved **P**hoto**L**uminescence
ZPL	**Z**ero **P**honon **L**ine

Physical Constants

Speed of Light	$c = 2.997\,924\,58 \times 10^{8}\,\mathrm{m\,s^{-1}}$
Planck's Constant	$h = 6.626 \times 10^{-34}\,\mathrm{J\,s^{-1}}$
Reduced Planck's Constant	$\hbar = 1.054 \times 10^{-34}\,\mathrm{J\,s^{-1}}$
Permittivity of Free Space	$\epsilon_0 = 8.85 \times 10^{-12}\,\mathrm{F\,m^{-1}}$

List of Symbols

F_P	Purcell Factor	
V	Mode Volume	$\mu\mathrm{m}^3$
β	Radius of Curvature	$\mu\mathrm{m}$
τ	Lifetime	ns
γ	Emitter Decay Rate	Hz
QE	Quantum Efficiency	
DW	Debye Waller Factor	
$\mathcal{N}$	Photon number	
$\mathcal{F}$	Finesse	
$\mathcal{L}$	Round Trip Loss	
Q	Quality factor	
$\mathcal{B}$	Cavity Emission Efficiency	
q	Longitudinal Mode Index	
L	Cavity Length	$\mu\mathrm{m}$
$\Delta\lambda$	Free Spectral Range	nm
$\delta\lambda$	Spectral Linewidth	nm
ω_0	Mode Waist	$\mu\mathrm{m}$
$\rho(\omega)$	Optical Density of States	
R	Reflectance	
T	Transmission	
n	Refractive Index	
$\mathcal{E}$	Electric Field	$\mathrm{V\,m^{-1}}$
g_0	Atom Cavity Coupling Rate	Hz
κ	Cavity Decay Rate	Hz
ξ	Dipole Orientation Factor	

$\mathcal{R}$	Effective Atom Cavity Coupling Rate	Hz
$\langle \mathcal{N} \rangle$	Single Photon Efficiency	

For Ajibola, Olaitan, Aanu and Glory Adekanye. In loving memory of Prince Lawrence Bamidele Adekanye.

1 |

Introduction

1.1 Quantum Technologies

Over the last two decades, developments in harnessing the unique properties of quantum mechanics have led to the inception of new quantum technologies, which will help realise the second quantum revolution [1]. The ability to create, store and process information encoded within these systems is set to revolutionise communication security and computing capabilities over the coming decades. Recent developments have become sufficiently advanced and have led to the availability of several commercial quantum key distribution (QKD) systems, which offer enhanced cryptography [2]. With industry standards now being set, these systems can be extended towards other capabilities, including quantum communication networks, quantum metrology and quantum computing. Governments and industries are beginning to invest heavily in this avenue of research, due to its proximity towards the creation of physical working devices. A vast number of systems have being brought forward for the development of such technologies, and these involve the quantum state of light playing a key role. The properties of photons (such as transmission at the speed of light), make them extremely valuable for the transfer of quantum information between remote locations.

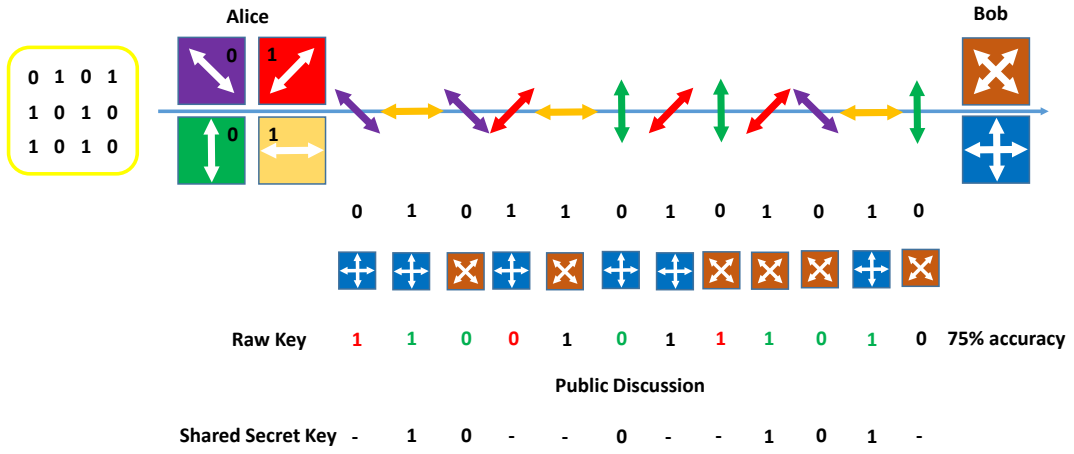


FIGURE 1.1: An example demonstration of the BB84 protocol for quantum key distribution. The two communicating parties (Alice and Bob) create a shared secret key by exchanging quantum bits with value of the bit encoded in the photon polarisation.

1.2 Quantum Key Distribution

At present, QKD is the most promising quantum information task to become a viable quantum technology. The primary aim of QKD is to enable secure communication between two parties (conventionally called Alice and Bob), preventing an eavesdropper (known as Eve) from obtaining the information sent between them (Figure 1.1) [2]. Conventional cryptography relies on mathematical approaches, of which the security is dependent on the amount of processing power available to an eavesdropper. The security of QKD is based on the principles of quantum physics and there is unconditional security without imposing any restriction on the eavesdropper [3]. Alice and Bob are connected by two channels, a quantum channel to share the quantum signal, and a classical channel to send classical messages [3]. The quantum channel is any medium which allows the propagation of light such as an optical fibre or free space. The act of Eve extracting information of the quantum state of the photon is a form of measurement. A fundamental postulate of quantum mechanics is that "*one cannot perform a measurement without perturbing the*

system". When applied to communication, this aspect of quantum mechanics can be used to detect the presence of an eavesdropper. This principle forms the basis of several commercial QKD systems [4].

There are two main QKD schemes used to achieve quantum encryption; preparation and measurement, or entanglement based protocols [5]. In 1984, Charles H. Bennett of IBM and Gilles Brassard of the University of Montreal developed the first (preparation and measurement) protocol for QKD, known as the BB84 protocol [6]. This method uses photon polarisation to transmit the information, using four quantum states constituting two bases - usually rectilinear ($|\updownarrow\rangle$, $|\leftrightarrow\rangle$) and diagonal ($|\swarrow\nearrow\rangle$, $|\nwarrow\searrow\rangle$). The two states within a basis are orthogonal to each other ($|\langle\updownarrow|\leftrightarrow\rangle|^2 = 0$) and maximally conjugate to any other state from the other basis ($|\langle\updownarrow|\swarrow\nearrow\rangle|^2 = 0.5$). Alice can therefore create a string of quantum bits (qubits) which are sent to Bob for measurement through the quantum channel (Figure 1.1). The basis used to create and measure these qubits can then be compared on a classical channel to determine the error rate, without revealing the value of the measured result. The correctly measured bits are used to create a key which is then used to encode the information. Therefore, the presence of an eavesdropper can only reduce the bit rate, and no information is revealed. Since it's initial proposal (1984) [6] and demonstration (1992) [7], QKD has rapidly matured to the point of commercial availability, with at least four companies offering commercial QKD devices, and several more carrying out active research.

1.3 Single Photon Sources

A critical component of these quantum technologies is a triggered single photon source, a light source which can generate a single photon on demand. Three properties are required to describe the ideal single photon source:

- A vanishing probability of emitting two or more photons, characterised by the second-order correlation function $g^{(2)}(0)$. A high single photon purity guarantees the security of quantum communication [1].
- A high efficiency ($\langle \mathcal{N} \rangle$) of single photon generation per excitation event, where $\langle \mathcal{N} \rangle = 1$ for a deterministic single photon source. The value of $\langle \mathcal{N} \rangle$ depends on where the single photon probability is measured, such as at the output of the source, the end of an optical fibre, or on a detector. The frequency of excitation will also determine absolute brightness (cts/s) of the source.
- The creation of a pure quantum state, making successive photons indistinguishable. The indistinguishability is characterised by the mean photon wavepacket overlap M, which can be measured through Hong-Ou-Mandel (HOM) interference [8].

All three of these parameters are crucial for quantum information processing (QIP) applications, but QKD protocols such as BB84 do not require indistinguishable photons. Apart from QKD, the use of single photon sources may enable significant developments in applications such as quantum metrology and imaging, yielding devices with precision and resolution beyond the quantum noise limit [9, 10]. Various processes are being developed to create single photons, but a distinction must be made between a true single photon source, and a source of single photons. As current true single photons sources are expensive and cumbersome, alternative approaches are predominantly utilised for the production of single photons.

The earliest inception of a practical photon source for QKD involved the attenuation of a laser. Lasers can be inexpensive, are available at numerous wavelengths and can function at high excitation rates. Therefore, these sources are sufficient enough for applications such as QKD [2] and have been used in the vast majority of demonstrations [3, 11]. As number of photons per pulse follows a Poissonian distribution, one can reduce the laser

intensity to a regime where the probability $\langle \mathcal{N} \rangle$ of each pulse containing a single photon is low, and therefore multiple photons negligible. Most experiments use a low average photon number $\langle \mathcal{N} \rangle = 0.1$, meaning 90% of the pulses are empty and ∼5% of the non-empty pulses contain multiple photons [2]. However, the coherent properties of such a source is very different to a true single photon source and a laser's second-order correlation function is equal to one at all times. There is then a balance between the source efficiency and probability of multi-photon emission.

The security of QKD may be compromised by the inevitable multi-photon pulses originating from the attenuated laser source. This opens an avenue for a photon number splitting (PNS) attack, where an eavesdropper can preferentially transmit some photons to Bob to maintain the same detection rate at Bob, while measuring a number of single photon pulses[12–14]. By doing this, Eve can determine part or all of the key while remaining hidden. To negate this possibility, the mean photon number can be reduced, but this restricts the rate and distance over which QKD can function. Recently developed decoy state protocols use pulses of varying intensity, and correlate the transmission of these pulses to detect PNS attacks [15]. This protocol has allowed attenuated laser sources to operate with $\langle \mathcal{N} \rangle = 0.5$, leading to several successful demonstrations of QKD over distances up to 400 km [16]. The key rate of QKD over such distances reduces dramatically, with a working practical limit of ∼80 km. For example, an optical fibre of 1000 km in length with a 10 GHz ideal source would yield a detection rate of 0.3 photons per century [17]. One proposed solution is the use of a trusted node network, where several repeaters create quantum keys using the previous node, daisy-chaining the key across the network. This approach eliminates the problem of photon loss while extending the range of QKD, but has security and logistical drawbacks. The trust requirement currently employed by decoy-state QKD may be removed by relying on entanglement in QKD protocols, where quantum repeaters form the backbone of the network [5, 18–21].

In contrast to attenuated laser pulses, spontaneous parametric down conversion (SPDC) produces two photon states. In this process, a birefringent crystal is excited by a pump laser, and the non-linear optical properties lead to a spontaneous splitting of the high energy photon into a photon pair [22]. The emission of these photons is probabilistic rather than deterministic, which restricts its use in certain applications. The two created photons conserve energy and momentum and may be correlated in varying degrees of freedom including energy, polarisation and direction [3]. As a result of this, one photon can be used to herald the creation of the other (extremely useful for entanglement experiments), or simply as a single photon. Several inorganic crystals display the non-linearity required for SPDC, such as KD_2PO_4, BaB_2O_4 and $LiNbO_3$, with these materials chosen to satisfy the output and pump wavelengths of interest [3]. Unfortunately, SPDC is immensely inefficient with a highest reported conversion efficiency of $\langle \mathcal{N} \rangle = 4 \times 10^{-6}$ [23]. Another critical issue with SPDC, is that the probability of creating k pairs scales with pump intensity to the kth power [24]. The single photon purity and indistinguishability both deteriorate rapidly with brightness, decreasing the utility of SPDC in applications.

1.3.1 Solid-State Emitters

An alternative method of producing single photons is to use solid-state systems which feature atom-like emitters [16]. The spontaneous emission from these pseudo two-level systems inherently generates single photons which can be extracted for the desired application (Figure 1.2). These systems are promising candidates for the creation of photonic technologies as they are stationary, can be addressed individually and some function at room temperature [16]. Due to this, solid-state room temperature compatible systems provide a greater ease of integration into existing quantum networks [25]. For solid-state

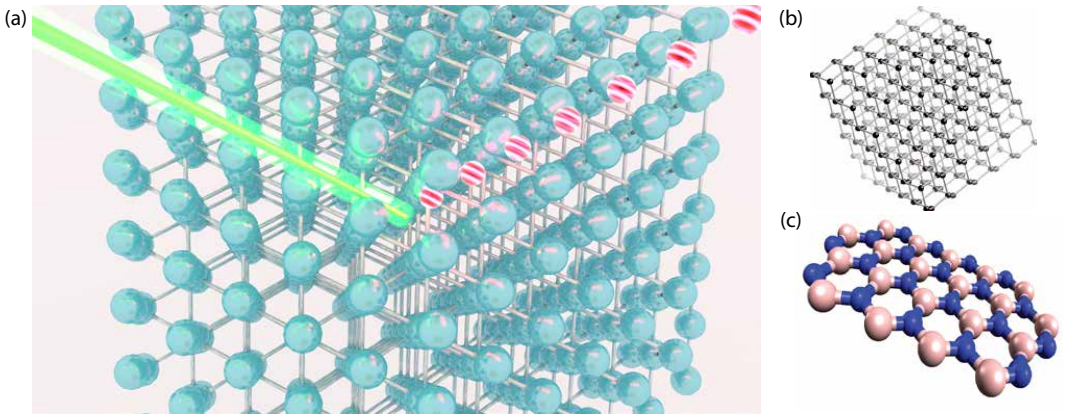


FIGURE 1.2: (a) Artistic interpretation of single photon emission from defects in bulk 3D crystals when excited with sub-bandgap illumination (illustrated with a green incoming laser beam). The most studied crystals include diamond (b) and hexagonal boron nitride (c). Created by Dr Shannon Nicley.

emitters, the description of the ideal single photon source can be expanded to: photostable emission, narrow emission spectrum, short excited state lifetime (ps $< \tau <$ ns), two level system without shelving or metastable states, fully polarised in absorption and emission, and finally, Fourier-transformed limited indistinguishable photons [25].

There are several optically active systems which readily display quantum effects, and especially single photon emission. Examples include single trapped atoms (or ions), organic dyes, aromatic molecules and solid-state emitters [26]. These systems can possess excellent optical properties but each presents individual stumbling blocks to scalability and integration for practical applications. For example, self-assembled InAs/GaAs quantum dots have displayed the highest all-around single photon performance, with near-ideal single photon emission characteristics and count rates on the order of $\sim$GHz [27]. Quandela [28] and Sparrow Quantum [29] are two companies currently with these QD single photon sources on the market. However, due to their shallow confinement potential, these ideal properties are only observed at cryogenic temperatures, and at present can

not be reproduced under ambient conditions [16]. While Group III-nitride QDs can operate at room temperature, the best single photon purity achieved is 87%, which is poor compared to >99% obtained from QDs operating at cryogenic conditions [30]. Encouraging results have been achieved with room temperature compatible sources such as the nitrogen-vacancy (NV) and silicon-vacancy (SiV) centres in diamond [31]. There are also new quantum emitters emerging in novel materials, such as defects in two-dimensional hexagonal boron nitride (hBN) [32]. In summary, there is no single system which satisfies all the requirements for an ideal single photon source, meaning there is a great emphasis on discovering new and efficient sources of single photons.

1.4 Optical Microcavities

Although these atom-like systems display single photon emission, this property alone is not sufficient to develop them into a viable technology. Sources such as InAs/GaAs QDs require complex experimental setups and large cryogenic apparatus, limiting their scope strictly to research laboratories and at an extreme expense [24]. For room temperature emitters, the single photon emission efficiency can be poor, and indistinguishability non-existent. This is because they emit photons in random directions in space, with strong associated dephasing mechanisms [1]. Quantum Communications Victoria (QCV) previously commercialised a fibre-coupled NV centre single photon source with limited success, as the broad emission profile of the defect is an inhibiting factor for practical applications [33]. It remains crucial to engineer these optical properties, such as emission frequency and spectral profile in order to complement the transmission window of the quantum channel. A promising approach is the use of optical microcavities [34]. These micro-scale resonators provide a means to enhance the rate of single photon production while functioning at ambient temperatures.

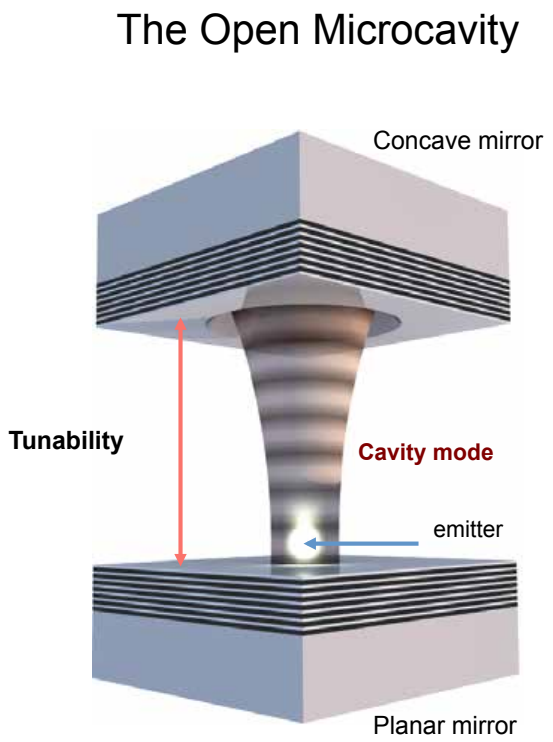


FIGURE 1.3: A schematic of the open-access microcavity. Reproduced from [35].

The confinement of an emitter in this environment enhances its interaction with the optical field while giving control over the emission profile. Therefore, the microcavity provides a platform which maximises the potential of these emitters, while overcoming the challenges which have prevented previous sources from achieving industrial impact. There are several cavity coupling strategies, with each unique example aiding in the push towards the practical realisation of photonic quantum technologies. This thesis will demonstrate the enhancement of solid-state emitters using the open-access microcavity platform, making them more viable for use as single photons sources within quantum technologies. The open-access microcavity is formed from two independent highly reflective Fabry-Perot mirrors with a planar-hemispherical geometry. The high degree of control is a key benefit of the open-access approach, providing excellent output beam

characteristics and an increased collection efficiency of the emitted photons.

1.5 Thesis Outline

The aim of this project is the creation of a room temperature single photon source, based on the emitter-cavity platform. Before the presentation of the properties of this potential device, this thesis will discuss several experiments which lead to its creation, and will be structured as follows:

Chapter 2: Literature Review

In this review, I will discuss some of the published literature concerning properties of solid state emitters and their suitability towards the development of photonic quantum technologies. The focus will be specifically on defects in diamond and hexagonal boron nitride. Following this, some literature on optical resonators will be reviewed, including photonic crystal cavities and open-access microcavities. The review will then concentrate on how open-access microcavities are distinguished from the alternate strategies in terms of the practical realisation of single photon source. Finally, the single photon properties of the cavity enhanced room temperature sources will be compared to the leading cryogenic quantum dot sources.

Chapter 3: Theoretical Background

This chapter will describe the fundamental elements required to understand the emitter cavity coupling process. Firstly, the behaviour of solid-state emitters will be described, with key concepts such as the quantum efficiency, excited state lifetime and single photon emission introduced. Secondly, the optical microcavity will be presented including a

description of the Hermite-Gaussian beam which describes the optical modes of the resonator. Finally, the theory of cavity quantum electrodynamics in the regime of the weak coupling limit will be given. This will be compared to free-space emission to define the Purcell factor, giving an insight to the limits of solid-state emitters within optical microcavities.

Chapter 4: Experimental Methods

The processing of the planar and featured mirrors which form the microcavity will firstly be discussed, where the importance of the focused ion bean (FIB) will be seen. Following this, the fabrication method for the creation of emitters in solid-state nanodiamond and hexagonal boron nitride will be described. The confocal microscope used in this project, as well as the protocols for optical spectroscopy and the various measurements involved will be explained in detail. Finally, a thorough description of the cavity coupling procedure will be given, including the mounting process required to reach sub-micron cavity lengths.

Chapter 5: Single Photon Emission Characterisation of NV Centres in Nanodiamonds

In this first experimental chapter, the optical properties of single NV centres in nanodiamonds will be discussed. The experimental methods introduced in the previous chapter will be used to survey several NV centres to show the generally observed behaviour of these defects. An in depth analysis of a specific NV centre will be shown, as this NV centre will be used for upcoming cavity coupling experiments in the following chapter. The efficiency and photo-stability of NV centres will be discussed, to determine the suitability of the NV centre as a practical source of single photons. It will be shown that the NV centre is a sufficiently robust defect for prolonged use within a single photon source device.

Chapter 6: NV Centre Cavity Coupling

This chapter will present the results of the emitter-cavity coupling process for NV centres from two nanodiamond samples. The spectral properties of the FIB milled cavities will be characterised before further experiments using single NV centres. It will be shown that the cavity induced enhancements in the spectral density of photons into a single optical mode, as well as increasing the single photon purity. FDTD simulations will be used to complement the experimentally observed changes in excited state lifetime, giving more information on the NV centre's quantum efficiency. Key device parameters such as the efficiency and saturation count rate will be specified.

Chapter 7: Hexagonal Boron Nitride Single Photon Source

This final experimental chapter will present the results obtained from experiments on defects in hexagonal boron nitride. A large survey of these emitters from three samples will be shown, highlighting general properties and the promising characteristics of defects in this material. Further characterisation of a single emitter will be presented. This defect was successfully coupled to a microcavity and these results will be compared to those obtained from other hBN cavity coupling strategies and results. The single photon specifications and defect robustness will also be compared to NV centres in nanodiamond.

Chapter 8: Conclusion and Future Outlook

In this final chapter, the key results previously presented will be summarised, followed by a discussion on the future outlook of the emitter-cavity single photon source. It will be shown that the NV centre in diamond displays favourable attributes towards the realisation of a robust single photon source device. The preliminary schematics of a prototype single photon source based on the emitter-cavity platform will be shown, and the expected device characteristics will be compared to other single photon sources coming to market.

2 | Literature Review

2.1 Introduction

Emerging quantum technologies aim to exploit quantum mechanical effects to enhance the capabilities of applications including cryptography, nanoscale sensing and information processing. Several platforms have been suggested and explored thoroughly, with a strong option being the use of single photon emitters as the fundamental building blocks. Single photon emission has been observed in a variety of materials, including solid-state emitters [16], quantum dots [24], trapped atoms (or ions) [36], single molecules [37] and carbon nanotubes [38]. Solid-state materials featuring atom-like emitters combine the scalability and convenience of a host material with the distinguished optical properties of atoms. The choice of emitter remains non-trivial as each material presents individual detrimental effects which must be mitigated. This review will describe the photo-physical properties of three prominent solid-state emitters which function at room temperature. I will describe their integration with various optical resonators approaches, showing how their emission properties are improved towards the realisation of an ideal single photon source. I will conclude by presenting the specifications of the leading solid-state single photon source which operates at cryogenic temperatures, and compare it to the best parameters achieved by the room temperature sources.

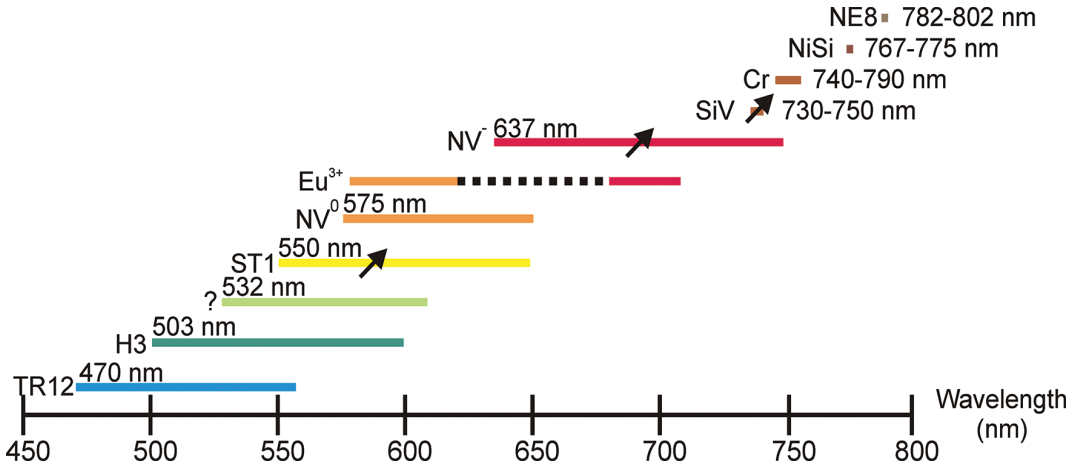


FIGURE 2.1: Spectral map of the various single emitters in diamond within the visible region. Reproduced from [31].

2.2 Diamond-based Emitters

Diamond, a material generally known for it's use in jewellery, is also a host to over 500 luminescent colour centres [31]. These colour centres are formed from defects in the crystal, usually a missing atom, an impurity atom and combinations of such imperfections. With diamond possessing one of the largest band gaps of known materials, these defects perturb the energy level structure within the band gap, introducing discrete levels in this formally forbidden region. Optical excitation between these new electronic states may result in the emission of a photon upon relaxation from the excited state. Due to the large band gap, the emitted photons are not absorbed by diamond and so can be collected externally. In addition, the diamond host material provides favourable properties such as chemical inertness, high mechanical strength and an unmatched thermal conductivity.

The plethora of optically active defects in diamond (Figure 2.1) display emission spanning from the near-infrared to the ultraviolet wavelengths [31], with many displaying

photo-stability at room temperature. However, only a small few are bright enough to observe single photon emission [39], or studied sufficiently to observe entanglement [40] and Purcell enhancement [41]. The above-mentioned properties are also observed in nanoscale diamond particles (nanodiamonds). With nanodiamonds being smaller than the focus of an excitation laser, there is an absence of total internal reflection and they exhibit low fluorescence background. Therefore, for certain applications, nanodiamonds exhibit superior properties to bulk diamond. These distinct properties have pioneered ever increasing research into diamond-based emitters.

2.2.1 Nitrogen-Vacancy Centre

The negatively charged nitrogen vacancy defect (NV centre) is one of the many colour centres observed in diamond [31, 42]. Over the course of the last decade, the NV centre has been established as a leading candidate for a solid state quantum emitter [16]. NV centres are remarkably popular as they display a variety of photo-physical properties such as sensitivity to magnetic fields, temperature and pressure and high photo-stability [43]. In addition to this, its unique spin dependent relaxation pathway creates a polarisation of the spin, enabling the optical readout of the spin state [44]. With this, the NV centre can be used as a stable source of single photons carrying the information of spin state of the centre.

The colour centre is formed by a substitutional nitrogen atom with an adjacent vacancy (Figure 2.2 (a)), and due to the symmetry, forms a well isolated quantum system. The defect complex has six electrons, five from neighbouring carbon and nitrogen atoms, with an additional electron trapped at the defect site, forming the negatively charged state NV^- [25]. NV centres can be reliably fabricated by a variety of methods depending on the required application. These include ion implantation of nitrogen [25], ion irradiation

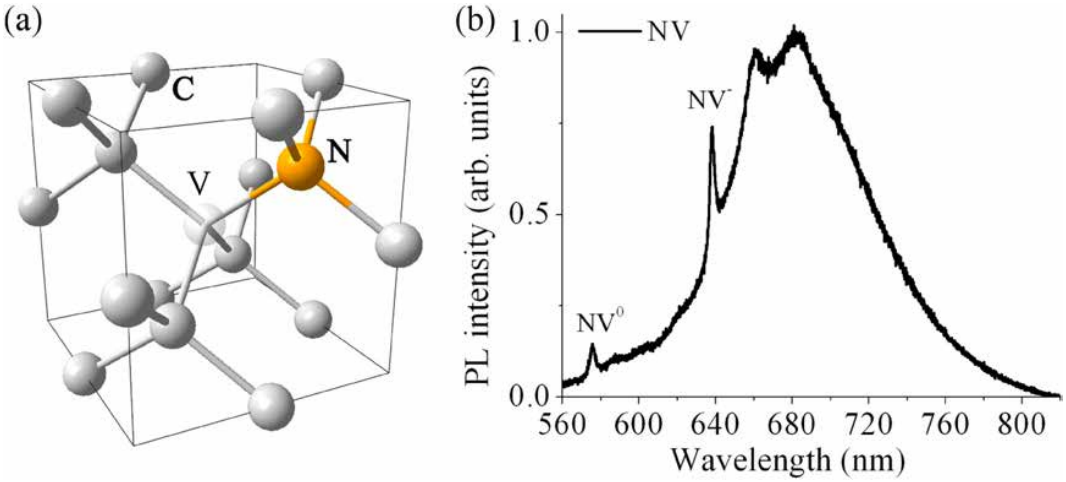


FIGURE 2.2: (a) Crystal structure of the NV centre in diamond. (b) Room-temperature PL spectrum showing the ZPL of the neutral- (575 nm) and negatively-charged (637 nm) NV centre. Reproduced from [25].

to create vacancies [45, 46] and laser writing of vacancies [47] - all followed by subsequent annealing to allow vacancy migration and subsequent NV centre formation.

The NV centre's emission spectrum features a zero-phonon line (ZPL) at 637 nm and is dominated by a broad phonon side band (PSB) extending up to 800 nm (Figure 2.2 (b)). However, as only the ZPL emission provides indistinguishable photons, the small fraction of emission into the ZPL (4%) means the NV centre has a low efficiency for quantum information processing [40, 48]. The excited state lifetime of the NV centre is dependent on the host material, varying between 12 – 60 ns depending on whether situated in bulk diamond or nanodiamond. The relatively long lifetime limits the maximal excitation and emission rate. Despite the presence of non-radiative transitions via the shelving states, the quantum efficiency of the NV centre is estimated as 0.7 in bulk diamond [44] but as low as 0.05 in nanodiamond (up to 0.9) [49]. Due to the high refractive index of diamond, single NV centres in the bulk diamond display lower count rates than nanodiamonds, with typical count rates of the order 10^4 and 10^5 cts/s respectively.

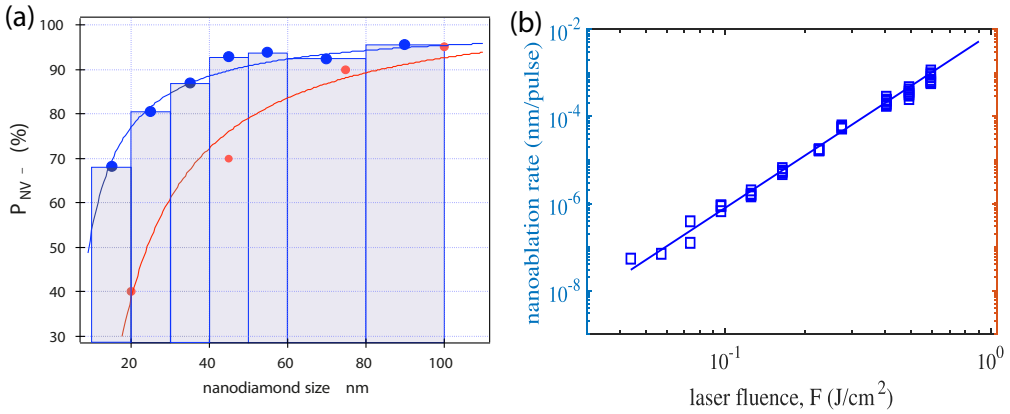


FIGURE 2.3: (a) Proportion of negatively charged NV defects P_{NV^-} as a function of nanodiamond size before (red) and after (blue) air oxidation [50]. (b) Surface etching rate of diamond under femtosecond excitation, adapted from [51].

The photo-stability of NV centres is unparalleled, especially when compared to other emitters functioning at room temperature [52]. The distance of the NV centre to the surface has been established as a key factor in maintaining photo-stable emission [53], with larger nanodiamonds displaying a greater proportion of NV^- to NV^0 emission, as seen in Figure 2.3 (a) [50]. However, high peak power pulsed excitation has been shown to induce photo-ionisation (to NV^0) [54] and nanoablation (Figure 2.3 (b)) [51]. Both of these effects involve complex charge transfer processes and photo-chemical changes to the diamond host material which are yet to be fully characterised. The neutral charge state displays photo-luminescence under the same excitation conditions, but the defect becomes optically inactive in the positively charged state, leading to complete quenching [55].

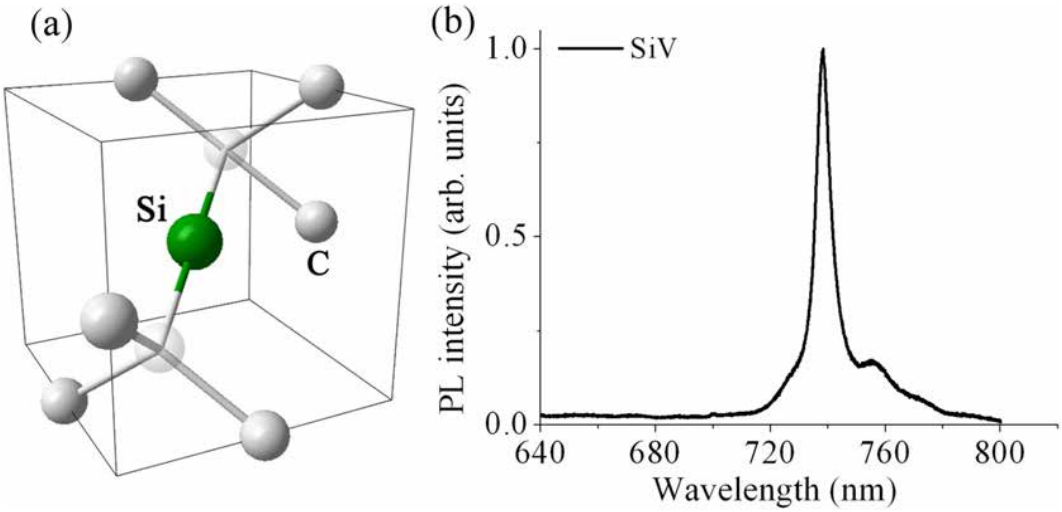


FIGURE 2.4: (a) Crystal structure of the SiV centre in diamond. (b) Room-temperature PL spectrum showing the ZPL at 738 nm. Reproduced from [25].

2.2.2 Silicon-Vacancy Centre

The negatively charged silicon vacancy defect (SiV centre) is the most common silicon defect in diamond and presents many advantages compared to NV centre. It is formed of a silicon atom splitting two vacancies (Figure 2.4 (a)) and possesses inversion symmetry. Due to this, the SiV is less susceptible to local environment fluctuations. SiVs display single photon emission, with a ZPL centred at 738 nm (Figure 7b). In contrast to the NV centre, the SiV's ZPL is much stronger with a DW factor of ∼0.7 [25]. This narrow spectrum would minimise pulse dispersion in optical networks compared to the NV centre. Moreover, the emission is mostly linearly polarised, even at room temperature - a property that is highly desirable in quantum cryptography. The excited state lifetime is extremely short (∼1 ns), but this is associated with significant non-radiative decays leading to a low quantum efficiencies of ∼0.05 [56, 57]. Regardless, the brightest count rates observed from SiV centres are up to 6 Mcts/s [56, 57].

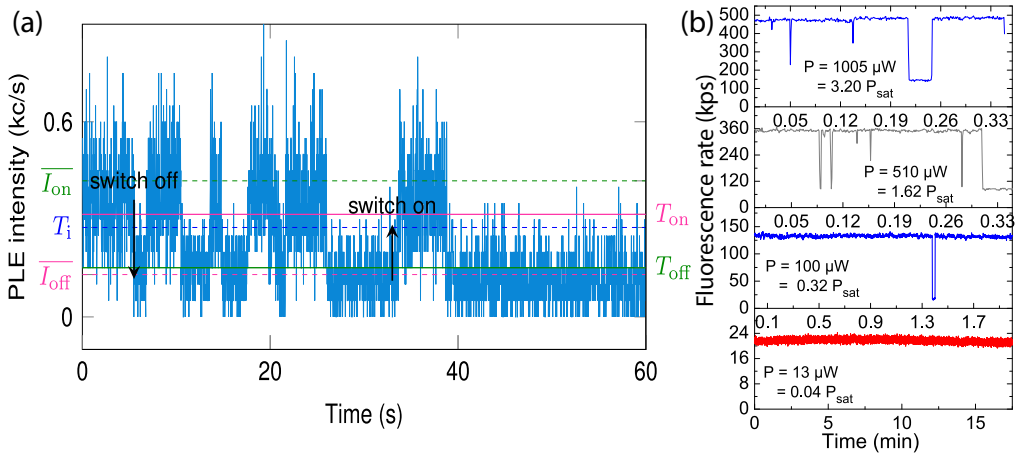


FIGURE 2.5: (a) Blinking of SiV^- fluorescence under resonant excitation at 30 nW, where the SiV centres were observed to change between two discrete fluorescence levels [62]. (b) Fluorescence time trace of SiV^- centres showing increased instability with increasing laser powers. Adapted from [57].

Unfortunately, the incorporation of single silicon atoms into nanodiamonds is extremely challenging. Silicon defects occur rarely in natural diamond, but the presence of silicon substrates in CVD grown diamond commonly leads to silicon defects being formed in the diamond. For diamonds grown on silicon or silica substrates, silicon atoms diffuse into the crystals and form clusters of inseparable SiVs [58, 59]. Though there are methods to reduce this effect, such as creating free electrons using a blue laser and surface treatments for greater impurity control - these are added complications for practical systems which are unnecessary for the NV centre. However, stable SiV centres in nanodiamonds have been recently successfully fabricated by methods such as wet milling from polycrystalline diamond films [60] and HPHT processing of hydrocarbons and hydrocarbon-silane compounds [61].

Despite the SiV possessing inversion symmetry, the shielding effects of the native symmetry of the defect are reduced as the centre becomes more distorted. This results in

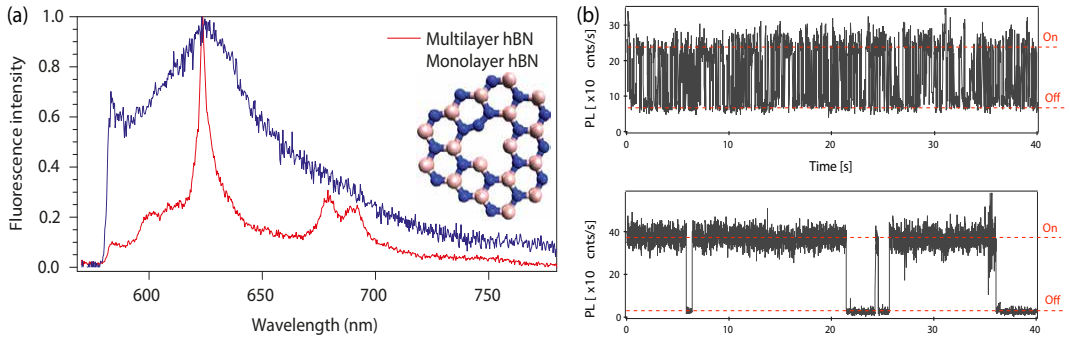


FIGURE 2.6: (a) Room-temperature PL spectra of a defect centre in monolayer and multi-layer hBN. Inset shows an illustration of the hBN nitrogen anti-site defect. Reproduced from [32]. Two examples of typical PL time traces recorded from different individual defects in a high-purity hBN crystal at an excitation power of 10 μW. The switching rate between the on and off states varies significantly from one emitter to another. Reproduced from [64].

additional coupling to phonons which broaden the ZPL emission [60, 62]. The linewidth and position of the SiV ZPL is therefore affected by strain in the diamond lattice due to modified electron-phonon coupling [60]. The ZPL position can vary between 730 – 750 nm for different different SiV centres due to individual stresses [31]. In addition to this, SiVs in nanodiamonds do not display the same photo-stablity as NVs under excitation (Figure 2.5) [63]. Blinking is generally related to the temporary loss of photo-excited electrons or charges which influence the defect's charge state [57]. Impurities and dislocations also act as trap charges and therefore also influence the defect's charge state [60]. The SiV centre's neutral state fluoresces weakly with a ZPL at 946 nm and is thought to be the origin of the defect's blinking and eventual photo-bleaching [62]. Surface treatments may be used to enhance the stability of photo-stable SiV centres [57].

2.3 Hexagonal Boron Nitride

Atomically thin van der Waals materials are emerging as burgeoning platforms which offer novel properties that enable a broad range of optical, electro-optical and quantum-optical functionalities [65–67]. Several of these two-dimensional materials have displayed single photon emission, including transition metal dichalcogenides (TMDs) such as tungsten diselenide (WSe_2) [16]. The defects are usually attributed to localised weakly bound excitons within a relatively small band gap ($\sim$1 – 2 eV) and so only function at cryogenic temperatures [68]. hBN is a wide bandgap semiconductor and exhibits unique electronic properties, high thermal conductivity and chemical inertness [69]. Analogous to graphene, 2D hBN features a honeycomb structure with sp^2 covalent bonding of boron and nitrogen. Due to its bandgap of 5.95 eV, hBN is a potential host to several optical defects which may be sufficiently deep within the band gap to be isolated individually by sub-bandgap excitation [69]. In 2016, Tran *et al.* reported stable room temperature single photon emission from multi-layer flakes of hexagonal boron nitride [32]. Initial density functional theory investigations believed the defect to be an anti-site nitrogen vacancy (N_BV_N), where a nitrogen atom is found at a boron site neighbouring a vacancy (Figure 2.6 (a) inset) [32, 70]. Several techniques have been used to fabricate the defect, including electron beam irradiation [71] and ion implantation [72], plasma etching [73], followed by (or purely just) thermal annealing [74]. These methods provide experimental evidence that the defect originates from a native vacancy. As subsequent annealing leads to a random distribution of emitters, laser writing has also been utilised to produce localised emitters [75].

The defect exhibits varying photo-stability, emission wavelength and ZPL linewidth suggesting the optical dynamics are potentially associated with the local environment of the emitter [64]. Figure 2.6 (a) shows the emission spectrum of the defect in both mono- and

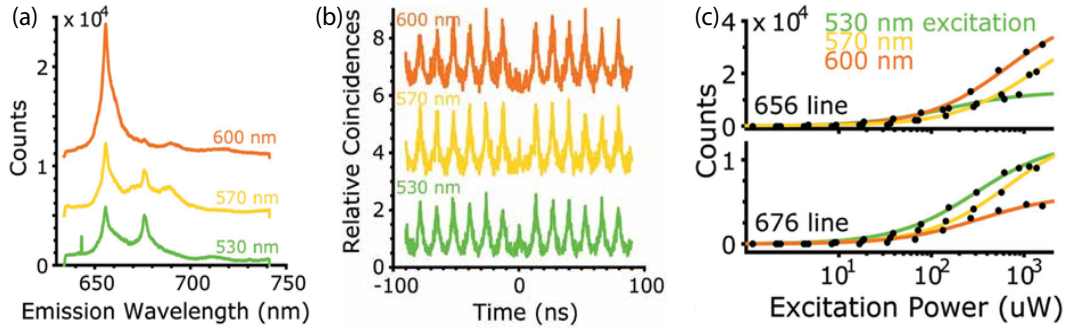


FIGURE 2.7: hBN emission properties with varying excitation wavelength. (a) Emission spectrum showing two distinct peaks at 656 and 676 nm. (b) HBT measurements show improving single photon emission as the emission at 656 nm becomes more dominant, showing the presence of two emitters within the same focal spot. (c) Saturation measurements for the two emission lines, showing a change in the saturation count rate with excitation wavelength. Reproduced from [76].

multi-layer hBN. Much like in diamond where the NV and SiV centres in larger nanodiamonds display greater photo-stability, Tran *et al.* found that multi-layer flakes exhibited improved spectral properties compared to mono-layer flakes (Figure 2.6 (a)) [32]. The multi-layer defect displays a narrow ZPL (2 – 5 nm) generally found between 400 – 800 nm, with red-shifted phonon side bands and a DW factor of ∼0.8 [77]. Grosso *et al.* modelled tuning of the emission ZPL by applying strain along varying crystal axes, confirming strain as a cause for the deviating ZPL position [78]. The asymmetry of the ZPL is associated with phonon interaction [79], while the PSB energy shift corresponds to a well known phonon mode in hBN [80, 81]. The excited state lifetimes are between 2 – 5 ns, resulting in saturation counts of 2 – 5 $\times$ 10^6 cts/s, brighter than those typically recorded from NV centres and comparable to the brightest SiV centres. Single photon correlation measurements reveal photon bunching ($g^{(2)}(0) > 1$) indicating the presence of a non-radiative relaxation pathway with a long-lived metastable state [64]. Most hBN defects exhibit pronounced blinking behaviour as shown in Figure 2.6 (b). Termination by high quality Al_2O_3 has shown promise as a means to stabilise hBN emission [82].

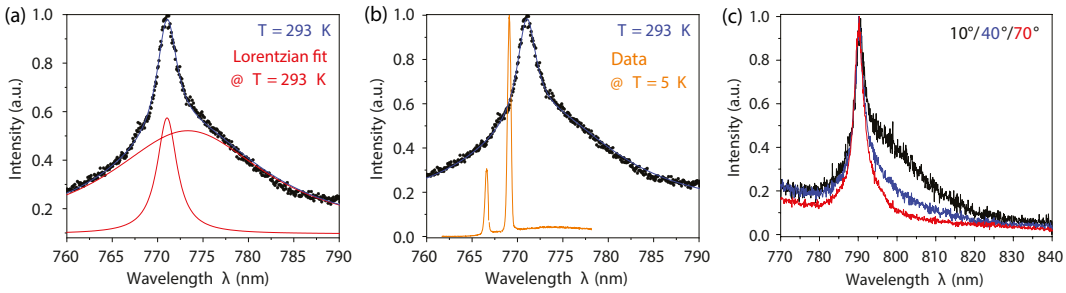


FIGURE 2.8: PL spectra of a typical emitter in hBN at room (a) and cryogenic temperature (b). The black dots are the measured data, with the blue lines represent the bi-Lorentzian fits to the data at room temperature. The two red lines of (a) represent the individual Lorentzian fits of the two transitions. The orange curve in (b) is the emission spectrum at 5 K. (c) Polarisation dependent emission spectra of a typical hBN emitter. Reproduced from [83].

Schell *et al.* have shed light on the defect's previously elusive electronic structure [76] (Figure 2.7). By varying the excitation wavelength away from conventional 532 nm, differing emission spectra were observed, verifying the previous discovery of strong misalignment between absorption and emission dipoles [84] - indicative of a multi-level system. This work revealed the dependence of both the quantum and excitation efficiency on the excitation wavelength. This is a stark difference to pseudo-two-level systems like the NV centre where the quantum efficiency is independent of the excitation wavelength. In hBN, it appears that multiple states compete with the radiative decay channel for direct excitation. Schell *et al.* found defects with emission at 656 nm and 676 nm were most efficiently excited at 590 nm and 540 nm respectively. Using this optimised excitation, defects in hBN have an estimated quantum efficiency between 0.5 – 1 [76, 85]. The emission centre was thought to consist of a single linearly polarised dipole transition, with excitation and emission polarisabilities of 86 and 71 % [32]. However, the emission dipole is supposed to show near unity polarisability, which may infer the presence of another transition with different polarisation behaviour. In order to explain this, Bommer *et al.* have provided evidence of the hBN ZPL consisting of two independent electronic transitions,

where the asymmetric ZPL lineshape was reproduced by two Lorentzian lines (Figure 2.8 (a)). By cooling the defect to 5 K, the previously single ZPL transition shows two clearly distinguishable Gaussian lines (Figure 2.8 (b), indicative of an inhomogeneous broadening mechanism such as spectral diffusion. Figure 2.8 (c) shows polarisation dependent spectra, displaying a strong variation in the dominant transition lineshape. Therefore, if the two dipoles contributing to the ZPL have different relative polarisations, the defect will not display the expected unity emission polarisability.

2.4 Optical Resonator Approaches

Imminent quantum technologies will have demanding requirements on not only photon generation, but also collection and detection, especially for applications involving indistinguishable photons [40]. For example, advancements in the collection and detection rates of emitted photons from single defects will improve the sensitivity in metrology applications and allow quantum information to be processed faster. There are several strategies which have successfully demonstrated an increased collection efficiency [86], such as the use of solid immersion lenses (SIL) [87] and circular bulls-eye gratings [88]. This is specifically an issue for emitters within high refractive index host materials such bulk diamond, as efficient photon collection is hindered by refraction of the emitted light at the diamond-air interface [89].

The SIL method has been shown to deliver a factor of $\sim$10 enhancement in the collection efficiency with respect to bare diamond, improving to $\sim$30% [25]. By milling/etching a SIL with an equal refractive index onto the diamond surface, no refraction occurs. The range of angles over which light can be collected, defined as the numerical aperture (NA), is increased by this refractive index (Figure 2.9 (a)–(c)). This has resulted in count rates

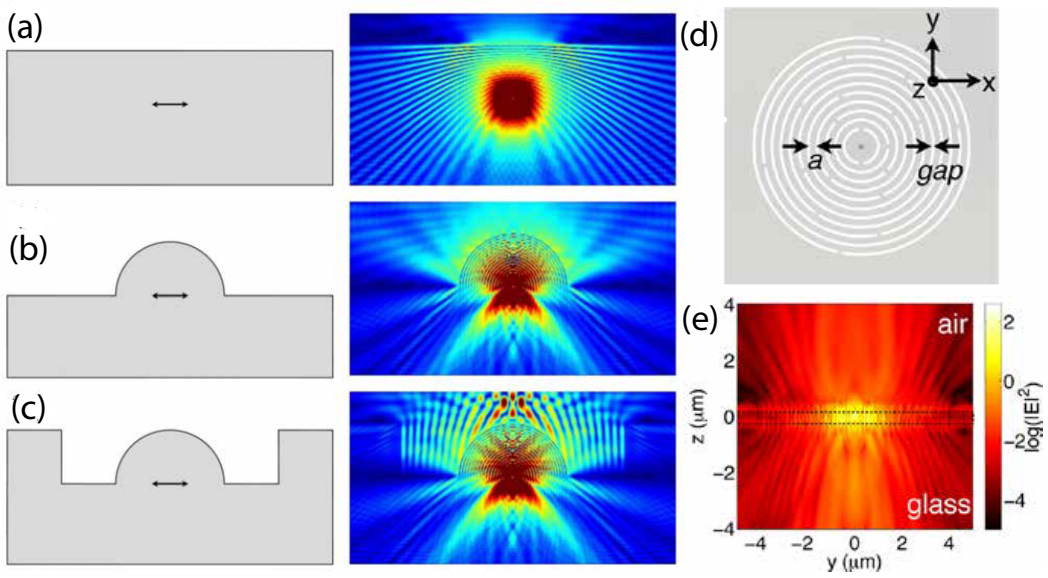


FIGURE 2.9: Electric field intensity plots from a dipole (a) beneath a diamond surface, (b) at the centroid of a SIL, (c) at the centroid of a SIL with trenches, reproduced from [87]. (d) Schematic of a circular grating and (c) the electric field distribution of a dipole at the centre of the bullseye, reproduced from [88].

of $\sim 1 \times 10^6$ cts/s for a single NV centre [25]. Both the premier results for both QKD and quantum entanglement with NV centres have utilised this method [40, 63, 90]. More recently, the circular bulls-eye grating has also being shown to deliver a collection efficiency of $\sim$30%. This structure consists of concentric slits etched into diamond, surrounding an NV centre, as seen in Figure 2.9 (d). With an appropriate grating thickness, the periodicity of the structure results in constructive interference for out of plane emission (Figure 2.9 (e)), increasing the collected photon count rate to $\sim 3 \times 10^6$ cts/s for a single NV centre [88].

There is however a more sumptuous approach, to not only increase the collection efficiency, but to also engineer the emission properties of the emitter. In 1946, Purcell

discovered a substantially altered spatial mode density inside a cavity, such that the spontaneous emission rate can be enhanced [91]. This is known as the Purcell effect. The Purcell factor F_P, describes the ratio between spontaneous emission in a cavity mode to that of free space:

$$F_p = \frac{3(\lambda/n)^3}{4\pi^2}\frac{Q}{V} \tag{2.1}$$

where Q is the quality factor, and V the cavity mode volume. The probability of spontaneous emission into the cavity is given by $\mathcal{B} = F_p/(F_p + 1)$. Hence in principle, for large Purcell factors, photon emission into a single spatial mode can be achieved with an efficiency near unity [34].

Cavity quantum electrodynamics (CQED) describes the interaction between photons and atoms within an optical cavity [1]. This fundamental field of science continues to have major applications in quantum technologies. In recent years, optical cavities with dimensions on the micron scale have been fabricated [92, 93]. This ensures that the resonant modes are well distributed throughout the emitter's spectrum [34], such that the emitter only couples to a single mode [94]. These microcavites come in a variety of architectures, each offering their own unique insight into CQED. In the following section, photonic crystal cavities and open-access microcavities will be discussed, as these offer small mode volumes and compatibility with the previously discussed emitters.

2.4.1 Photonic Crystal Cavities

A photonic crystal cavity (PCC) has a periodic variation (can be 1, 2, or 3–dimensional) of its refractive index. When this periodicity is on a length scale comparable to the photon wavelength, photons will propagate in discrete modes defined by the patterning of

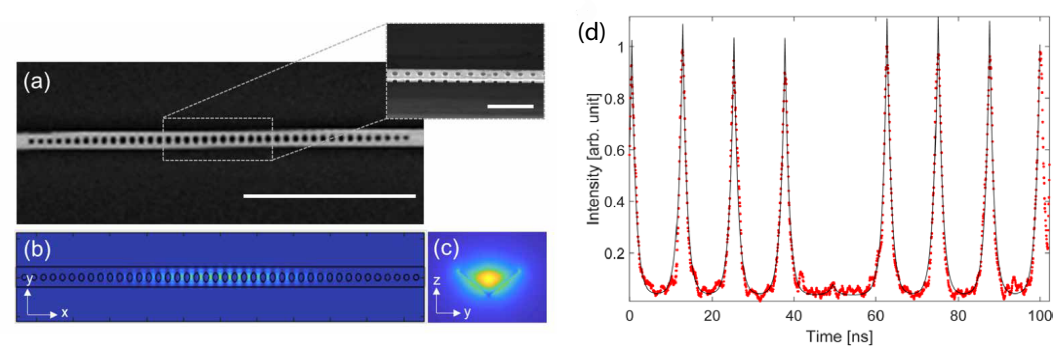


FIGURE 2.10: (a) SEM images of a nanobeam photonic crystal cavity fabricated from single crystal diamond. (b) Electric-field intensity profile of the fundamental cavity mode of the photonic crystal cavity. (c) Cross-sectional electric field intensity profile of the fundamental cavity mode of the photonic crystal cavity. (d) Second-order correlation measurement of the cavity coupled SiV^- center emission under pulsed excitation, yielding $g^{(2)}(0) = 0.04$. Reproduced from [17].

this environment [34]. When a disturbance is introduced to the crystal periodicity, an artificial emission channel is created [95]. These microcavity modes can have volumes of the order λ^3. A PCC with periodicity in all directions would be an ideal structure for the complete control of spontaneous emission [95]. However, this requires pattering at the optical wavelength, making these 3D structures extremely hard to fabricate. Regardless, progress has being made with 1D and 2D PCCs with these displaying small mode volumes and high Q-factors [34]. For 2D PCCs, the initial challenge was how to achieve confinement in the vertical direction. This was solved by the use of thin semiconductor slabs with a high refractive index, thus creating a vertical refractive index contrast [96]. This effect can be used to eliminate another dimension to create 1D PCCs [97, 98]. Diamond is such a material ($n = 2.4$) and also contains a host of optically active defects, such as the NV and SiV centres.

Theoretical studies have yielded potential Q-factors in the range 10^4 – 10^6 for these structures [96, 97]. Riedrich-Moller *et al.* achieved tunablity through repeated thermal etching, allowing coupling to an SiV centre [97]. The cavity modes were shifted by 15 nm without significant degradation of the quality factor [97]. This resulted in a Purcell factor of 20, and a factor of 2.8 increase in the intensity of the SiV ZPL [97]. Hausmann *et al.* have also demonstrated the tuning of PCC cavity resonances through Xe gas deposition [99]. In 2018, Zhang *et al.* fabricated a 1D PCC with a mode volume of V=$1.8(\frac{\lambda}{n})^3$ and Q ~10^4 [17] (Figure 2.10). SiV centres were grown by chemical vapour deposition into a single crystal plate of Type IIa diamond. Gas tuning was used to bring the cavity mode into resonance with one of the SiV transitions. The cavity-coupled emitter exhibited a 10-fold reduction in lifetime and 42-fold enhancement in the emission intensity [17].

2.4.2 Open-Access Microcavities

The open-access microcavity is made up of two independent highly reflective mirrors separated by empty space. The most basic design of a cavity is to arrange two planar mirrors opposite each other. If perfectly parallel, resonant light will be confined in one dimension with photons collected through the less reflective of the mirrors. A useful quantity is the finesse $\mathcal{F}$, which is related to the number of round trips made by the photons before leaking out of the cavity. Despite this simplicity, Dumiege *et al.* displayed a factor of 2 enhancement in collection efficiency of an NV centre [100]. The Fabry-Perot cavity was formed of two distributed Bragg reflectors (DBRs) with a moderate finesse ($\mathcal{F} \sim 60$). While this is a positive result, the microcavitation can be improved upon by creating a hemispherical surface on one of mirrors. A planar-hemispherical cavity provides longitudinal and transverse confinement and is used extensively in laser technology [101].

The challenge of this approach is to create these hemispherical features with sufficiently

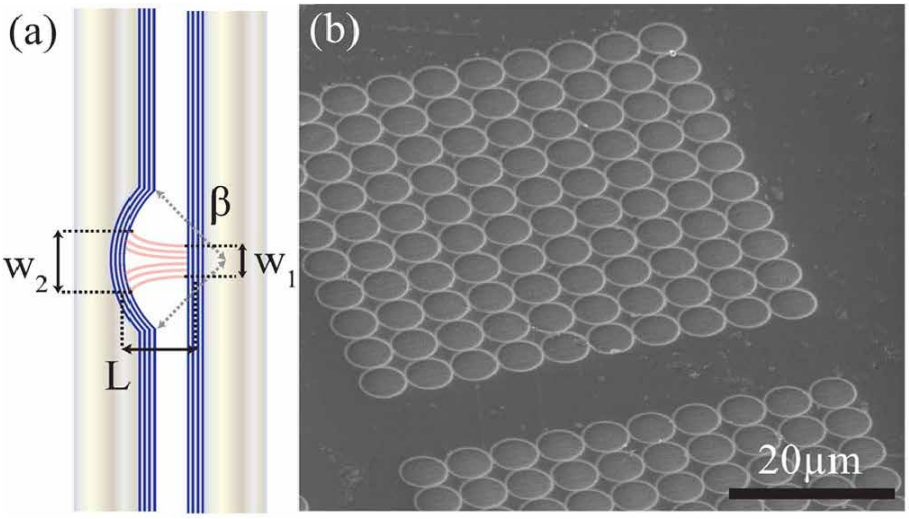


FIGURE 2.11: (a) Schematic of the planar-hemispherical microcavity. (b) Electron micrograph of an array of concave features milled into silicon. Reproduced from [92].

small radii of curvatures (β), to allow the minimisation of the mode volume, combined with high finesses. Several methods have being used to create these concave features. These include; the electrochemical deposition of microspheres for templating [102], bubble trapping in molten silica [103] and wet etching techniques [104]. These methods achieved finesses up to $\sim 10^3$ and RoCs down to $\beta = 10$ μm. However, the techniques of Focused Ion Beam milling (FIB) and CO_2 laser ablation have now surpassed the others.

In 2010, Hunger *et al.* used a pulsed CO_2 laser to ablate the surface of silica substrates, leaving concave imprints on the surface [105]. The laser-induced heating causes melting and evaporation, resulting in an extremely low surface roughness and high finesse cavities ($\mathcal{F} \sim 10^5$). The laser wavelength is 10.6 μm and this provides the diffraction limit for the this technique, with the smallest RoCs achieved being 13 μm [106, 107]. Also in 2010, Dolan *et al.* demonstrated even smaller features using FIB milling (Figure 2.11) [92], providing more precise control than the CO_2 ablation method. Features with $\beta = 5$,

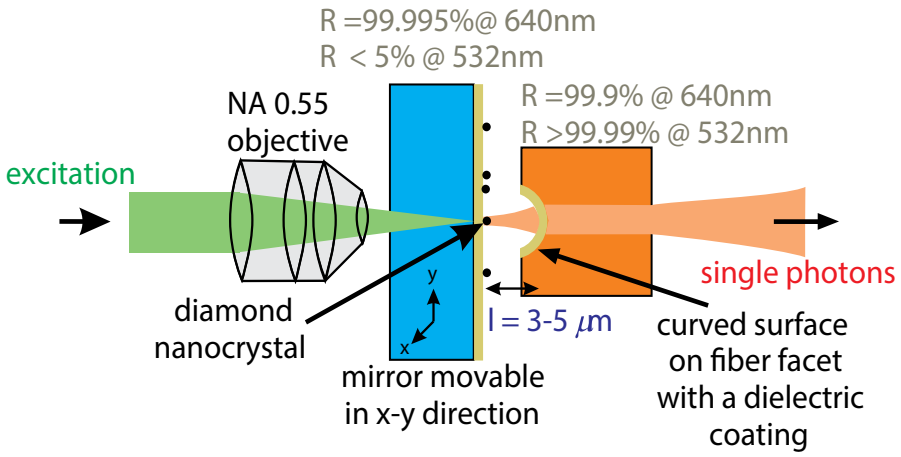


FIGURE 2.12: Fabry-Perot cavity consisting of a concave mirror on a fiber facet and a plane mirror onto which NDs have been spin coated. Reproduced from [109].

12 and 25 μm were milled onto silica substrates [92]. Since then features of $\beta = 1.5$ μm have being created [93], with finesses of $\sim 10^4$. These techniques have produced mode volumes of $2.3(\frac{\lambda}{n})^3$ and $1.9(\frac{\lambda}{n})^3$ respectively [108].

The first experiments coupling a single NV centre to open-access microcavities were performed in 2013 by Albrecht *et al*, using a fibre integrated cavity [109] (Figure 2.12). These experiments were performed at room temperature, where the NV-cavity coupling proceeds within the bad emitter regime of CQED. The effective Q-factor will always be limited by the broad NV emission spectrum, as only a fraction of the emission is coupled to a cavity mode. However, the broad nature of the NV emission spectrum allowed the single photon emission into cavity modes to be tuned over a large spectral range, presenting the possibility of using the NV as a wavelength-tunable single photon source.

The large RoC of their concave feature (71.6 μm) resulted in no increase in the spontaneous emission rate ($F_P = 10^{-2}$). However, they found the NV's homogeneous broadening helped channel emission into the cavity modes [109]. Saturation measurements for the free-space and cavity coupled emission showed photon spectral densities of 4.5 photons/(s GHz) and 41 photons/(s GHz) respectively, an order of magnitude enhancement for the cavity emission. If translated into a spectral window as wide as the TEM_{00} mode, the free space spectral density would yield a saturation count of 2 photons/s, 3 orders of magnitude smaller than the 3700 photons/s observed [109], confirming cavity enhanced emission.

To explain these results, Albrecht et al. developed a model of the NV-cavity coupling process, building on the work of Auffeves *et al.*, which describes solid-state emitter-cavity coupling [110, 111]. In this model, the NV centre is presented as a two-level system with excited state $|e\rangle$, and n vibronic ground states ($|g_0\rangle$,...$|g_n\rangle$), as seen in Figure 2.13 (a). The ZPL (γ_0) and PSB (γ_i) transitions undergo a natural broadening from the decay rate from the excited state. At room temperature, there are two additional line broadening mechanisms. Firstly, all transitions feature pure dephasing due to phonon scattering. Secondly, the PSB transitions experience further radiative broadening due to the short lifetimes of the levels $|g_i\rangle$ [109]. Figure 2.13 (b) shows the difference in width of the $|e\rangle \rightarrow |g_n\rangle$ transitions with these additional dephasing mechanisms accounted for.

With this description of the NV emission spectrum, the contributions of the individual transitions to the cavity coupling were accounted for. It is clear that tuning the cavity mode through the different PSB sub-levels will still lead to "feeding" of the emission into the cavity mode due to the width of these dephased transitions. Figure 2.13 (b) inset presents a schematic of the coupling mechanism. $\mathcal{R}_0$ represents the effective coupling rate between the cavity and ZPL transitions, which is a reversible process. The feeding

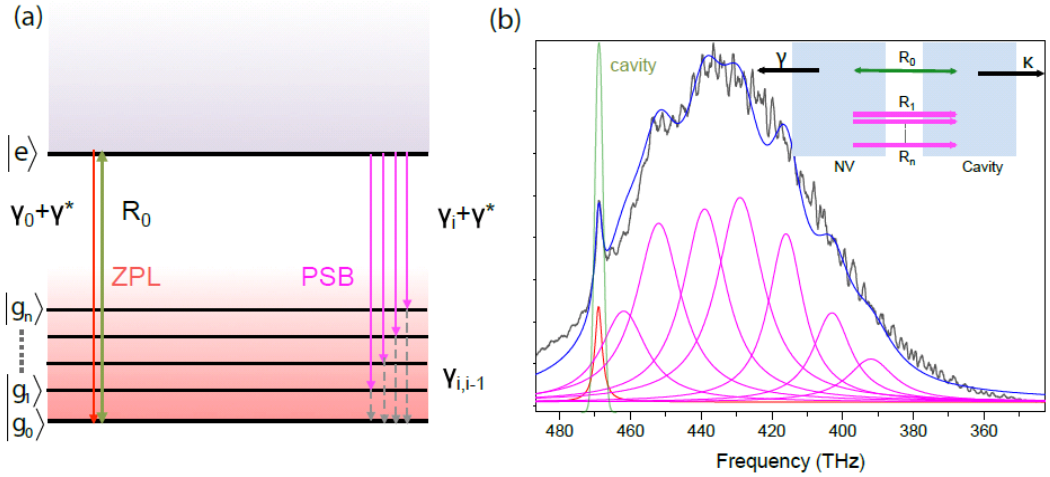


FIGURE 2.13: (a) NV optical transition from the excited state $|e\rangle$ to ground states $|g_i\rangle$. The associated natural and pure-dephasing rates $\gamma_i + \gamma^*$ are shown, including the additional rate $\gamma_{i,i-1}$ of the non-radiative vibronic transitions. (b) Experimental spectrum of the NV centre at room temperature. The spectrum (dark grey) is well reproduced by a series of Lorentzians, giving the ZPL (red) and PSB (pink). A cavity mode (green) is shown at the ZPL position. Adapted from [109]

of the cavity from the PSB transitions with rates $\mathcal{R}_i$ are uni-directional, and the coupling rate is defined as:

$$\mathcal{R}_i = \frac{4g_i^2}{\kappa + \gamma + \gamma_{i,i-1} + \gamma^*} \frac{1}{1 + (\frac{2\delta_0}{\kappa+\gamma+\gamma_{i,i-1}+\gamma^*})^2} \tag{2.2}$$

Where $\gamma = \gamma_0 + \gamma_1 + ...\gamma_n$. The final terms on the right hand side of Equation 2.2 describe the detuning of each transition from the cavity resonance. All the parameters in this model were determined experimentally (γ^* = 15 THz, $\gamma_{i,i-1}$ = 65 – 85 THz) and used to predict the efficiency of NV-cavity ZPL coupling at low temperatures.

Benedikter *et al.* have also used the fiber cavity to couple to SiV centres, but with a concave mirror size of β = 26 μm [112]. Due to their narrower emission spectrum (FWHM ~7 nm) and large DW factor (~0.8), SiV centres are more favourable to achieve cavity

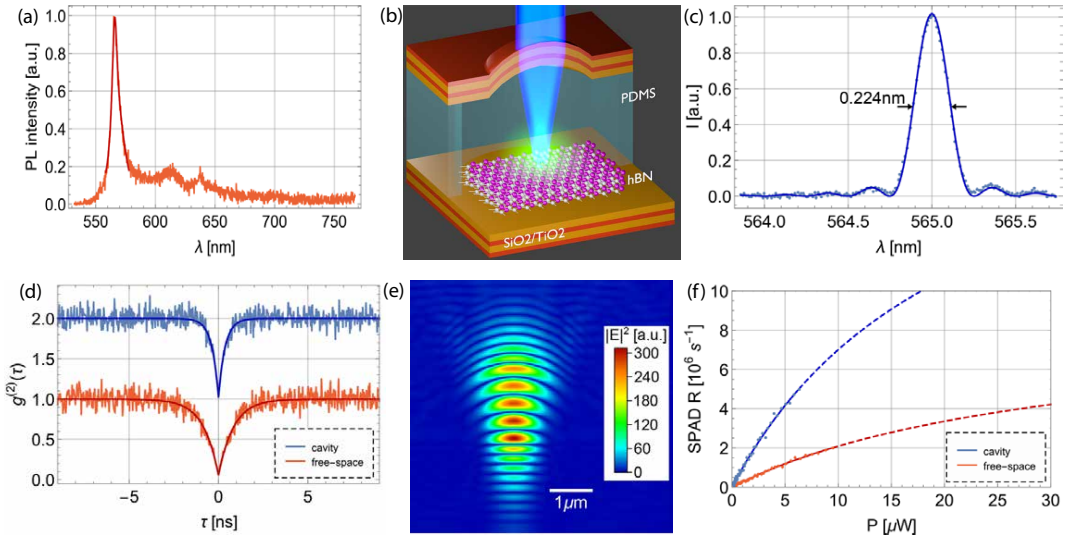


FIGURE 2.14: (a) Free-space emission spectrum from the defect showing a ZPL at 565 nm and FWHM of 6 nm. (b) The open cavity consists of a planar and hemispherical mirror, with a PDMS spacer used to set the cavity length. (c) The cavity narrows the emission spectrum down to a FWHM of 0.22 nm. (d) Second-order correlation measurement showing a decrease in $g^{(2)}(0)$ from 0.05 to 0.02, and shortening of the lifetime from 837 ps to 366 ps. (e) Electric field profile of a dipole emitter in the cavity obtained using FDTD simulations. The field maximum is located at the position of the dipole on the planar mirror. (f) The cavity increases the saturation count, and decreases the saturation power. Reproduced from [85].

enhanced emission. This fibre cavity displayed a finesse of $\sim 4 \times 10^4$ at 740 nm and mode volume $3.4\lambda^3$, leading to a collection efficiency of emitted photons of 90%. The spectral density was 5.4×10^4 photons/(s GHz), 20 times larger than any other previous room temperature experiments involving SiV centres. Although limited by the low quantum efficiency of the emitters, the cavity induced a 31% decrease in the excited state lifetime and a high photon count rate of 4.1 Mcts/s into a single cavity mode.

While hexagonal boron nitride can be used to fabricate photonic crystal cavities, the large variation in ZPL wavelength make the spectral matching to the cavity mode difficult [113]. Therefore, the open cavity platform is much more favourable for the enhancement

of hBN emission (Figure 2.14). Vogl *et al.* used a microcavity of planar hemispherical geometry with $\beta = 2.7$ μm. Both planar and featured mirrors were coated with 9 pairs of SiO_2/TiO_2 resulting in a measured reflectivity of 99.2% at 565 nm. The cavity mode linewidth of 0.169 nm at 565 nm corresponds to a Q-factor of $Q = 3345$. Multi-layer hBN flakes were fabricated using an oxygen plasma as this is known to create defects with ZPLs between 550 – 570 nm [73], before transfer onto the planar mirror. A PDMS film was sandwiched between the two mirrors to lock the cavity to a chosen length. This film compressed linearly with the driving voltage of the actuator, giving a cavity mode tuning resolution of 102 nm/V. The presence of the cavity induced a decrease in the excited state lifetime from 837 ps to 366 ps, and the quantum efficiency of the defect was calculated to be 51%. The cavity also modified the saturation behaviour, with an increased saturation count rate at lower excitation power, due to both the Purcell effect and enhanced collection efficiency of the emitted photons. The use of a lower excitation power assists the stability of the defects and no blinking or bleaching was observed [85]. Although not specified, the saturation count of the hBN-cavity device appears to be $\sim 2 \times 10^7$ cts/s, the brightest value achieved for any room temperature source.

2.4.3 Micropillar Enhanced QD Source

The most prominent single photon sources displaying the best overall performance are semiconductor quantum dots (QD). Self-assembled epitaxial QDs have been widely investigated, with a large variety of materials displaying emission from UV to near infrared spectral range [114]. Depending on the bandgap of the material, single photon emission can be achieved at temperatures ranging from room temperature (nitride III-V) to cryogenic (InGaAs). The most substantial progress has been made using III-V semiconductors, with InAs/GaAs as the most popular choice of material. InAs and GaAs are both covalently bonded direct-bandgap semiconductors, with bandgap energies of E_g(InAs)

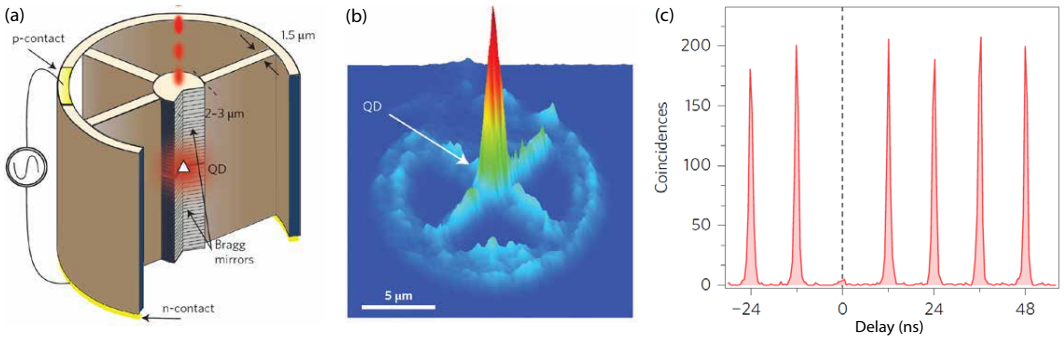


FIGURE 2.15: (a) Schematic of the micropillar-coupled QD. (b) PL map of the connected device, with the bright emission at the centre arising from the coupled QD. (c) Second-order correlation measurement of the device at 2.45P$_{sat}$, showing near-perfect single photon emission with $g^{(2)}(0) = 0.024$. Reproduced from [27]

= 0.43 eV and E_g(GaAs) = 1.52 eV at 4 K, and a 7% lattice mismatch between them. The deposition of InAs on GaAs leads to the formation of a wetting layer, a planar layer which is bi-axially compressed to the GaAs lattice [115]. As crystal growth proceeds, the accumulated strain increases and the energy of the system is minimised by the creation of Indium rich islands [116]. These islands are 10 – 30 nm laterally and 2 – 5 nm out of the plane [117]. The epitaxial growth of GaAs on top of these islands leads to three-dimensional confinement, yielding optical transitions between 900 – 1000 nm at 4 K.

These QD sources may be excited both optically and electrically [118, 119]. With electrical excitation, QD sources are not limited by the repetition rate of the pump laser and can be excited at rates up to 1 GHz [120]. Because of the high refractive index of GaAs ($n \approx 3.5$), only a small fraction of the QD emission can be collected (0.5% for a 0.5NA objective)[121]. This necessitates the use of an optical cavity, to not only increase the emission rate, but improve the extraction of these photons into a useful mode [34, 122, 123]. These QDs have large optical dipoles, and narrow spectral linewidths resulting in a good coupling to guided optical modes. Control of the spontaneous emission of QDs was

first demonstrated in the late 90s and early 2000s. This has been developed and demonstrated for single QDs in micropillar, microdisk and PCC cavities [24, 124]. Bennett *et al.* used a simple 12-layer planar semiconductor cavity to increase the collection efficiency from 0.5% to 2.6 $\pm$ 0.3%. This approached was further developed by using micropillar and oxide-confined microcavites, improving the collection efficiency to 14 $\pm$ 1% at an excitation rate of 80 MHz [123, 125].

In 2017, Somaschi *et al.* demonstrated near-optimal single photon emission from an electrically driven InGaAs QD coupled to a micropillar cavity at 4 K (Figure 2.15) [27]. The micropillar cavity induced a high extraction efficiency and the single photon efficiency at the first lens was measured as 60%. When driven at an excitation rate of 500 MHz, the source can deliver a single photon count rate of 300 Mcts/s, far superior to the sources discussed in the previous section (Table 2.1). Under resonant excitation, the single photon purity and indistinguishability reached values of $g^{(2)}(0) = 0.0028$ and $M = 0.9956$ [27]. The first experiment using this source displayed Boson sampling up to five orders of magnitude faster than any previous implementation using heralded photon sources [126]. With this achievement, the QD-micropillar system has been commercialised and is available for procurement from Quandela [28].

2.5 Conclusion

This chapter has discussed the key characteristics of the most prominent solid-state emitters. The ideal single photon source based of one of these emitters must meet several requirements, with photo-stability and room temperature functionality as imperative prerequisites for practical functionality. The most promising emitter is the nitrogen-vacancy centre in diamond, as it exhibits photo-stable single photon emission at room temperature

Source	Brightness (cts/s)	Lifetime (ns)	Temperature	Linewidth (nm)
NV[127]	$\sim 5 \times 10^5$	30	RT	~ 70
NV-SIL[128]	$\sim 1 \times 10^6$	18	RT	~ 70
NV-Cavity[129]	$\sim 9 \times 10^4$	19	RT	0.35
NV-Cavity[130]‡	$\sim 2 \times 10^6$	11	RT	16
SiV[56]	$\sim 3 \times 10^6$	~ 1	RT	~ 1.5
SiV-Cavity[112]	$\sim 4 \times 10^6$	~ 0.5	RT	0.04
hBN[32]	$\sim 4 \times 10^6$	~ 3	RT	~ 4
hBN-Cavity[85]	$\sim 2 \times 10^7$	0.36	RT	0.22
QD-PCC[131]‡	$\sim 8 \times 10^6$	~ 0.16	4K	Lifetime-limited
QD-Micropillar[27]‡	$\sim 3 \times 10^8$	~ 0.10	4K	Lifetime-limited

TABLE 2.1: Summary of the achieved device specifications of solid-state single photon emitters, including the various cavity enhanced approaches. The brightness values quoted are detected values, unless specified with ‡ to show measured/predicted values after the first lens. The NV-based specifications are for nanodiamonds.

[39]. However, the excited state lifetime limits the brightness of the NV, and the emission spectrum is extremely broad (∼70 nm) - which enhances the effects of dispersion in optical networks [2]. Although single SiV centres are becoming easier to manufacture [62], the frequency of blinking and low quantum efficiency places a ceiling on deliverable device efficiencies [112]. Defects in hBN provide short excited state lifetimes, narrow emission profiles and potentially near unity quantum efficiencies under optimal excitation [76]. However, their proximity towards the surface leads to instability and provides an avenue for the quenching of emission.

In order to achieve a high device efficiency, an optical microcavity can be used to enhance the spontaneous emission rate of these emitters, while channelling this enhanced emission into well-defined spatial modes. Photonic crystal cavities and open-access microcavities have been discussed, with both systems offering mode volumes on the order of $\sim \lambda^3$ and Q factors in the range $10^4 - 10^6$ [93, 97]. One key feature that is required for a realistic cavity-coupled system is some method of tuning the cavity resonances. Even though

PCCs offer the lowest mode volumes, and can be constructed around a pre-characterised emitter, the technical overhead required to tune the cavity modes is not optimal [97]. The open-access microcavity enables tunablity of the cavity resonances far beyond those offered by other microcavity structures [34]. Moreover, the open geometry also allows direct comparison between emission properties of the same emitter before and after the use of the microcavity, providing direct evidence of the cavity enhanced emission [41, 129]. This resonator is compatible with any emitter which may be deposited on the mirror surface, with a variety of materials available to complement the emission wavelength. Therefore, open-access microcavities are well suited to aiding the drive towards the practical realisation of a true single photon source. The properties of the discussed emitters and cavity systems are presented in Table 2.1. It is clear that at present, QD sources provide the most optimal single photon characteristics. However, there is much still room for development with room temperature sources, which will present much simpler and robust alternatives for use in a wider range of environments.

3 |

Theoretical Background

3.1 Introduction

This chapter will outline the essential theoretical background required to describe the coupling of single defects to optical resonators. I will begin with a brief summary of optical transitions in solid-state systems in relation to their single photon emission properties. This is followed by a description of the planar Fabry-Perot resonator, where key cavity parameters such as the finesse and quality factor will be highlighted. To describe the optical modes of the planar-hemispherical cavity, the Gaussian beam will be presented, including the relationship between the Hermite-Gauss modes and the tailoring of light-matter interaction. This will lead to a discussion on the theory of CQED, compared to spontaneous emission in a free space optical density of states. It will be demonstrated that the optical microcavity can increase the optical density of states, leading to an enhancement in the spontaneous emission rate, known as the Purcell effect. Finally, the chapter will conclude with the consequences of the Purcell effect on single photon emission from solid-state emitters in the "bad emitter/good cavity" regime.

3.2 Solid-State Emitters

The electronic properties of solid-state materials are typically described by their band structure. Materials such as diamond and boron nitride exhibit extremely large band gaps, making them predominantly optically transparent. However, the presence of impurities or defects can create discrete energy levels within the band gap. These defect states may be accessible by optical excitation, behaving as pseudo-atomic systems located within a host matrix. Following excitation, the characteristic length of time before decay to the ground state is known as the excited state lifetime τ. This lifetime is described as the inverse of the sum of all possible decay routes from the excited state $\tau = (\sum_i \gamma_i)^{-1}$, where the index i labels the different decay channels. The decay channel of most interest is the radiative decay channel, in which a photon is emitted as a means of relaxation, with a decay rate γ_{rad}. We can define the quantum efficiency as the proportion of radiative decay to all decay processes:

$$QE = \frac{\gamma_{rad}}{\gamma_{rad} + \gamma_{nr}} \tag{3.1}$$

Where γ_{nr} describes all the non-radiative decay channels. For a homogeneous transition, the linewidth of the emission profile will be a Lorentzian of linewidth (FWHM) $\delta\omega = \frac{2\pi}{\tau}$. This natural broadening is a direct result of the energy-time uncertainty [132, 133]. It is more common for emitters to display additional broadening from inhomogeneous sources, most of which originate from the local environment of the emitter, such as fluctuating local fields due to the presence of charge traps. Therefore, emitters at room temperature rarely display lifetime-limited linewidths.

This direct transition from the excited state (E_1) to the ground state (E_0) is commonly referred to as the Zero Phonon Line (ZPL). Unlike in atomic systems, solid-state emitters regularly display vibronic structure, where radiative transitions occur via the assistance of

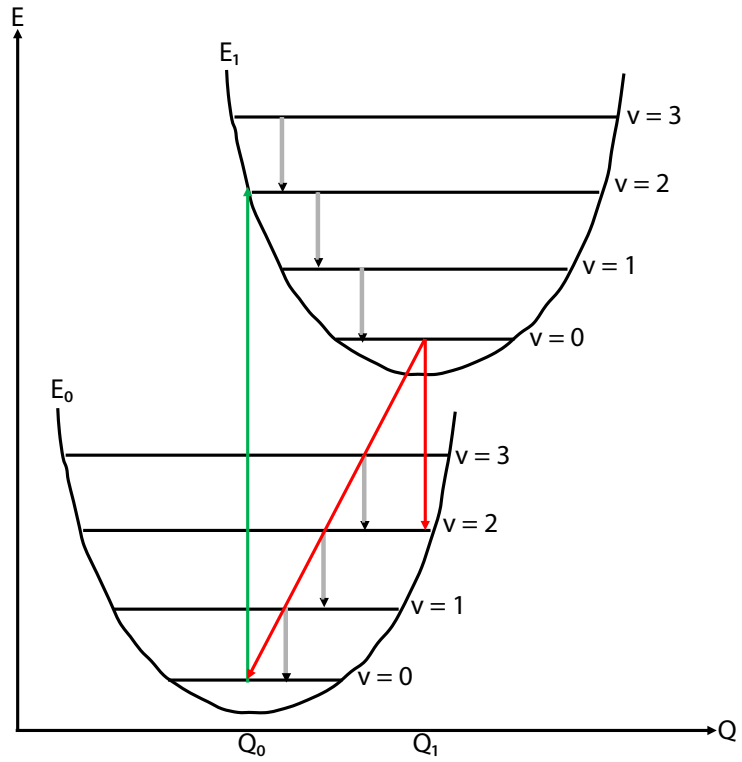


FIGURE 3.1: Franck-Condon configuration diagram of solid-state systems. E_0 and E_1 are the ground and excited electronic states, which have a harmonic dependence on the generalised nuclear coordinates Q_n. The vibrational manifolds for each state are represented by the horizontal lines. The diagonal line represents the zero vibration transition (ZPL), with the dashed lines representing non-radiative vibrational transitions.

lattice phonons (Figure 3.1). The Born-Oppenheimer approximation states that: *electron displacement occurs much more rapidly than nuclei displacement, due to the difference in their relative masses* [134]. Therefore, the nuclei are treated as static during the transition. Upon non-resonant excitation, an electron is promoted to a higher order vibrational state of the electronic excited state ($E_1, v > 0$). There is a redistribution of the electric charge, causing the nuclei to undergo a displacement from their original position (Q_0) to a new equilibrium position (Q_1). Energy is lost by rapid relaxation through the vibronic levels until equilibrium is reached, at the ground vibronic state of the excited electronic state ($E_1, v = 0$).

Relaxation from the ground vibronic state of the electronic excited state (E_1, v=0) can now proceed via a transition to an excited vibronic state of the ground electronic state (E_0, v>0). This phonon-assisted process results in the emission of photons with a lower energy than the ZPL, known as the phonon side band (PSB). The strength of PSB is dependent on the overlap of the vibronic wave functions involved in the electronic transitions. The fraction of light into the ZPL relative to the total emission is known as the Debye-Waller (DW) factor. Emitters with minimal nuclear rearrangement will have the greatest overlap of vibrational wavefunctions and maximal DW factors. For the NV centre, DW = 0.04, while $DW \sim$ 0.7 for the SiV and hBN defects.

3.2.1 Single Photon Emission

The NV and SiV centre in diamond, as well as defects in hexagonal boron nitride, exhibit optical transitions featuring a single electron between electronic states which result in the emission of single photons. A general statistical measure of single photon emission is the second-order correlation function $g^{(2)}(\tau)$ which is defined as:

$$g^{(2)}(\tau) = \frac{\langle I(t)I(t+\tau\rangle}{\langle I(t)\rangle \langle I(t+\tau)\rangle} \tag{3.2}$$

Where the brackets $\langle ...\rangle$ denote the time averaged value of the arguments. At long time delays, the correlation function tends towards unity for all types of light. This signifies a lack of correlation between photon detection events. For classical light, $g^{(2)}(0) \geq 1$, while for coherent light, $g^{(2)}(0) = 1$. Quantum emitters create single photons generally separated by the lifetime of the excited state, and this behaviour is known as anti-bunching. These single photons can be described as Fock states (or number states) $|\mathcal{N}\rangle$, where $\mathcal{N}$

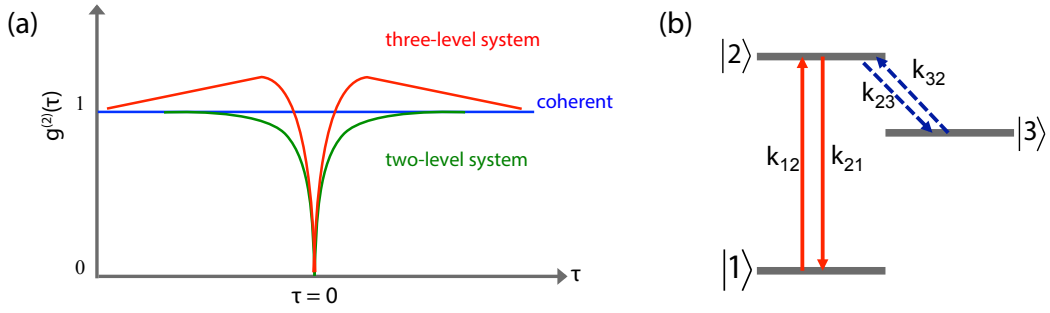


FIGURE 3.2: (a) HBT histogram behaviour for coherent light (blue), a two level quantum system (green) and a corresponding three level system (red). (b) An example three level system with transition the relevant transiton rates k_{ij} shown.

describes the number of quanta in the state. The correlation function at zero time delay is reduced to:

$$g^{(2)}(0) = 1 - \frac{1}{\mathcal{N}} \tag{3.3}$$

Therefore, a perfect source yields a value of $g^{(2)}(0) = 0$, while $g^{(2)}(0) < 0.5$ indicates a predominantly single photon emitter. However, these solid-state systems are non-ideal, especially at room temperature. They can display non-radiative decay pathways, such as inter-system crossing and forbidden transitions - which all cause a deviation from a simple two-level system. We must consider the effect of these mechanisms on the observed photon statistics. For the basic two-level system, the factors affecting the correlation function are the excitation rate and the spontaneous emission lifetime. At high excitation powers, it is often observed that there is increased pumping into metastable states. This results in photon bunching at intermediate time delays such that $g^{(2)} > 1$ (Figure 3.2). Both the excited and metastable state have an associated lifetime, τ_1 and τ_2. The solution for the second-order correlation function for the three-level system was derived by Kurtsiefer *et*

al. and expressed as [39]:

$$g^{(2)}(\tau) = 1 + c_1 e^{-\frac{|\tau|}{\tau_1}} + c_2 e^{-\frac{|\tau|}{\tau_2}} \tag{3.4}$$

In the low power limit, τ_1 tends towards the spontaneous emission lifetime of the excited state. The coefficients $c_{1,2}$ and $\tau_{1,2}$ reveal interdependencies on the inter-system crossing rates, and vary with the excitation pumping rate.

3.2.2 Saturation

Following spontaneous emission, the system has to be recycled into the excited state before another photon can be emitted. The rate constants k_{ij} seen in Figure 3.2 (b) are used to describe the transitions between the ground ($|1\rangle$) and excited state ($|2\rangle$). When subject to a suitable source of excitation enabling this transition to occur, the rate of excitation (k_{12}) is proportional to the excitation power (P_{ex}):

$$k_{12} = aP_{ex} \tag{3.5}$$

Where a is a constant of proportionality dependent on the characteristics of the excitation (e.g. polarisation) and the transition dipole moment. Ignoring effects such as ionisation or two photon absorption, the probability of subsequent photon absorption vanishes while in this excited state for the emitter lifetime τ. The populations of the ground (ρ_1) and excited state (ρ_2) sum to unity ($\rho_1 + \rho_2 = 1$). Ignoring coherences, the population dynamics are governed by the rate equations:

$$\begin{pmatrix} \dot{\rho}_1 \\ \dot{\rho}_2 \end{pmatrix} = \begin{pmatrix} -k_{12} & k_{21} \\ k_{12} & -k_{21} \end{pmatrix} \cdot \begin{pmatrix} \rho_1 \\ \rho_2 \end{pmatrix} \tag{3.6}$$

Under continuous excitation, the system reaches a steady state when $\dot{\rho}_1 = \dot{\rho}_2 = 0$. The equilibrium population of the excited state is given by:

$$\rho_2(t \longrightarrow \infty) = \frac{k_{12}}{k_{12} + k_{21}} \tag{3.7}$$

Using Equations 3.5 and 3.7, the photon emission rate I is defined as:

$$I(P_{ex}) = k_{21}\rho_2 = \frac{k_{21} \cdot aP_{ex}}{aP_{ex} + k_{21}} = \frac{k_{21}P_{ex}}{P_{ex} + P_{sat}} \tag{3.8}$$

Where the saturation power is defined as $P_{sat} = k_{21}/a$. From Equation 3.8, the maximal photon emission rate with $P_{ex} >> P_{sat}$ is $I(P_{ex} \longrightarrow \infty) = k_{21}$. This basic description gives insight into the physical process of saturation, allowing the comparison of different solid-state emitters. While this simple model fails to include the presence of additional levels like shelving states, the saturation behaviour remains the same, but with added dependencies on the rate constants between these new levels.

3.3 Optical Resonators

A good starting point for the discussion of optical resonators is the Fabry-Perot resonator, formed by two planar mirrors of a given reflectivity (Figure 3.3). A full description can be found in References [135] and [136]. Certain frequencies (ν_F) will satisfy the boundary conditions imposed by the two mirrors, and these are known as the resonant frequencies. For such a cavity with two mirrors separated by distance L, the resonant frequencies obey:

$$\nu_F = q\frac{c}{2L} \tag{3.9}$$

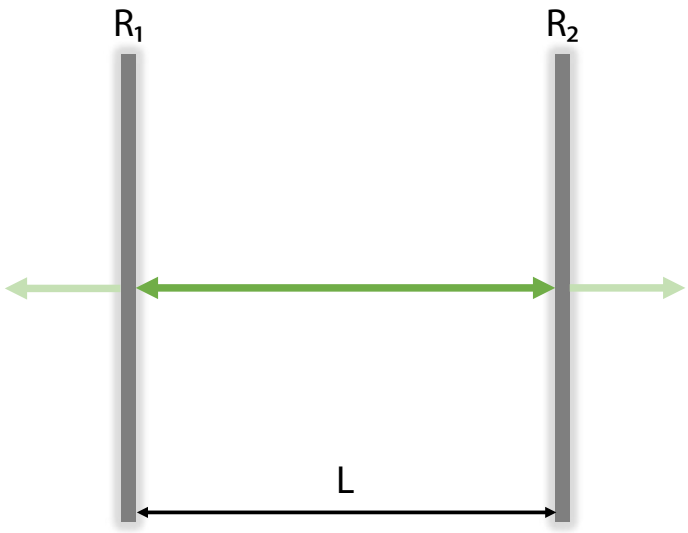


FIGURE 3.3: The Fabry-Perot optical resonator, formed by two opposing mirrors of reflectivity R, separated by distance L. Asymmetric reflectivities lead to transmission through the mirror and loss from the cavity.

where q is the number of antinodes between the mirrors, also known as the mode index. The separation between each consecutive resonant frequency is $\Delta\nu = \frac{c}{2L}$, and this is known as the free spectral range (FSR). Knowledge of the FSR allows the spectral calculation of the cavity length. Another key metric for the cavity is the finesse $\mathcal{F}$, which describes the number of round trips made by a photon before exiting the cavity. For a perfect cavity with mirrors of reflectivity $R = 1$, the finesse would be infinite (Figure 3.4). In reality, for cavities with $R < 1$, the finessed is defined as:

$$\mathcal{F} = \frac{\pi(R_1 R_2)^{1/4}}{1 - \sqrt{R_1 R_2}} \tag{3.10}$$

Although this expression is independent of the cavity length, there are often alternative means of intra-cavity scattering. These additional loss mechanisms can be described by

the total round-trip loss factor $\mathcal{L}$:

$$\mathcal{L} = 2\alpha_s L + ln\frac{1}{R_1} + ln\frac{1}{R_2} \tag{3.11}$$

Where α_s is the scattering coefficient due to the surface roughness of the mirror. For mirrors with high reflectivities ($R \approx 1$), the finesse is related to the total loss factor by:

$$\mathcal{F} = \frac{2\pi}{\mathcal{L}} \tag{3.12}$$

Therefore, electric field within the cavity is attenuated and decays at a rate related to the photon lifetime within the cavity τ_c by $\kappa = 1/\tau_c$. The cavity decay rate is a key parameter which will be discussed later in this chapter. The breakdown from this strict resonance condition results in a characteristic spectral linewidth $\delta\nu$;

$$2\pi\delta\nu_c = \kappa \tag{3.13}$$

The finesse can then be related to the cavity's spectral properties by:

$$\mathcal{F} = \frac{\Delta\nu_{FSR}}{\delta\nu} = \frac{\Delta\lambda_{FSR}}{\delta\lambda} \tag{3.14}$$

The Q-factor is a figure of merit that describes the ability of a cavity to store energy and allows a simple comparison between different cavity geometries. The Q-factor can be related to the finesse by:

$$Q = \frac{2\pi \times Maximum\ Energy\ Stored}{Energy\ Loss\ Per\ Cycle} = \frac{\nu}{\Delta\nu} = \frac{\lambda}{\delta\lambda} = q\mathcal{F} \tag{3.15}$$

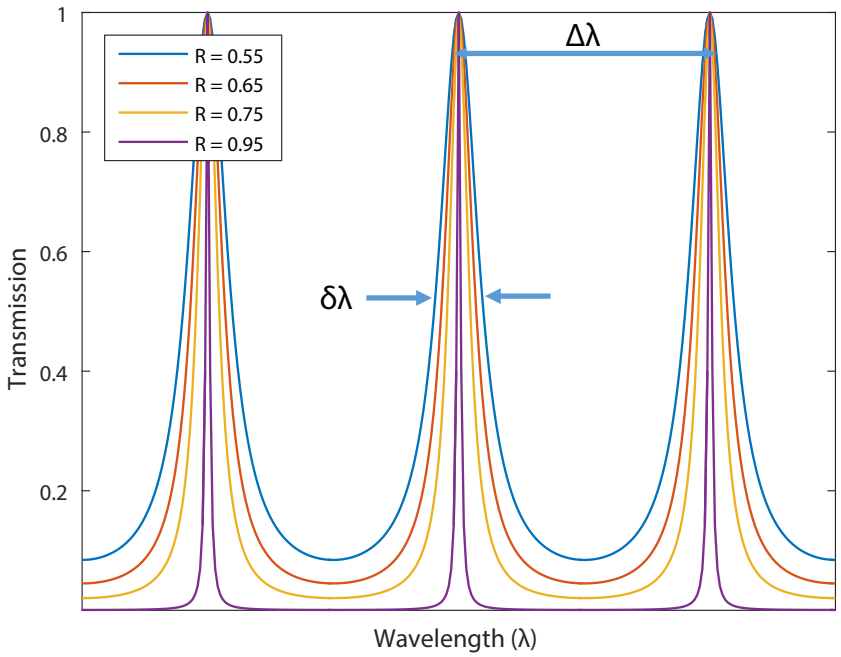


FIGURE 3.4: The mode spectrum of the Fabry-Perot resonator in terms of λ. As the reflectivites of the mirrors increase, the width of the Lorentzian line ($\delta\lambda$) decreases. The free spectral range $\Delta\lambda$ is also indicated.

In summary, the planar cavity has been used to introduce several key parameters. Optical resonators may be used to sample a large range of Q-factors with varying cavity length (or mode index). However, in order to achieve sufficient photon confinement and small mode volumes, spherical mirrors are required.

3.3.1 The Gaussian Beam

The spherical mirrors used in this thesis are well described by a paraboloidal waveform curvature, and thus the Gaussian beam fully characterises the optical modes of these resonators. The wavefront along the optical axis can be described by ray optics, but the wavefront normals are defined to deviate from the optical axis by a small angle (Figure 3.5). This is known as the paraxial approximation. The full derivation for the solution of the Gaussian beam can be found in Reference [136], and the most useful expressions

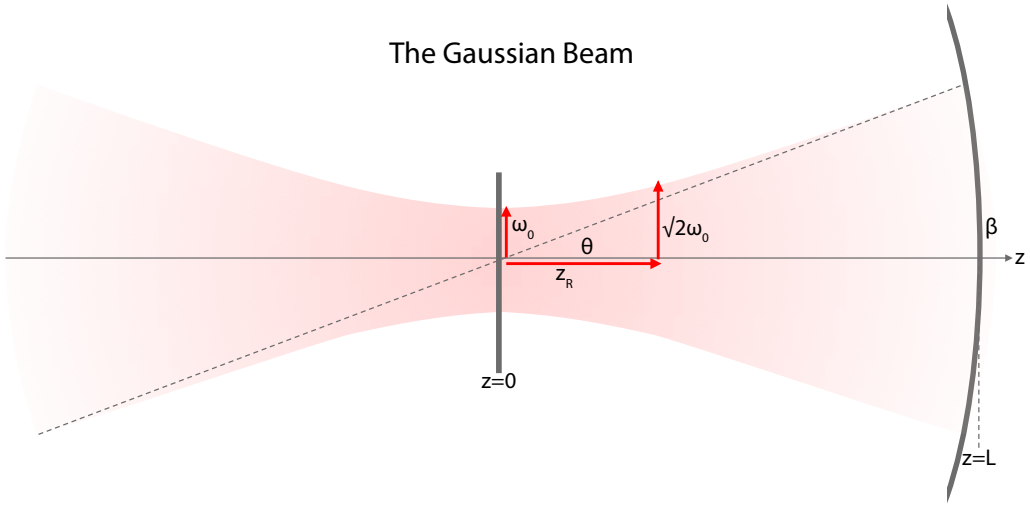


FIGURE 3.5: The Gaussian beam within a planar-hemispherical cavity. The beam waist $\omega(z)$ is minimum at $z = 0$. Away from the beam waist, the beam diverges with an angle θ. The hemispherical mirror is located at a cavity length $z = L$ with radius of curvature β.

will be presented. As the beam propagates away from it's focal point, it's behaviour can be described by the parameters beam waist $\omega(z)$ and radius of curvature $\beta(z)$ and Gouy phase $\zeta(z)$. In order to define these functions concisely, it is useful to define the Rayleigh range, z_R, which is the distance along the optical axis where the beam waist $\omega(z) = \sqrt{2}\omega_0$. The value of z_R can be shown to be:

$$z_R = \frac{\pi\omega_0^2}{\lambda} \tag{3.16}$$

With the Rayleigh range, the terms $\omega(z)$, $\beta(z)$ and $\zeta(z)$ can be expressed as:

$$\omega(z) = \omega_0\sqrt{1 + \frac{z^2}{z_R^2}} \tag{3.17}$$

$$\beta(z) = z + \frac{z_R^2}{z} \tag{3.18}$$

$$\zeta(z) = arctan\left(\frac{z}{z_R}\right) \tag{3.19}$$

The final useful entity is the divergence angle, which defines the numerical aperture (NA) of the beam. This is a particularly useful in determining the efficiency of cavity coupled emission to external optics. It can be expressed in terms of ω_0 by:

$$NA = sin(\theta) = sin\left(\frac{\lambda}{\pi\omega_0}\right) \tag{3.20}$$

Gaussian beams are ubiquitous in modern optics and this beam profile is also formed by planar-hemispherical cavity geometries. For this type of cavity, the beam waist is located at the planar mirror. The radius of curvature of the hemispherical mirror at a given cavity length completes the required boundary condition for Gaussian modes to be formed. Specifically, these modes are formed in the regime of $L \leq \beta$. More precisely, the mode stability condition is defined as:

$$0 \leq g_1 g_2 \leq 1 \tag{3.21}$$

Where $g_i = 1 - L_i/\beta_i$. For the mirror in Figure 3.5, $g_1 = 1$ as $\beta_1 \longrightarrow \infty$. Therefore, the mode waist on the concave mirror of radius of curvature β must be well within the bounds of the feature diameter in order to avoid clipping losses at the edge of the concave profile.

3.3.2 The Hermite-Gaussian Beam

The solutions for the Gaussian beam may also produce alternative solutions to those presented above, namely the Hermite-Gaussian beam. The Hermite-Gaussian beam describes

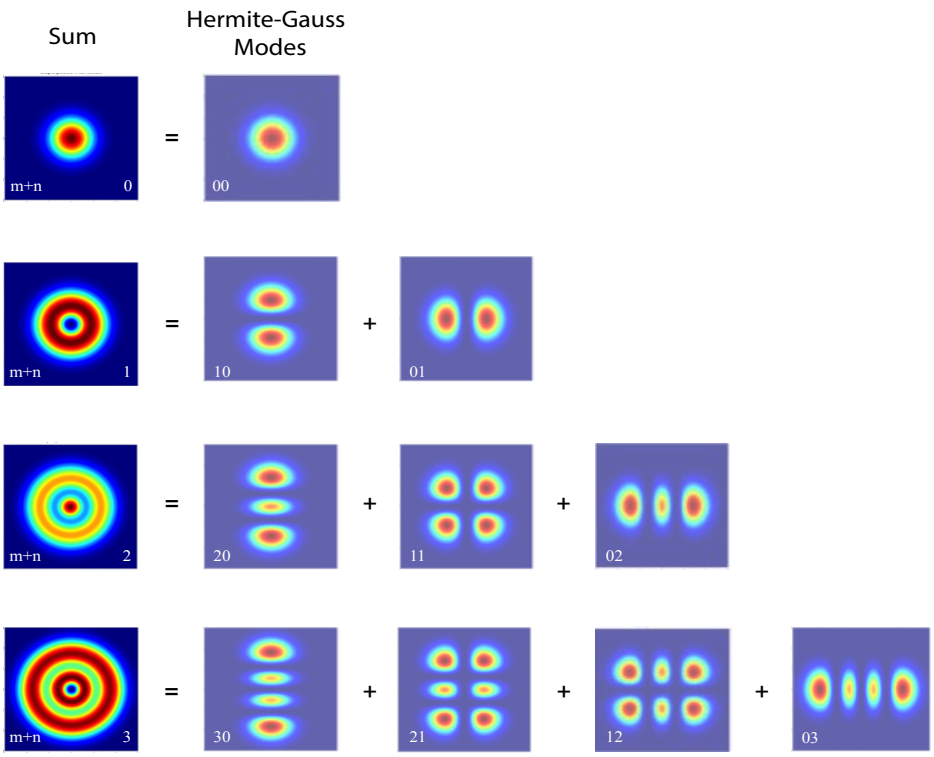


FIGURE 3.6: Transverse electric field distribution of the Hermite-Gauss modes. Under cylindrical symmetry, these are energetically degenerate and classified by the sum of their eigenvalues.

cavity modes with higher order solutions, known as transverse modes, as they provide additional structure in the x-y plane. This solution introduces the eigenvalues (m, n) of the Hermite polynomials. The sum of eigenvalues $m, n = 0$ delivers the lowest order solution, which recovers the original Gaussian beam solution. Therefore, $m+n$ provides a labelling method of "TEM$_{m,n}$", where TEM stands for Transverse Electric Magnetic.

The higher order transverse modes are made up of spatially distinct but energetically degenerate electric field profiles. Figure 3.6 shows the spatial distribution of these modes until the $m+n = 2$ index. The mode waist, which is defined as the point where the electric

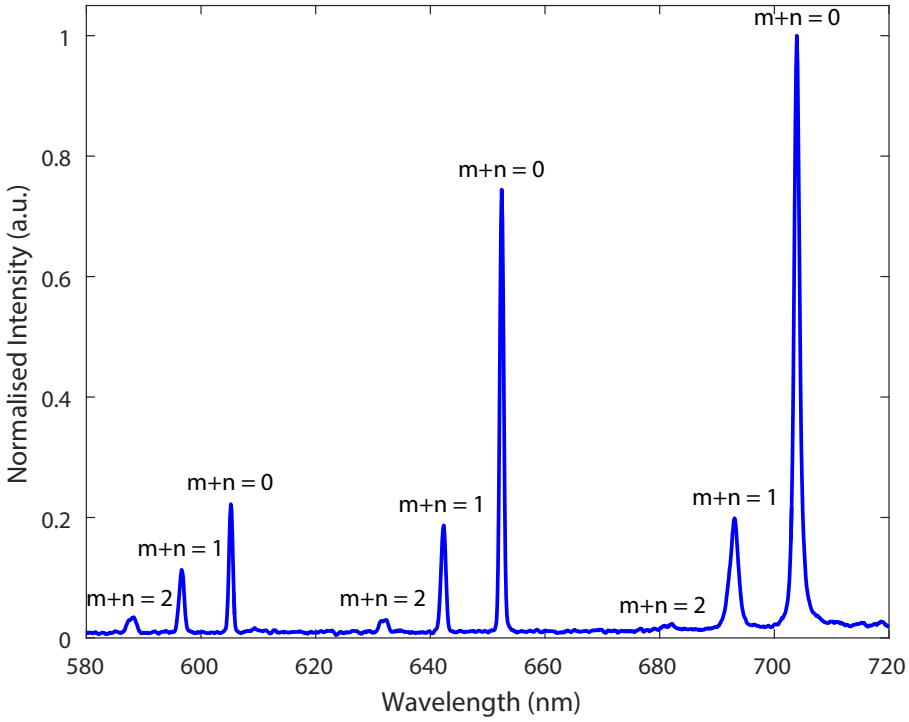


FIGURE 3.7: Transverse mode spectrum for a $\beta = 8$ μm feature at a cavity length of 4.4 μm. The peaks are labelled by the sum of the (m, n) eigenvalues for each longitudinal mode index q. The higher order transverse mode are energetically degenerate, and are composed of spatially separate Hermite-Gauss/Laguerre Gauss modes.

field intensity falls to $1/e^2$ of it's maximum value, decreases with a higher mode index. Consequently, this increased beam divergence reduces the coupling into external optics. The spectral profile of the longitudinal and transverse modes for a given mode number can be seen in Figure 3.7, where the higher order modes are at lower wavelengths relative to the TEM$_{00}$ mode. Both longitudinal (TEM$_{m+n=0}$) and transverse modes (TEM$_{m+n\geq 1}$) wavelengths are fully described by the equation:

$$\nu_{q,m,n} = \frac{c}{2L}\left[q + (m+n+1)\frac{arccos(\sqrt{g_1 g_2})}{\pi}\right] \tag{3.22}$$

The mode volume, V, of the electric field within the cavity is a final quantity required to

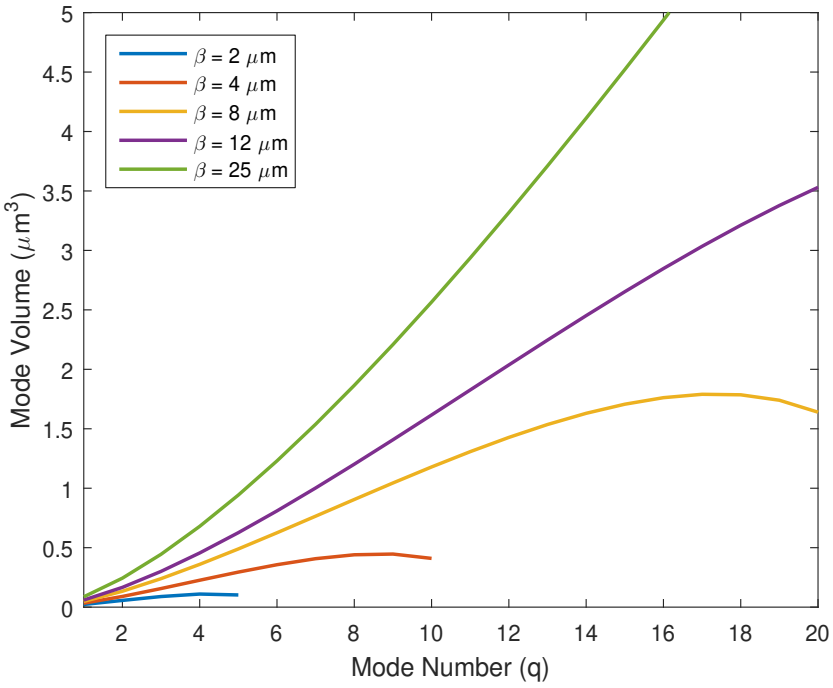


FIGURE 3.8: Mode volumes for different radii of curvatures using Equation 3.23, plotted as a function of mode number q for $\lambda = 690$ nm.

fully understand the emitter-cavity coupling experiments in this work. It can be derived by integrating the required Gaussian beam solution over the dimensions of the cavity. For a planar-hemispherical resonator, the result for the TEM_{00} is of a simple analytic form:

$$V = \frac{\pi\omega_0 L}{4} = \frac{\lambda L^2}{4}\sqrt{\frac{\beta}{L} - 1} \tag{3.23}$$

This mode volume includes the fraction of the field penetrating into the mirror layers which will be discussed further below. Figure 3.8 displays the anticipated mode volumes for cavities of varying radii of curvatures as a function of mode number. Theoretically, extremely low mode volumes down to 0.1 μm^3 may be reached, but achieving such short cavity lengths presents technical challenges.

3.3.3 Distributed Bragg Reflectors

Thus far, the resonators discussed have been ideal systems without consideration given to the materials necessary to create such near perfect systems. The best conventional silvered (or metallic) mirrors offer reflectivities of ∼95%, over a broad range of wavelengths. These mirrors provide sufficient finesses for broad emitters, which will dominate the effective Q-factor of the system, but they are not optimal for narrow emitters. In addition, the inherent auto-fluorescence of metallic mirrors limits the minimum of the $g^{(2)}(0)$ value. Distributed bragg reflectors (DBRs) do not display persistent auto-fluorescence and can be manufactured to produce a desired reflectivity at a given wavelength. DBRs are constructed from alternating layers of high and low refractive index materials with layer thicknesses of $\frac{\lambda}{4n}$, where n is the refractive index of each material and λ the required wavelength of maximum reflectivity. Their principle of operation are as follows:

- Light incident on an interface will be partially transmitted and reflected.
- Propagation across a boundary from a low to high index medium results in a π phase shift of reflected light, and does not occur in the opposite scenario.
- Each layer possesses a thickness of $\frac{\lambda}{4n}$ which ensures the reflected component from each interface is in phase.
- Stacking multiple layers together creates reflectivities approaching unity.

The reflected and transmitted components at each interface are governed by the Fresnel equation, with escalating complexity as the number of interfaces increases. A full mathematical description can be found in Hecht [135]. It is assumed that the dielectric materials are non-magnetic. The boundary conditions of Maxwell's equations require the tangential component of the electric field $\mathcal{E}$ and magnetic field $\mathcal{H}$ to be continuous across the interface, allowing the relation of this component to the field across the interfaces.

This can be generalised to multiple interfaces to give a reflected intensity for an N-pair DBR stack at normal incidence:

$$R = \left[\frac{n_{or}n_H^{2N} - n_{sub}n_L^{2N}}{n_{or}n_H^{2N} + n_{sub}n_L^{2N}}\right]^2 \tag{3.24}$$

Where n_H and n_L are the high and low refractive indices, and n_{or} and n_{sub} are the originating and substrate medium. The reflectivity is mostly determined by the number of layer pairs and their refractive index contrast, with this contrast also dictating the reflection bandwidth. The presence of this reflectivity profile affects the radiation pattern of emitters in close proximity. For emitters such as the NV which emit photons over a wide range of wavelengths, the collection efficiency at each wavelength ($\eta_{coll}(\lambda)$) is not constant over the whole emission spectrum. The total power emitted by a dipole (P_{em}) in dielectric media is described in Reference [137], using the sum of parallel and perpendicular polarisation contributions:

$$P_{\parallel}(\alpha,\theta,\phi) = \frac{3}{8\pi}sin^2(\theta)sin^2(\phi) \tag{3.25}$$

$$P_{\perp}(\alpha,\theta,\phi) = \frac{3}{8\pi}(cos(\theta)sin(\alpha) + sin(\theta)cos(\alpha)cos(\phi))^2 \tag{3.26}$$

Where α is the azimuthal angle between the optical axis and the emission direction, ϕ is the polar angle, and θ is the angle between the dipole and the optical axis. The collection efficiency is found by integrating these quantities over the solid angle given by the numerical aperture:

$$\eta_{coll}(\theta) = \int_0^{arcsin(NA)}\int_0^{2\pi}(A_{\parallel}P_{\parallel} + A_{\perp}P_{\perp})sin(\alpha)d\phi d\alpha \tag{3.27}$$

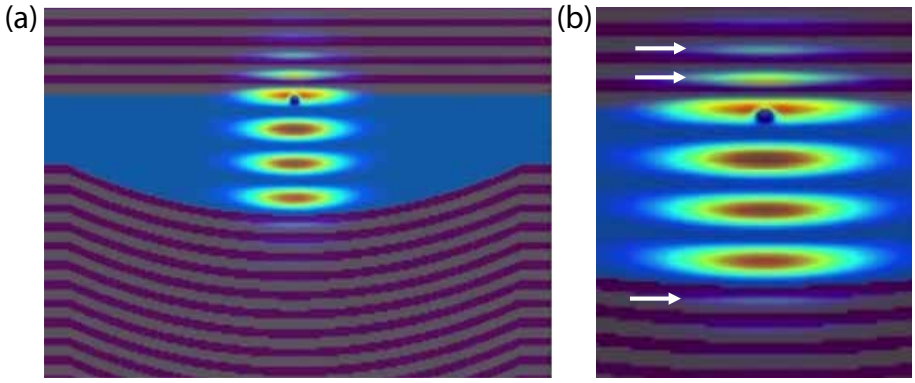


FIGURE 3.9: (a) FDTD simulation of the intensity distribution for a planar-hemispherical cavity with $q = 4$ between the mirrors. The layers are made of high (purple) and low (grey) refractive index materials of thickness $\frac{\lambda}{4n}$. The cavity medium has $n = 1$. (b) A close-up profile of the cavity mode. The white arrows indicate antinodes penetrating into the mirror stack.

Where A_i includes terms describing the interference of the directly emitted and reflected light in both polarisations. From this, the average collection efficiency ($\langle \eta_{coll} \rangle$) of the emitter on a DBR structure can determined from the collection efficiency of the dipole radiation pattern over the emitter's spectral profile ($S(\lambda)$) using:

$$\langle n_{coll} \rangle = \frac{\int \eta_{coll}(\lambda) S(\lambda) d\lambda}{\int S(\lambda) d\lambda} \tag{3.28}$$

DBR mirrors also display the unique feature of penetration of the electric field into the coating layers (Figure 3.9). As a result of this, the properties of the surface are dependent on the terminating layer. A high index terminating layer produces a node at the substrate-air interface, with an antinode penetrating into the substrate. Conversely, a low index termination produces an antinode at the interface. This design feature allows an emitter deposited on the mirror surface to interact with the electric field maximum. The geometric penetration depth of these interfaces (d_H and d_L) can be calculated from the equations in Reference [138]. The adapted expressions for the open cavities used in this

thesis are:

$$d_H = \frac{\lambda}{4\tilde{n}\Delta n} \tag{3.29}$$

$$d_L = \frac{\lambda\tilde{n}}{4\Delta n} + \frac{\lambda\Delta n}{2\pi^2\tilde{n}} \tag{3.30}$$

Where the terms $\tilde{n}$ and Δn are:

$$\tilde{n} = 2\left(\frac{1}{n_H} + \frac{1}{n_L}\right)^{-1} \tag{3.31}$$

$$\Delta n = n_H - n_L \tag{3.32}$$

For typical coating materials such as SiO_2 and Ta_2O_5, the refractive indices are $n_L \simeq 1.45$ and $n_H \simeq 2.1$. More significant than the geometrical penetration depth is the optical penetration depth, which is given by:

$$L_{H,L} = \tilde{n}d_{H,L} \tag{3.33}$$

The total optical penetration depth is then the sum of the penetration depths of both cavity mirrors. The cavity length calculated from the FSR is specified as the optical cavity length L_{opt}, which includes both the penetration depth L_{pen} and mirror separation L_{geo}. L_{opt} can be found when Equation 3.14 is expressed in terms of λ. The optical cavity length is then:

$$L_{opt} = \frac{\lambda_1\lambda_2}{2\Delta\lambda_{FSR}} \tag{3.34}$$

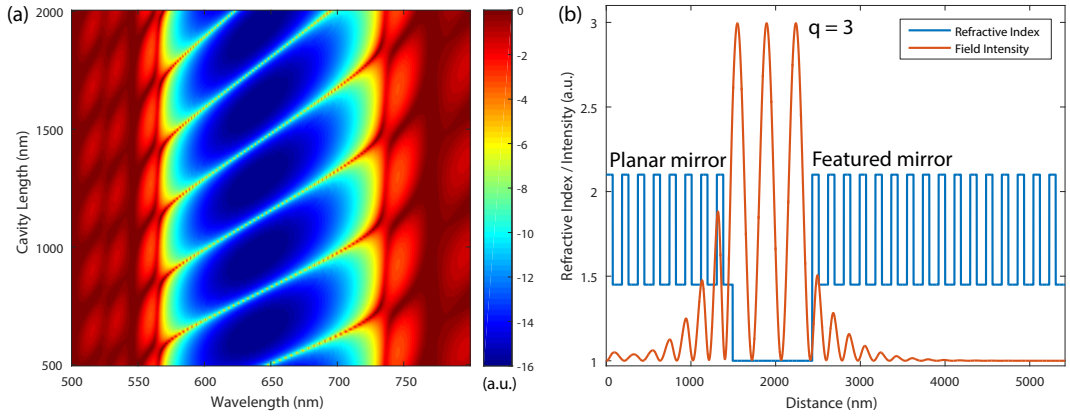


FIGURE 3.10: Transfer matrix simulation of a one-dimensional cavity. The planar mirror and featured are made of 8 and 16 pairs of DBR layers. (a) Cavity transmission intensity as a function of wavelength and mirror separation. The figure is plotted on a log scale so the resonances can be resolved. (b) Field distribution in a cavity together with the refractive index sequence of the mirrors. The penetration into the low and high terminated mirrors can be seen.

Where λ_1 and λ_2 are the wavelengths of subsequent fundamental modes, and $L_{opt} = L_{geo} + L_H + L_L$. Although DBR mirrors can provide extremely high finesses, the penetration of the field into the substrate limits the reduction of the mode volume. For clarity, the mode number q will be expressed as the number of antinodes between the mirrors, excluding any antinodes penetrating into the mirror stack.

A quantitative understanding of the transmission and reflection properties of these dielectric structures can be obtained using the transfer matrix method. In this method, the effect of the dielectric media on the electromagnetic field is described as a complex matrix which contains information on the refractive index and thickness of the material. The components of Equation 3.24 can be calculated at an extremely low computational cost. The core program (tmm 0.1.7) was written by Steve Brynes and is freely available online on the Python Package Index (PyPi) repository [139]. It was adapted by Dr Sam Johnson, formerly of the Photonic Nanomaterials Group to deliver properties of interest

such as cavity resonances. The cavity can be constructed from a sequence of high and low refractive index media to create the physical structures used in experiments. Figure 3.10 (a) shows the cavity transmission as a function of wavelength and cavity length for the cavity formed by the mirror sequence in Figure 3.10 (b).

3.4 Cavity Quantum Electrodynamics

The principal theme of this thesis is the interaction between light and matter. Cavity quantum electrodynamics (CQED) describes such interactions in a cavity and can be applied to a variety of systems. The starting point for the theoretical description of CQED is the electromagnetic vacuum field $\mathcal{E}_{vac}$, which permeates through all space. This field has a finite zero-point energy which can be found most simply from the treatment of light as a quantum harmonic oscillator. This zero-point energy, E can be equated to the vacuum electric and magnetic fields, $\mathcal{E}_{vac}$ and $\mathcal{B}_{vac}$ through:

$$E = \frac{1}{2}\int\int\int \epsilon_0 \mathcal{E}_{vac}^2 + \mu_0^{-1}\mathcal{B}_{vac}^2 dV = \int\int\int \epsilon_0 \mathcal{E}_{vac}^2 dV = \frac{1}{2}\hbar\omega \tag{3.35}$$

We make use of the fact that the electric and magnetic fields evenly contribute to the time averaged energy. From Equation 3.35, the vacuum electric field is then:

$$\mathcal{E}_{vac} = \left(\frac{\hbar\omega}{2\epsilon_0 V}\right)^{1/2} \tag{3.36}$$

In fact, spontaneous emission occurs as a consequence of the interaction of this vacuum field with an excited state atom. Optical resonators have the ability to modify this field

by changing the mode volume V_0. With this capability, it is useful to define the coupling rate, g_0 which defines the coupling of a quantum system to an optical microcavity:

$$\hbar g_0 = \mu_{12}\mathcal{E}_{vac} \tag{3.37}$$

$$g_0 = \left(\frac{\mu_{12}^2\omega}{2\epsilon_0\hbar V_0}\right)^{1/2} \tag{3.38}$$

Where μ_{12} is the matrix element of the electric dipole transition. It is clear that a reduction in the mode volume increases the rate of interaction. In reality, the cavity coupling interaction is inhibited by two factors, namely the cavity-photon decay rate κ, and the emitter decay rate γ. The emitter decay rate γ is of specific importance as it encompasses all emission processes, whether into the cavity or into free space, as emission occurs in all directions. The relative magnitude of the parameters κ, γ and g_0 determine the boundary of CQED regimes. When $g_0 \gg \kappa, \gamma$, the interaction is in the strong coupling regime. In this regime, the coupling rate dominates the loss mechanisms, leading to a coherent and reversible exchange of energy between the emitter and cavity. This regime is beyond the scope of this work and will not be discussed further.

When $\kappa, \gamma \gg g_0$, the loss processes dominate the cavity coupling rate, and is known as the weak coupling regime. However, an enhancement in the light-matter interaction may be attained through the reduction of the mode volume, which alters the cavity decay rate. This is known as the Purcell effect [91], where the rate of spontaneous emission changes in the presence of a modified optical density of states. Within the weak coupling regime, a further distinction can be made between the relative rates of decoherence. The 'good emitter/bad cavity' ($\kappa > \gamma \gg g_0$) regime describes a spectrally narrow emitter in a broad cavity mode, while the 'bad emitter/good cavity' regime ($\gamma > \kappa \gg g_0$) represents a

broad emitter within a narrow cavity mode. The 'bad emitter/good cavity' regime is more applicable to the coupling of the emitters used in this thesis.

3.4.1 Free Space Emission

Optical density of states

To begin the description of free space emission, we must first quantify the optical density of states (DoS). These optical states refer to the modes in which photons may be emitted into. A simple treatment involves the counting of these states through the method outlined by Fox [140]. A volume V can be described as a cube with sides of length d, such that $V = d^3$ (Figure 3.11). An electromagnetic field present in this region takes the form:

$$\mathcal{E}(\mathbf{r}, t) = \sum_k \mathcal{E}_k e^{i(\mathbf{kr} - wt)} \tag{3.39}$$

The summation is over all the possible $\mathbf{k}$ vectors of the travelling waves, each with an angular frequency of ω. Gauss' law of electrostatics states that when applied to a vacuum, the divergence of the field must be zero ($\nabla \cdot \mathcal{E} = 0$). For the electric field distribution in Equation 3.39, applying this relation gives:

$$\nabla \cdot \mathcal{E}_{total}(\mathbf{r}, t) = \sum_k \mathbf{k} \cdot \mathcal{E}_k e^{i(\mathbf{kr} - wt)} = 0 \tag{3.40}$$

This is only true when $\mathbf{k} \perp \mathcal{E}_\mathbf{k}$, so the electric field is always pointing perpendicularly to the wave's direction of travel. Each $\mathbf{k}$-vector can have an arbitrary combination of 2

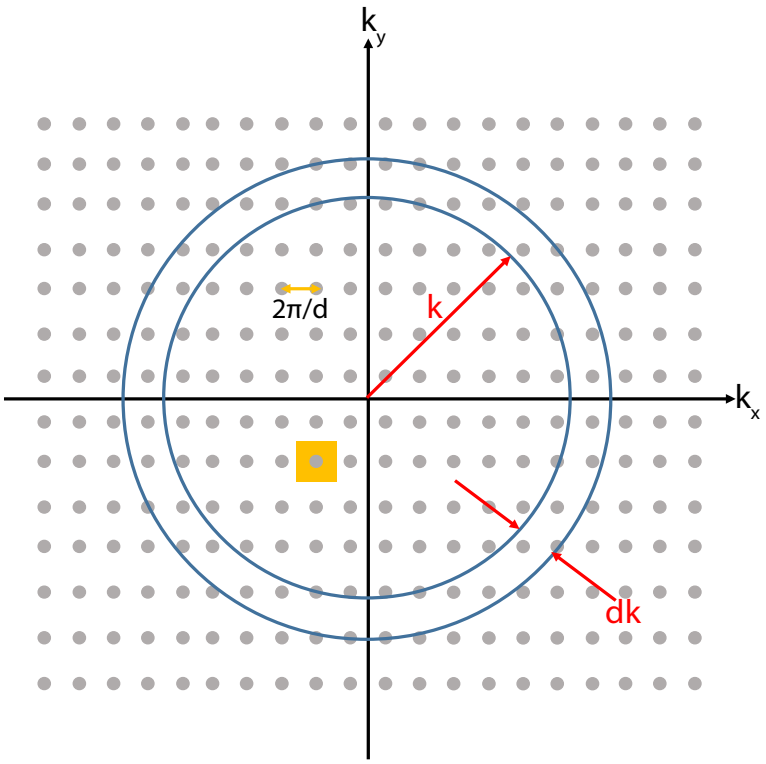


FIGURE 3.11: A 2D schematic of the density of states in k-space. Each point represents a permitted k-state taking up an area $(2\pi/d)^2$, shown by the orange square. dk represents an infinitesimal shell of k-space used in the calculation for the optical density of states. Adapted from [140]

orthogonal polarisations, which can be accounted for by multiplying the total number of **k** vectors by 2. The permitted **k** vectors are then:

$$\mathbf{k} = (k_x, k_y, k_z) = \frac{2\pi}{d}(n_x, n_y, n_z) \tag{3.41}$$

The permitted **k**-states are each separated by $\frac{2\pi}{d}$, each occupying a volume $V = (\frac{2\pi}{d})^3$. To obtain the density of states, we must determine the number of states within k and $k + dk$, where the magnitude of the vector **k** is calculated as $k = \sqrt{k_x^2 + k_y^2 + k_z^2}$. The density of states ρ, can then be found by calculating the volume of an infinitesimal shell of radius k,

and dividing by the volume per **k**-state:

$$\rho(k)dk = \frac{4\pi k^2 dk}{(2\pi/d)^3} = V\frac{k^2}{2\pi^2}dk \tag{3.42}$$

This density of states in **k**-space can be mapped onto the density of photon states at their corresponding angular frequencies $\rho(\omega)$ using $\omega = ck$. We must remember that there are two possible polarisations for each **k**-state, and also normalise by V to give:

$$\rho(\omega)d\omega = 2\rho(k)dk = \frac{\omega^2}{\pi^2 c^3} \tag{3.43}$$

Spontaneous Emission Rate

A good starting point for the discussion of the spontaneous emission rate is Fermi's golden rule. The derivation of this rule is from time dependent perturbation theory. For a two-level system, we assume the system can be fully described by a time-independent Hamiltonian, with a small perturbing Hamiltonian such that:

$$\hat{H}_{total} = \hat{H} + \hat{H}' \tag{3.44}$$

The perturbing Hamiltonian is small compared to $\hat{H}$. It can be written as the dot product of the electric dipole **p**, and the electric field $\mathcal{E}$:

$$\langle 1|\, \hat{H}'\, |2\rangle = -e\, \langle 1|\, \hat{\mathbf{r}}\, |2\rangle \cdot \mathcal{E} = \mu_{2\to 1} \cdot \mathcal{E} \tag{3.45}$$

If the perturbation is time-dependent, then it can cause the system to change it's state from an initial state $|2\rangle$, to a final state $|1\rangle$. This transition occurs via the electric dipole interaction, resulting in the emission of a single photon with an energy corresponding to

the energy difference between the two states. The rate of this transition is also dependent on the DoS of the final state at the emission frequency $\rho(\omega)$. Fermi's golden rule can then be expressed as:

$$\gamma_{2\to1} = \frac{2\pi}{\hbar^2} |\langle 1| \hat{H}' |2\rangle|^2 \rho(\omega) = \frac{2\pi}{\hbar^2} |M_{12}|^2 \rho(\omega) \tag{3.46}$$

Where, M_{12} is the matrix element for the transition. This electric dipole interaction will depend on the electric transition dipole μ_{12} and the electromagnetic field which interacts with the dipole, which in free space, is the vacuum field:

$$|M_{12}|^2 = \frac{1}{3}\mu_{12}^2 \mathcal{E}_{vac}^2 = \frac{\mu_{12}^2 \hbar\omega}{6\epsilon_0 V_0} \tag{3.47}$$

The factor of $\frac{1}{3}$ represents the average dipole alignment factor for an atom in free space. Finally, using $\rho(\omega)d\omega = \frac{\omega^2}{\pi^2 c^3}$, the transition rate of spontaneous emission in free space is:

$$\gamma_{fs} = \frac{\mu_{12}^2 \omega^3}{3\pi\epsilon_0 \hbar c^3} \tag{3.48}$$

3.4.2 Cavity Coupled Emission

To determine the DoS of a cavity, we begin with a simple assumption that there is only a single cavity mode available, with a frequency of ω_0. The DoS $\rho(\omega)_{cav}$ is taken to be a normalised Lorentzian function centred at ω_0:

$$\rho(\omega)_{cav} = \frac{2}{\pi\delta\omega_0} \frac{\delta\omega_0^2}{4(\omega-\omega_0)^2 + \delta\omega_0^2} \tag{3.49}$$

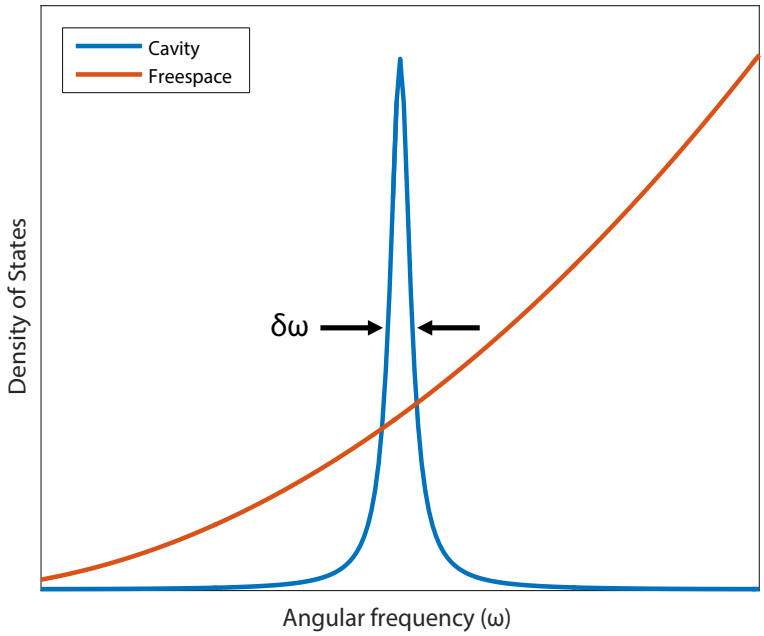


FIGURE 3.12: Density of states in terms of angular frequency for free space emission and a single cavity mode.

Where $\delta\omega$ is the linewidth of the Lorentzian peak, and is related to the Q-factor by $Q = \omega_0/\delta\omega$. This function is plotted in Figure 3.12 along with the free space density of states for comparison. When at resonance ($\omega = \omega_0$), Equation 3.49 reduces to $\rho(\omega_0) = 2Q/\omega_0$. Using this cavity modified DoS, Fermi's Golden Rule gives the transition rate as:

$$\gamma_{cav} = \frac{2Q\mu_{12}^2}{V_0\epsilon_0\hbar}\xi^2\frac{\delta\omega_0^2}{4(\omega-\omega_0)^2+\delta\omega_0^2} \tag{3.50}$$

Where ξ is the normalised dipole orientation factor between the emitter dipole $\mathbf{p}$ and the cavity field $\mathcal{E}$:

$$\xi = \frac{|\mathbf{p}\cdot\mathcal{E}|}{|\mathbf{p}||\mathcal{E}|} \tag{3.51}$$

Having now defined the spontaneous emission rate in free space and into a cavity mode,

it is only natural to divide the cavity transition rate by the free space transition rate. This is known as the Purcell factor F_P. Here c/ω is replaced by $\lambda/2\pi$:

$$F_P = \frac{3\lambda^3}{4\pi^2}\frac{Q}{V_0}\xi^2\frac{\delta\omega_0^2}{4(\omega-\omega_0)^2+\delta\omega_0^2} \tag{3.52}$$

With the condition of perfect spatial alignment of the emitter dipole and cavity field ($\xi = 1$) at the cavity resonance ($\omega = \omega_0$), the Purcell factor is finally expressed as:

$$F_P^{max} = \frac{3\lambda^3}{4\pi^2}\frac{Q}{V_0} \tag{3.53}$$

They key identity in the Purcell factor is the ratio of Q/V. To enhance emission into a cavity mode, one can either increase the Q-factor of the resonator or decrease the mode volume. A reduction in the mode volume leads to an increased interaction with the vacuum field, increasing the rate of spontaneous emission. Meanwhile, increasing the Q-factor suppresses emission not resonant with the cavity.

3.4.3 Bad Emitter Regime

As previously stated, the emitter linewidths in this thesis are broader than the cavity modes (Figure 3.13). For these two independently broadened linewidths, their resultant interaction is a convolution of their Lorentzian profiles. This convolution alters the Q-factor in Equation 3.53, which now features contributions from both linewidths to become the effective Q-factor Q_{eff}:

$$Q_{eff} = \frac{1}{Q_{em}+Q_{cav}} = \left(\frac{\lambda_{em}}{\delta\lambda_{em}}+\frac{\lambda_{cav}}{\delta\lambda_{cav}}\right)^{-1} \tag{3.54}$$

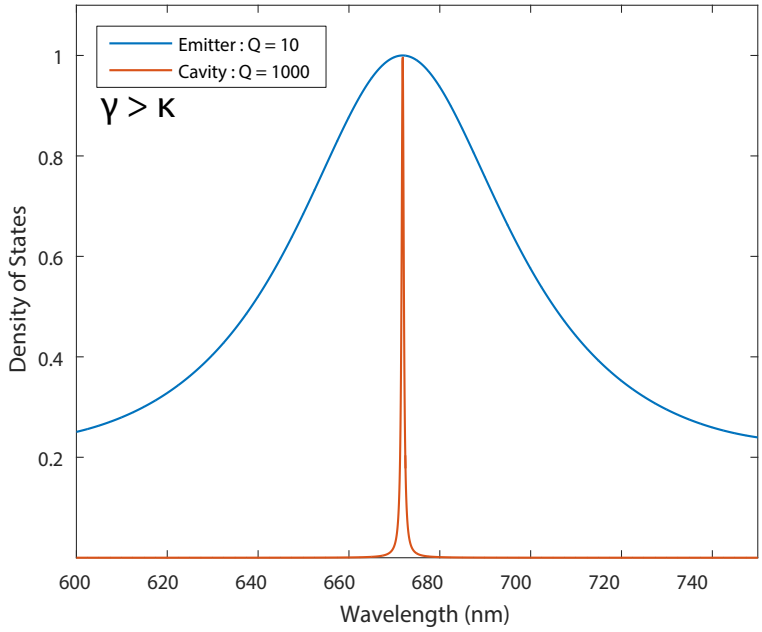


FIGURE 3.13: The bad emitter/good cavity regime, where the emitter linewidth is greater than the cavity linewidth.

Where Q_{em} and Q_{cav} are the emitter and cavity Q-factors. Therefore, Q_{eff} will be dominated by the contribution with the broadest linewidth, which will be the emitter - limiting the magnitude of the Purcell effect. The Purcell factor in Equation 3.53 is now the effective Purcell factor $F_{P,eff}$. The mode volume is now the most crucial parameter making it essential to reach the shortest cavity lengths possible. The derivation of Equation 3.53 has assumed that the density of states within the cavity is solely for a single cavity mode. In reality, the cavity mode may only subtend a small solid angle, allowing the coupling of emission into both cavity modes and free space density of states. In this regime, the non-cavity mode density of states may be related to the free-space density of states by a suppression factor α, where $0 \leq \alpha \leq 1$. Although α is typically taken to be unity, the presence of the cavity will reduce the free-space density of states, and increasingly so for smaller mode volumes. Therefore, the calculated values of $F_{P,eff}$ can be related to the experimental results for the change in the lifetime of the emitter inside the emitter by:

$$\frac{\tau_{fs}}{\tau_{cav}} = F'_{P,eff} = F_{P,eff} + \alpha \tag{3.55}$$

Where τ_{fs} and τ_{cav} are the measured lifetimes on the free-space and for cavity coupled emission. A useful metric is the cavity emission efficiency $\mathcal{B}$, which is quantified as:

$$\mathcal{B} = \frac{\gamma_{cav}}{\gamma_{cav} + \gamma_{fs}} = \frac{F_P}{F_P + \alpha} \tag{3.56}$$

The rate model developed by Auffeves *et al.* provides an alternative method to determine the cavity emission efficiency [110, 111]. Equation 2.2 describes the effective coupling rate between the atom and the cavity mode. From the perspective of the emitter, the cavity mode is another loss mechanism, with an effective rate given by:

$$\mathcal{R}_{eff} = \frac{R \cdot \kappa}{R + \kappa} \tag{3.57}$$

The cavity emission efficiency is then:

$$\mathcal{B} = \frac{\mathcal{R}_{eff}}{\gamma + \mathcal{R}_{eff}} \tag{3.58}$$

3.5 Finite Difference Time Domain Simulations

Finite Difference Time Domain (FDTD) (Software: Lumerical Solutions [141]) simulations are able to computationally account for the electromagnetic environment of the emitters. The fundamental ability of FDTD is to act as a tool to investigate the propagation of electromagnetic waves within photonic structures. The program allows the user

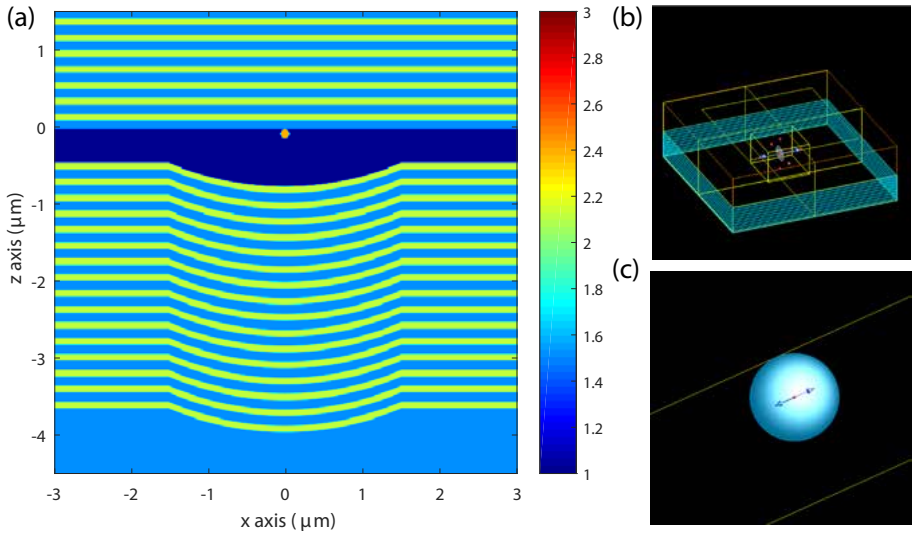


FIGURE 3.14: (a) Refractive index monitor data showing the DBR layers of the planar and featured mirror. A 100 nm nanodiamond can be seen in the planar mirror. (b) Planar mirror structure with dipole on the surface. The yellow boxes are the different monitors used to obtain data from the simulation. (c) A closer view of the spherical nanodiamond with the dipole located inside.

to construct a cavity, defining structural parameters such as cavity length, radius of curvature, refractive indices and DBR layer thickness. In the simulation, the origin of the electromagnetic radiation is a dipole emitter defined within a host material at a given orientation. The simulation region is divided into an array of three dimensional units known as "Yee" cells, all with a defined refractive index. The cell dimensions are chosen such that they are much less than the wavelengths of interest, and intricacies of the structural interfaces can be resolved. For simple regions such as the planar mirror, the mesh size can be relatively large. However, spherical surfaces such as the concave mirror require a much finer mesh as in Figure 3.14 (a). Typical fine and course mesh sizes are 5 and 15 nm, but most simulations are performed with the finest mesh size. Monitors are placed at positions of interest to record various variables such as the Q-factor and electric field (Figure 3.14 (b)). Upon initialisation of the simulation, the program calculates the propagation of emitted light through each cell by solving Maxwell's equations across the

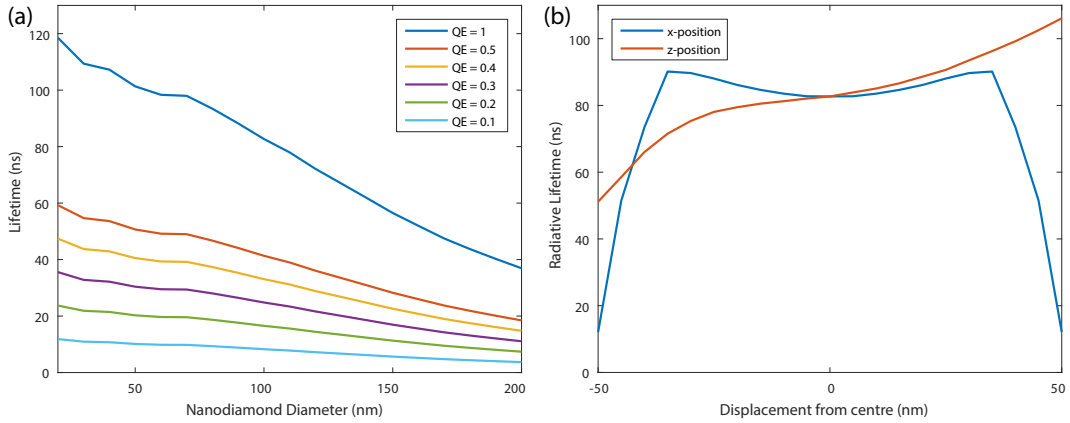


FIGURE 3.15: FDTD simulations of NV centre's lifetime in a nanodiamond on the DBR substrate. (a) The change in total lifetime with nanodiamond diameter at different quantum efficiencies. The QE = 1 line corresponds to the pure radiative lifetime. (b) Radiative lifetime dependence on the position of the dipole within a 100 nm nanodiamond.

interface. Typical time increments are ∼5 fs, and total simulation time ∼10 ps, in order to allow the field to fully decay.

FDTD simulations can be used to help quantify the relative contributions of the radiative and non-radiative processes. As an example, Figure 3.15 shows the results for the radiative lifetime of a dipole within a spherical nanodiamond. These simulations were performed with the nanodiamond on the DBR mirror substrate, which will alter the dependence of the radiative lifetime compared to a nanoparticle in free-space. Firstly, a simulation was performed to determine the radiative lifetime of a centrally located dipole within a spherical diamond nanocrystal of varying diameter (20 – 200 nm). Secondly, the position of the dipole was varied laterally and vertically within a 100 nm nanodiamond. Figure 3.15 (a) shows the dependence of the NV centre's radiative lifetime with nanodiamond diameter. As the size of the nanodiamond increases, the radiative lifetime decreases as expected, due to a greater optical density of states. Also plotted are the predicted excited state lifetimes for several values of quantum efficiency.

Chew evaluated the spontaneous emission rate for a dipole inside a spherical dielectric particle in air, with a size much smaller than the emission wavelength [142]. This expression shows a suppression of the radiative rate by a factor of $9/n(n^2+2)^2$ ($\approx$ 0.062 for diamond) compared to the rate in a bulk material with an equivalent refractive index. Using the lifetime of an NV centre in bulk diamond (12 ns) [39], this expression would predict a lifetime of $\sim$ 194 ns in nanodiamonds. This result is independent of the position of the dipole within the particle. For 50 and 100 nm spherical nanodiamonds in free-space, FDTD shows suppression factors of 0.075 and 0.098 relative to the bulk, comparable to the result from Chew. However, the FDTD result in Figure 3.15 (a) is more appropriate for this project as it accounts for both the presence of the DBR substrate and size of the nanoparticle hosting the dipole - both variables which affect the radiative lifetime. Figure 3.15 (b) shows the dependence of the lifetime on the vertical and lateral position of the dipole within a nanodiamond with diameter of 100 nm. For the vertical displacement, as the dipole approaches the mirror substrate, the greater optical density of states available due to the high refractive index layers decreases the radiative lifetime compared to when near the nanodiamond surface. The lateral position has a small effect on the lifetime until the dipole approaches the edge of the nanodiamond.

3.5.1 Purcell Factor Analysis

In order to discern the modification of the spontaneous emission behaviour of a dipole within a microcavity, FDTD can be used to determine the Purcell factor as a function of wavelength ($F_P(\lambda)$). This function gives a description the total dielectric environment experienced by the dipole. $F_p(\lambda)$ is calculated from the total power radiated from the dipole in free space, and then comparing that to the total power radiated from the same dipole within the cavity. For a direct comparison to experiments, $F_p(\lambda)$ must also be

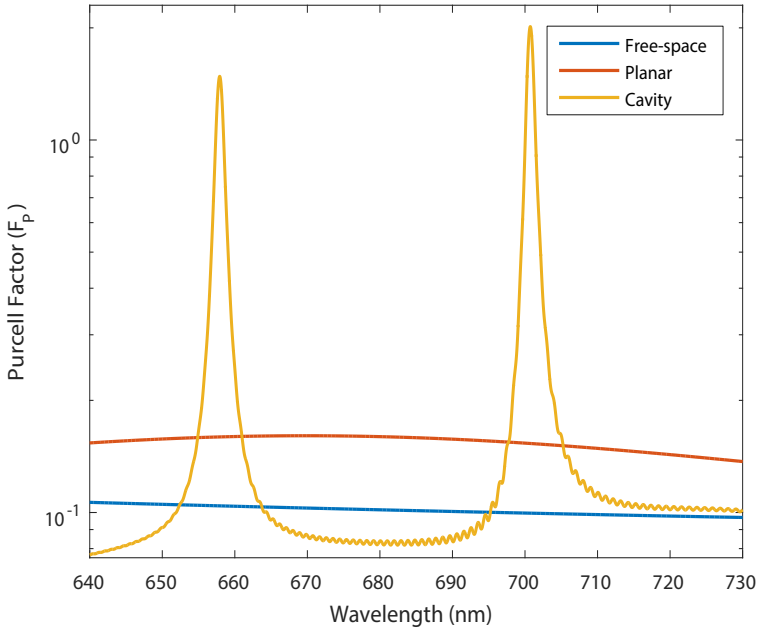


FIGURE 3.16: Purcell factor as a function of wavelength for free-space, half-space and cavity coupled emission. The figure is plotted on a log scale for clarity. The dipole is hosted within a 100 nm nanodiamond. The planar mirror and featured mirror have reflectivities of 97.5% and 99.997% at 690 nm. The cavity is positioned at the $q = 3$ mode index.

determined for the dipole on the planar mirror, as true free-space measurements are not possible. Therefore three Purcell factors are required to give an accurate characterisation of experimentally observed results:

- $F_p(\lambda)_{fs}$ - The free-space Purcell factor of a dipole within its host environment. As the host material is on the nanoscale, this is a suppression in the emission rate relative to the bulk.
- $F_p(\lambda)_{hs}$ - The half-space Purcell factor due to the dipole being on a DBR mirror, which provides a modified density of states compared to free-space.
- $F_p(\lambda)_{cav}$ - The cavity Purcell factor due to the increased optical density of states within the cavity modes.

Figure 3.16 shows a comparison between the three Purcell factors. The free-space curve follows the behaviour of Equation 3.43, as does the half-space curve but with an enhancement due to the presence of the DBR mirror. The cavity Purcell factor shows the enhancement at wavelengths resonant with the cavity modes, with suppression at off-resonant wavelengths. The value of F_P for each cavity mode obtained from the simulation can be confirmed through an analytic expression using the Q-factor and V parameters also from the simulation. This treatment for a dipole within a host material inside an optical cavity has been performed by Santori *et al.* [143] for nanodiamonds, with the ideal Purcell factor for a given mode expressed as:

$$F_P = \frac{3}{4\pi^2}\frac{\lambda^3}{n_c^3}\frac{Q}{V}\frac{n_c}{n_d}\left|\frac{\mathbf{E}(\mathbf{r}_{NV})}{\mathbf{E}(\mathbf{r}_{max})}\right|^2 \tag{3.59}$$

Where n_c and n_d are the refractive indices at the maximum of the cavity mode and of the nanodiamond, $\mathbf{E}(\mathbf{r}_{max})$ and $\mathbf{E}(\mathbf{r}_{NV})$ are the electric field strength at the maximum of cavity mode, and of the NV centre.

To describe the total dielectric environment experienced by the dipole, we define the effective Purcell factor $F'_{P,eff}$. This is necessary as changes in the dipole's spontaneous emission rate occur due to the total optical density of states experienced from all the available cavity modes. For free-space emission, this parameter ($F'_{P,fs}$) is found by integrating the Purcell spectrum over the emission spectrum of the dipole:

$$F'_{P,fs} = \frac{\int F_{P,fs}(\lambda)S(\lambda)d\lambda}{\int S(\lambda)d\lambda} \tag{3.60}$$

The effective half-space and cavity Purcell factors ($F'_{P,i}$) can now be determined by integrating $F_{P,i}(\lambda)$ over the emission spectrum of the dipole, and normalising by the integral

for the free-space effective Purcell factor:

$$F'_{P,i} = \frac{\int F_{P,i}(\lambda)S(\lambda)d\lambda}{\int F_{P,fs}(\lambda)S(\lambda)d\lambda} \tag{3.61}$$

However, it must be remembered that the Purcell effect only acts on the radiative part of the decay rate. Assuming the non-radiative decay rate for the free-space, half-space and cavity scenarios is the same ($\gamma_{nr}^{fs} = \gamma_{nr}^{hs} = \gamma_{nr}^{cav}$), the cavity decay rate is $\gamma^{cav} = F'_{P,cav} \cdot \gamma_{rad} + \gamma_{nr}$, while the half-space decay rate is $\gamma^{hs} = F'_{P,hs} \cdot \gamma_{rad} + \gamma_{nr}$. The relation between these half-space and cavity decay rates can be measured from the emitter lifetime where $\tau_i = 1/\gamma_i$. From here, these relations can be used to determine the ratio of γ_{rad} and γ_{nr}:

$$\frac{\gamma_{cav}}{\gamma_{hs}} = \frac{F'_{P,cav}\gamma_{rad} + \gamma_{nr}}{F'_{P,hs}\gamma_{rad} + \gamma_{nr}} = \frac{\tau_{hs}}{\tau_{cav}} \tag{3.62}$$

$$\frac{\gamma_{rad}}{\gamma_{nr}} = \frac{\frac{\tau_{hs}}{\tau_{cav}} - 1}{F'_{P,cav} - \frac{\tau_{hs}}{\tau_{cav}}F'_{P,hs}} \tag{3.63}$$

Equations 3.62 and 3.63 will be used in Section 6.3 to evaluate the quantum efficiency of NV centres in nanodiamonds. The cavity Purcell spectrum ($F_{P,cav}(\lambda)$) also provides a means to calculate the coupling efficiency into a cavity mode. The fraction of emission into the mode is found by integrating the product of the Purcell spectrum with the emission spectrum over the width of the mode ($\Delta\lambda$), and normalising by the same integral but over the total emission spectrum:

$$\mathcal{B} = \frac{\int_{\lambda_0 - \frac{\Delta\lambda}{2}}^{\lambda_0 + \frac{\Delta\lambda}{2}} F_{P,cav}(\lambda)S(\lambda)d\lambda}{\int_{\infty}^{\infty} F_{P,cav}(\lambda)S(\lambda)d\lambda} \tag{3.64}$$

3.6 Conclusion

This chapter has established the theoretical framework for the coupling of solid-state defects to optical microcavities. A few of the most important cavity parameters have been highlighted, through the planar Fabry-Perot resonator. Details of the Gaussian modes have being presented, which will play a large role in the efficient extraction of light from the emitter-cavity systems in the upcoming chapters. The full derivation of the Purcell factor has been elaborated, which expresses the importance of spectral and positional tuning to maximise emission into the cavity modes. It has been shown that the defects used in this thesis are firmly in the "bad emitter/good cavity" regime of CQED, which will limit the magnitude of expected enhancements. The analysis of Purcell factor obtained from FDTD simulations has also been shown, allowing a direct comparison of theory to experimental results.

4|

Experimental Methods

4.1 Introduction

In this chapter, the experimental methods involved in producing successful emitter-cavity coupling will be described. I will introduce the laboratory equipment and measurement routines used to record the data to be presented in the following chapters. Firstly, the cavity fabrication process will be presented, including the use of focused ion beam (FIB) milling to create hemispherical features, and the coating of DBR layers to produce highly reflective mirrors. I will then discuss how samples of each emitter are created and the deposition of their solutions. From here, I will introduce the confocal microscope developed for single emitter analysis and how the samples are housed in the microscope. The key measurement capabilities of this system will be given a thorough description, with example results and error analysis of crucial single photon emission characteristics. This microscope is constructed such that these measurements can be performed on the same emitter both inside and outside the cavity. It will be demonstrated how the cavity is created around a chosen defect, including the alignment of the two mirrors.

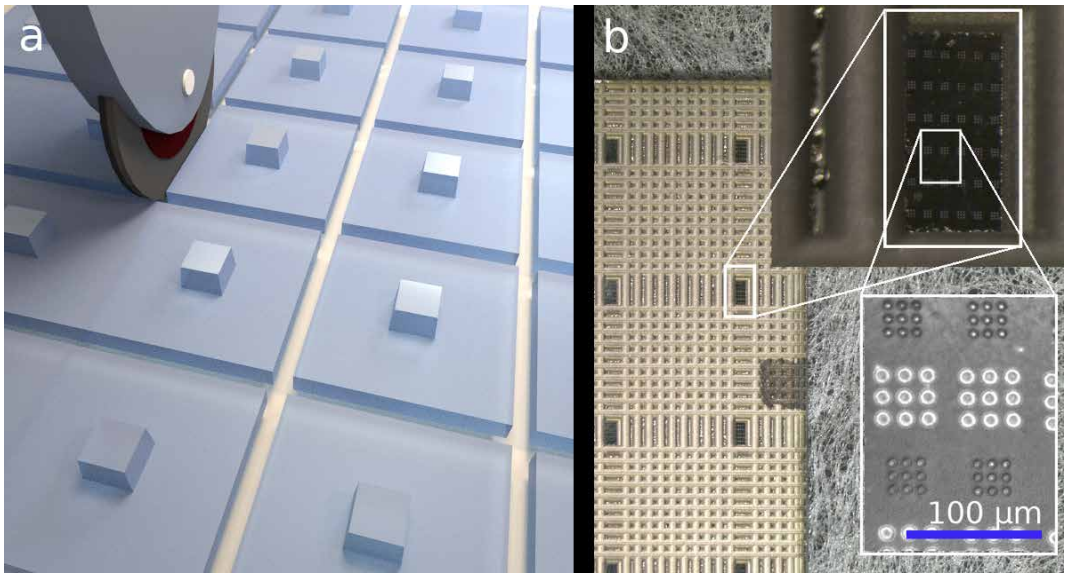


FIGURE 4.1: (a) Artistic interpretation of the substrate hosting the plinths. (b) Optical image of the substrate following FIB milling and coating. The insets show the hemispherical features on the plinths. Reproduced from [144]

4.2 FIB Milling and Mirror Coatings

The open-access microcavity is distinguished from alternative resonator approaches due to the decoupled nature of the substrates. The cavity consists of a planar mirror and a hemispherical mirror. The fabrication of these mirrors was carried out at the University of Oxford by Aurelien Trichet and Shazeaa Ishmael of the Photonic Nanomaterials Group. The processing steps differ for the planar and hemispherical mirrors, but both involve the use of FIB milling. As the cavity coupling process involves bringing these two mirrors together with a separation of $\sim$1 μm, it is helpful to reduce the lateral dimensions of one of the surfaces. The process begins with a fused silica substrate (UQG Optics, PFS-5005) which is cut with a silicon dicing saw to leave rectangular elevated features known as plinths, as seen in Figure 4.1. These plinths protrude by 200 μm above the rest substrate and have lateral dimensions of 300μm $\times$ 300μm. Secondly, a $\sim$50 nm conductive layer

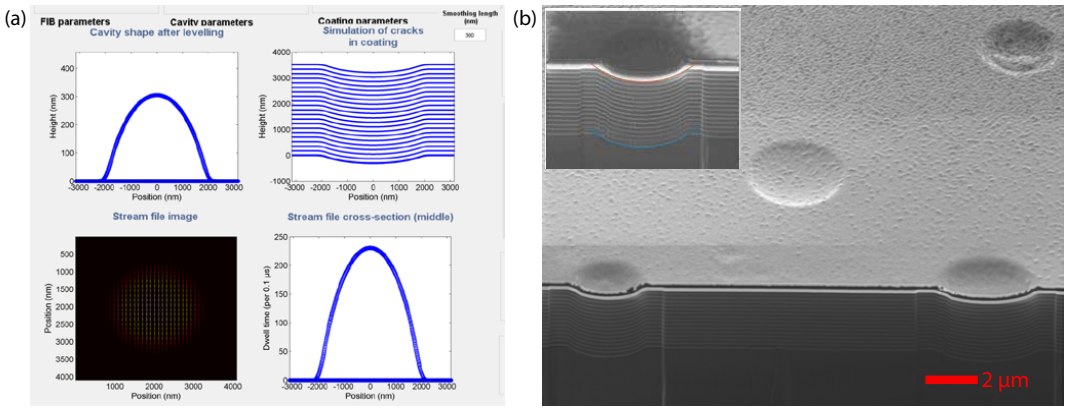


FIGURE 4.2: (a) Stream file created by the FIB software for a 8 μm feature, highlighting the feature dimensions and dwell times required to produce this feature. (b) SEM image of a cross-section of milled features of varying sizes. The inset shows the cross-section of a $\beta = 4$ μm feature, where the 16 pairs of DBR layers can be seen.

of gold is sputtered onto the surface to avoid charging from the electron microscope and deflection of the gallium ion beam. Figure 4.2 (a) shows the script file of the FIB (FEI FIB200) used to mill the concave features seen in Figure 4.2 (b) into the surface of the plinth.

The large surface area available allows several features with varying radii of curvatures ($\beta = 2 - 25$ μm) to be distributed on the plinth. The dwell time and beam current of the FIB beam have been calibrated such that a desired feature geometry can be produced accurately. The diameter of the beam is varied between 5 nm and 1 μm to achieve smooth and accurate features. A subset of these features is verified with Atomic Force Microscopy (AFM) to confirm the precision of the desired feature geometry. Milled surfaces typically display surface roughness on the order of $\sim$1 nm, making them suitable for high reflectivity mirror coatings. Following milling and removal of the gold layer, the substrates are sent to an external company (LayerTec GmbH) for DBR mirror coating. Alternating layers of high and low refractive index materials are deposited by Ion Beam Sputtering,

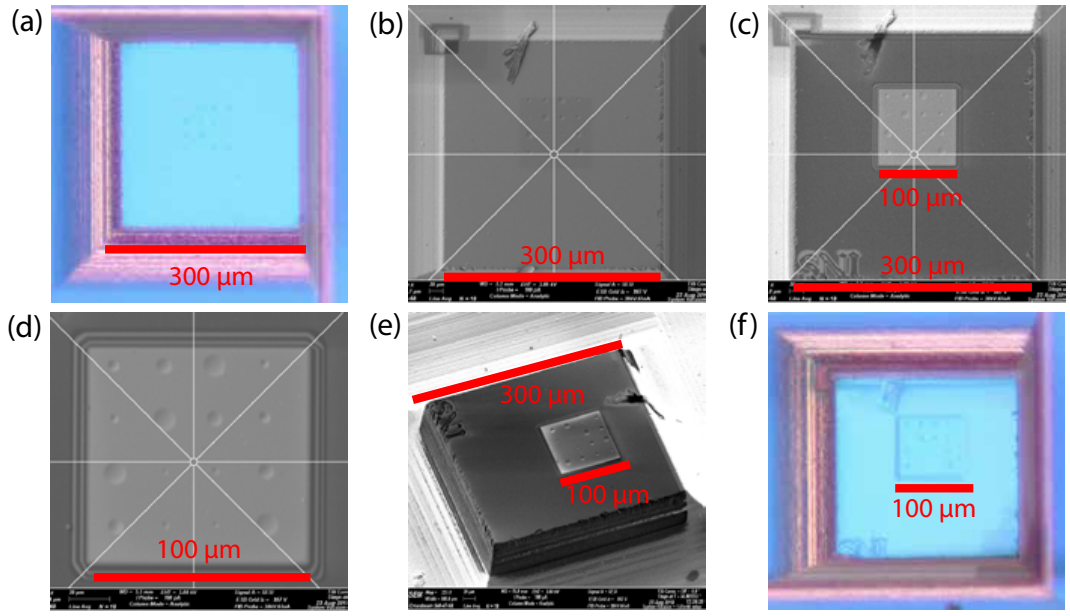


FIGURE 4.3: (a) Optical image of a 300 μm plinth with hemispherical features visible in the centre. (b) - (e) SEM images of the plinth during the milling process to leave a further raised platform. (f) Optical image of the final plinth now with a lateral dimension of ~100 μm.

specifically SiO_2 ($n = 1.45$) and Ta_2O_5 ($n = 2.1$). The layer thickness d is chosen such that $d = \frac{\lambda}{4n}$, where λ is the position of maximum reflectivity and n the refractive index of the material in that layer. This position should match (or be very close to) the maximum wavelength of each emitters spectrum. Mirrors with peak reflectivity of 640 nm and 690 nm have been used for both NV centres and hBN. Typical dielectric coatings consist of 8 – 16 pairs of SiO_2 and Ta_2O_5 (Figure 4.2 (b) inset) to give macroscopic reflectivities of up to ~99.997% at the desired wavelength.

In order to produce mirrors with these high finesses, the DBR layers must lay flat on the substrate with minimal distortion. It was found that plinths with dimensions on the order of 100 μm led to peeling of the deposited mirror from the substrate. This effect is not observed in plinths with dimensions of 300 μm. One must also take care with small β

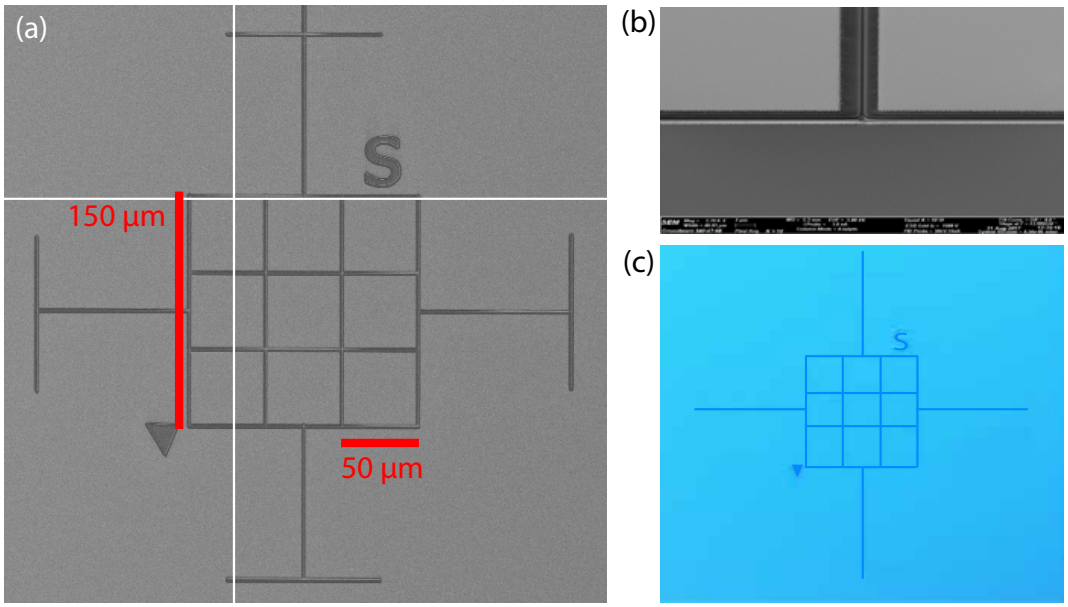


FIGURE 4.4: (a) SEM image of the registration grids on the planar mirror. (b) Closer view of the FIB mark, showing a sharp flat corners. (c) Optical image of the markings on the planar mirror. The FIB lines are enhanced due to the poor printing quality of the original image.

features, as with very small β, the feature may have sharp edges. Such an edged point can provide a path for cracks to propagate through the mirror during deposition. This translates to diffraction losses and reduction in the finesse, as the diameter of the mode on the curved mirror increases with cavity length. Therefore, the smallest β to be used in this thesis is $\beta = 4$ μm. Figure 4.3 describes the process used to further reduce the surface area of plinth. The FIB is used to mill away the area surrounding the features, leaving just a 100 μm sub-plinth raised above the larger plinth by 3 – 5 μm. This added height helps to further avoid the substrates coming onto contact away from the region of interest, while assisting the reduction in cavity length.

The planar mirror also begins as a circular fused silica substrate (UQG Optics, CFS-10[17, 20, 50]) before coating with DBR layers. The FIB is then used to mark registration grids

onto the planar mirror as in Figure 4.4. This is an essential design feature that allows the relocation of specific defects with the mirror facing towards or away from the optics. These registration features are located in the centre of the planar substrate, with square grids of 50 μm in size. The milling parameters of these features are; voltage = 30 kV, current = 15 nA and dosage = 0.7 – 0.75 nC/um. These parameters have been optimised to deliver sharp marks that do not disrupt the deposited mirror layers (Figure 4.4 (b)).

4.3 Sample Fabrication

In this section, I will give a brief overview of creation and deposition of fluorescent nanoparticles onto the dielectric mirrors outlined in the previous section. A substantial amount of experimental time has been invested in the optimisation of this process to maximise the probability of successful experiments. The emitters must be fixed on the mirror to enable efficient coupling to the electric field maximum within the cavity. Incremental improvements have been made to increase the photostability of the emitters such that prolonged experiments could be performed.

4.3.1 Spin Coating

The mirror substrates are cleaned by sonication (750 W Sonics Vibra-Cell VCX-750) in acetone for 30 mins while wrapped in a lens tissue. This is repeated with subsequent sonication in isopropanol and de-ionised water. Finally, the substrates are cleaned with an oxygen plasma, which evaporates organic residue from the surface, and terminates the surface with oxygen - making the surface hydrophillic. This step is extremely beneficial as the samples used in this thesis are dissolved in water - allowing uniform deposition of the nanoparticles (Figure 4.5). The nanoparticle solutions are sonicated for 1 hour to break up aggregates and improve the dispersion of the solution. A single 100 μL droplet is

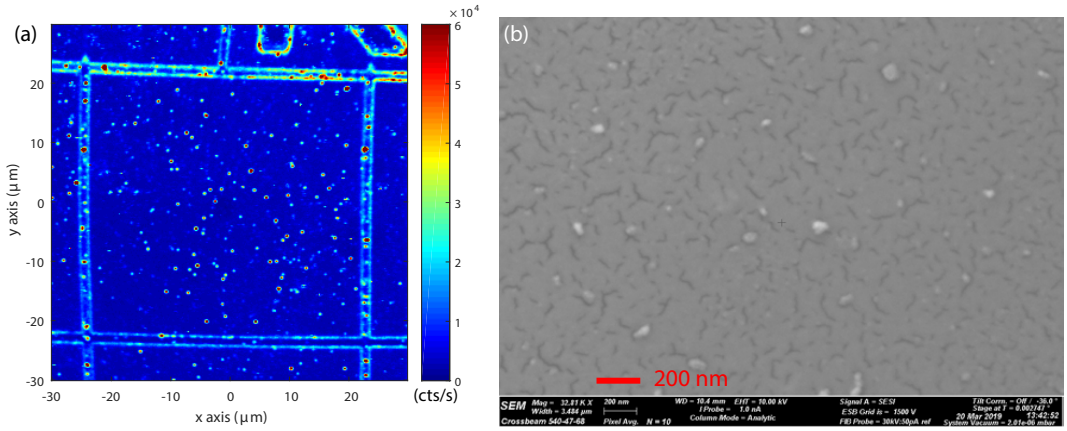


FIGURE 4.5: (a) PL image of a typical distribution of fluorescent nanodiamonds. The FIB marked registration features enclose a 50μm$\times$50μm area. (b) SEM image of dispersed nanodiamonds on the planar mirror substrate.

added using a pipette on the mirror and spin coated in a multistep program. The mirror is rotated stepwise at 200, 300, 400 and 500 RPM for 1 min each to allow a uniform spread of the solution over the surface and sufficient time for the nanoparticles to adhere to the substrate. Finally, the mirror is rotated at 2000 RPM for 1 minute to remove excess solution. To increase the density of emitters, this process can be repeated (typically 5 times), or a or a higher concentration of nanoparticle solution may be used.

4.3.2 NV Centres in Nanodiamond

The nanodiamonds used in this work are commercially available (FND Biotech) high pressure high temperature (HPHT) material, dispersed in de-ionised water [145, 146]. To create vacancies, the nanodiamonds are dispersed on a copper ribbon which is then rolled through an ion beam (He^+) (Figure 4.6 (a)). The nanodiamonds are then annealed at 600 – 800°C to allow vacancy migration and trapping of the vacancy by a nitrogen atom. The ion beam intensity is chosen to maximise the probability of a single NV being created per nanodiamond. In reality, most of the fluorescent nanodiamonds will contain 2 – 4 NV centres, but a sufficient proportion ($\sim$10%) are found to display single photon

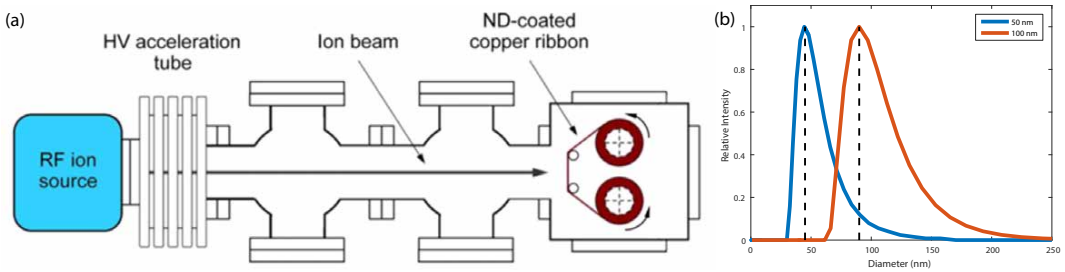


FIGURE 4.6: (a) Schematic of the ion beam facility used for the routine production of the nanodiamonds in this thesis [46]. (b) Size distribution of the two nanodiamond distributions.

emission. The nanodiamonds are then annealed in an oxygen environment at ∼400 °C to induce oxygen termination. Oxygen termination renders the nanodiamond surface hydrophillic which results in a well dispersed solution on the planar mirror. Moreover, NV centres in oxygen terminated material favour the NV^- over NV^0 charge state, as the graphitic surface content is removed [147, 148]. Two nanodiamond solutions were used, with mean diameters of 50 and 100 nm (Figure 4.6 (b)). These samples were found to aggregate over time, making regular sonication necessary before use.

4.3.3 Hexagonal Boron Nitride Nanoflakes

The hBN sample was prepared by collaborators at the Univeristy of Technology, Sydney Australia (Professor Igor Aharonovich and Dr Toan Tran). Commercial hBN nanoflakes (Graphene Supermarket) are dispersed in a water/ethanol mixture following exfoliation from bulk hBN. These nanoflakes have diameters of ∼200 – 300 nm and are 2 – 5 monolayers thick. The solution is dropcast onto an 300 nm thick oxide silicon substrate. The substrate was then annealed at 350 °C for 30 mins in an Argon atmosphere (1 Torr) to promote the migration of vacancies, resulting in the activation of optically active emitters. Figure 4.7 describes the process used to transfer the hBN nanoflakes onto the planar mirror. Poly(methyl methacrylate) (**PMMA**) was spin coated onto the substrate at 3000

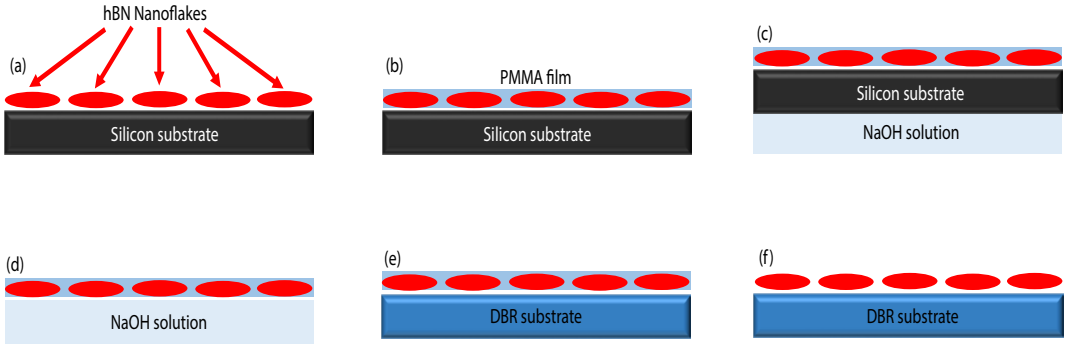


FIGURE 4.7: (a)–(f) Transfer process of hBN nanoflakes onto the planar mirror substrate.

rpm for 1 min, to form a ∼100 – 200 nm thick layer of PMMA. The substrate was then baked at 120 °C on a hotplate for 2 mins to cure and adhere the polymer to the substrate. To transfer the nanoflakes to the dielectric mirror, the substrate was floated on a NaOH solution (2 M) heated at 90 °C to etch away the silicon. This process leaves a membrane of PMMA-coated hBN nanoflakes floating on the surface of the solution. The membrane was then transferred into solutions of de-ionised water to rinse the alkaline solution away. From here, the DBR was used to scoop up the film and then dried at 120 °C to adhere the nanoflakes to the mirror. The hBN coated mirror was then soaked in acetone to dissolve the PMMA layer.

4.4 Confocal Microscope

The results to be presented in this thesis were achieved entirely using this home-built beam scanning confocal microscope (Figure 4.8). The key aspect of confocal microscopy is superior depth resolution. The image obtained from the excitation focus is focused through a pinhole before reaching the detector. When the aperture is positioned at the image plane of the microscope, it becomes confocal with the focal plane of the excitation source. Therefore, the pinhole suppresses scattered light and fluorescence originating

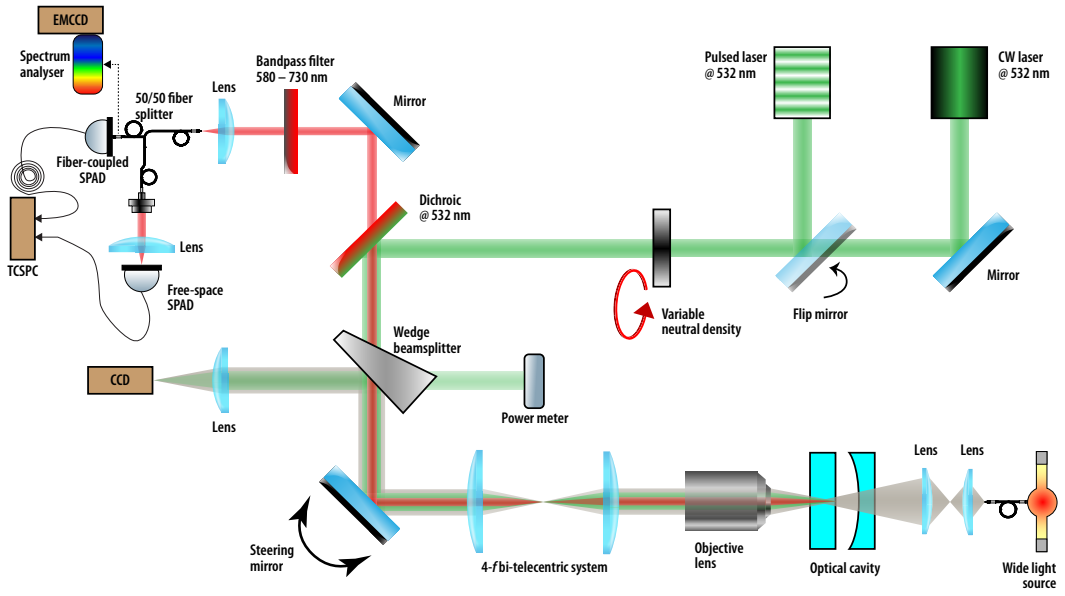


FIGURE 4.8: Schematic of the custom built multi-purpose room temperature confocal microscope. All optical components are mounted onto an optical table.

from outside the focal plane. In the study of single photon emitters, the elimination of light not emanating from the emitter is crucial to achieving high single photon purities. With this system, we can achieve a near diffraction limited focus, allowing the imaging of individual defects. With a numerical aperture (NA) of 0.85, and excitation wavelength of 532 nm, the expected resolution is ∼380 nm. Figure 4.9 shows a PL image of a single emitter with a FWHM of 461 nm. This resolution is sufficient to distinguish individual fluorescent nanodiamonds or hBN nanoflakes provided they are well separated.

To enable the complete characterisation of the defects, there are two primary excitation sources at 532 nm, one continuous wave (CW) laser (Oxxius LCX-532L, 250 mW) and a pulsed laser (PicoQuant LDH-PFA-530B). The CW laser is a free space beam and is used mostly for photoluminescence (PL) imaging and photo-bleaching. The PicoQuant laser can be driven at a repetition rate of 5 – 80 MHz by an external driver (PicoQuant PDL

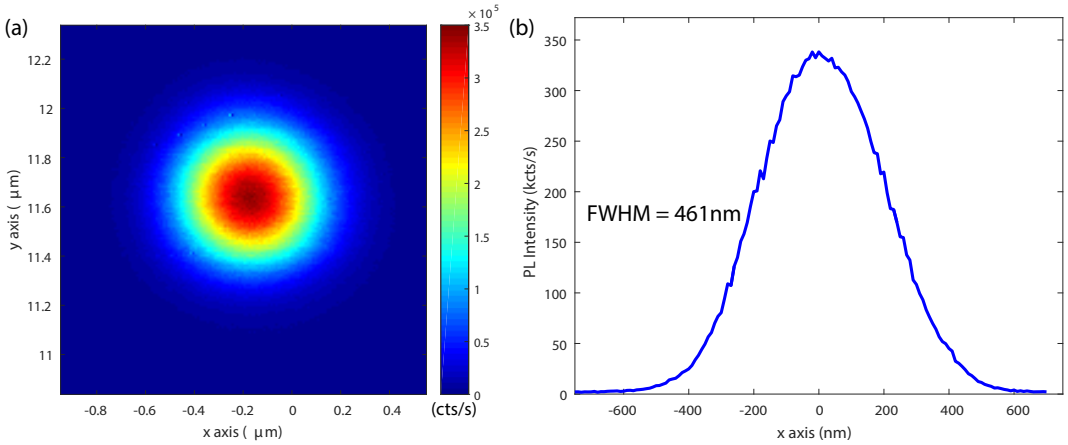


FIGURE 4.9: (a) PL image of a single emitters showing a Gaussian distribution. (b) Cross-section of the PL image in (a) where the focal spot has a FWHM of 461 nm.

800-B) and the emission is coupled to a single mode fibre. This fibre output is collimated by a lens and a flip mirror is used to match the beam paths, allowing switching between the two excitation methods. The intensity of the excitation sources is modulated using a varying neutral density filter attached to a software controlled stepper motor (Arduino Uno R2). This filter allows saturation measurements to be performed on numerous emitters in an automated sequence. Following the neutral density filter, a 550 nm dichroic mirror is used to reflect the excitation while transmitting PL above 550 nm. A wedged beam splitter reflects ∼8% of the incoming light towards a power meter (ThorLabs PM100D console with S120C sensor) allowing continuous monitoring of the laser power. A steering mirror (Newport FSM 300-01) scans the excitation beam through a 4 – f (f = 100 mm) telecentric lens pair. This telecentric system ensures the collimated beam enters the objective lens through the centre, while allowing a large field of view to be imaged (100μm $\times$ 100μm). This is extremely advantageous as a large number of emitters may be sampled with a single image.

The excitation is focused by a 100$\times$ 0.85 N.A air objective lens with variable coverslip

correction (Olympus LCPLFLN100×LCD). The fluorescence is collected by the same objective lens and passes through the dichroic mirror and is filtered by a bandpass filter (Semrock FF01-665/150-25, 590 – 740 nm) to further eliminate background and transmitted laser light. The PL is then focused into a 105 μm multimode fibre (Thorlabs, TM105R5S1A) which acts as a pinhole and a ∼50:50 beam splitter. The first output is directed onto a free space single photon avalanche diode (SPAD, Excelitas SPCM-AQRH-14-TR). The second output can either be coupled to a fibre-coupled SPAD or spectrometer (Andor Kymera 193I–A) with a Peltier cooled CCD (Newton DU940P-BV). This spectrometer is equipped with two gratings (300 and 1800 lines/mm) providing spectral resolutions of 0.96 nm and 0.12 nm. In order to image the sample, a white light source (ThorLabs MWWHF2) is directed onto the laser focus, and reflected onto the webcam by the wedge beamsplitter.

4.5 Hanbury-Brown Twiss and Lifetime Measurements

In order to identify suitable single defects, photon correlation measurements are performed using a Hanbury-Brown Twiss (HBT) interferometer (Figure 4.10 (a))[149]. The fluorescence is separated into two outputs by a fibre splitter, with each output focused onto a SPAD. The HBT measurement is performed by a time correlating single photon counter (TCSPC, Swabian Instruments TimeTagger 20), which measures the time of arrival of photons onto both SPADS. The TimeTagger is then used to create a histogram of the difference in time of arrivals between the two detectors ($\langle I(t)I(t+\tau)\rangle$). This histogram is related to the second-order correlation function $g^{(2)}(\tau)$ (Equation 3.4) introduced in Section 3.2.1 by the expression:

$$g^{(2)}(\tau) = \frac{\langle I(t)I(t+\tau)\rangle}{I_1 \cdot I_2 \cdot t_{bin} \cdot t_{total}} \tag{4.1}$$

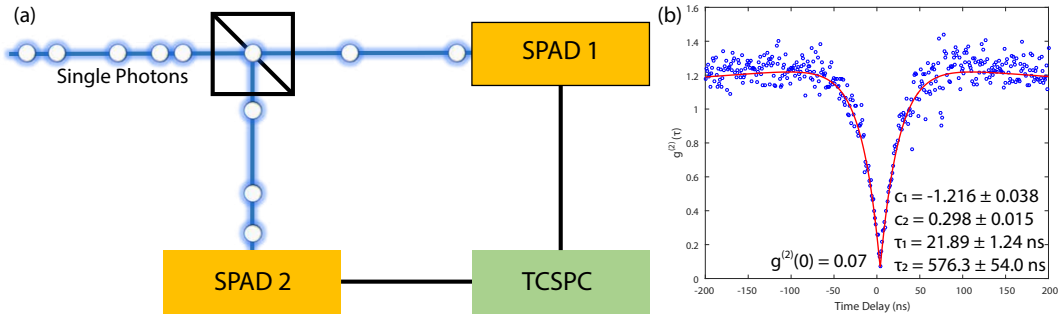


FIGURE 4.10: (a) Basic setup of the HBT measurement. (b) An example second-order correlation measurement for a single NV centre in a nanodiamond. The fit parameters of Equation 3.4 are included.

Where the normalising factor is obtained from experimentally observed parameters. $I_{1,2}$ is the average intensity on each detector, t_{bin} the histogram bin width and t_{total} the total measurement time. Following this normalisation, the value of $g^{(2)}(\tau)$ at $\tau = \infty$ should be unity. The data is then fit with Equation 3.4 ($g^{(2)}(\tau) = 1 + c_1 e^{-\frac{|\tau|}{\tau_1}} + c_2 e^{-\frac{|\tau|}{\tau_2}}$) which describes the emitter as a 3-level system. τ_1 is related to the excited state lifetime, while τ_2 is related to the lifetime of the non-radiative decay pathway. The fit parameters for an example measurement are shown in Figure 4.10 (b).

When performed on the perfect single photon emitter, $g^{(2)}(0) = 0$, but this is rarely seen experimentally. Continuous wave excitation constantly produces background emission, resulting in $g^{(2)}(0)$ being greater than 0 (Figure 4.10 (b)). The sources of background photons include the contributions to fluorescence from the mirror substrate, the potential presence a nearby weakly emitting defect, transmission of laser light through the collection optics and detector dark counts. During the HBT measurement, the source of photons is either from the emitter of interest or these background sources. The probability of each detection event is P_{em} and P_{bkg}. P_{em} is related to the signal (S) and background (B) count rates during the measurement by $P_{em} = \left(\frac{S}{S+B}\right)$. At long time delays, the

following detection events add to unity:

$$P_{em}^2 + 2P_{em}P_{bkg} + P_{bkg}^2 = 1 \tag{4.2}$$

For a perfect single emitter:

$$g^{(2)}(0) = 1 - P_{em}^2 = 2P_{em}P_{bkg} + P_{bkg}^2 = 1 - \left(\frac{S}{S+B}\right)^2 \tag{4.3}$$

Therefore the true correlation function when taking uncorrelated background light into account is found by:

$$g^{(2)}(\tau) = \frac{g_{raw}^{(2)}(\tau) - (1 - P_{em}^2)}{P_{em}^2} \tag{4.4}$$

4.5.1 Pulsed HBT Measurements

When performed under pulsed excitation, the HBT measurement gives a Poissonian distribution allowing us to quantify the ratio of single photon to multi-photon emission events. The short excitation pulse length ($\sim$100 ps) limits the contribution of background fluorescence compared to the CW measurement. The repetition period of excitation must be greater than the emitter lifetime (3 – 5 $\times\tau$) to allow sufficient time for the complete decay from the excited state. Typical excitation rates are 5 – 10 MHz for the NV centre, and 10 – 40 MHz for defects in hBN. Figure 4.11 (a) shows a typical pulsed HBT measurement for a single NV centre. The peaks shaded in green occur due to single photon detection events, and are separated by the time delay between successive excitation pulses ($\pm$ 200 ns in Figure 4.11 (a)). To be consistent with the CW measurement in Figure 4.10 (b), the single photon purity is found from the integrated area of the peak at $\tau = 0$, compared to

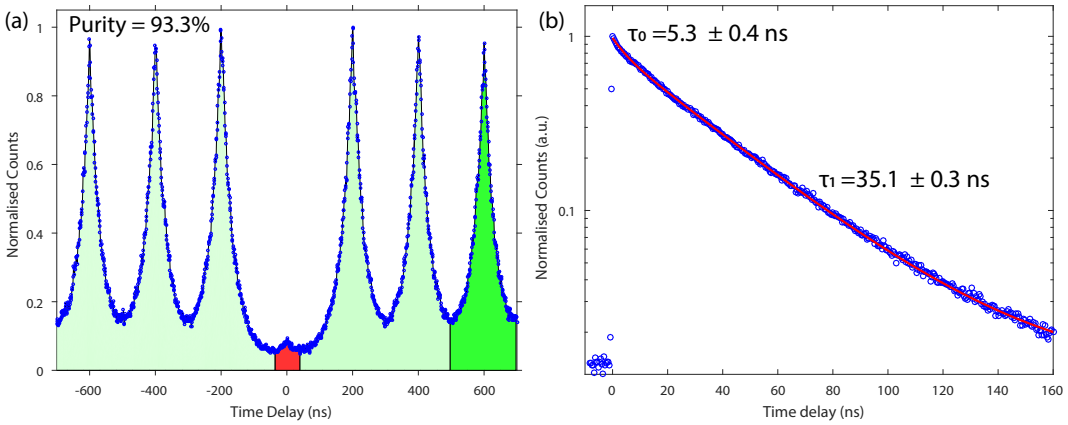


FIGURE 4.11: (a) Pulsed HBT measurement of a single NV centre with a single photon purity of 93.3%. The regions shaded in green occur due to single photon events. The central red area is used to calculate the ratio of single photon to multi-photon emission events, along with the area of a peak at $\tau = \infty$. (b) TRPL measurement for the same NV centre fit with two exponential decays. The longer decay is assigned to the NV lifetime, giving a value of 35.1 $\pm$ 0.3 ns

a peak at $\tau = \pm\infty$ ($Purity = 1 - \frac{A(\tau=0)}{\langle A(\tau=\pm\infty)\rangle}$) [118]. The limits of the central integral are chosen from the position where the adjacent single photon peak decay reaches the baseline level and is shaded in red in Figure 4.11 (a). The baseline level is determined by detector dark counts and stray light from the laboratory. Using the raw data presented in Figure 4.11 (a), the single photon purity is found to be 93.3%. If dark count and stray light contributions are subtracted, the single photon purity increases to 96.5%.

The slope of the single photon decay peak can be used to infer the emitter's excited state lifetime. For the result in Figure 4.11 (a), the lifetime from this method is found to be 33.9 ns. To determine the defect lifetime directly, time-resolved photo-luminescence measurements (TRPL) are performed, as in Figure 4.11 (b). The TRPL is measured by correlating the excitation trigger from the pulse driver with the time of arrival of a photon

on the detector using the HBT method. The data is fit by two exponential decays:

$$I(t) = I_0 + A_1 e^{\frac{-(t-t_0)}{\tau_0}} + A_2 e^{\frac{-(t-t_0)}{\tau_1}} \tag{4.5}$$

Where I_0 is the baseline due to the background, A_i the intensity of each exponential fit, t_0 the start of the decay and τ_i the lifetime components. The terms A_i are unrelated to c_i from Equation 3.4. The first component (τ_0) is attributed to background fluorescence and is fixed in the range 2 – 10 ns, while τ_1 is attributed to the defect's excited state lifetime. Figure 4.11 (b) shows the two lifetime components τ_0 and τ_1, with τ_0 = 5.3 $\pm$ 0.4 ns and τ_1 = 35.1 $\pm$ 0.3 ns. The value of τ_1 obtained form the TRPL fit is similar to the value obtained from the pulsed HBT measurement.

4.6 Saturation Measurements

An important characteristic of an emitter is the saturation intensity (I_{sat}), which is the maximum photon count rate that be be produced by the emitter. This value serves as a measure for the brightness of each single photon source. As described in Section 3.2.2, Equation 3.8 shows that under continuous excitation, increasing the excitation intensity (P) will increase the probability of photon absorption until the emitter lifetime limits the maximum rate of photon absorption. The substrate fluorescence also contributes to the detected count rate. This background contribution typically increases linearly with excitation power and modifies the saturation behaviour:

$$I(P) = \frac{I_{sat} \cdot P}{P + P_{sat}} + B \cdot P \tag{4.6}$$

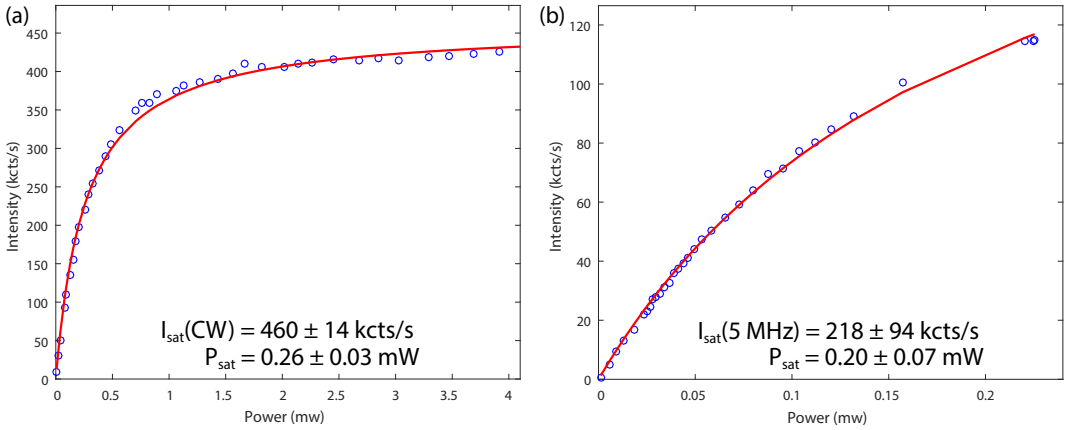


FIGURE 4.12: Saturation measurements under continuous wave (a) and pulsed excitation (b) for NV42. These curves are fit with equation 4.6 with the error bars shown.

Where $I(P)$ is the power dependent count rate, I_{sat} is the saturation count rate, P_{sat} is the saturation power and B is a background term. To perform this measurement, the stepper motor is used to rotate the variable neutral density filter, which varies the excitation power over a range of four orders of magnitude of the initial source power. The stepper motor dwells at a given power for 250 ms, while the count rate is measured by a SPAD and power by the power meter. Due to its position in the confocal microscope (Figure 4.8), the power meter records $\sim 8\%$ of the actual excitation power, and this is corrected for in the software following the measurement. Fig 4.12 (a) shows a typical CW saturation curve for an NV centre (NV42), with the data fit by Equation 4.6. The CW saturation count is found to be $I_{sat} = 460 \pm 14$ kcts/s.

When performed under pulsed excitation, the saturation measurement can be used to determine the efficiency of the single photon source, and the quantum efficiency of the emitter. With pulsed excitation, the emitter can only produce a photon at intervals defined by the excitation frequency (f). Similarly to the TRPL measurement, this excitation rate is chosen such that that the emitter has sufficient time to decay from the excited

state. Figure 4.12 (b) shows the saturation measurement of NV42 performed at an excitation rate of 5 MHz, with I_{sat}(5MHz) = 218 $\pm$ 94 kcts/s. For measurements performed at lower excitation frequencies (5 – 10 MHz), the error bars for I_{sat} can be large, as the excitation laser may not provide enough energy per pulse to reach saturation. However, the fit shows great agreement with the measured data points. The single photon efficiency ($\langle \mathcal{N} \rangle$) is then simply the ratio of the saturation count ($I_{sat}(f)$) and excitation frequency (f). With an appropriate frequency of excitation ($f_{exc} \geq \frac{1}{3\tau}$), the QE of the emitter is:

$$QE = \frac{I_{sat}(f)}{f_{exc} \langle \eta_{coll} \rangle \eta_{sys}} \tag{4.7}$$

Where $\langle \eta_{coll} \rangle$ is the average collection efficiency of the objective lens, and η_{sys} is the total system efficiency following the objective lens. η_{sys} is a product of the transmission efficiency (η_{trans}) of the optical components and detection (η_{det}) efficiency of the detectors. Transmission measurements were performed to verify the specified transmission efficiencies from the component manufacturers, and used to determine the total system transmission. It was found that η_{sys} = 0.32 $\pm$ 0.02. Once the emission spectrum is collected, $\langle \eta_{coll} \rangle$ is calculated from Equation 3.28 for each emitter. A Mathematica script was written by Julia Benedikter (Laser Spectroscopy and Quantum Physics group at Ludwig Maximilian University of Munich) to determine $\eta_{coll}(\lambda)$ over the emitters's spectral profile ($S(\lambda)$) on the DBR mirror. With the system efficiency determined, the count rate at the back aperture of the objective lens is used as a figure of merit for the single photon source. This value will be compared to the other sources described in Table 2.1.

After extensive high power excitation, the emitters used in this project can display intermittent fluorescence. To negate this, coarse steps can be used during the saturation measurement to reduce the total time spent under excitation. Therefore, it is necessary to use as moderate excitation powers as possible when performing all measurements. This is

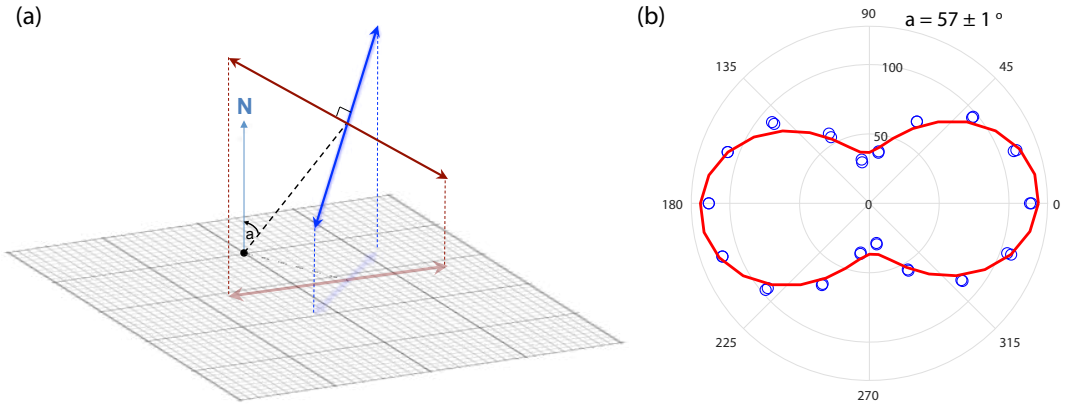


FIGURE 4.13: (a) Schematic showing the angle of the two NV dipoles to the plane of the substrate. (b) Example polarisation measurement performed for a single NV centre with a defect angle $a = 57 \pm 1$ °.

done by optimising the linearly polarised excitation source to match the emitter's dipole orientation, increasing the excitation efficiency - thereby reducing the saturation power. The dipole of each emitter lies at an arbitrary polar angle (a) to the normal of the planar substrate (Figure 4.13 (a)). A half-wave plate is used to vary the orientation of the excitation beam to determine the projection of these dipoles onto the substrate plane. The dependency of the count rate ($I(\theta)$) on the polarisation angle is described by Malus' Law:

$$I(\theta) = I_0 + \Delta I cos^2(\theta + \phi_0) \tag{4.8}$$

Where I_0 is the intensity minima, $I_0 + \Delta I$ is the peak intensity, and ϕ_0 represents the initial orientation of the emission dipole projection on the substrate plane. The angle of the defect to the optical axis is found by:

$$a = \arccos\left(\sqrt{\frac{I_{min}}{I_{max}}}\right) \tag{4.9}$$

Where I_{min} and I_{max} are the minimum and maximum count rate of the polarisation

measurement. Figure 4.13 (a) shows the NV centre's two degenerate dipoles which are at right angles to reach other along the defect axis [150]. For an NV centre with both dipoles lying in the plane, no change is expected in the fluorescence intensity as the overlap of laser orientation will always sum to the same total as it rotates over the two dipoles. Conversely, for single dipole defects, large polarisibilities are expected, as the laser polarisation can be orthogonal to the defect dipole. Figure 4.13 (b) shows an example measurement performed on an NV centre where defect angle is found to be $a = 57 \pm 1\ ^{\circ}$ to the optical axis.

4.7 Cavity Coupling Setup

The mirror with spin coated emitters is attached to a steel sample holder by nail varnish. The nail varnish provides sufficient strength to hold the sample, easy application and rapid removal. The sample holder disk is custom made by the Department of Physics engineering workshop and mounted onto an X-Y positioner (ThorLabs CXY2) by 4 small magnets (RS Components 792-4559) (Figure 4.14 (a)). This mounting mechanism allows easy removal and rotation of the holder, such that the registration grids can be vertically aligned for consistency between measurements. Most importantly, the holder can be flipped to allow cavity construction around a chosen defect. The X-Y positioner is fixed on a linear translation stage, driven by a differential micrometer (ThorLabs DRV517). This stage allows 12.7 mm of manual travel and 20 μm of piezo driven travel, giving greater control of the z-position, along with the steering mirror controlled X-Y positioning of the laser focus. The characterisation of emitters begins with the mirror facing towards the objective lens, known as the "sunny side up" configuration. In this mode of operation, the emission from the defect is directed towards the objective lens, resulting in bright images where single defects can be easily resolved (Figure 4.14 (b)).

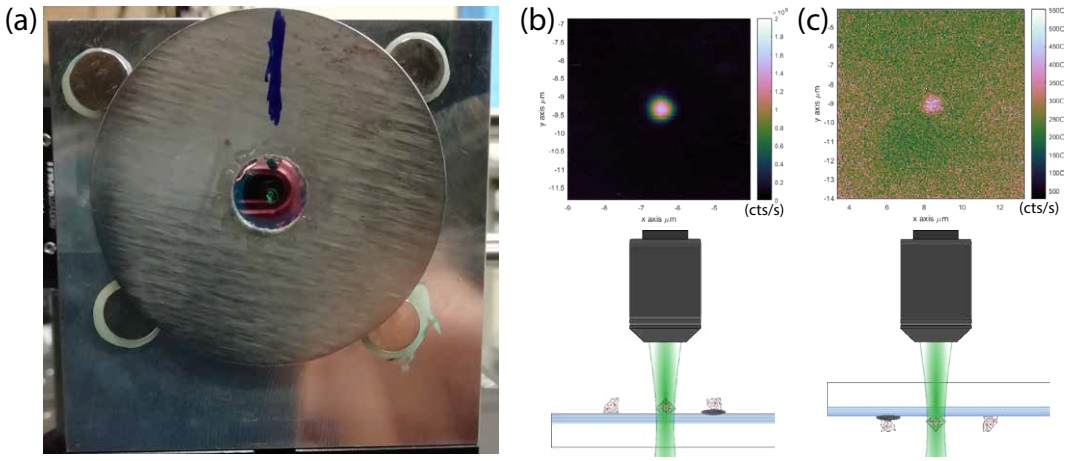


FIGURE 4.14: (a) Image of the sample holder mounted by magnets, with the planar mirror located centrally. (b) PL image of a single defect in the sunny side up configuration. (c) PL image of the same single defect in the sunny side down configuration.

When under optical excitation, the mirror substrates were found to provide a source of background fluorescence, which is problematic to single photon emission. Although the direct source of the fluorescence is unclear, the coatings display a relatively uniform emission spectrum, which was found to photo-bleach with time. Figure 4.15 (a) shows a central dark spot where the laser spot has decreased the background fluorescence. The rate of this reduction is dependent on the laser power, reducing quicker at higher laser powers. The inset of Figure 4.15 (a) shows this reduction at a laser power of 45 mW over 5 minutes. Following sufficient background bleaching (16 hours at 45 mW), a large PL image (60 μm $\times$ 60 μm) is taken (Figure 4.15 (b)). Each visible peak is labelled by the imaging software, given an index and coordinate. From here, second order correlation measurements are performed to deduce which are single emitters. Finally, all the characterisation techniques previously described (fluorescence spectrum, CW and pulsed saturation measurement, lifetime measurement, pulsed second order correlation) are performed. A note is also made on the emission stability of each defect. This process includes several automated steps, allowing the sampling of over 100 emitters per day. These steps

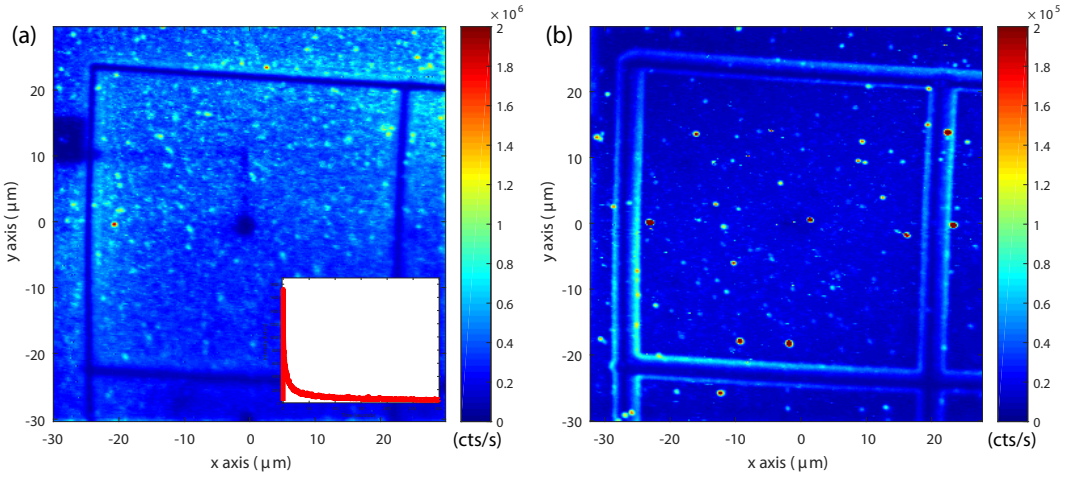


FIGURE 4.15: PL images of background fluorescence before (a) and after (b) 16 hours of photo-bleaching at 45 mW. Inset of (a) shows the count trace for decreasing background fluorescence with time over 5 minutes of photo-bleaching at 45 mW.

can be repeated in different areas of the planar mirrors until there are a sufficient amount of emitters with the desired properties. The emitters can then be ranked on these results, with the most suitable taken forward for cavity coupling. The area (5μm $\times$ 5μm) around the best defects are typically photo-bleached further to maximise single photon purity.

To begin the cavity coupling process, the mirror is inverted, which now requires the emitters to be imaged through the substrate, known as the sunny side down configuration. The coverslip correction of the objective lens is adjusted to the thickness of the substrate to correct for aberrations. However, as the mirror is designed to reflect light at the emission wavelength, the PL signal is far weaker, making it difficult to deduce the precise location of the desired emitters. Thankfully, the registration features remain visible, meaning the rough location of the chosen emitters can be established. Depending on the emitter, a portion of the total emission may lie outside the region of maximum reflectivity, enabling some fluorescence to be detected through the substrate. Alternatively, the brightness of the defect may be sufficient to observe fluorescence despite only a small fraction leaking

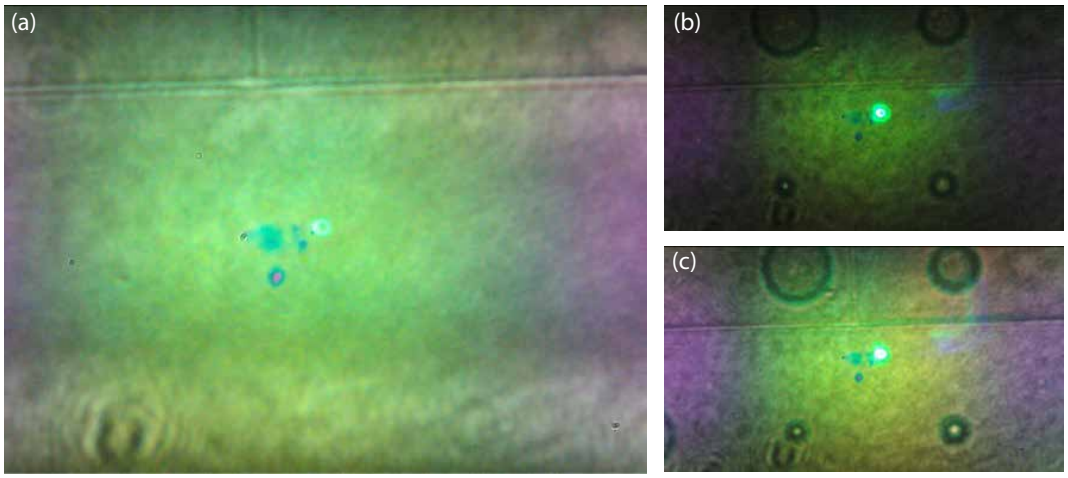


FIGURE 4.16: (a) Webcam image of horizontal interference fringes formed between the two mirrors, indicative of vertical misalignment. (b) and (c) show the dark then bright image observed in optimal alignment as the distance between the mirrors is closed. These correspond to the fringes moving into in the page, as opposed to vertically/horizontally when misaligned.

through the mirror. This situation requires PL images with longer integration times as in Figure 4.14 (c).

To form the cavity, the featured mirror is mounted on a NanoMax piezoelectric stage (ThorLabs MAX311D/M with BPC303 controller), which is fixed onto a linear translation stage (ThorLabs DTS50/M). This stage is driven towards the planar mirror by coarse manual actuators, fine manual actuators and piezoelectric control, over distances of 50 mm, 4 mm and 20 μm respectively. The featured mirror was glued onto a 3-D printed pedestal (Formlabs Form 2 with Clear Resin) and this assembly is screwed on the piezo stage by a kinematic mount (ThorLabs HMM001 with HMA001 adapter plate). This kinematic mount offers an angular range of 6 °, allowing the plinth to be made parallel with the planar mirror. With the piezo-control system, the stage can produce bi-directional repeatability of 50 nm, sufficient for fine positioning of the features around an emitter.

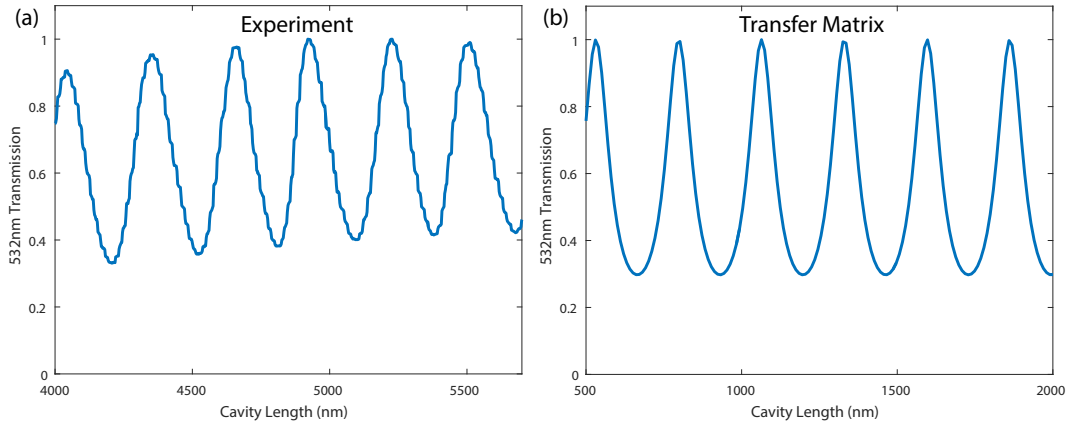


FIGURE 4.17: 532 nm transmission through the cavity with changing cavity length, (a) measured experimentally, and (b) obtained from the transfer matrix method.

The cavity is aligned by white light illumination of the two mirrors. The white light source penetrates between the mirror and creates interference fringes which can be observed on the webcam (Figure 4.16 (a)). The angular mismatch between the planar parts of the two mirrors creates these fringes due to different path lengths in the cavity resonance condition. These become more evident at cavity lengths of below 10 μm. Changing the cavity length causes these fringes to travel in a direction which maintains the cavity length of their resonance. This gives an indication of the tilt required to reduce the angle between the mirrors. Figure 4.16 (a) shows fringes which move vertically as the cavity length changes, indicating a difference in cavity length between the top and bottom of the plinth. This process is repeated iteratively until the fringes travel perpendicularly to the mirror surfaces (Figure 4.16 (b)–(c)). A bandpass filter is used at a wavelength partially reflected by the mirror to give the most contrast in the fringe intensity. This is a necessary step as it allows cavity lengths of <2 μm to be reached, enabling the formation of stable stable modes with the smallest mode volumes.

During the closing of the cavity, the 532 nm laser transmission is monitored by placing the

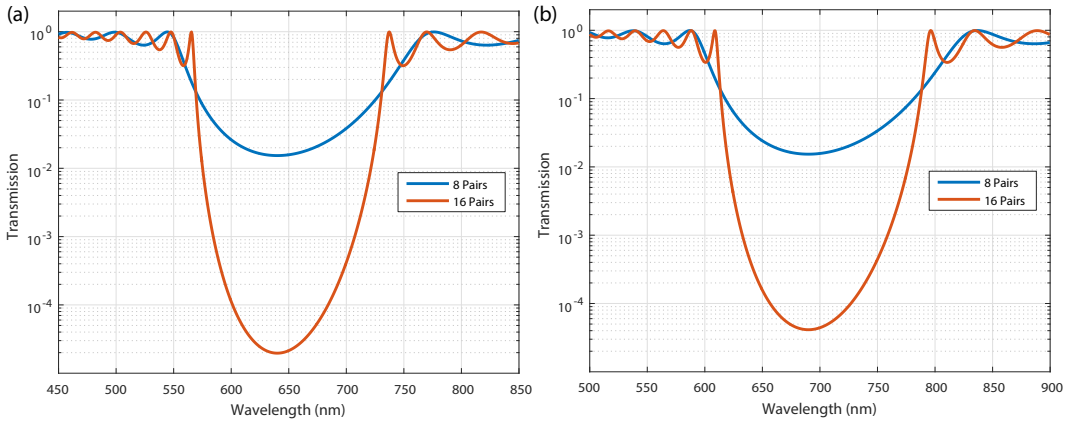


FIGURE 4.18: Transfer matrix calculations of the mirror coatings for 8 and 16 pair DBRs centred at 640 nm (a) and 690 nm (b). These figures are shown on a log scale for clarity.

power meter behind the featured mirror. The intensity of this transmitted beam oscillates as the cavity length is changed. As the cavity is closed, the oscillation stops when the two mirrors are in contact. Figure 4.17 (a) shows the experimentally recorded intensity of the 532 nm laser transmission through the cavity with changing cavity length. A vertical linecut of Figure 3.10 (a) is taken at 532 nm to produce the theoretical transmission of the 532 nm laser seen in Figure 4.17 (b).

The resonance condition within the cavity is given by $qn\lambda = 2L$. Taking the derivative, we find $dL/d\lambda = qn/2 = L/\lambda$. From this, $dL/L = d\lambda/\lambda$ meaning the magnitude of change in wavelength is inversely proportional to the cavity length. Therefore, for short cavity lengths, a small change in the cavity length results in large changes in the cavity mode position and linewidth. To successfully observe high quality modes, the components on the NanoMax stage and the stage itself, are all rigidly fixed to the optical table, minimising vibrations between the two mirrors. With the cavity now formed, the asymmetric mirror reflectivies ensure the leakage of photons towards the objective lens. Assuming a lack of

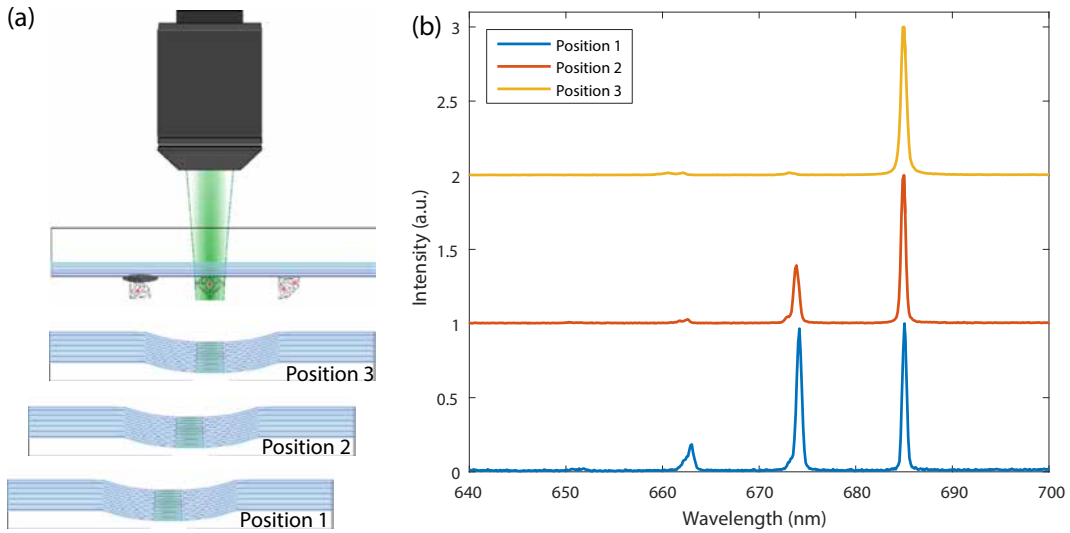


FIGURE 4.19: (a) Lateral positioning of the featured mirror relative to the planar mirror. Position's 1, 2 and 3 are all at the same cavity length, but but with different lateral alignment. (b) Cavity coupled spectra during the optimisation of the lateral position, where the emission into the TEM_{00} mode is maximised.

intra-cavity losses, the fraction of transmitted light through the planar mirror is:

$$\frac{1-R_p}{1-R_fR_p} \approx \frac{T_p}{T_f+T_p} \tag{4.10}$$

Where $R_{f,p}$ are the reflectivities of the featured and planar mirrors and $T_{f,p}$ the transmission. The addition of more DBR layer pairs to the featured mirror pushes the planar outcoupled fraction towards unity. The planar and featured mirror reflectivies ($R_p - R_f$) used in this thesis are 97.5 $\pm$ 0.5 % and 99.997 % respectively (Figure 4.18).

With the two mirrors now approximately parallel, the excitation laser can be focused onto a chosen defect, and a specific concave feature brought directly infront. The open nature of the cavity allows movement of the two substrates relative to each other. Due to the absence of a feedback mechanism, regular optimisation is required to account for

drift in the cavity length and the feature's lateral position. The planar mirror is kept stationary and the steering mirror is used to optimise the X-Y position of the laser focus onto the defect. Meanwhile, the featured mirror is positioned using the NanoMax stage to maximise emission of the emitter into the cavity modes. Figure 4.19 shows the lateral optimisation to maximise counts into the TEM_{00} mode. The measurements previously performed in the sunny side up configuration can now be performed in the cavity to determine the effect of cavity coupling on the single photon emission properties of the defects.

4.8 Conclusion

This chapter has presented the experimental methods involved in acquiring the results to be presented in this thesis. The length of this chapter is by no means reflective of the substantial amount of time used to optimise these methods, thereby making cavity coupling experiments routine. The cavity coupling process has been fully described, beginning from the fabrication of hemispherical features by the FIB, through to the identification of emitters facing away from the collection lens. The key steps for successful experiments can be summarised as:

- FIB milling of hemispherical features onto the plinth.
- DBR coating of planar and featured substrates.
- FIB milling of registration features onto the planar mirror.
- Nanoparticle deposition onto planar mirror
- Single emitter characterisation.
- Planar mirror inversion and alignment of cavity mirrors.

- Cavity coupling of selected features to chosen emitters.

Improvements in plinth miniturisation and mirror alignment are required to allow cavity lengths $<$600 nm to be reached. Theoretical simulations will be used to support the experimentally observed data, providing insights into the sources of loss and optimal cavity configuration for the emitter-cavity system.

5 |

Single Photon Characterisation of NV Centres in Nanodiamonds

5.1 Introduction

NV centres within nanodiamond crystals are used extensively throughout this thesis. With size distributions between 30 – 250 nm, they can be readily included within open-cavity systems, without affecting the minimal separation achievable between the mirror substrates. This chapter will present the optical characterisation of single NV centres within nanodiamonds at room temperature. It will be shown that single NV centres are readily observed in these nanodiamond samples through the use of HBT measurements. A full characterisation of the optical properties will take place, with particular prominence given to "NV232" - which will be presented separately for clarity. Time resolved photoluminescence measurements will be serve as a benchmark to detect potential cavity induced enhancement in the emission rate when the emitter is placed within the optical resonator. The cavity coupling results to be displayed in Chapter 6 will include those for this emitter. Finally, the efficiency and long term stability of a few NV centres in nanodiamonds will be investigated. These preliminary results will be used to assess their suitability as a robust single photon source.

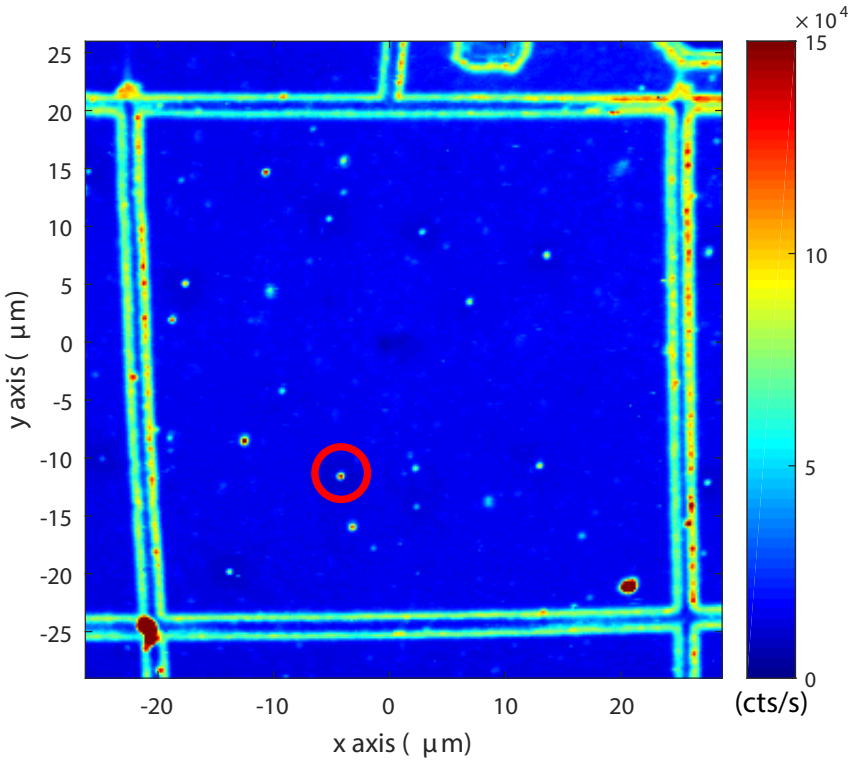


FIGURE 5.1: PL image of nanodiamonds with NV centres dispersed on the planar mirror substrate, with NV232 circled in red. The image is taken with a x100 0.8NA objective lens.

5.2 Single Emitter Survey

The nanodiamonds used in this study were fabricated and spin coated onto mirror substrates as described in Section 4.3.2. A large photo-luminescence image (60μm $\times$ 60μm) is taken and a typical dispersion of emitters is shown in Figure 5.1, with the defect "NV232" circled in red. The FIB marked registration features enclose an area of 50μm $\times$ 50μm. This grid underwent $\sim$32 hours of photo-bleaching at 45 mW to reduce the background contribution, thereby making the emitters more visible. Each bright spot corresponds to an emitter with emission in the 590 – 740 nm collection window, and so should be from the negatively charged NV centre. Over 500 single NV centres have

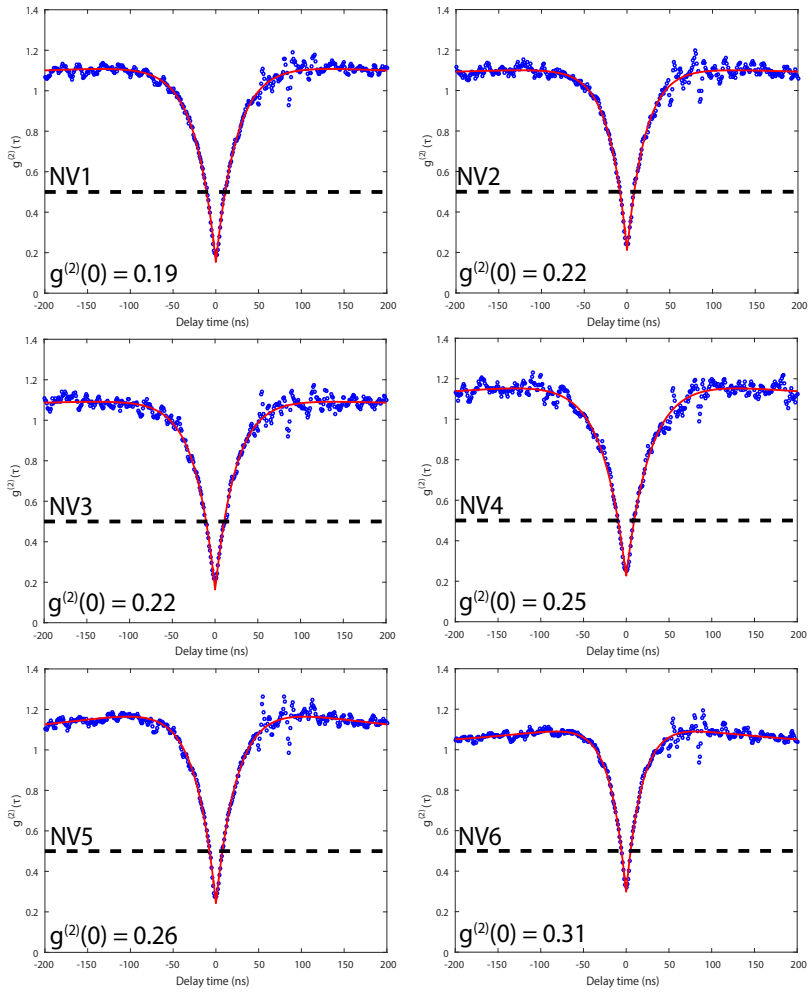


FIGURE 5.2: Continuous wave HBT measurements of single NV centres within the 50μm $\times$ 50μm registration grid. The black dashed line represents the value of $g^{(2)}(0) = 0.5$. The red lines show the fit from Equation 3.4.

been characterised over the course of this project. The key results for six single NV centres from the same sample will be displayed. These six emitters are chosen as they are representative of the general properties observed from bright single NV centres in nanodiamonds. This survey includes; HBT measurement to verify single photon emission, emission spectrum to verify the NV centre as the emitter, saturation measurement to quantify the maximum photon output and time resolved photo-luminescence (TRPL) to

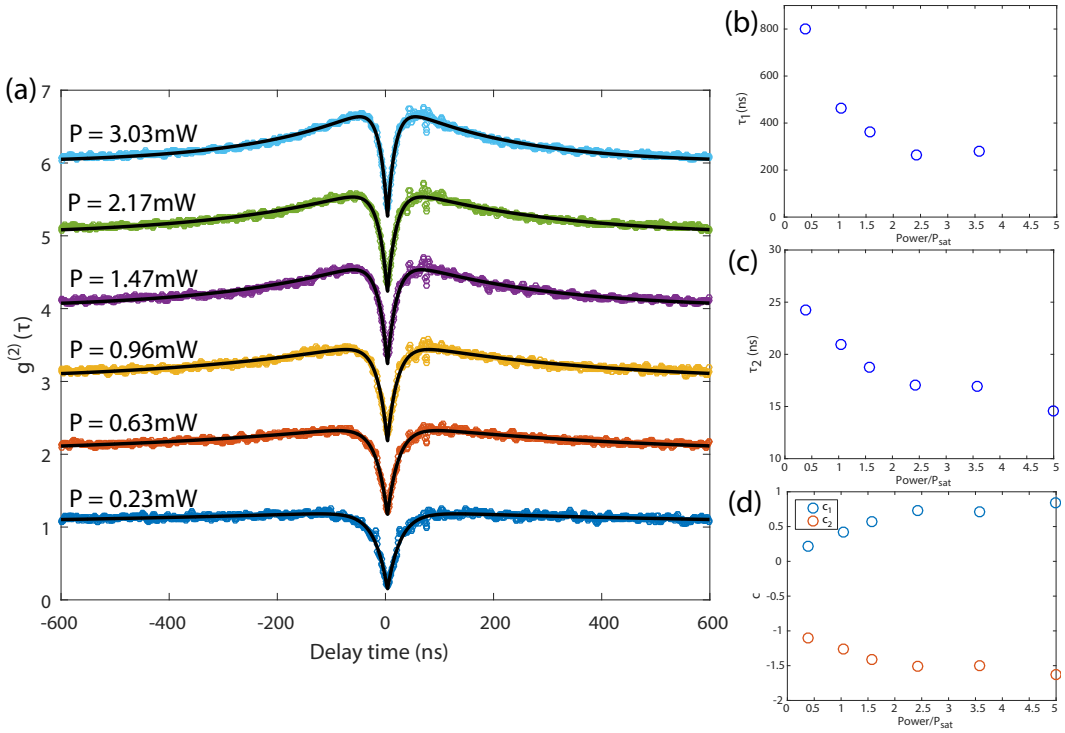


FIGURE 5.3: (a) Power dependent HBT measurements of a single NV centre. The data points are all fit to equation 3.4. Each data set is displaced vertically by 1 for clarity. (b)-(d) Evolution of the fit parameters of equation 3.4 as a function of the saturation power P/P_{sat}.

determine the excited state lifetime.

Figure 5.2 presents the CW HBT measurement for the six single emitters located within the FIB marked registration grid. These measurements were performed at an excitation power of 640 μW. The behaviour of $g^{(2)}(\tau)$ is described by Equation 4.1, and these chosen NV centres all display $g^{(2)}(0)$ values below 0.5. Typical signal to noise (SNR) ratios are $(\frac{S}{B}) \sim$ 10–20. Therefore, using Equation 4.4, single NV centres under CW excitation on the mirror substrate tend to display values of $g^{(2)}(0)$ $\sim$0.22, before further photobleaching.

The NV centre is not a simple two level system and is known to possess a metastable shelving state [39]. The presence of a metastable shelving state may significantly reduce the excited state population, limiting the achievable emission rate. In addition, the ground and excited electronic states feature spin sub-levels, which can modulate the observed fluorescence. Therefore, it is important to understand the internal rate dynamics of each emitter. This can be done through HBT measurements at varying excitation powers, to deduce the intrinsic decay rates of the emitter [39]. Figure 5.3 (a) shows an example for the power dependence of the $g^{(2)}(\tau)$ function (Equation 3.4) for NV24. A clear bunching effect is observed at intermediate time-delays, which can be attributed to pumping into the singlet manifold. This effect is more pronounced with increased excitation power.

The fit parameters for this power dependence are summarised in Figure 5.3 (b)–(d). Using the limiting cases at high ($P \to \infty$) and low excitation powers ($P \to 0$), the decay rates of the three-level system (k_{21}, k_{23} and k_{31}) can be approximated as described in Reference [39]. The key values required from the fitted data are $c_1^{\infty} = 0.87 \pm 0.01$, $\tau_1^{\infty} = 213 \pm 3$ ns and $\tau_2^{(0)} = 24.3 \pm 0.7$ ns. The rate parameters from these fitted values are $k_{21} = 39 \pm 0.1$ MHz, $k_{23} = 2.2 \pm 0.04$ MHz and $k_{31} = 2.5 \pm 0.04$ MHz. The radiative decay rate k_{21} is of most interest, and is an order of magnitude larger than the non-radiative decay rates. Similar rates are reported in Reference [109], showing the radiative channel as the dominant decay route. The excited state lifetime is estimated by $\left(k_{21} + \frac{k_{23} \cdot k_{31}}{k_{23}+k_{31}}\right)^{-1}$, giving $\tau = 24.9$ ns, which is typically in the range observed for nanodiamonds [150–153].

The room temperature emission spectra of these emitters are shown in Figure 5.4. Each of these spectra have been normalised for comparison. NV1–6 feature predominantly NV^- character with a ZPL at ~637 ± 4 nm and a broad phonon side band. The variation in the ZPL position is attributed to the strain in the nanodiamond, which is much greater than in bulk diamond. The local strain for an NV centre is dependent on the nanodiamond size

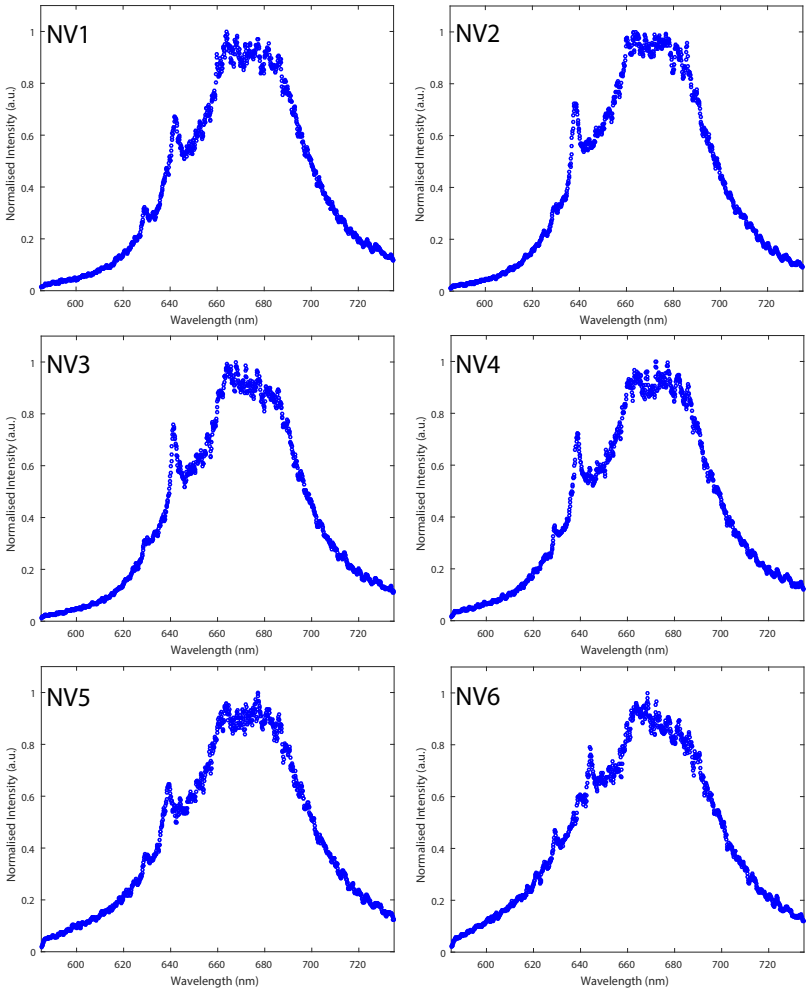


FIGURE 5.4: Spectral survey of single NV centres in nanodiamond on the DBR mirror. The data has been normalised for comparison. All the emitters show characteristic NV^- emission spectra

and position of the defect within the nanodiamond. It must be noted that the presence of the DBR substrate modifies the observed spectrum as the mirror reflectivity is maximum at 640 nm for the emitters in Figure 5.4. As a result, the PSB emission which would normally be maximum at ∼700 nm is now most prominent at ∼670 nm. For NV centres on a DBR with maximum reflectivity at 690 nm, the spectra maximum will be at ∼690 nm.

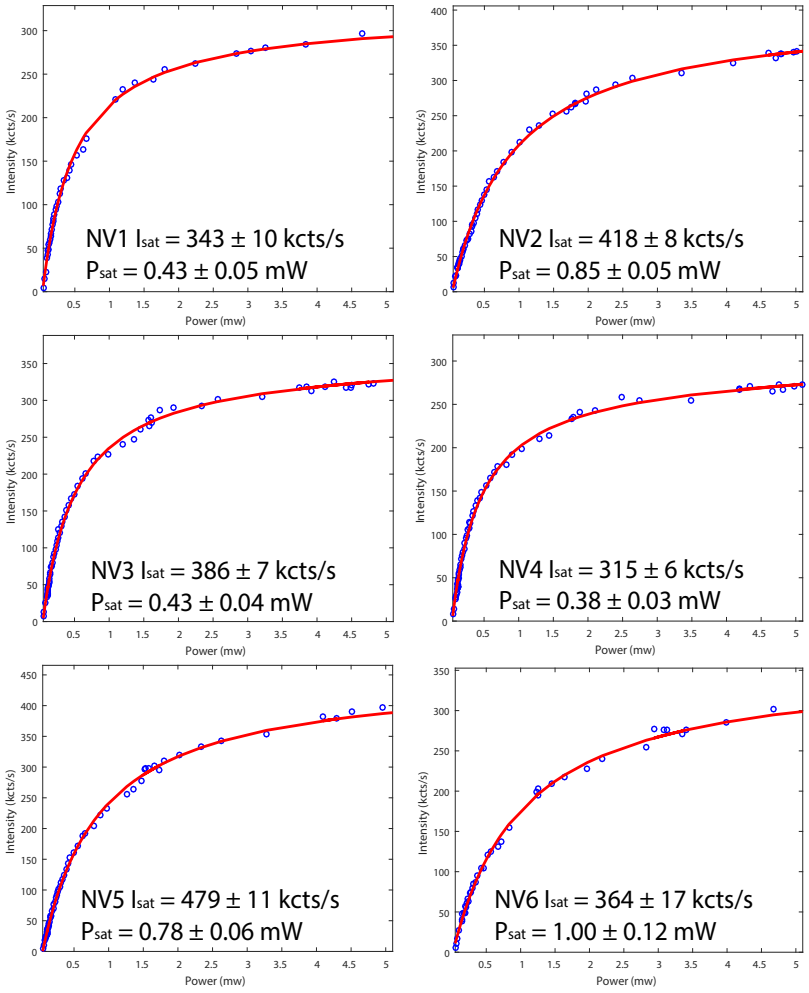


FIGURE 5.5: CW saturation measurements highlighting the variation in maximum photon output of the emitters.

Figure 5.5 shows the CW saturation measurement for these emitters. The saturation behaviour is fit with Equation 4.6, revealing saturation counts (I_{sat}) values typically in the range ∼250 – 500 kcts/s. The limiting factor for this value is the excited state lifetime of the defect and the quantum efficiency of radiative emission. NV centres in bulk diamond have a lifetime of 12 ns [98], but those in nanodiamond typically feature much longer lifetimes as seen in Figure 5.6. The data is fit with Equation 4.5, accounting for a fast background decay ($\tau_{bkg} < 8$ ns), and a longer decay attributed to the NV centre. Time

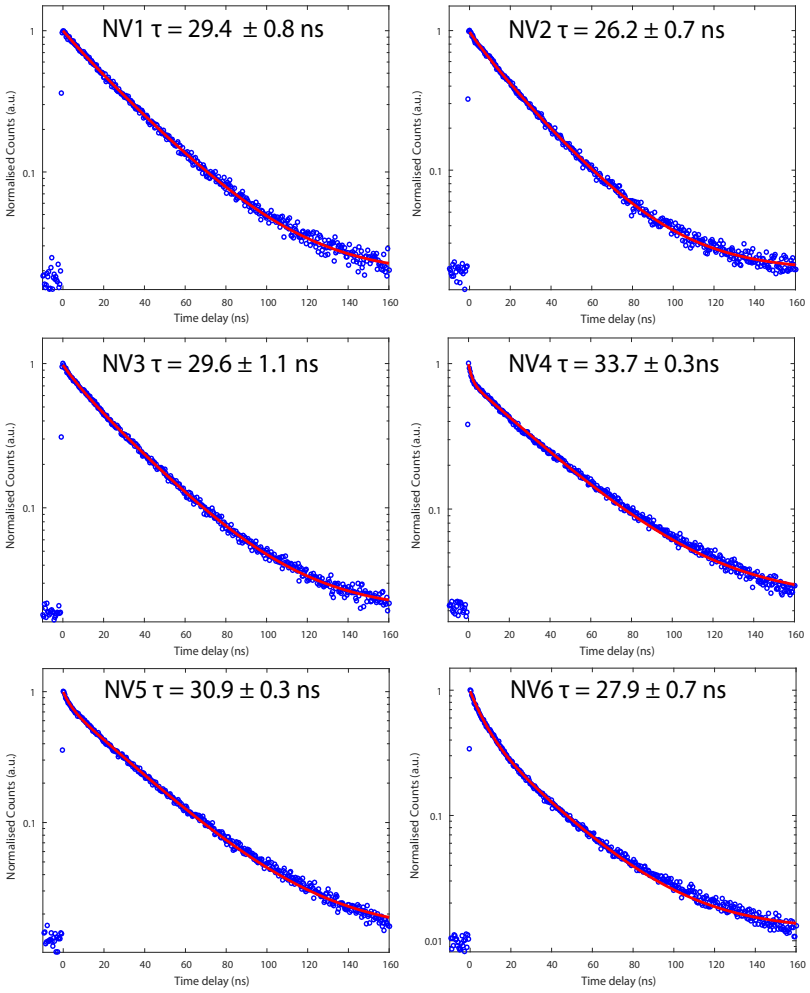


FIGURE 5.6: PL excited state lifetime data for the NV centres. The data is fit with a bi-exponential decay to separate the background contribution from the NV centre lifetimes.

resolved PL measurements reveal the excited state lifetime of NV centres to be in the range 20 – 60 ns, depending on the individual nanodiamond. This increased lifetime compared to bulk diamond is often attributed to the reduction in the optical density of states as the size of the host crystal is reduced, limiting the rate of spontaneous emission [153]. However, emitters with the shortest excited state lifetimes do not always correspond to the highest saturation counts, as the excited state lifetime is a combination of the radiative and non-radiative lifetimes, and this will be discussed later in this chapter.

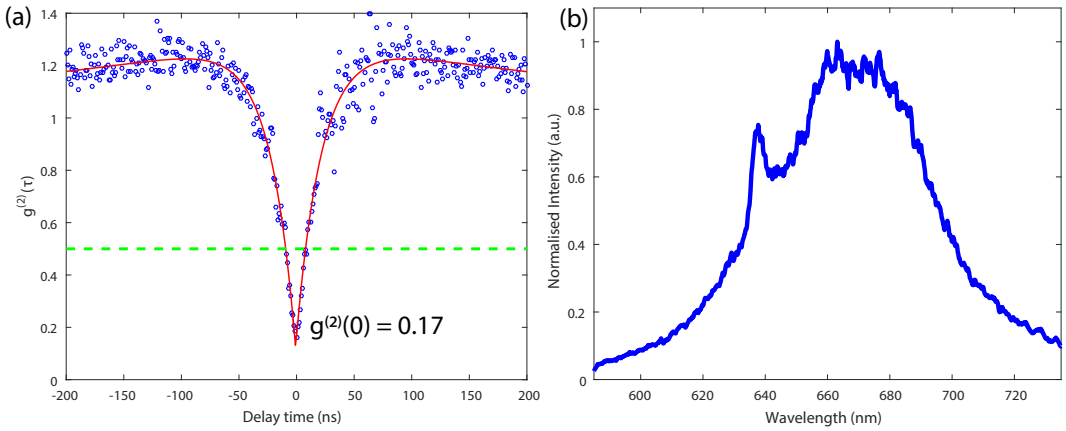


FIGURE 5.7: (a) CW HBT of NV232 confirming single photon emission. (b) Room temperature emission spectrum of NV232.

5.3 Properties of NV232

The properties of NV232 are presented separately to the previous NV centre survey as a more in depth analysis is required. This emitter will be utilised for cavity coupling results to be presented in Chapter 6. NV232 originates from the 50 nm nanodiamond sample shown in Figure 4.6 (b). The CW HBT measurement in Figure 5.7 (a) shows clear single photon emission, with a value of $g^{(2)}(0) = 0.17$. As previously mentioned, the contribution of the background limits the data at $\tau = 0$ reaching $g^{(2)}(0) = 0$. The observed SNR ratio of 12 gives an expected $g^{(2)}(0) = 0.15$, very close to the measured value of $g^{(2)}(0) = 0.17$. The emission spectrum of NV232 displays characteristic NV^- features with a FWHM of $\sim$60 nm, as seen in Figure 5.7 (b).

Many applications for single photon sources require the deterministic generation of photons, and so, the single photon emission properties of NV centres must be characterised under pulsed excitation. A photon correlation measurement was also performed for

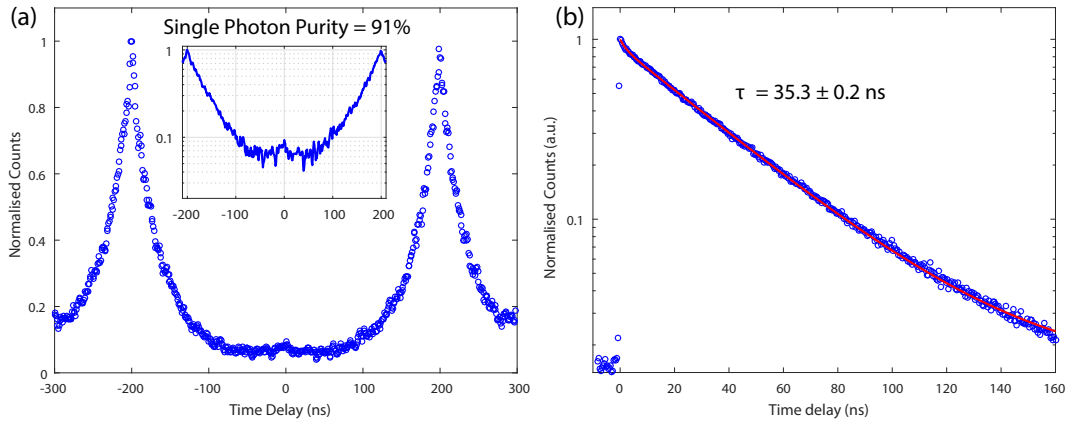


FIGURE 5.8: (a) Pulsed HBT measurement performed at a repetition rate of 5MHz. The lack of a peak at $\tau = 0$ clearly shows single photon emission, with a single photon probability of 91%. The inset is log-scaled for clarity. (b) TRPL measurement for NV232 shows a single exponential decay with an excited state lifetime of 35.3 ns.

NV232 using the HBT method, but under pulsed excitation (Section 4.5.1). The measurement was performed at a excitation frequency of $f = 5$ MHz, equating to a 200 ns gap between sequential excitation pulses. This value was chosen to allow the excited state population sufficient time to decay to the ground state before the next excitation pulse. Figure 5.8 (a) shows two peaks 200 ns either side of a small peak at $\tau = 0$. Using the integrated area under the central peak and those at $\tau = \pm$ 200 ns (as in Figure 4.11 (a)), the single photon purity is found to be 91%. Similarly to the CW measurement, the uncorrelated substrate auto-fluorescence contributes to the central peak, which when removed would lead to even higher single photon purities. Figure 5.8 (b) shows the TRPL measurement for NV232, which was found to have an excited state lifetime of 35.5 $\pm$ 0.2 ns.

The CW saturation count (I_{sat}) collected over the 590 – 740 nm window is 274 $\pm$ 14 kcts/s (Figure 5.9 (a)) with a saturation power (P_{sat}) of 0.47 $\pm$ 0.06 mW. To decrease the saturation power, it is necessary to rotate the orientation of the laser to the optimum angle

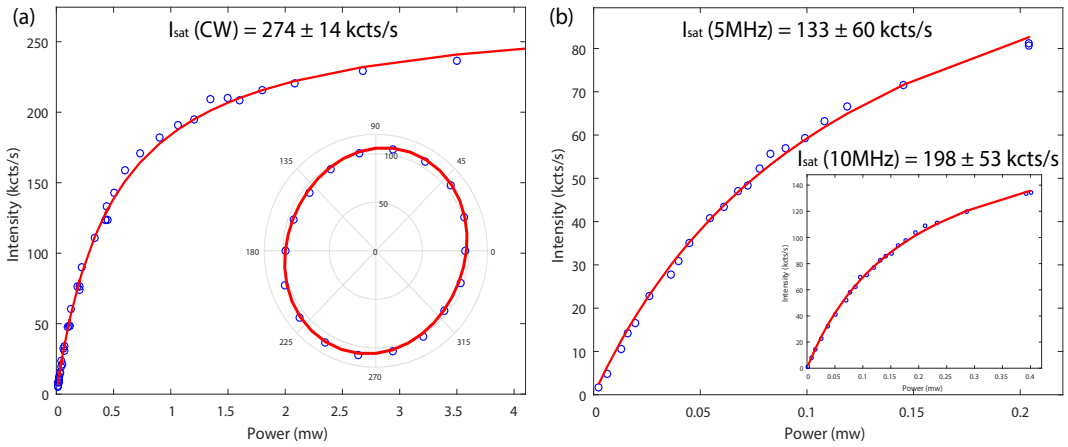


FIGURE 5.9: (a) Continuous wave saturation measurement for NV232 over the 590 – 740 nm spectral window. Inset shows the polarisation measurement for NV232 revealing the orientation of the defect. (b) Pulsed saturation measurement at 5 MHz used to determine the efficiency of NV232. Inset shows the saturation measurement at 10 MHz.

for NV232, increasing the efficiency of excitation. Figure 5.9 (a) inset shows the excitation polarisation optimisation, revealing the angle of NV232 to be 21 $\pm$ 2 $^\circ$ to the substrate plane. The efficiency of NV232 can be estimated from the saturation count obtained under pulsed excitation. With an excited state lifetime of 35.3 ns, these measurements were performed at excitation frequencies of 5 and 10 MHz. The single photon efficiency at the detectors is then:

$$\langle \mathcal{N} \rangle = \frac{I_{sat}(f)}{f} \tag{5.1}$$

The saturation counts for NV232 under pulsed excitation are I_{sat}(5MHz) = 133 $\pm$ 60 kcts/s and I_{sat}(10MHz) = 198 $\pm$ 53 kcts/s. These pulsed I_{sat} values correspond to detection efficiencies of 2.58% and 1.97% respectively. The efficiency under CW excitation can be approximated similarly to pulsed excitation, but using the excited state lifetime as the time delay between excitation events. The CW saturation count of NV232 is 274

$\pm$ 14 kcts/s, which is 0.97% of the inverse of the excited state lifetime. With these values, there appears to be a decrease in efficiency with increasing excitation rate. These low efficiencies led to an investigation on the sources of losses, including both the optical system, and the internal efficiency of the NV centre in nanodiamonds.

5.4 NV Centre Efficiency

NV centres in bulk diamond are usually described as emitters with near unity quantum efficiencies, such that the radiative decay rate has a strong influence on the measured excited state lifetime [44]. However, NV centres in nanodiamonds have been found to display a range of radiative and non-radiative decay rates leading to largely varying quantum efficiencies between 0.05 – 0.9 [49, 152, 154]. The distribution of these values is ascribed to the size, geometry and specific position of the NV centre within the nanodiamond host and is reflected by the wide range of excited state lifetimes. As the measured lifetime is a combination of both radiative and non-radiative lifetimes, the particular geometry of each nanodiamond makes it difficult to predict the relative contributions of these processes. The excited state lifetimes of single NV centres in both 50 and 100 nm nanodiamond samples have been measured (Figure 5.10). The most frequently occurring lifetime range for both of these samples is 30 – 36 ns. These results are very similar to those observed by Mohtashami *et al* [152]. The 50 nm sample does show a wider distribution of lifetimes, potentially due to a higher surface area to volume ratio, as the presence of surface states can induce more non-radiative decay pathways [153]. Using the analytical resulted derived by Chew ($\tau_{ND} \sim 0.062 \cdot \tau_{bulk}$) [142], the radiative lifetime for the NV centre in nanodiamond is expected to be $\sim$ 193 ns, much larger than those observed in Figure 5.10. As the emission is not purely radiative, a reduced excited state lifetime is expected, dependent on the quantum efficiency of each emitter.

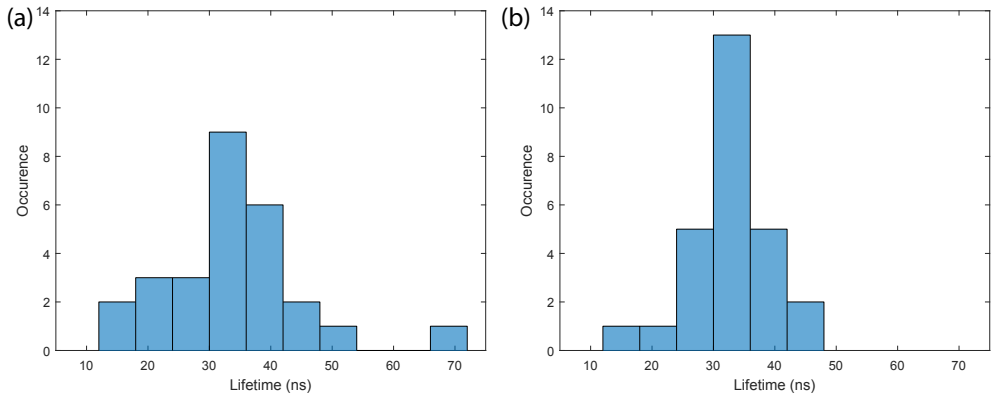


FIGURE 5.10: Histogram of single NV centre lifetimes from (a) 50 nm and (b) 100 nm nanodiamond samples.

A simple method used in this thesis to estimate the quantum efficiency is to perform saturation measurements under pulsed excitation. As opposed to CW excitation, in this regime, the frequency of excitation is known, and can be directly related to the photon output rate from the emitter as in Equation 5.1. The quantum efficiency is then estimated from Equation 4.7. As in Section 5.3, a repetition rate of $f = 5$ MHz is generally used for NV centres. Only the brightest emitters under pulsed exitation are chosen, where the NV dipole is assumed to lie in the plane of the mirror substrate. The system efficiency was measured in Section 4.6 giving $\eta_{sys} = 0.32 \pm 0.02$. The collection efficiency for NV232 was determined using Equation 3.27, giving $\langle \eta_{coll} \rangle = 0.46$ for the 0.85 NA objective. This value is comparable to the collection efficiency obtained from FDTD simulatons ($\eta_{coll} = 0.50$) for the same system with a 0.8NA objective [155]. Using the calculated and measured values of $\langle \eta_{coll} \rangle$ and η_{sys}, the saturation count of NV232 (I_{sat}(5MHz) = 133 kcts/s) equates to an estimated quantum efficiency of $QE = 0.18 \pm 0.07$. The I_{sat} values of the brightest NV centres under pulsed excitation observed in this thesis at 5 MHz are typically in the range 120 – 150 kcts/s, when measured over the 590 – 740 nm spectral window. These values deliver quantum efficiencies on the lower end of the previously reported QE

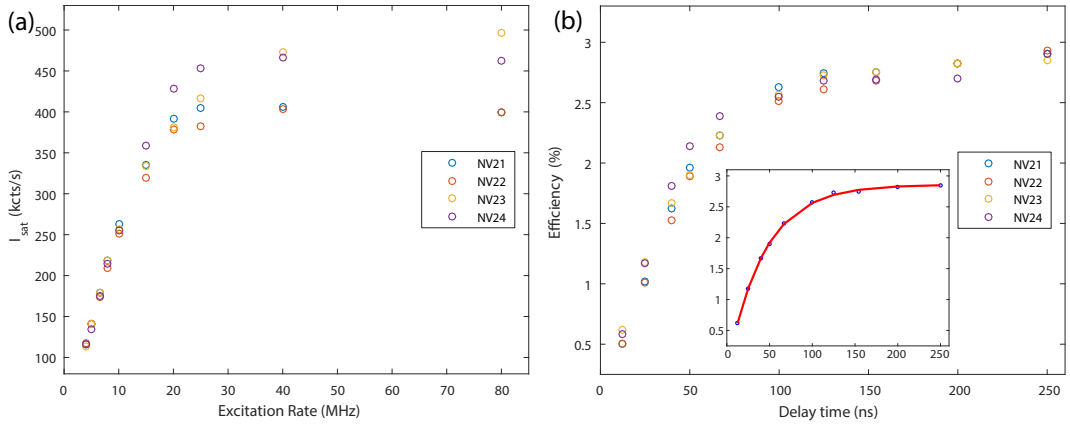


FIGURE 5.11: (a) Saturation count dependence on the excitation rate for single NV centres. (b) System efficiency of the same single NV centres with increasing delay time between excitation events. (Inset) Example fit for the efficiency behaviour of NV23 using Equation 5.2.

range of NV centres in nanodiamonds, despite coming from one of the brightest NV centres. This measurement was repeated for several other bright single NVs (NV21 – 24) in 100 nm nanodiamonds (Figure 5.11 (a)). They all showed similar saturation counts at an excitation rate of 5 MHz (I_{sat} = 135 – 141 kcts/s), despite possessing different lifetimes. This result infers that the QE of nanodiamonds are much lower than typically reported, and this will be probed further in the following Chapter.

Following the results at 5 MHz, further pulsed saturation measurements were performed at increasing excitation rates. After three excited state lifetimes, it is expected that the population of the excited state will have decreased by 95% ($e^{-3} \sim 0.05$), thus the emitter should be ready for re-excitation. Therefore, a near equal efficiency should be maintained with a time delay of 3τ between excitation pulses. For a single photon source, this would mean a greater photon flux due to the increased rate of excitation, but at the cost of a slight ($\sim$5%) reduction in efficiency. Figure 5.11 (a) displays the observed saturation count at each excitation rate, with Figure 5.11 (b) the corresponding system efficiency of

those I_{sat} values, calculated from equation 5.1. The saturation count of all these emitters display comparable behaviour, increasing with the excitation rate until approaching saturation at ∼30 – 40 MHz. However, the efficiency appears to increase with an increased time delay between subsequent excitation pulses (decreasing excitation rate). This behaviour is fit with the expression:

$$\langle \mathcal{N} \rangle = A - Be^{\frac{\tau_{exc}}{\tau_{rec}}} \tag{5.2}$$

Where A is the maximum efficiency at large excitation delays, τ_{exc} is the time delay between excitation pulses and τ_{rec} is the recovery lifetime for radiative emission. The recovery lifetime describes the timescale over which the defect can be re-excited following decay from the excited state. These values of τ_{rec} for NV21 – 24 are summarised in Table 5.1. The recovery lifetime is an important parameter that must be accounted for when optimising the efficiency and total photon output of an NV centre based single photon source. For NV21, NV22 and NV24, the recovery lifetime is comparable to the excited state lifetime as expected. For NV23, the recovery lifetime is much longer than the excited state lifetime. Power dependent HBTs were performed on NV21 – 24 to deduce the rate parameters of the assumed three-level system of these NV centres. For simplicity, these are expressed as lifetimes ($\tau_i = \frac{1}{k_i}$). The lifetime of the excited state for radiative (τ_{21}) and non-radiative (τ_{23} and τ_{31}) transitions are presented in Table 5.1. These lifetimes are combined to give a total lifetime for decay to the ground state from the HBT method:

$$\tau_{HBT} = \left(\frac{1}{\tau_{21}} + \frac{1}{\tau_{23} + \tau_{31}} \right)^{-1} \tag{5.3}$$

While the τ_{HBT} values calculated from this method do not match those measured directly from the TRPL measurement, their relative values agree with those from the TRPL measurement. It is known that the three-level structure typically used to describe the NV

Emitter	τ_{21} (ns)	$\tau_{23}(ns)$	τ_{31} (ns)	τ_{HBT} (ns)	τ_{TRPL} (ns)	τ_{rec} (ns)
NV21	33.4	134	238	30.7	40.6	40.3
NV22	34.5	132	233	31.5	39.1	43.9
NV23	14.6	91	111	13.6	19.3	43.1
NV24	22.6	130	270	21.4	31.2	30.7

TABLE 5.1: Summary of various lifetimes describing the rate dynamics of single NV centres.

centre does not fully describe the internal dynamics of the NV centre. The ground ($^3A_2$) and excited (^3E) states are triplet states which under zero magnetic field split into spin sub-levels $m_s = 0$ and $m_s = \pm 1$. The use of continuous excitation polarises the electron into the $m_s = 0$ spin sub-level, but the polarisation behaviour of the spin under pulsed excitation is much less studied. These different excited state spin sub-levels are known to possess different lifetimes [150], which may be involved with the recovery process. In addition to the spin sub-levels, there are two intermediate singlet states that provide the non-radiative decay pathway; a short-lived $^1A_1$ state and a long-lived ^1E state, which are merged together into level $|3\rangle$ in this model. Therefore, while power dependent HBT measurements support the directly measured NV excited state lifetimes, they do not provide insight into the difference between the excited state lifetime and recovery time of NV23. Although the origin of this difference is unknown, a potential cause may be the distance from the NV centre to the surface. Surface states are known to perturb the electronic structure, and may lead to a larger involvement of the spin sub-levels in the population dynamics of the emitter.

5.5 NV Centre Stability

In order for a nanodiamond based single photon source to be commercially viable, photostability is an essential specification. It is crucial for the emitter to display neither bleaching, blinking or spectral jumps. The NV centre is conventionally described as a perfectly

photo-stable colour centre, displaying long term photo-stability. This is generally true in bulk diamond, where the defect is located deep within the lattice. However, the behaviour of nanodiamonds under long term excitation is much less quantified. Over the numerous defects studied in this work, degradation in the emission properties of the NV are regularly observed. This is particularly the case under pulsed excitation, which is known to induce photo-ionisation of NV^- to NV^0 [54]. The probability of charge state conversion is related to nanodiamond size and the proximity of the defect to the nanodiamond surface [53], as surface states can induce charge state switching to NV^0, thereby quenching the NV^- emission [50].

Figure 5.12 shows the intermittent behaviour of NV7. Experiments on this defect had been performed periodically over nine months with the emission properties remaining unchanged. However, the use of the defect for the alignment of a pulsed excitation source lead to the observed PL instability shown in Figure 5.12 (b) and (c). A PL spectrum was taken during periods of intermittent fluorescence and showed the emission profile to consist of both NV^- and NV^0 character, with a significant increase in the spectral profile at wavelengths below 640 nm. The nanodiamond based device must be able to maintain photo-stability for $>$1000 hours of operation at the desired operating excitation rate of the device, which is 5 – 10 MHz. Performing this test over 1000 hours at an excitation rate of 5 MHz was not practically feasible, but the same number of excitation pulses can be delivered at 80 MHz in a shorter time span, corresponding to a testing time of 62.5 hrs. With a typical excited state lifetime of $\sim$ 33 ns, a delay time of 12.5 ns between excitation events may lead to photo-ionisation of the electron. This has been shown to be a two-photon process scaling quadratically with laser power [156–159]. The pulsed laser used for this test delivers an average power of 4 mW, with a peak power of 500 mW per pulse. Therefore, this stability test is expected to be a far more rigorous test than realistic excitation conditions of average power $\leq$ 0.5 mW.

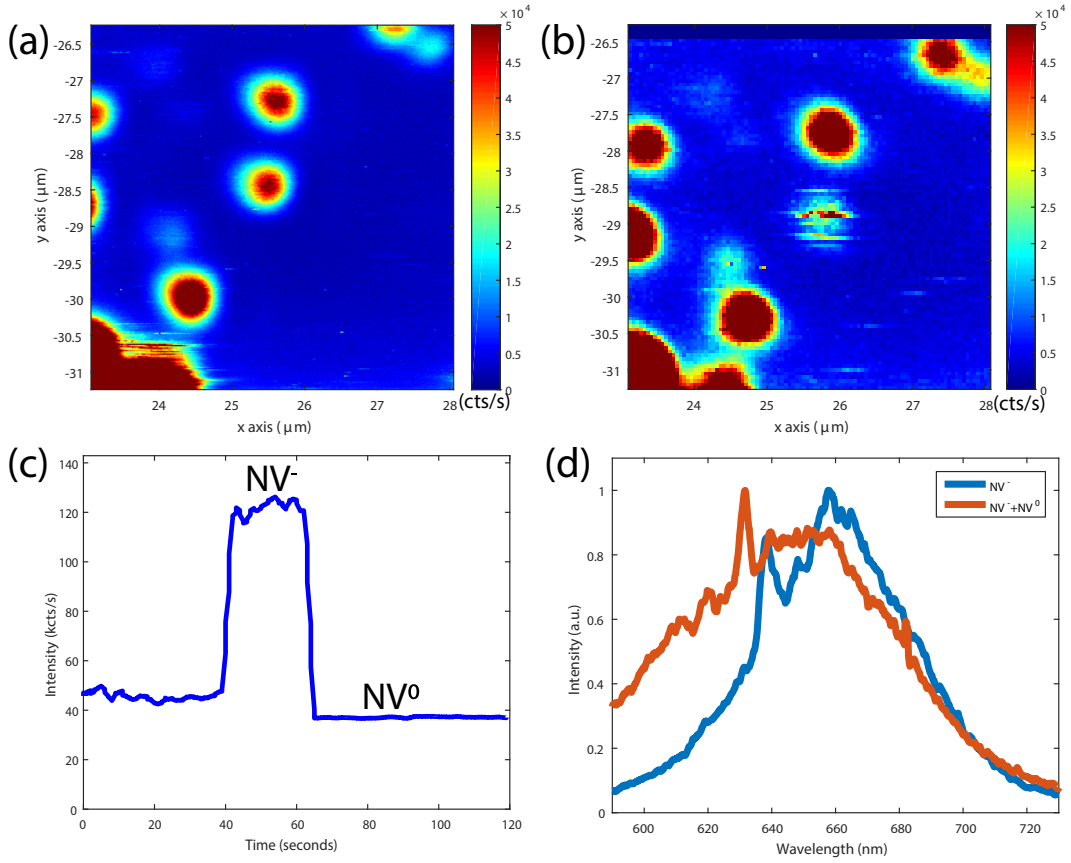


FIGURE 5.12: (a) PL image of a stable NV centre (NV7). (b) PL image of NV7 displaying intermittent fluorescence over the duration of the scan. (c) Normalised PL count trace of NV7 switching between two states. (d) PL spectra of NV7 highlighting contributions from the NV^- and NV^0 states.

The defect NV232 which was previously characterised displayed near perfect photo-stability under both CW and pulsed excitation, making it a good choice to observe long term stability. Following 62.5 hrs of excitation at 80 MHz, NV232 showed a decrease in PL count rates under both CW and most significantly pulsed excitation (Figure 5.13). Figure 5.14 (a) shows a decrease in the CW saturation count by 34% from 274 $\pm$ 14 kcts/s to 182 $\pm$ 11 kcts/s. Correspondingly, the excited state lifetime was found to increase by 31% from 35.3 $\pm$ 0.2 ns to 46.9 $\pm$ 0.6 ns. The nanodiamonds from the 50 nm sample were found

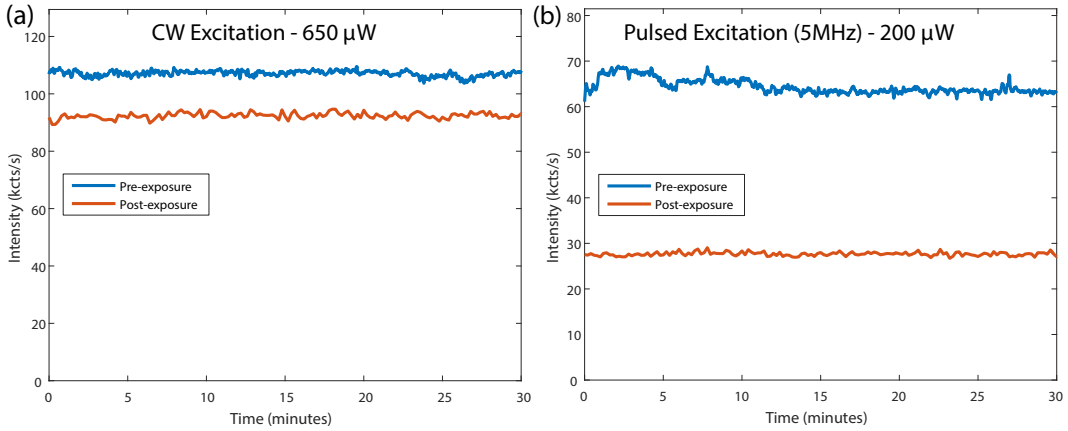


FIGURE 5.13: PL count traces of NV232 under CW (a) and pulsed (b) excitation following long term high power exposure. The CW count trace was recorded at a laser power of 650 μW. The pulsed excitation measurement was performed at a excitation rate and power of 5 MHz and 200 μW.

to display varying excited state lifetimes with prolonged pulsed excitation on several occasions. A possible explanation for the change in excited state lifetime and subsequent decrease in photon count rate may be the reduction in size of the host nanodiamond, induced by the high peak power pulsed excitation.

From Fermi's golden rule (Equation 3.46), the spontaneous emission rate is dependent on the local density of states, while the observed excited state lifetime is also dependent on the contribution of non-radiate decay pathways. Beginning from bulk diamond, as the size of the diamond crystal decreases, the local density of states (LDOS) also decreases resulting in an increased radiative lifetime (Figure 3.15 (a)). However, further reduction in the nanodiamond size leads to the increasing contribution of non-radiative decay pathways which decrease the observed excited state lifetime [154]. Kononenko *et al.* have used high intensity laser pulses to etch away diamond surfaces, creating craters on the order of 1 μm in depth [51], showing the possibility of laser-induced ablation of diamond.

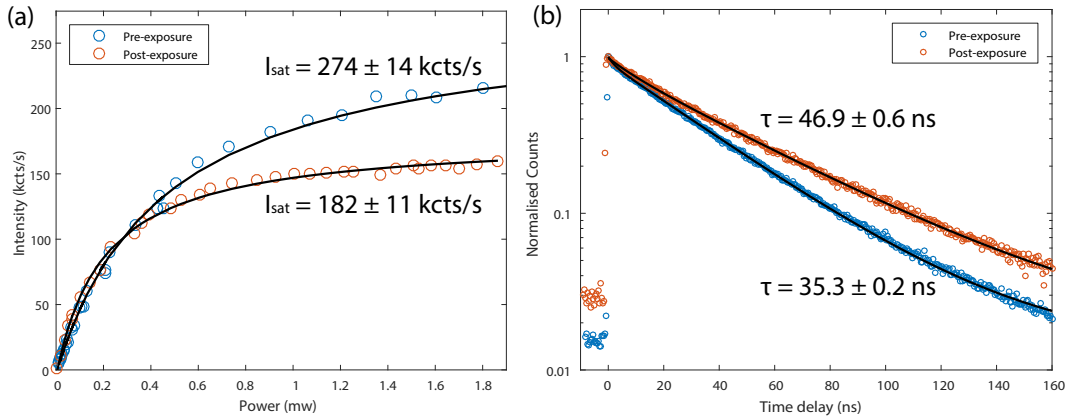


FIGURE 5.14: (a) CW saturation measurement for NV232 before and after exposure. (b) PL lifetime measurements showing an increase in the excited state lifetime.

Inam *et al.* reported the threshold for increasing non-radiative decay contributions is in nanodiamonds below a diameter of 150 nm, but is dependent on the defect position within the nanodiamond [154]. NV232 originates from the 50 nm nanodiamond solution (Figure 4.6 (b)), but the exact size of this nanodiamond is unknown and the majority (65%) of the distribution is greater than 50 nm. Due to the photo-stability of this emitter, it is speculated that the defect is located very centrally within a nanodiamond potentially on the larger end of the distribution, and is sufficiently protected from the environment. The changing of non-radiative pathways tends to manifest as instability in the PL, and is usually a strong indication of the eventual quenching of emission. As blinking or bleaching was not observed in NV232, non-radiative contributions are assumed to remain constant, and only an increased excited state lifetime is observed. This result motivated the use of a larger nanodiamond sample, which should in principle increase the probability of an NV centre being centrally located within the nanodiamond, guaranteeing prolonged device operation.

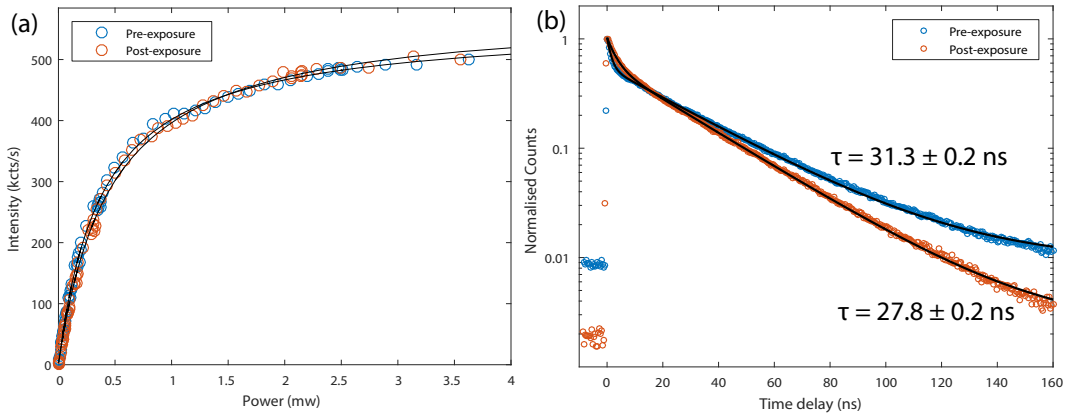


FIGURE 5.15: (a) CW saturation measurement for NV18 before and after exposure showing an increase from 553 ± 11 kcts/s to 577 ± 16 kcts/s. (b) PL lifetime measurements showing a decrease in the excited state lifetime, from 31.3 ± 0.2 ns to 27.8 ± 0.2 ns.

These accelerated stability tests were repeated for NV centres from the 100 nm nanodiamond solution. The first test on NV18 showed promising results (Figure 5.15). The continuous wave saturation measurement showed negligible changes in behaviour as seen in Figure 5.15 (a), increasing by 4% from 553 ± 11 kcts/s to 577 ± 16 kcts/s. This increase is mostly likely due to improved alignment of the microscope. More interestingly, the excited state lifetime showed an 11% decrease, from 31.3 ± 0.2 ns to 27.8 ± 0.2 ns. In order to obtain greater insight to the variation of emission properties, the experiment was reconfigured to include sequential measurements of the excited state lifetime and emission spectrum at regular intervals, while constantly monitoring the PL count rate. An auto-focus script was added to realign the emitter in (x, y, z) to the position of maximum fluorescence between the measurements.

The same 100 nm nanodiamonds were spin-coated onto a mirror substrate with maximum reflectivity at 690 nm. Single defects were located and characterised, and the

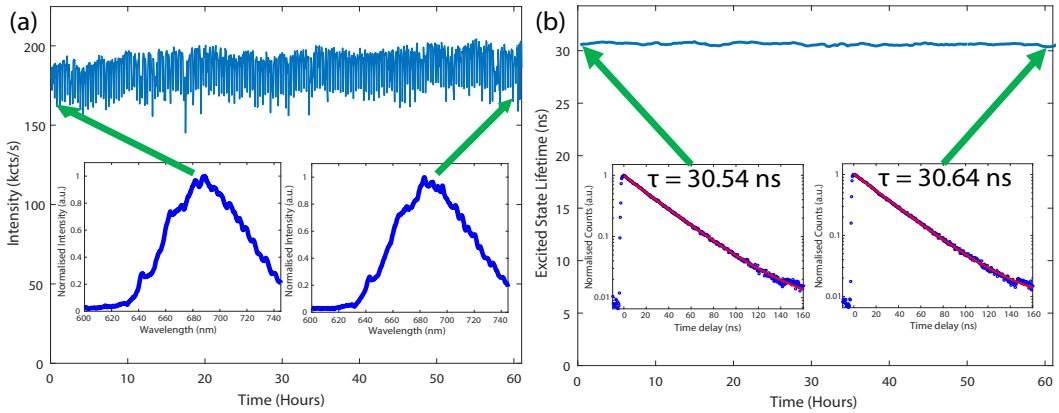


FIGURE 5.16: (a) Fluorescence intensity of NV11 over 62.5 hrs of pulsed excitation. The inset show the PL spectra at the beginning and end of exposure. (b) Excited state lifetime of NV11 during the long term exposure. Inset shows two TRPL measurements at the beginning and end of exposure.

results of this experiment for NV11 can be seen in Figure 5.16. The defect shows remarkable photostability over the length of the measurement. The regular dips in the count trace are a result of the scheduled reduction in excitation frequency from 80 MHz to 5 MHz so that the excited state lifetime could be measured. The emission spectrum showed minimal changes over the course of the measurement, confirming the emitter remained in the negatively charged state. NV11 showed an average fluorescence intensity of 187 $\pm$ 11 kcts/s, meaning a 6% variation in the count rate. The average excited state lifetime was 30.6 $\pm$ 0.2 ns, varying by $<$1% over the course of the experiment.

The result for NV11 presents the ideal situation for the nanodiamond based single photon source, where emission stability is observed over both short (minutes) and long (hours) time periods. It is extremely likely that NV11 lies centrally within a large nanodiamond from the 100 nm sample, where any potential laser-induced effects did not perturb the emission characteristics. When repeated for another defect (NV12) from the same 100 nm nanodiamond solution, the results were similar (Figure 5.17). Much like NV11, NV12

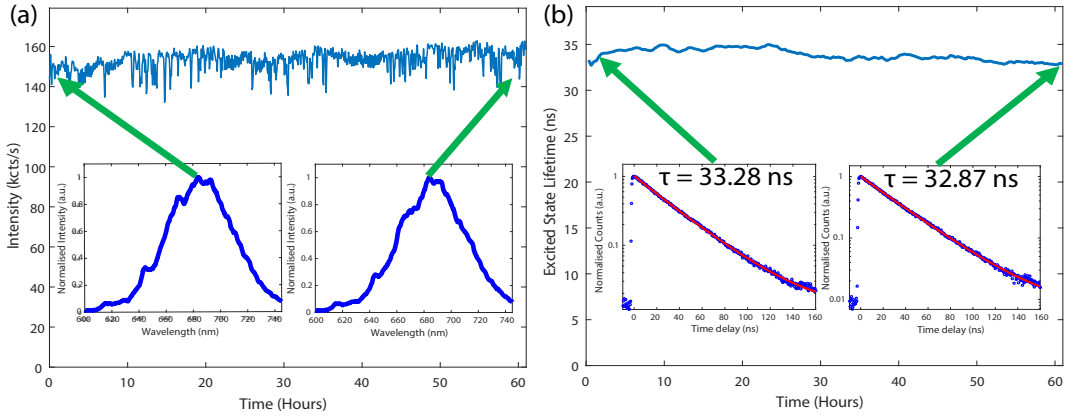


FIGURE 5.17: (a) Fluorescence intensity of NV12 over 62.5 hrs of pulsed excitation. The inset show the PL spectra at the beginning and end of exposure. (b) Excited state lifetime of NV12 during the long term exposure. Inset shows two PL lifetime measurements at the beginning and end of exposure.

displayed an average count rate of 153 ± 5 kcts/s and average excited state lifetime of 33.9 $\pm$ 0.7 ns, meaning variations of 3% and 2% respectively. This is also combined with a lack of change in NV12's spectral profile (Figure 5.17 (a) inset). Comparable results were found for another defect from this sample.

NV centres in the 50 nm sample were expected to show much more erratic behaviour as the defects should be closer to nanodiamond surface. NV13 was exposed to the same pulsed excitation conditions as NV11 and NV12 with the following results. Over the first 62.5 hrs, NV13 showed a relatively stable fluorescence intensity of 153 $\pm$ 12 kcts/s (Figure 5.18 (a) inset). The excited state lifetime showed a slight decrease over this time period with an average of 46.2 $\pm$ 1.6 ns (Figure 5.18 (b) inset), inferring the increase in non-radiative decay. It was decided that the exposure would continue past the 62.5 hr point to observe the behaviour of the defect until eventual bleaching. Figure 5.18 (a) shows the onset of a more erratic PL intensity after this point. The excited state lifetime also showed large variations due to the increasing and varying contributions of

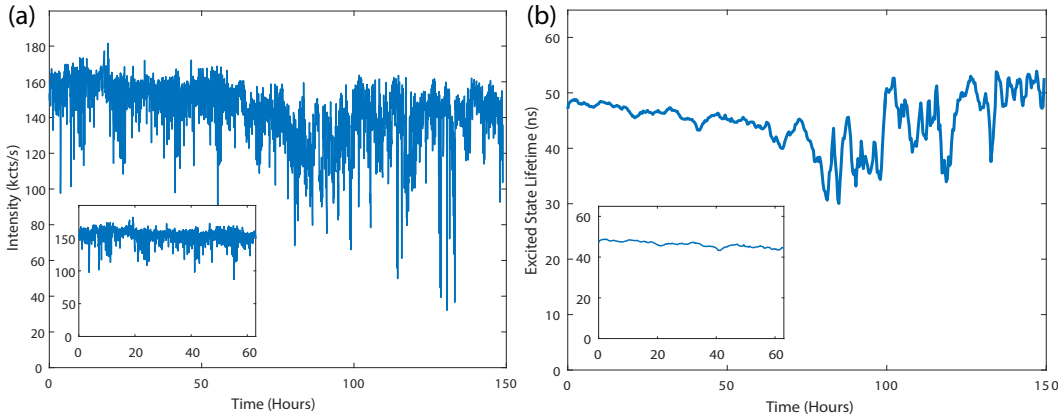


FIGURE 5.18: (a) Fluorescence intensity of NV13 over 150 hrs of pulsed excitation. (b) Excited state lifetime of NV13 during the long term exposure. Insets show the fluorescence intensity and PL lifetime during the first 62.5 hrs of exposure.

non-radiative decay pathways, ranging between 30 – 54 ns.

The radiative lifetime is directly related to the size of the nanodiamond as shown in Figure 3.15 (a). If the presumption of decreasing nanodiamond size is true, we expect an increase in the radiative lifetime over the course of this measurement. With knowledge of the excited state lifetime (a combination of both radiative and non-radiative lifetimes) and the fluorescence intensity, the time dependence of the fluorescence intensity can be expressed as:

$$I(t) = I_0 \frac{\gamma_{rad}(t)}{\gamma_{total}(t)} \tag{5.4}$$

Where I_0 is the an arbitrary constant, and γ_{total} is the sum of radiative and non-radiative decay rates. Equation 5.4 can be rearranged to make γ_{rad} the subject, which is simply the

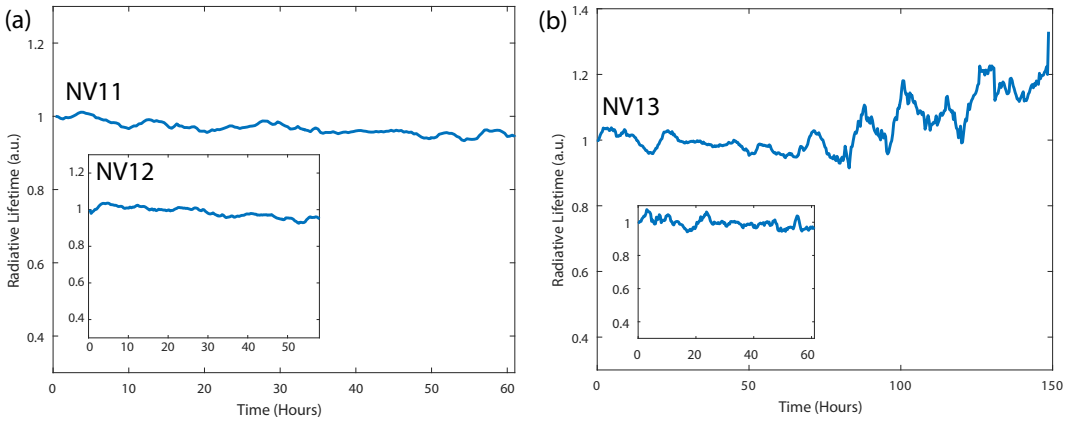


FIGURE 5.19: (a) Radiative lifetime of NV11 over 62.5 hrs of excitation. The inset show the same measurement for NV12. (b) Radiative lifetime of NV13 during over 150 hrs. Inset shows the radiative lifetime over the first 62.5 hrs.

inverse of the radiative lifetime:

$$\tau_{rad}(t) = I_0 \frac{\tau_{total}}{I(t)} \tag{5.5}$$

Figure 5.19 shows the radiative lifetime for NV11, NV12 and NV13 over the long exposures. As the value of $I(t)$ is extremely important, the periodic auto-focusing process must achieve optimal realignment in order to not skew the result of Equation 5.5. The lateral and vertical alignment processes were performed by different software at alternating times in order to not interfere with each other. The radiative lifetime for NV11 appears to decrease slightly to 0.95 of the original value. This is also reflected in NV12, where the radiative lifetime also decreases to 0.95 of the original value. The reason for this is likely the reduction in amplitude of the first exponential (background decay term) of the bi-exponential fit (Equation 4.5) over time due to photo-bleaching - skewing the fit for the NV component. NV13 also displays this slight reduction to 0.97 of the original value after the first 62.5 hrs (Figure 5.19 (b) inset). However, following this, the radiative lifetime begins to increase as expected, implying a reduction in the size of the nanodiamond.

Although sufficient photo-stability has been observed with these certain examples from the 100 nm sample, it remains crucial to devise a method of determining photo-stability without the ablation of the nanodiamond.

5.6 Conclusion

This chapter has presented a detailed investigation into the emission properties of single NV centres, forming the foundation for the coupling of these emitters to optical micro-cavities. This has included the characterisation of the NV centre's efficiency and stability under pulsed excitation. It has been shown that single NV centres are readily found in both 50 and 100 nm nanodiamond solutions. The excited state lifetimes have been shown to be much smaller than the simulated radiative lifetimes for a dipole in a spherical nanodiamond of the same size. This has been related to a non-unity quantum efficiency of NV centres, with the brightest emitters shown displaying estimated quantum efficiencies of up to $\sim$20%. The decrease in system efficiency with increasing excitation rate has been described by the recovery time τ_{rec}, which may differ from the excited state lifetime. With these known parameters, the excitation rate can be optimised to deliver both high efficiencies and a high single photon output rate.

The suitability of a nanodiamond single photon source has also been investigated through long term exposure to pulsed excitation. A larger sample size of these measurements is required in order to definitively quantify the expected length of photo-stability for these emitters. However, the nature of this experiment is extremely time consuming. That being said, the general behaviour of these results highlights the importance for the NV centre to be sufficiently isolated from the environment. Therefore, 100 nm nanodiamonds should be used for the NV-centre single photon source as they will offer a greater probability of NV photo-stability. While larger nanodiamonds (>150 nm) would offer even greater

stability, it remains extremely difficult to manufacture single NV centres with increasing nanodiamond size [53]. In addition to this, the implications of using larger nanodiamonds for cavity coupling are yet to be determined, and will be discussed in the next chapter.

6

NV Centre Cavity Coupling

6.1 Introduction

This chapter will describe the room temperature cavity coupling of single NV centres in nanodiamonds to FIB milled open-access microcavities. It is hoped that the presence of the cavity may be used to enhance the emission rates of the NV centre. However, a key challenge when using NV centres at room temperature is the broad emission linewidth ($\sim$70 nm). Due to this, the effective Q-factor is low and thus low mode volumes of the order λ^3 are vital. Firstly, characterisation of the cavity coupled emission from varying radii of curvatures will be shown, including the tuning of successive longitudinal modes through the NV centre's emission spectrum. This will highlight the importance of minimising the cavity length, such that improvements in the collection efficiency, and potential Purcell enhancement may be observed. From here, the cavity coupling results for NV232 will be presented, showing a direct comparison of the half-space and cavity-coupled single photon emission characteristics. FDTD simulations will be used to compare the expected coupling efficiency into the cavity modes, and account for the sources of loss observed experimentally. This will then be repeated for NV25, a single NV centre from the 100 nm nanodiamond sample. NV25 is located on a mirror with peak reflectivity at 690 nm. It is expected that this system should increase the coupling efficiency and this will be shown for different radii of curvatures. This will demonstrate the open-access microcavity as a platform to sample a large subsection of CQED parameter space. These results form

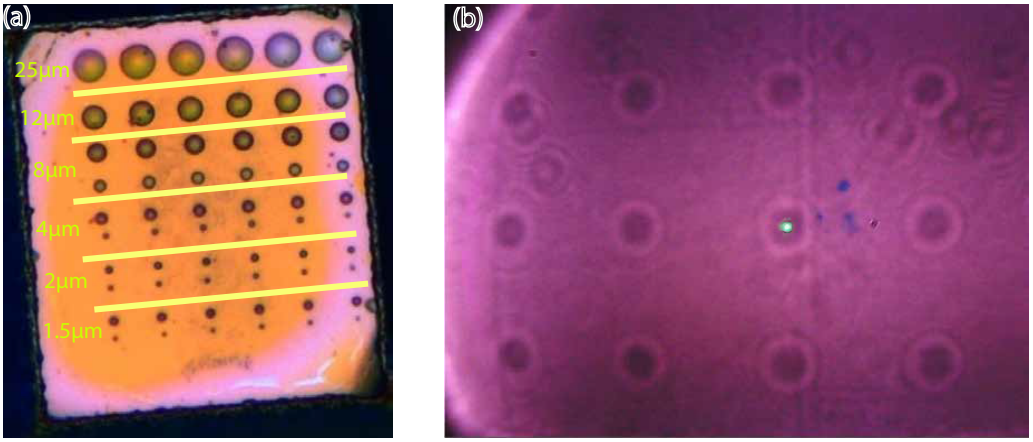


FIGURE 6.1: (a) Optical microscope image of 640 nm plinth with the different radii of curvature features labelled. (b) White light transmission image of this plinth seen through the planar mirror. The registration grid of the planar mirror are also visible.

a key part of this thesis, highlighting the viability of the emitter-cavity platform as the foundation of a true single photon source.

6.2 Open Cavity Characterisation

The preliminary cavity coupling experiments to be presented were performed using mirrors with peak reflectivity at 640 nm using the process described in Chapter 4. The mirror pair configuration is planar[8]:featured[16], with measured reflectivities of 97.5 $\pm$ 0.5% and 99.997%. Using Equation 3.10, the predicted finesse is $\mathcal{F} = 257$. This low value of finesse was purposely chosen to increase the cavity photon decay rate, minimising the opportunities for intra-cavity scattering losses.

The emitters are imaged through the planar mirror as in 4.14 (c). Figure 6.1 shows the 640 nm plinths used to couple to the single defects, featuring cavities with radii of curvatures (β), with $\beta = 1.5{-}25$ μm. This plinth has lateral dimensions of $\sim$100μm$\times$100μm.

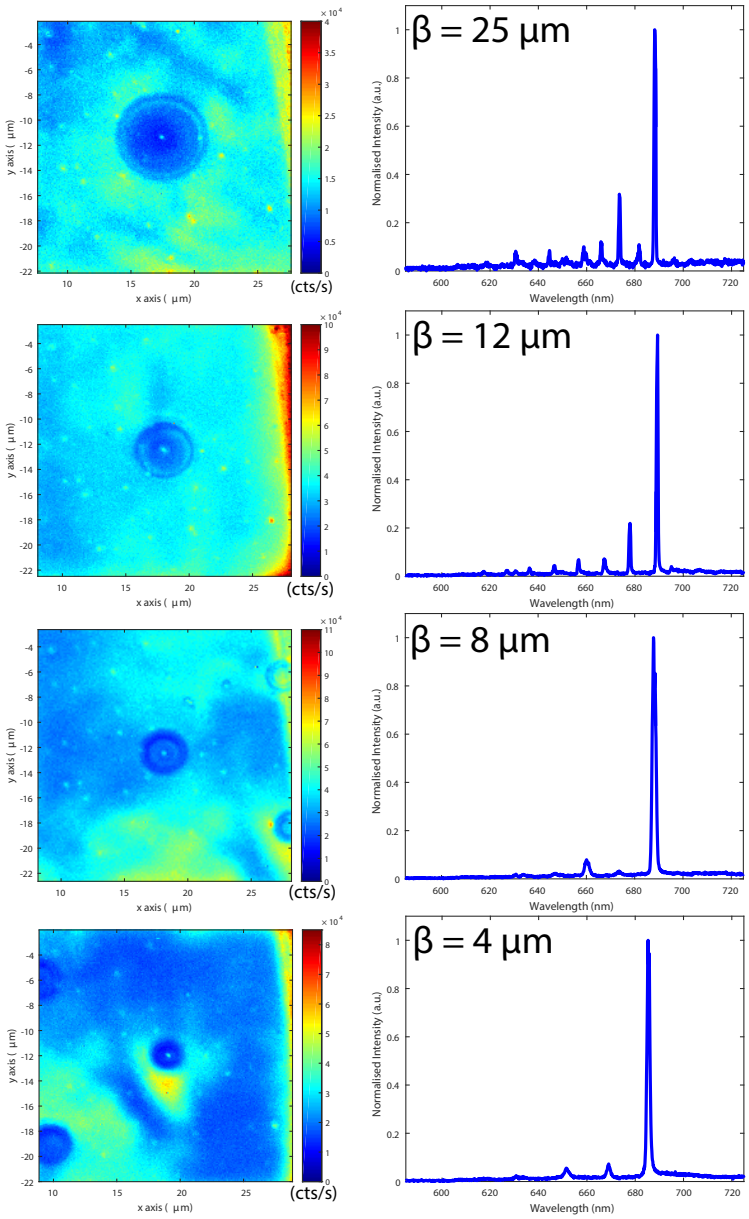


FIGURE 6.2: Single defect coupling to varying radii of curvature features. The PL images show a bright spot located centrally within a larger circle, corresponding to the emitter fluorescence within the hemispherical feature. The cavity coupled spectra show the decrease in coupling to higher order transverse modes as β decreases.

The features with $\beta = 1.5-8$ μm have two sets of cavities of varying depth. The upper row of these RoCs in Figure 6.1 (a) are labelled as deep (depth $\approx$ 600 nm) with the lower

row labelled shallow (depth ≈ 300 nm). The magenta ring around the edge of the plinth is indicative of the DBR layers peeling off the silica substrate, which is a recurring issue with plinths of this size. Figure 6.1 (b) shows the white light transmission of this plinth through the planar mirror. The laser focus is visible which allows the desired cavity to be placed behind the chosen emitter.

Figure 6.2 shows the fluorescence spectra and PL images obtained from coupling the same NV centre to features of varying β. The NV centre's emission is now coupled into the cavity modes, with the higher order modes also being populated. The cavity length was minimised such that there are three anti-nodes between the mirrors ($q = 3$). This ensures the cavity modes were well dispersed leaving only one family of modes within the detection window. The quality of the lateral alignment is determined by the coupling to the different transverse modes. For example, the electric field of the first transverse mode ($m + n = 1$) has a node at the centre. Optimal positioning of the cavity results in maximal coupling to modes with an even value of $m + n$, as seen for the $\beta = 25$ and 8 μm features. As β is reduced, the TEM_{00} mode increasingly dominates the measured spectrum, with the transverse mode spacing increasing. This is explained by the larger numerical apertures of the higher order transverse modes in the smaller β cavities, leading to clipping losses at the edge of the concave feature. In addition, the higher order modes do not couple as well into microscope optics.

From this point, the majority of the results to be presented are for coupling using the $\beta = 8$ μm features as they displayed the greatest cavity coupled emission intensity from this plinth. Figure 6.3 shows the cavity coupled spectra for the row of shallow $\beta = 8$ μm (8s"x") features. The observed count rates from these cavities are within $\pm 5\%$ showing great repeatability of the FIB milling process. Using Equation 3.14, the cavity finesse can be calculated from the cavity mode linewidths and FSR, giving a value of $\mathcal{F} = 93$. This is

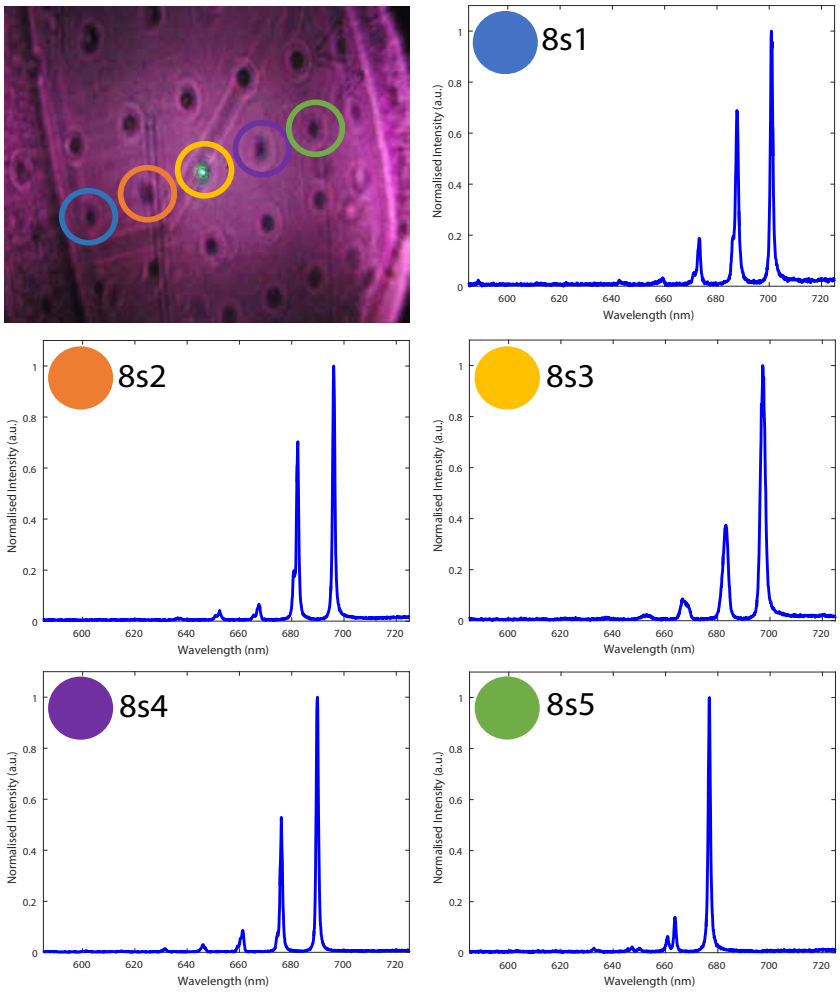


FIGURE 6.3: Cavity coupled spectra of a single defect to different $\beta = 8$ μm shallow features.

much smaller than the expected value from Equation 3.10 where the reflectivities of the mirror predict $\mathcal{F} = 257$. The sources of loss include instability of the cavity length, scattering by the nanodiamonds and imperfect sphericity of the concave features [92]. The separation of the higher order transverse modes can be used to determine the effective optical radius of curvature of the features using the relation:

$$\beta_{opt} = L\left[sin\left(\frac{2\pi\Delta_t\lambda L}{\lambda_1\lambda_2}\right)\right]^{-2} \tag{6.1}$$

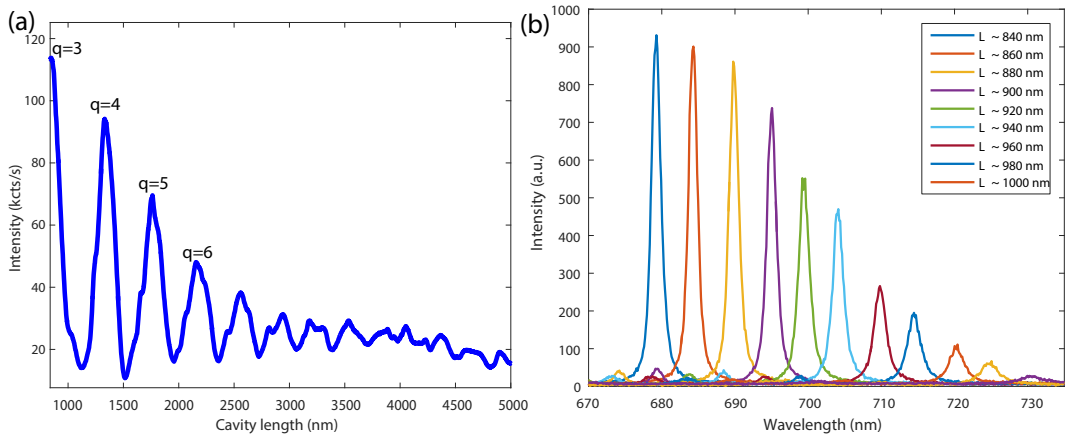


FIGURE 6.4: (a) Enhanced photon count rates for a $\beta = 8$ μm feature closed around a single NV centre. The distance has been adjusted for the optical penetration depth and the antinodes between the mirrors are labelled. (b) The collected spectra from the maximum of the $q = 3$ peak of (a) to the minimum before the $q = 4$ peak.

Where L is the cavity length, $\Delta_t\lambda$ is the transverse mode spacing for the transverse modes at λ_1 and λ_2. For the $\beta = 8$ μm features in Figure 6.3, the average optical radius of curvature was found to be $\beta_{opt} = 14.3 \pm 0.9$ μm, exceeding the physical value of β. This has been previously reported by Trichet *et al.*, particularly at cavity lengths below 2 μm [93]. The reason for this discrepancy is lack of consideration of the penetration depth of the electric field into the dielectric coatings. The geometric penetration depth of these interfaces (d_H and d_L) can be calculated from the Equations 3.29 and 3.30, giving $d_H = 155$ nm and $d_L = 468$ nm. The geometrical thicknesses of these layers are $d_{Ta_2O_5} = 76$ nm and $d_{SiO_2} = 110$ nm. Therefore, the field penetrates a few layers into the mirror stack before decaying, as seen in Figures 3.9 and 3.10 (b). The optical penetration depth is described by Equation 3.33, which gives $L_H = 246$ nm and $L_L = 746$ nm. The total optical penetration depth is then the sum of the penetration depths of both cavity mirrors ($L_{pen} = 992$ nm).

Figure 6.4 (a) shows the effect of the cavity length on the detected photon count rate

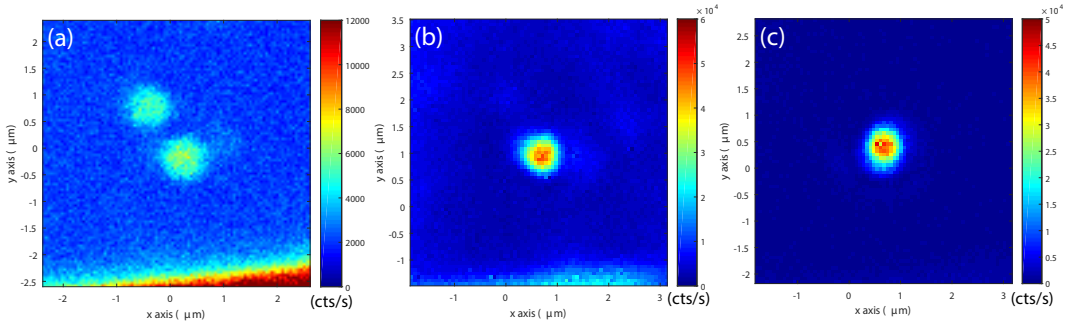


FIGURE 6.5: PL images of NV centre emission with the mirror facing away from the objective (a), the central emitter coupled to the cavity modes (b), and the TEM_{00} mode emission (c).

from a single NV centre coupled to a $\beta = 8$ μm feature. As the cavity length is reduced, oscillations in the cavity coupled fluorescence intensity are observed, corresponding to successive longitudinal modes sweeping through the NV centre's emission. As the number of anti-nodes between the mirror reduces, the collection efficiency of the cavity increases, with the lowest mode index reached being for $q = 3$. The physical cavity length has been adjusted for the penetration depth into the DBR mirror coatings calculated above. Figure 6.4 (b) shows the spectra at sequential points over the $q = 3$ peak in Figure 6.4 (a), with the largest intensity when the TEM_{00} mode is located at 680 nm.

With the emission now coupled into the cavity modes, a band-pass filter can be used to isolate this emission from the residual auto-fluorescence. Figure 6.5 (a) shows the PL image of two emitters when the mirror inverted, facing away from the objective. Figure 6.5 (b) shows the same region, but with the central emitter coupled to a $\beta = 8$ μm feature. The surrounding auto-fluorescence is greatly reduced, including the fluorescence of the other emitter. In Figure 6.5 (c), a 8 nm band-pass filter is used to isolate the TEM_{00} emission, making the cavity coupled emission the only visible feature, negating all background sources of photons. The emission into this filtered single mode will be maximised and used to determine the single photon properties of the NV-cavity system.

6.2.1 Summary

This section has presented some preliminary cavity characterisation results following the systematic alignment scheme described in Section 4.7, allowing cavity coupled single photon sources to be constructed and optimised deterministically. NV centres in nanodiamonds have been coupled to various FIB milled concave features. For the plinth shown in Figure 6.1, the features with $\beta = 8$ μm were found to give the greatest enhancement in count rates and stability of the cavity modes. It has been demonstrated that a mode index of $q = 3$ can be reached with this room temperature system described in Sections 4.4 and 4.7, with a physical cavity length of 900 – 1000 nm between the two mirrors. The cavity linewidths were found to be 1.3 – 1.5 nm, much narrower than the full NV centre emission spectrum. As a single cavity mode can be isolated, this allows the mode coupling efficiency to be established, and a direct comparison between the half-space and cavity coupled single photon properties.

6.3 NV232 Cavity Coupling

This section will present the cavity coupling results for NV232, which was previously characterised in Chapter 5. NV232 showed clear single photon emission under both CW and pulsed excitation, with a value of $g^2(0) = 0.17$ and single photon purity of 91%. The saturation counts under CW and pulsed excitation at 5 MHz were 274 $\pm$ 14 kcts/s and 133 $\pm$ 60 kcts/s, with the quantum efficiency estimated as 0.18 $\pm$ 0.07. Finally, the excited state lifetime was 35.3 $\pm$ 0.2 ns. These key parameters will be compared to those obtained from cavity coupled emission to deduce the effectiveness of this open-cavity system. Figure 6.6 shows the PL images used to locate NV232. With the mirror facing the objective lens 6.6 (a), NV232 is clearly visible, with the inset scan showing a clear point-like emitter. Figure 6.6 (b) shows a markedly lower quality image, as the emission

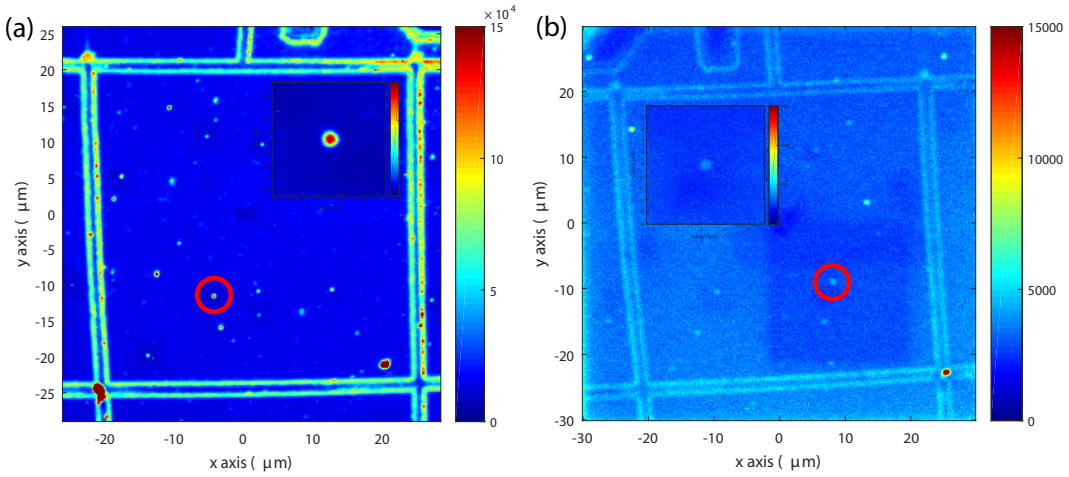


FIGURE 6.6: PL image of the registration grid where NV232 is located with the mirror facing towards (a) and away (b) from the objective, with NV232 circled in red. The insets show $5\mu m \times 5\mu m$ scans around NV232.

is mostly reflected away from the objective. A smaller 20μm $\times$ 20μm area around NV232 was further photo-bleached to help improve the S/B ratio, making the emitter more visible.

From here, NV232 is coupled to a $\beta = 8$ μm feature, with the cavity length adjusted to the $q = 3$ mode index. The lateral alignment is adjusted such that coupling into the TEM_{00} is maximised. Figure 6.7 (a) shows the half-space and resulting TEM_{00} spectra following the lateral optimisation. The TEM_{00} intensity was found to be maximum at 690 nm, with a peak intensity over three times greater than the half-space spectrum and a (FWHM) linewidth of 1.4 nm. To quantify the mode coupling efficiency, the saturation intensity for the TEM_{00} mode was was measured (6.7 (b)), and found to be 123 $\pm$ 8 kcts/s, meaning 45% of the total emission is coupled into this single mode. This is a large improvement on the 18% coupling efficiency reported by Dolan *et al.* [129], due to the improved alignment protocol described in Section 4.7. Integration of the half-space spectrum over the 8 nm spectral band used to isolate the TEM_{00} shows just 11% lies within

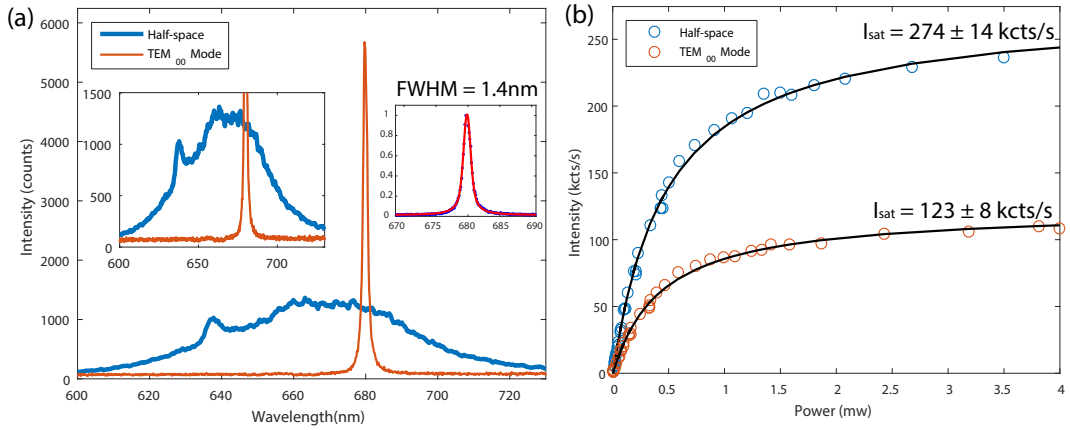


FIGURE 6.7: (a) PL spectra of the half-space and TEM_{00} emission. Both profiles are normalised to the same integration time to show the relative intensities. The insets show the half-space spectral profile and TEM_{00} linewidth. (b) Saturation curves for the half-space and TEM_{00} modes, used to quantity the mode coupling efficiency.

this window. Therefore, were the cavity to act just as a filter, the saturation count is expected to be 30 kcts/s. Using the linewidths of both emission profiles, the spectral density has increased from 3.9 kcts/ (s nm) in half-space to 93.2 kcts/(s nm) in the TEM_{00} mode – a 23.9 times increase. This large gain in the spectral density of photons clearly proves cavity enhanced emission is beyond simple spectral filtering.

Second order correlation measurements were performed for the cavity coupled emission to confirm single photon emission was still being displayed. Figure 6.8 shows the results when performed under both CW (a) and pulsed excitation (b). The CW HBT dataset shows a decrease in the value of $g^{(2)}(0)$ from 0.17 to 0.03. The inset of Figure 6.8 (a) shows the PL image of the TEM_{00} mode emission, displaying an isolated bright spot with no other features present. This is a result of both cavity-enhanced emission and spectral filtering of the single mode removing all sources of background contributions, explaining the very low value of $g^{(2)}(0)$. This result is confirmed by the pulsed HBT measurement (Figure 6.8 (b)) which shows an increase in single photon purity from 91% to 97%. It

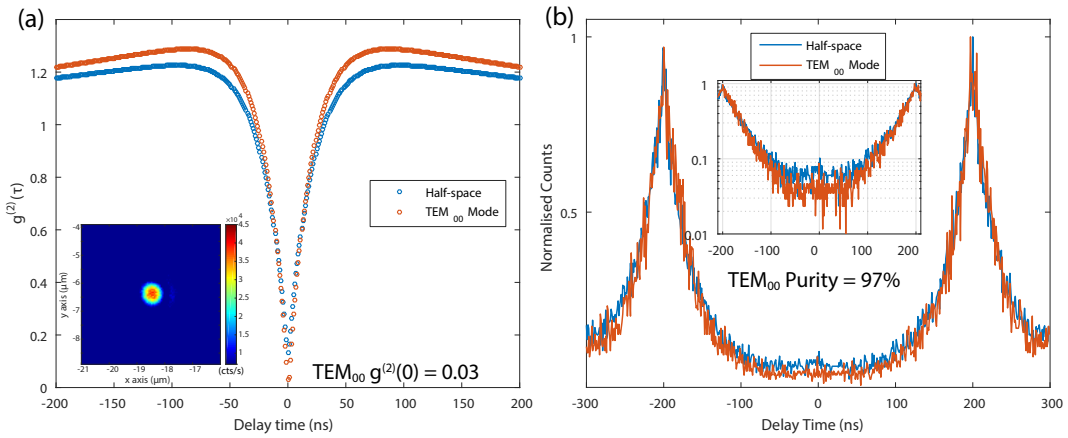


FIGURE 6.8: Second order correlation measurements for the half-space and TEM_{00} emission under CW (a) and pulsed (b) excitation. Insets of (a) show the PL image of the filtered TEM_{00} emission and Lorentzian fit of the TEM_{00} mode.

must be stated that the recorded HBT data has not being corrected for background contributions. When corrected for background contributions, $g^{(2)}(0) = 0.01$ and the single photon purity is 99%.

Figure 6.9 (a) shows the saturation behaviour of NV232 inside and outside of the cavity under pulsed excitation. The TEM_{00} saturation count rate is 61 $\pm$ 30 kcts/s compared to 133 $\pm$ 60 kcts/s for half-space emission. These results for pulsed excitation shows a similar coupling efficiency (47%) to that obtained under CW excitation. Figure 6.9 (b) shows the excited state lifetime of NV232 to decrease slightly when coupled to the cavity, with a value of $\tau = 34.7 \pm 0.6$ ns compared to $\tau = 35.3 \pm 0.2$ ns in half-space. Such small changes in the excited state lifetime are regularly observed for NV centres coupled to open-access microcavities [109, 130, 160, 161]. In addition to the NV centre's low Q-factor, the quantum efficiency (QE) of the defect will limit the observation of a reduction in the excited state lifetime from the Purcell effect.

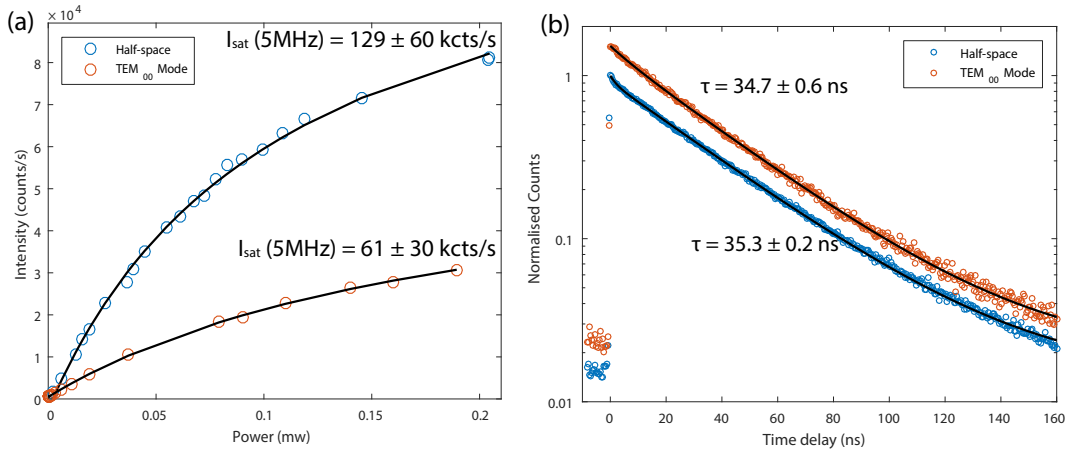


FIGURE 6.9: (a) Saturation curves taken at a repetition rate of 5 MHz for the half-space and TEM_{00} emission. (b) TRPL measurement showing a slight reduction in the excited state lifetime when coupled to the cavity.

6.3.1 Discussion

The Purcell factor compares the rate of emission into the cavity with that of free-space (or half-space), and with the presented data above, a comparison can be made. The NV centre's emission spectrum is much broader than the cavity linewidth placing this emitter-cavity system firmly within the bad emitter regime. Therefore, the ideal Purcell factor (F_P) will be reduced to an effective Purcell factor ($F_{P,eff}$). One method to quantify this experimentally is to compare the saturation count into the TEM_{00} mode ($I_{TEM_{00}}$) to total half-space saturation intensity (I_{hs}) collected for each spectral profile (Figure 6.7) [160]. The experimental collection efficiency in each case must be considered carefully as these vary for both scenarios. The effective Purcell factor can then be expressed as:

$$F_{P,eff} = \frac{I_{TEM_{00}}}{I_{hs}} \frac{\eta_{hs}}{\eta_{TEM_{00}}} \tag{6.2}$$

Where η_{cav} and η_{hs} are the TEM_{00} and half-space collection efficiencies. Additional losses

in the detection path and the detection efficiency are assumed to be equal for both cases. The transmission of the cavity coupled emission through the planar mirror is found from Equation 4.10, giving a value of $T_P = 0.996$. The divergence of the TEM_{00} mode for the 8 μm feature at the $q = 3$ index gives $NA \sim 0.37$, suggesting all of this emission is collected by the objective lens of $NA = 0.85$. The half-space collection efficiency is described in Chapter 3, and for an objective lens with $NA = 0.85$, the collection efficiency for NV emission on the planar mirror gives $\eta_{fs} = 0.46$. Using these values, the effective Purcell factor is found to be $F_{P,eff} = 0.21 \pm 0.02$.

The effective Purcell factor can also be determined from Equation 3.53, by replacing the Q-factor with the effective Q-factor (Q_{eff}) expressed in Equation 3.54. For the NV-cavity system, $Q_{eff} \sim 10$ due to the NV centre's broad emission dominating the cavity contribution. By using the optical cavity length, the mode volume of the TEM_{00} mode can be approximated from Equation 3.23. For the $q = 3$ mode, this analytic expression gives a value of $V = 1.02$ μm^3 or $V = 3.71$ λ^3, making $F_{P,eff} = 0.19$, in close with the experimentally determined value from Equation 6.2. Due to the NV centre's small Q-factor, the parameter of most importance is the mode volume. Past NV cavity coupling results have obtained effective Purcell factors of $F_{P,eff} = 0.02$ ($V = 24.2$ λ^3) [109], $F_{P,eff} = 0.005$ ($V = 58.9$ λ^3) [160], $F_{P,eff} = 0.12$ ($V = 5$ λ^3) and $F_{P,eff} = 0.6$ ($V = 1$ λ^3) [130].

Equation 3.55 describes the change in excited state lifetime due to the presence of the cavity. Assuming the free-space density of states within the cavity is the same as in the absence of the cavity ($\alpha = 1$), Equation 3.55 gives an effective Purcell factor of $F'_{P,eff} = 1.21$. This result clearly does not describe the observed value of $F'_{P,eff} = 1.02$, due to the suppression of free-space density of states. In addition, the values of $F_{P,eff}$ determined from Equations 6.2 and 3.53 have used parameters solely dependent on the TEM_{00} mode. Experimentally, the maximal count rate is dependent on the efficiency of coupling to the

TEM_{00}. However, the decay rate within the cavity is dependent on the total optical density of states available due to all the cavity modes, including the suppression of non-resonant modes. In principle, the saturation and ideal Purcell factor equations could be used to quantify the true value of $F_{P,eff}$, provided that the collection efficiencies, mode volume of the higher order modes and free-space density of state suppression can be calculated accurately. In order for $F_{P,eff}$ to be determined correctly, FDTD simulations have been performed to replicate the dielectric environment within the cavity.

FDTD Simulation

For the simulation of this NV-cavity system, a 50 nm spherical nanodiamond with the dipole located at the centre 25 nm from the mirror surface was used. The dipole is given a broad spectral profile similar to that of the NV centre PSB. The simulations were run for the 50 nm nanodiamond in free-space, on the planar mirror (R = 0.975 at 640 nm) and the cavity coupled configuration (β = 8 μm, q = 3, R = 0.9999 at 640 nm). The program is able to monitor the total emitted power from the dipole as a function of wavelength. From this, the Purcell factor is then the ratio of the optical power in each case compared to bulk diamond. Figure 6.10 (a) shows the Purcell factor spectrum ($F_{P,eff}(\lambda)$) for the free-space, half-space cavity coupled scenarios. The cavity Purcell spectrum shows two cavity modes at 660.3 nm and 689.7 nm. As the dipole is located directly on the cavity axis, there is no coupling into transverse modes with odd values of $m + n$. Therefore, these two modes correspond to the $TEM_{20/02}$ (660.3 nm) and TEM_{00} (688.7 nm) modes. Their transverse mode separation (28.4 nm) is very similar to the experimentally observed value of 28.6 nm. Using the TEM_{00} mode linewidth (1.4 nm), the experimentally determined Q-factor is Q_{exp} = 485. This simulation gives an theoretical Q-factor of Q_{theo} = 503 for this mode, very close to the observed value.

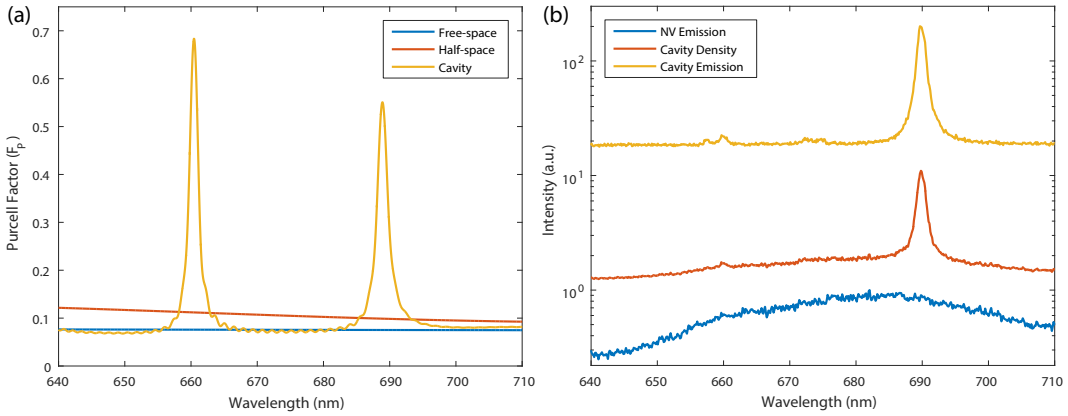


FIGURE 6.10: (a) FDTD simulation results for the Purcell factor as a function of wavelength for NV232 on the planar DBR mirror and in the cavity. (b) Comparison of the NV emission spectrum to the cavity power density and experimental spectrum for NV232 at the $q = 3$ mode index. The cavity density is obtained by multiplying the cavity Purcell spectrum by NV232's half-space emission spectrum. The cavity emission spectrum is measured experimentally.

Away from these modes, there is a clear suppression of emission when compared to free-space and half-space. The Purcell factor of the cavity modes are 0.68 ($TEM_{20/02}$) and 0.55 (TEM_{00}). Using Equation 3.59, the maximum electric field of the TEM_{00} mode and electric field at the position of the NV centre were used to confirm the Purcell factor of the TEM_{00} mode. The square of the ratio of electric fields was found to be $\left|\frac{\mathbf{E}(\mathbf{r}_{NV})}{\mathbf{E}(\mathbf{r}_{max})}\right|^2 = 0.088$, with maximum of the electric field is above the planar mirror making $n_c = 1$. These simulated parameters give $F_P = 0.59$ for the TEM_{00} mode, sufficiently close to the value obtained from the numerical solution of the simulation. Figure 6.10 (b, blue) shows the emission spectrum of NV232 on the planar mirror. To obtain the total in-cavity power density, the Purcell factor spectrum ($F_P(\lambda)$) is multiplied by the emission spectrum ($S(\lambda)$) of NV232 on the planar mirror (Figure 6.10 (b, orange). The experimental emission spectrum at the maximum count rate of the $q = 3$ index is over-layed for comparison (Figure 6.10 (b, yellow), with these results displayed on a log scale for clarity. The experimental spectrum shows a minimal contribution of the $TEM_{20/02}$ mode to the detected intensity,

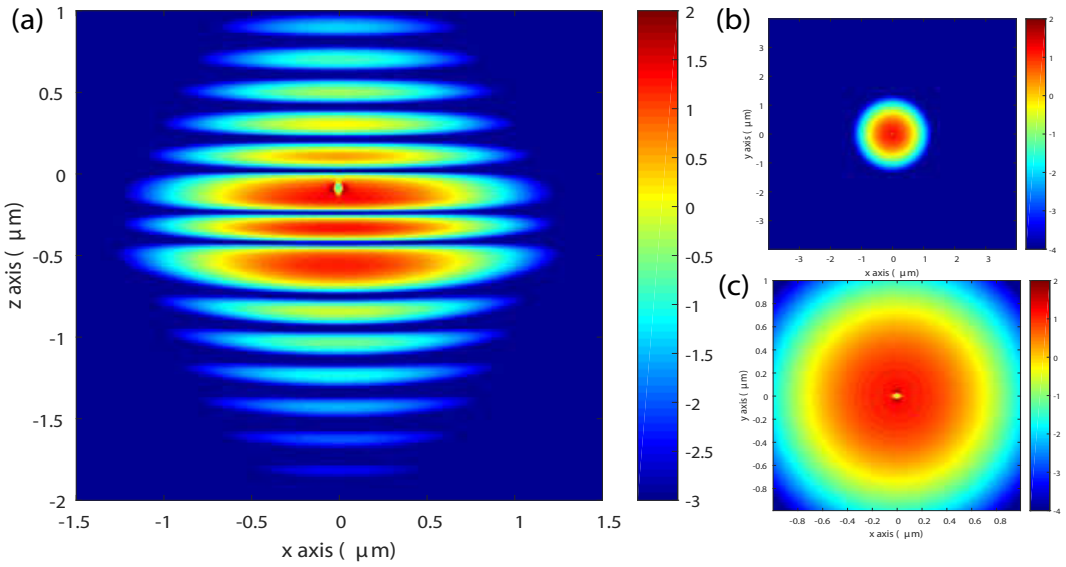


FIGURE 6.11: (a) FDTD simulation of the intensity distribution in the X-Z plane for a 50 nm nanodiamond within the optical cavity. The three anti-nodes between the cavity mirrors can be seen. (b) X-Y intensity distribution of the TEM_{00} mode at 690 nm, showing the intensity is localised at the centre of the cavity. (c) A closer view of the TEM_{00} mode distribution with the reduction in intensity within the nanodiamond due to it's refractive index. These intensity distributions are plotted on a log scale.

with an even smaller contribution for the $TEM_{01/10}$ mode. This feature highlights the central location of the nanodiamond within the cavity during the experiment. The saturation counts for the TEM_{00} mode approximated 46% of the total half-space emission to be within the TEM_{00} mode. Due to the spectral filtering of the half-space emission 590 – 740 nm, the measured I_{sat} value ignores contributions from emission above 740 nm. Using the cavity density in Figure 6.10 (b), Equation 3.64 provides a more accurate measure of the TEM_{00} emission efficiency, giving $\mathcal{B} = 0.33$.

Figure 6.11 shows cross-sections of the intensity distribution of the simulated geometry for the TEM_{00} mode at 690 nm. The nanodiamond is visible on the planar mirror surface with the concave mirror located below. The penetration of the electric field into the DBR

stacks can also be seen. The analytic value of $V = 3.71\lambda^3$ was found to be an overestimation of the true mode volume, as the optical cavity length used includes the penetration depth into the DBR stacks. The contribution to the mode volume of the field penetrating into the DBRs is smaller than that of the field between the two mirrors. The simulated mode volume was found to be $2.27\lambda^3$ when integrated over the whole TEM_{00} mode.

To determine the effective Purcell factor for the NV centre within this cavity geometry, $F_P(\lambda)$ (Figure 6.10 (a)) is averaged over the NV centre's emission spectrum $S(\lambda)$ by Equation 3.60. For an appropriate comparison to the experimental results, $F_{P,eff}$ for the half-space and cavity geometries are normalised by $F_{P,eff}$ for free-space using Equation 3.61. The free-space result shows $F_{P,eff} = 0.075$, meaning a suppression in the radiative decay rate compared to bulk diamond. This value is comparable to the suppression for the decay rate of a dipole within a nanoparticle compared to bulk predicted by Chew ($\gamma_{nano} \sim 0.062\gamma_{bulk}$). For the half-space and cavity effective Purcell factors, Equation 3.60 gives $F_{P,hs} = 0.104$ and $F_{P,cav} = 0.114$. Normalising by the free-space result (Equation 3.61) gives $F'_{P,hs} = 1.37$ and $F'_{P,cav} = 1.52$. With these values, Equation 3.63 gives $\gamma_{rad} = 0.14\gamma_{nr}$ and thus $QE = 0.13$. From the saturation measurements in Chapter 5, the QE of NV232 was determined to be 0.18 ± 0.07. This is not the true QE as relative to free-space the planar mirror enhances γ_{rad} by $F_{P,hs} = 1.37$. Accounting for this enhancement in Equation 3.1, gives the QE $= 0.14 \pm 0.05$. Therefore, the result based on the measured change in excited state lifetime gives QE = 0.13, which is within the error bars of the measured experimentally measured value.

The simulated result of the dielectric environment of NV232 within the open access microcavity reveals the low quantum efficiency as the reason behind the limited enhancement in the decay rate from the Purcell effect. NV centres in nanodiamonds have also been used in fiber-based cavity coupling experiments by Kaupp *et al.*, reaching a cavity length

of $\sim$ 350 nm (q = 1) [130]. With such a small cavity length and mode volume ($V = 1\lambda^3$), FDTD simulations predicted an effective Purcell factor of $F'_{P,eff}$ = 11 for cavity coupled emission relative to half-space emission. However, only a $\sim$3$\times$ reduction in the excited state lifetime was observed (20 ns $\rightarrow$ 7 ns). Although NV centres are usually quoted to posses quantum efficiencies up to 0.9, the lower than expected reduction in the excited state lifetime suggested that QE = 0.2 for the NV centre used in that experiment. The results from Kaupp *et al.* and NV232 provide further uncertainty to reported higher QE values for NV centres in nanodiamonds [49]. A QE of 0.7 for the NV centre in bulk diamond has already being proposed to map the most frequently observed excited state lifetimes in nanodiamonds to their local optical density of states [152, 153]. With this assumption, the NV centre's bulk radiative lifetime is $\sim$ 17 ns. Therefore, as a first approximation, the measured excited state lifetime of the defect in half-space can be related to the QE by the Purcell factor:

$$QE = \frac{\tau_{hs} \cdot F_{P,hs}}{17} \tag{6.3}$$

For NV232, Equation 6.3 gives QE = 0.21. This result only provides a rough estimate as the exact geometry of each nanodiamond is unknown. Especially given the fact that parameters such as dipole position and orientation are also uncertain. It must be stated that these results do not draw conclusions on the QE of NV centres in bulk diamond as this has been more rigorously studied by various methods [44, 150, 154]. Nevertheless, with the most commonly observed excited state lifetime of 30 –36 ns for NV centres in nanodiamonds (Figure 5.10), these FDTD results support the limit proposed by Chew and reveal the quantum efficiency of typically bright NV centres to be $\leq$0.25.

6.4 NV25 Cavity Coupling

The results from the previous section revealed the importance of the NV quantum efficiency on the magnitude of emission rate enhancement in the cavity. Over the course of this thesis, bright NV centres under pulsed excitation were readily found in nanodiamonds from the 100 nm sample, with prolonged emission stability. NV25 from this sample was chosen for further characterisation and the results for this NV centre will be presented. As with NV232, the measurements performed were carried out for NV25 on the planar mirror facing the objective lens, before inversion and coupling to optical microcavities. Apart from the larger size of the nanodiamond, the other key difference is the use of DBR mirrors with peak reflectivity at 690 nm, which is more favourable for the collection of the PSB of the NV centre. Therefore, improved collection efficiencies are expected. The featured mirror was also fabricated to maximise reflectivity at 690 nm, with an initial size of 300μm$\times$300μm, before being FIB milled to a size of 100μm$\times$100μm (Figure 4.3). This step was crucial in order to reach the lowest mode index of $q = 3$.

Figure 6.12 shows the characterisation results for NV25 with the mirror facing the objective lens. These results were obtained using an 0.85NA objective lens. The CW HBT measurement shows a dip zero time delay with $g^{(2)}(0) = 0.09$. This sample was photobleached over several days to remove the as much of the background contribution as possible, resulting in the extremely low value of $g^{(2)}(0)$. The emission spectrum shows a maximum at $\sim$690 nm, and this is due to the reflectivity of the planar mirror being maximum at this wavelength. Therefore, it is expected that this should improve the collection efficiency from NV25, also contributing to the enhanced S/B ratio seen in the CW HBT measurement. The pulsed HBT measurement confirmed the result of the CW HBT, displaying a single photon purity of 91%. The excited state lifetime was found to be 31.3 $\pm$ 0.5 ns, which is within the range for the most commonly observed excited state

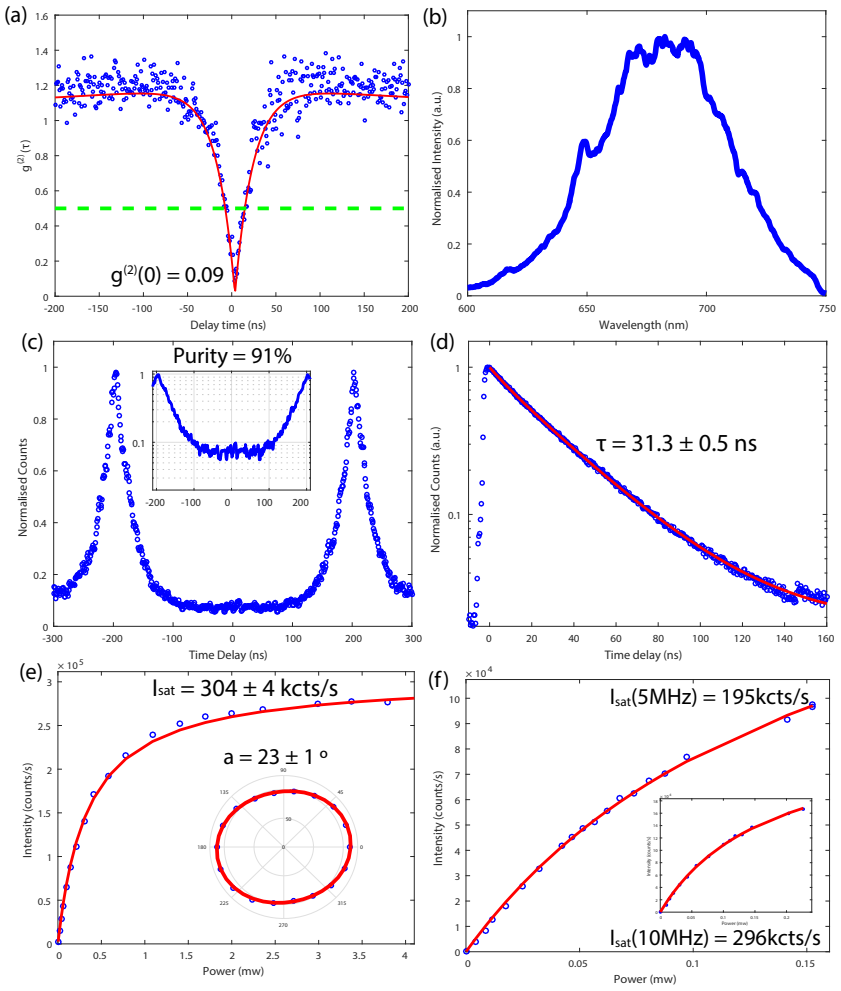


FIGURE 6.12: Characterisation of NV25 with the mirror facing the objective lens. (a) CW HBT measurement with a $g^{(2)}(0) = 0.09$. (b) Emission spectrum with a maximum at 690 nm. (c) Pulsed HBT measurement performed at 5 MHz with a single photon purity of 91%. (d) TRPL measurement showing an excited state lifetime of 31.3 $\pm$ 0.5 ns. (e) CW saturation measurement showing a saturation count of 304 kcts/s. The inset shows the polarisation measurement, with the NV defect angle at 23 $\pm$ 1 $^\circ$ to the plane. (f) Pulsed saturation measurement at 5 MHz showing a saturation count of 195 kcts/s. The inset shows the result at 10 MHz with I_{sat} = 296 kcts/s. The error bars for the pulsed saturation measurements are not displayed as they are comparable to the I_{sat} values.

lifetimes for this nanodiamond sample. The saturation count under CW excitation is 304 $\pm$ 4 kcts/s. This measurement was performed at the optimal excitation polarisation for

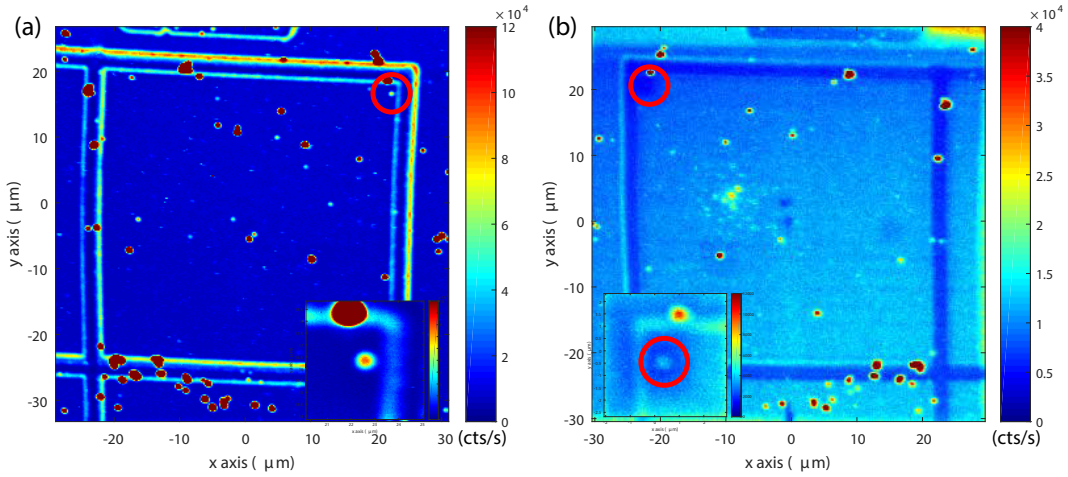


FIGURE 6.13: PL images of NV25 with the mirror facing towards (a) and away (b) from the objective lens. The insets show a 5μm×5μm scan centred on NV25 for both scenarios.

NV25 and the angle of the NV defect to the optical axis was found to be 23 $\pm$ 1 °.

Figure 6.12 (f) shows the saturation measurement for NV25 performed under pulsed excitation at 5 MHz with I_{sat}(5MHz) = 195 ($\pm$ 193) kcts/s. As previously mentioned, due to the low power of the pulsed laser, the saturation power can not be reached and so the error bars for the values of I_{sat} under pulsed excitation at low excitation rates are large. Regardless, the fit passes through the recorded data points with a good agreement. The collection efficiency was determined using the observed emission spectrum and integrating the wavelength dependent collection parameters over the spectrum yielding $\langle\eta_{coll}\rangle$ = 0.751. For NV25, the quantum efficiency on the planar mirror is estimated as QE = 0.16 ($\pm$ 0.15). Although the error bars for this value are large, the value is in good agreement with that of NV232, with the key difference in count rate being due to the enhanced collection by the 690 nm mirror. The saturation measurement was repeated at 10 MHz giving I_{sat} = 296 ($\pm$ 168) kcts/s. Therefore, it is expected that NV25 should show comparable enhancements within the cavity environment compared to NV232.

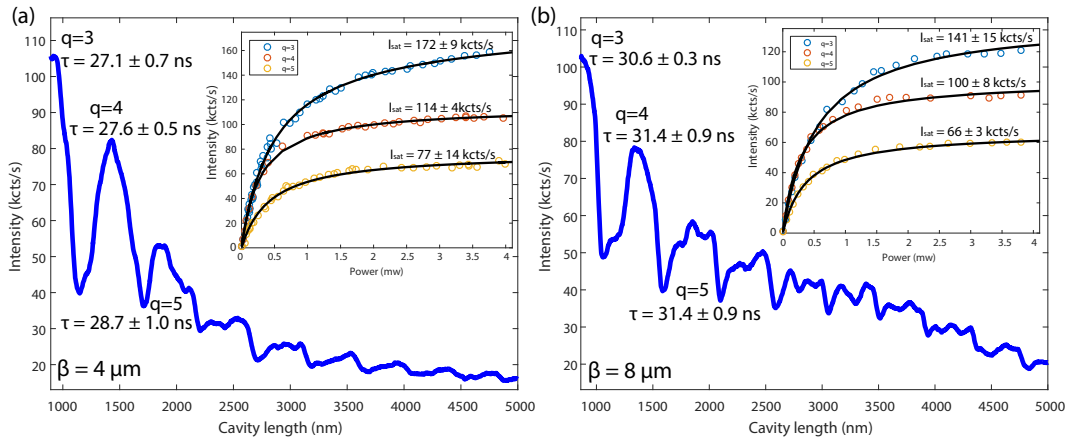


FIGURE 6.14: Cavity sweeps and saturation measurements as a function of mode index for $\beta = 4$ μm (a) and $\beta = 8$ μm (b) cavities. The insets show the saturation measurements for the TEM_{00} $q = 3$, 4, 5 of each feature. The excited state lifetime at each mode index is also noted.

Figure 6.13 shows the 60μm $\times$ 60μm PL images for the region of planar where NV25 is located, with the mirror facing towards (a) and away (b) from the objective lens. The inset images show the proximity of NV25 to the FIB marked registration features. This has previously proved to be an issue due to slight de-lamination of the mirror coatings near these marks. Fortunately NV25 appeared to be sufficiently far away from the registration features. Figure 6.13 (b) inset shows a bright emitter to the top right of NV25. This bright emitter provides an alignment source for the optimisation of the excitation and collection paths of the confocal microscope when the mirror is inverted. With NV25 located, the featured mirror can now be placed behind the emitter and the cavity length closed. NV25 was coupled to cavities with radii of curvatures of $\beta = 4$ and 8 μm.

The cavity was closed around the defect for both feature sizes resulting in the enhancement of the count rate through the planar mirror. Figure 6.14 (a) and (b) shows the oscillations observed as the cavity modes sweep through NV25's emission spectrum. The

lowest mode index reached with both cavities was $q = 3$, corresponding to a cavity length of $\sim$ 940 – 960 nm. For the $\beta = 8$ μm feature, the increase in count rate with decreasing cavity length occurs at a longer cavity length than the $\beta = 4$ μm feature. This is because stable cavity modes begin to form at cavity lengths comparable to the radius of curvature. Once the modes form, the rate of enhancement with decreasing cavity length is greater for the $\beta = 4$ μm feature. The excited state lifetime and saturation counts were recorded at the mode indices $q = 3$, 4, 5 for both features to map the enhancement of the cavity coupled emission (Figure 6.14).

The cavity coupling of NV25 to the $\beta = 4$ and 8 μm features has resulted in decreases in the measured excited state lifetime (Figure 6.14). These enhancements are greater for the $\beta = 4$ μm feature, with even the $q = 5$ mode ($\tau = 28.7 \pm 1.0$ ns) showing a smaller excited state lifetime than the $q = 3$ mode ($\tau = 30.6 \pm 0.3$ ns) for the $\beta = 8$ μm feature. This is explained by the mode volume of these features at their respective mode indices. For the $\beta = 4$ μm feature at $q = 5$, the mode volume from Equation 3.23 gives $V = 2.66\lambda^3$, compared to $V = 3.71\lambda^3$ for the $\beta = 8$ μm feature at $q = 3$. However, the TEM_{00} saturation count is also dependent on the solid angle enclosed by the mode. Therefore, the lowest mode index will always provide the largest saturation count. The TEM_{00} coupling efficiency of the $\beta = 8$ μm feature at $q = 3$ (46%) is comparable to that of NV232 (47%), with a similar decrease in excited state lifetime.

As the $\beta = 4$ μm feature gave the greatest enhancements, the upcoming results are obtained with this feature. Compared to NV232, this experiment was performed in a different laboratory in which the floor did not deliver the same vibration stability. Therefore, the cavity modes recorded over an integration time of 10 s displayed linewidths of 2 – 3 nm and a significant Gaussian character. Figure 6.15 (a) shows the TEM_{00} mode for NV25, with a linewidth of 1.7 nm. This cavity mode is fit with a pseudo-Voigt function

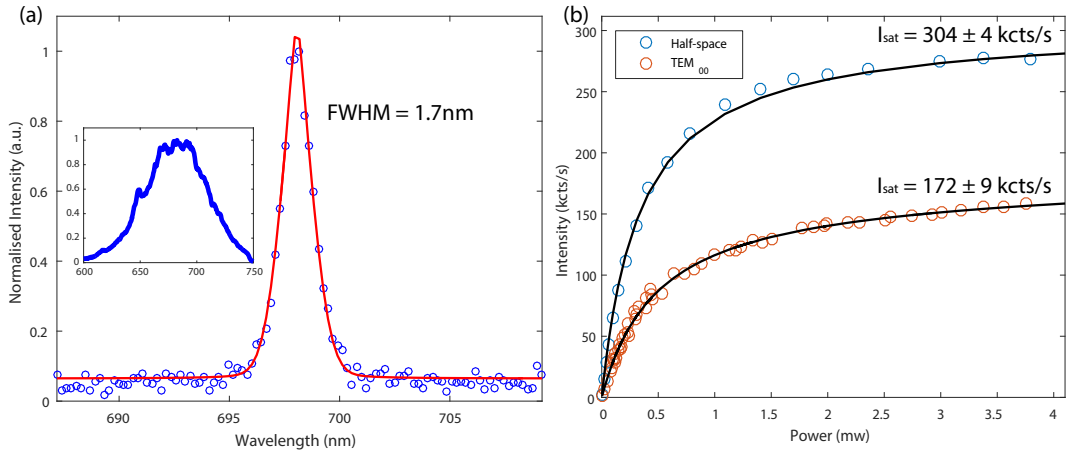


FIGURE 6.15: (a) Emission spectra of the TEM_{00} mode showing a linewidth of 1.7 nm. The inset shows the full emission spectrum for NV25. (b) CW saturation measurements for the full emission spectrum of NV25 and the TEM_{00} mode.

which is a linear combination of Lorentzian and Gaussian peaks. The mode in Figure 6.15 (a) displays 35% Lorentzian character and 65% Gaussian character. The saturation measurement for the TEM_{00} mode gave a saturation count of $I_{sat} = 172 \pm 9$ kcts/s, meaning 57% of the total emission is coupled into this single mode. This is a ∼10% increase in the coupling efficiency for the $\beta = 4$ μm compared to 46% for the $\beta = 8$ μm feature. The spectral density of photons has increased from 4.3 kcts/(s nm) to 101.2 kcts/(s nm) for the 4 μm feature - a 23.5 times enhancement. The $\beta = 8$ μm feature gave a 20.5 times enhancement to 88.1 kcts/(s nm).

The CW and pulsed HBT measurements for the cavity coupled emission can be seen in Figure 6.16. The inset of 6.16 (a) shows a 5μm×5μm PL image of the TEM_{00} emission. The near registration features are no longer visible and with NV25 remaining as the only distinguishing feature. Even the extremely bright defect close to NV25 is no longer visible. As with NV232, the filtered emission from the single mode increases decreases the

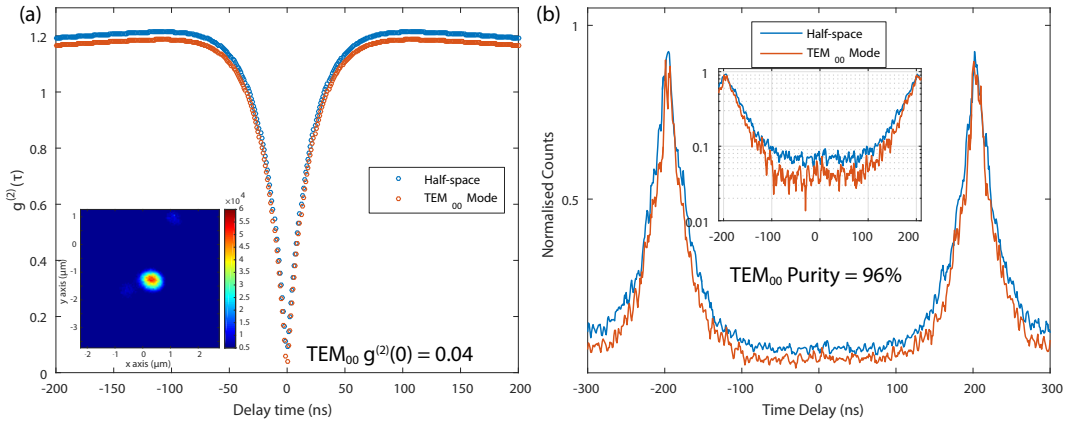


FIGURE 6.16: Continuous wave (a) and pulsed (b) HBT measurements of NV25's half-space amd TEM_{00} emission. The inset of (a) shows the PL image of the TEM_{00} emission.

minimum of the CW HBT from $g^{(2)}(0) = 0.09$ to 0.04. The pulsed HBT measurement seen in Figure 6.16 (b) also showed this change, with the single photon purity increasing from 91% to 96%. More interestingly, the change in excited state lifetime is also visible with the cavity coupled emission decaying quicker than in the half-space measurement. The inset of Figure 6.16 (b) is shown on a log scale, emphasising the reduction background level of the TEM_{00} emission.

The CW saturation measurement shown in Figure 6.15 (b) revealed 56% of the total emission spectrum was coupled to the TEM_{00} mode. This value should also be reproduced under pulsed excitation. Figure 6.17 (a) shows the saturation measurement for NV25 under pulsed excitation at a repetition rate of 10 MHz. For the TEM_{00} mode, $I_{sat} = 141$ kcts/s, compared to 296 kcts/s for half-space emission. This measurement was performed at 10 MHz due to the decrease in excited state lifetime seen in Figure 6.17 (b). A 13% decrease in the excited state lifetime was observed, from 31.3 ns on the planar mirror to 27.1 ns in the cavity. Therefore, an excitation rate of 10 MHz is $\sim$3 excited state lifetimes, giving NV25 sufficient time to relax from the excited state. Under pulsed excitation,

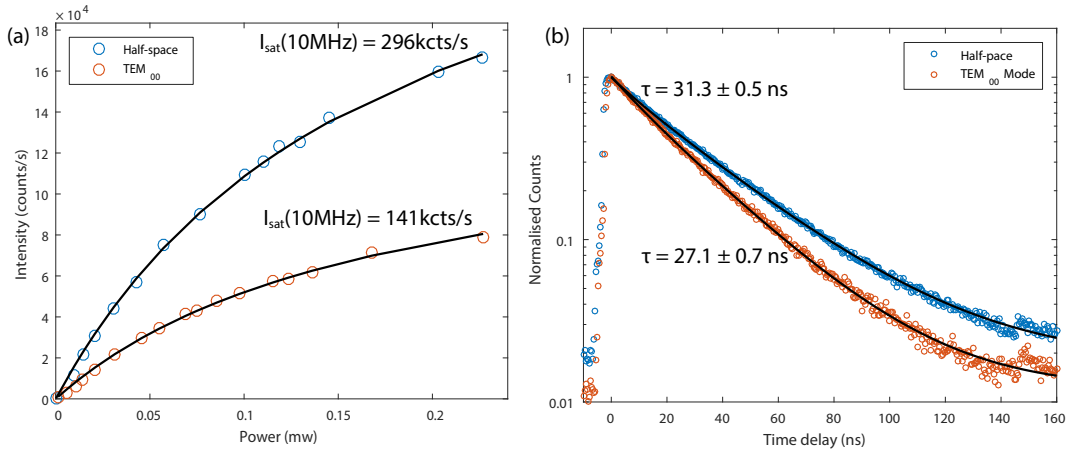


FIGURE 6.17: (a) Pulsed saturation measurement performed at 10 MHz for NV25's half-space and TEM_{00} emission. (b) TRPL measurement for half-space and TEM_{00} emission.

only 47% of the emission was coupled to the TEM_{00} mode for both 5 MHz and 10 MHz excitation rates. The reason behind the discrepancy between CW and pulsed excitation is the switching between two excitation sources in-situ while the emitter coupled. This system did not possess any sort of feedback mechanism and relied purely on passive stabilisation. The removal of a laser during the switch usually led to some misalignment. Also, the pulsed laser path also requires slight realignment each time and this proves extremely difficult when concerning filtered cavity coupled emission. Therefore, with a more optimised switching system for the excitation sources, a 56% coupling efficiency is also expected under pulsed excitation.

6.5 NV-Cavity Single Photon Source Specifications

The brightest NV open-cavity coupling results were reported by Kaupp *et al.* using the fiber-based optical cavity with a metallic coating on the planar mirror [130]. This metallic coating (33 nm) reduced the penetration depth into the planar mirror, decreasing the

mode volume ($V = 1\ \lambda^3$), thereby increasing the interaction of the electric field with the emitter. This device produced $\sim 2 \times 10^6$ kcts/s under CW excitation after the first lens, but the auto-fluorescence from the metallic planar mirror limited the lowest $g^{(2)}(0)$ values to ~0.2. In addition, the cavity linewidth at the lowest mode index ($q = 1$) was ~16 nm, giving a spectral density of 125 kcts/(s nm). For NV25, the detected spectral density under CW excitation is 101 kcts/(s nm), increasing to 268 kcts/(s nm) when taken after the objective lens, with $g^{(2)}(0) = 0.04$. Although the cavity system used in this thesis did not reach the same mode index for NV25, the linewidth of mode and extraction efficiency of the cavity coupled emission improve significantly on the results from previous reports [109, 129, 130, 161].

In order to reach the $q = 2$ index, further processing of the plinth (as in Figure 4.3) is required to reduce the dimensions to below 50μm $\times$ 50μm. This index has been reached on a single occasion for a previous experiment, with the cavity mode at 690 nm for a β = 4 μm feature possessing a linewidth of 2.5 nm when integrated over 10 s. The $q = 2$ mode has an NA of 0.51, and so the total mode would be collected by the objective lens (NA = 0.85). Figure 6.14 (a) shows the enhancement of the count rate with decreasing mode index for the $\beta = 4$ μm cavity. From this, a detected saturation count of >200 kcts/s under pulsed saturation at 10 MHz is expected. This corresponds to a count rate of >531 kcts/s after the obective lens, or a device efficiency of $\langle \mathcal{N} \rangle$ >5.3 %. These predicted values are underestimated, and based purely off an increased collection efficiency without the inclusion of further enhancement in the cavity emission rate by the Purcell effect.

6.6 Conclusion

In conclusion, single NV centres in nanodiamonds have been successfully coupled to open-access microcavities. The cavity was found to increase the spectral density of photons into a single mode, far beyond simple simple filtering. The NV232 cavity system comprised of a nanodiamond from the 50 nm sample with mirrors with peak reflectivity at 640 nm. The results were obtained at the $q = 3$ mode index for a feature with radius of curvature $\beta = 8$ μm, with the cavity inducing only a negligible change in emitter's excited state lifetime. Although the TEM_{00} mode is the mode chosen for optimal extraction of photons from the cavity, the rate of emission in the cavity is dependent on all the modes. Therefore, FDTD simulations were used to determine the true Purcell factor for the NV centre inside the optical microcavity. With consideration of the QE, the Purcell factor obtained from the simulation was found to be in good agreement with the experimentally observed change in excited state lifetime. Despite this small change in excited state lifetime, the cavity does provide efficient channelling into the cavity modes, with a coupling efficiency of 47% for the TEM_{00}. Under pulsed excitation at 5 MHz, the TEM_{00} emission yielded a saturation intensity of 61 kcts/s into a single mode of linewidth 1.4 nm. This corresponds to a detected efficiency of 1.22% with a single photon purity of 97%.

Following this, nanodiamonds from the 100 nm sample were also characterised with several candidates located. NV25 was chosen and then coupled to an optical microcavity with peak reflectivity at 690 nm and radius of curvature 4 μm with improved results. With the use of 100 nm nanodiamonds in combination with 690 nm mirrors, this system will offer increased photo-stability in addition to an enhancement in the cavity decay rate. The coupling efficiency was measured as 0.57 of the half-space emission intensity into the TEM_{00} mode with a linewidth 1.7 nm. The cavity coupled emission delivered a measured single photon purity of 96%. With a reduction in the dimensions of the plinth,

the $q = 2$ mode index can be reached. It is estimated that at this cavity length, $>$66% of the half-space emission will be coupled into a single mode, giving a device efficiency of $\langle \mathcal{N} \rangle > 5.3\%$ at 10 MHz. The triggered single photon count rate after the objective lens is predicted to be $>$531 kcts/s.

7

Hexagonal Boron Nitride Single Photon Source

7.1 Introduction

This final experimental chapter will present the characterisation of single defects in hexagonal boron nitride (hBN). hBN possesses outstanding chemical and thermal stability, with its large bandgap playing host to quantum emitters in the visible region. These promising attributes make hBN a favourable material towards the development of a room temperature single photon source. Although the exact nature of these defects are yet to be determined, they have been identified as a strong alternative to the NV centre for use as a single photon source. These defects were prepared with the fabrication method detailed in Section 4.3.3, with three total samples produced by Toan Trong Tran at the University of Technology Sydney. I will discuss results from each of these samples, including a spectral survey which shows large variations in the ZPL position and linewidth. The single emitters located within these samples show a wide range of photo-luminescence behaviour and highlight the unspoken experimental difficulty associated with hBN defects. Cavity coupling of these defects has been attempted with limited success, and the reasons for this will be discussed. The half-space and cavity enhanced results for the defect known as hBN40 will be presented in further detail. Finally, these results will be compared to the most recent demonstration of a hBN-cavity system with the key differences explained.

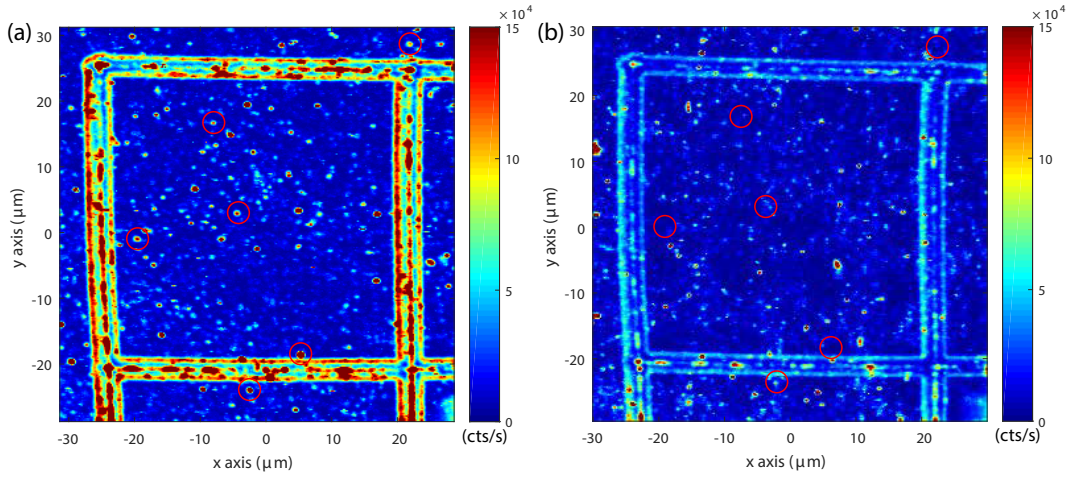


FIGURE 7.1: PL image of the registration grid featuring several hBN defects. (a) The initial PL image shows numerous bright spots and strong background auto-fluorescence. (b) The final PL image was taken following several PL measurements, and a total of 140 hours of photo-bleaching at a laser power of 1.4 mW. All of the previously circled points are no longer visible.

7.2 Single Emitter Survey

7.2.1 Sample 1

The preliminary characterisation of defects in hexagonal boron nitride from the first sample (Sample 1) provided an insight into the complications involved with using these defects as a single photon source. Specifically, the issue of photo-stability of these defects is rarely discussed, despite presenting a significant impediment to the development of a single photon source device. The hBN samples were transferred onto DBR mirrors with a peak reflectivity of 97.5 $\pm$ 0.5% at 640 nm. Figure 7.1 shows the PL image of a region on the planar mirror coated with hBN nanoflakes. The initial image in Figure 7.1 (a) shows numerous hBN defects emitting within the 580 – 740 nm window. Defects showing single photon emission are circled in red, and these were chosen for further characterisation. Due to substrate auto-fluorescence, the area was gently photo-bleached under

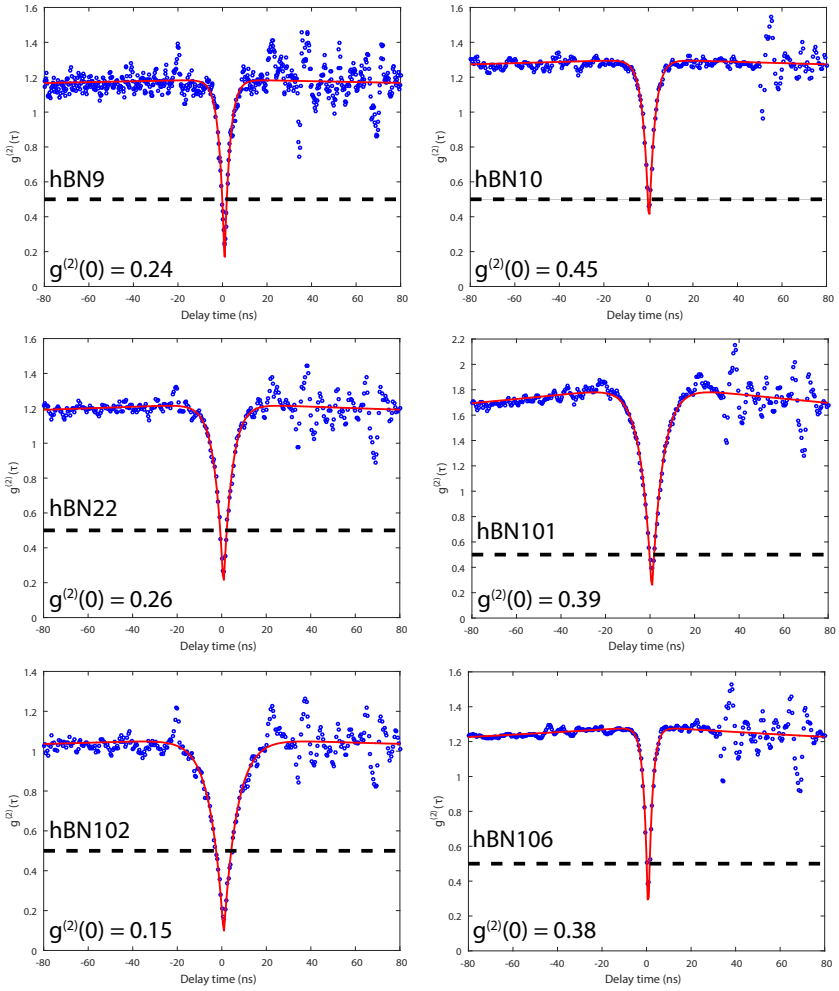


FIGURE 7.2: Continuous wave HBT measurements of single defects in hBN from the region circled in Figure 7.1. The black dashed line represents the value of $g^{(2)}(0) = 0.5$.

CW excitation at a power of 1.4 mW over 140 hours in total. This lead to the eventual loss fluorescence from all the chosen defects (Figure 7.1 (b)), in combination with the use of excitation for the measurement of emission properties. Figure 7.2 presents the CW HBT measurements from the circled emitters in Figure 7.1 (a). All of these chosen defects show single photon emission with $g^{(2)}(0) < 0.5$. The steepness of the central dip indicates different excited state lifetimes, which will be directly measured later.

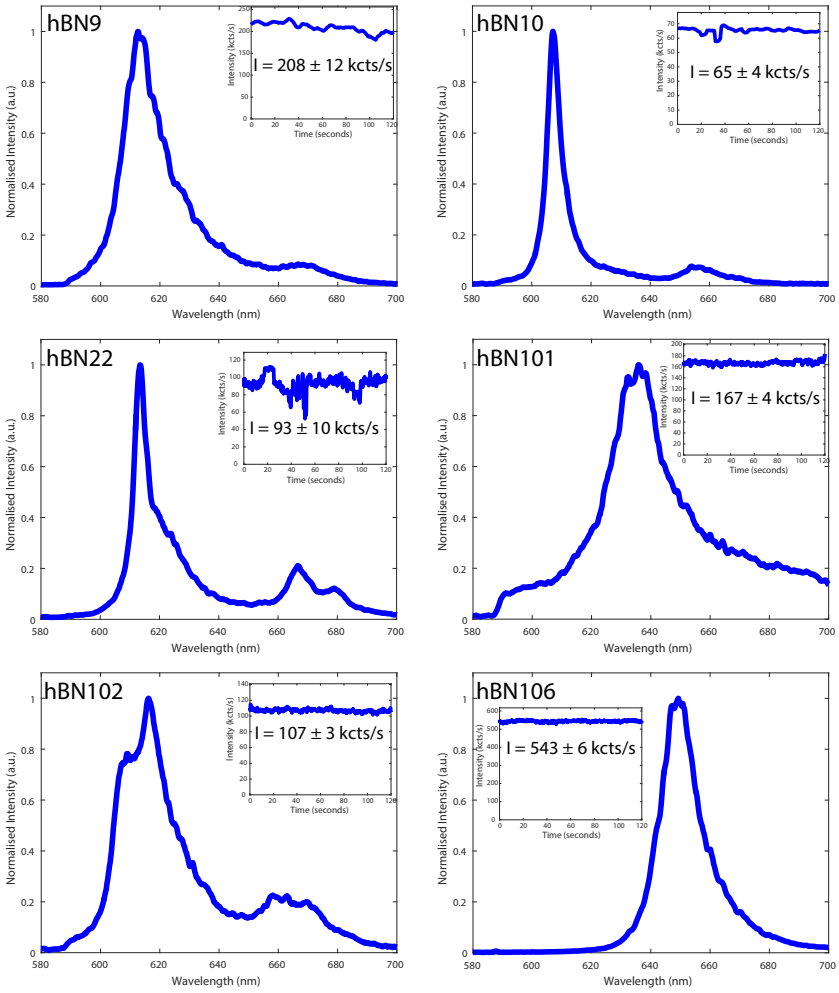


FIGURE 7.3: Spectral survey of single defects in hBN within the 580–730 nm window. The data has been normalised for comparison. The insets show the count trace measured simultaneously with the emission spectrum over two minutes.

Figure 7.3 shows the emission spectra of these defects recorded over two minutes. As varying photo-stability was observed, the count trace recorded at the same time to map stability onto their spectra. The emission spectra resemble those reported by Tran *et al.* [32] showing ZPLs of varying widths between 600 – 700 nm. The defects with a narrow emission ZPL (such as hBN10) are typically associated with multi-layer hBN material, and are expected to display improved photo-stability compared to defects with broader

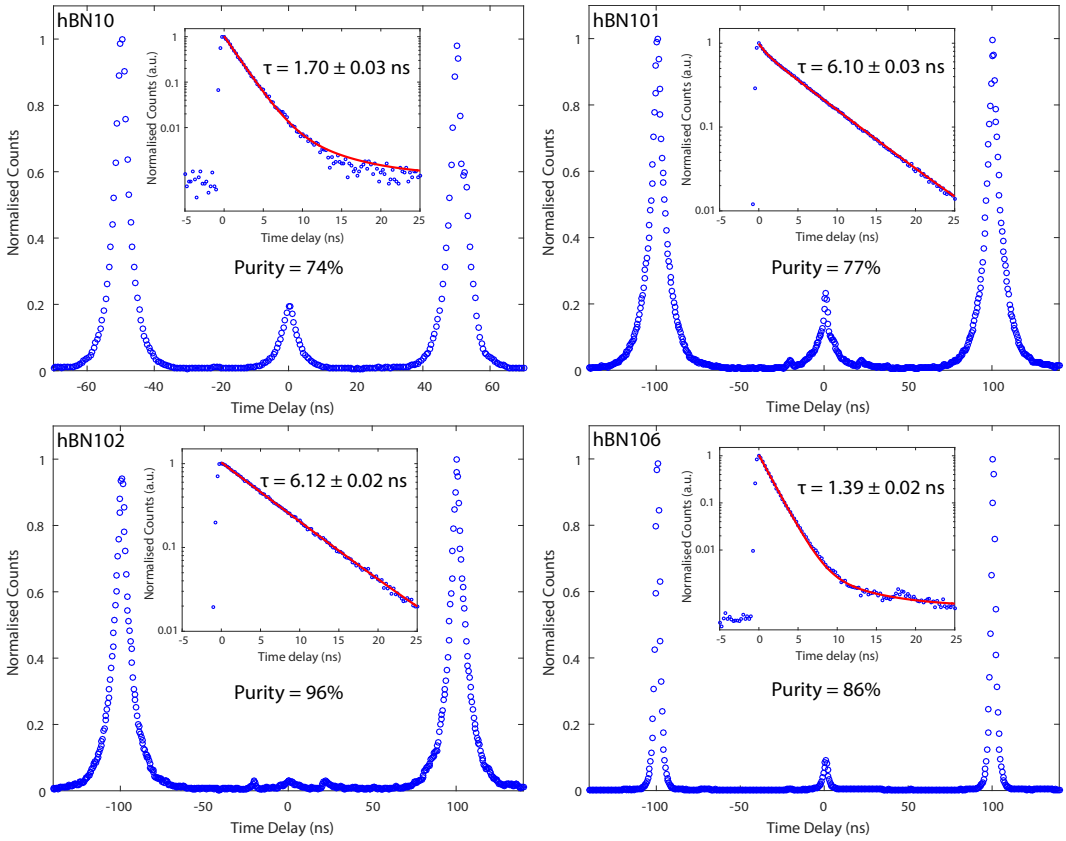


FIGURE 7.4: Pulsed HBT measurements of the surviving hBN defects. The insets show the TRPL measurement giving the excited state lifetime of each defect. The pulsed HBT measurement for hBN10 was recorded an an excitation rate of 20 MHz.

ZPLs (hBN101). Despite this, both of these defects display good photo-stability, varying in intensity by $\pm$ 4 kcts. Defects such as hBN10 and hBN22 present ideal emission spectra which would be more favourable towards cavity coupling, with large DW factors of 0.69 and 0.64 respectively. The emission spectrum for hBN102 features a "hump" on the left of the ZPL maximum, which may indicate the presence of a second defect with different ZPL position on the same nanoflake. However, the CW HBT from Figure 7.2 shows predominatly single photon emission with $g^{(2)}(0) = 0.15$.

Following the previous measurements under continuous excitation, the pulsed laser was used to excite the defects to record pulsed HBT and TRPL measurements. Once subject to the pulsed laser, hBN9 and hBN22 displayed intermittent fluorescence and photo-bleached within 30 seconds. Therefore no measurements under pulsed excitation could be performed. For the remaining defects, the pulsed HBT and TRPL measurements can be seen in Figure 7.4. These results show promising single photon purities compared to the CW HBT, all with purities $\geq$74%. hBN102 shows the most impressive result, with a single photon purity of 96%. The excited state lifetime of these defects show a range between 1–7 ns, typical for hBN defects [32, 72, 73].

The photo-stability of the remaining defects was found to degrade following the completion of the measurements in Figure 7.4. hBN10 and hBN102 photo-bleached leaving only hBN101 and hBN106 remaining. Figure 7.5 shows the recorded count trace and PL image of hBN101 and hBN106 before and after measurements performed under pulsed excitation. Figure 7.5 (a) shows that hBN101 remained stable with the count rate remaining near-constant over the both before (main, $\pm$ 4 kcts/s) and after (inset, $\pm$ 4 kcts/s) measurements. A PL image of hBN101 was taken following exposure to the pulsed laser (Figure 7.5), showing a typical image for the emission from a point source. For hBN106, the pulsed laser induced severe instability as seen in Figure 7.5 (c) inset. The instability increased significantly from $\pm$ 6 kcts/s to $\pm$ 115 kcts/s. This instability is visible on hBN106's PL image (Figure 7.5 (d)), where several dark spots and lines appear over the central maximum of the scan. This is due to the variation in PL intensity as the excitation laser scans over hBN106.

As many applications require triggered single photon generation over prolonged time periods, the instability of these defects under pulsed excitation is an important obstacle. Two-dimensional materials generally oxidise in ambient conditions, with the stability

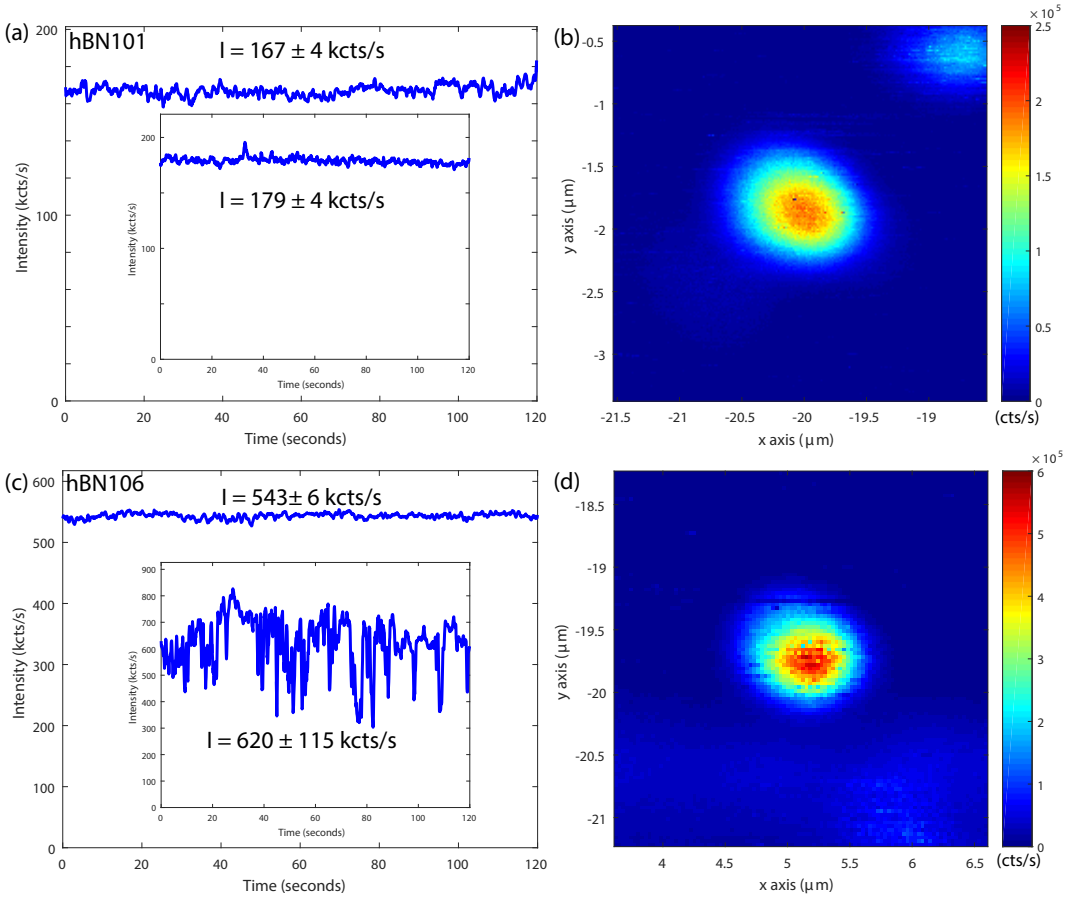


FIGURE 7.5: (a) Count trace for hBN101 before pulsed excitation, recorded for 2 minutes. The average PL intensity is $I = 167 \pm 4$ kcts/s. The inset shows the count trace following measurements under pulsed excitation showing $I = 179 \pm 4$ kcts/s. (b) PL image of hBN101 showing a typical bright spot. (c) Count trace for hBN106 before pulsed excitation showing $I = 543 \pm 6$ kcts/s . The inset shows the count trace following measurements under pulsed excitation. The PL signal is now unstable with $I = 620 \pm 115$ kcts/s. (d) PL image of hBN106 showing flickering of the PL intensity as the laser scans over the sample.

controlled by the oxygen dissociative absorption barrier. As the nanoflakes are typically a few atoms thick, small variations on the nanoflake surface can lead to large changes in the photo-physical properties, even in the absence of photo-excitation. Vogl *et al.* demonstrated hBN photo-stability over 8 months with monthly measurements of PL intensity and spectra [73]. The sample was left in ambient conditions when not in use and showed

an increasing linewidth over the eight months. These oxygen plasma-created defects displayed power dependent photo-stability under continuous wave excitation. For the defects in Figure 7.4, the average power of the pulsed laser used to perform the measurements is low ($P_{ave} \sim 0.45$ mW). However, the peak power of each laser pulse is extremely high ($P_{peak} \sim 500$ mW). With such a large amount of power incident in a short period of time (100 ps), the laser could feasibly induce interactions between the defect and surface or atmospheric species which can fill the vacancy - thereby quenching emission. All of the hBN defects presented in this section eventually photo-bleached, and no cavity coupling could be performed. Isolating the hBN nanoflakes from the environment (such as by encapsulation) may improve the photo-stability of the defects, but the encapsulating material must not affect the defects within the nanoflakes.

7.2.2 Sample 2

The second hBN sample (Sample 2) studied in this project presented more photo-stable defects with interesting properties. Figure 7.6 (a) shows the camera image of the region on the planar mirror where the stable defects were found. It was suggested that defects found in such areas with transfer residue remaining were more encapsulated from the environment. The sample was pre-characterised at the University of Technology Sydney to show the presence of sufficiently stable emitters with narrow emission spectra located within such areas. Figure 7.6 (b) shows the corresponding PL image. The residue visible on the webcam image is also present in the PL image. Several bright and photo-stable defects were found in this region, but only two (hBN38 and hBN86) showed potential single photon emission. These defects are circled in red.

The properties of hBN38 and hBN86 are presented in Figure 7.7. The emission spectra of these defects showed the presence of another strong transition close to the main ZPL

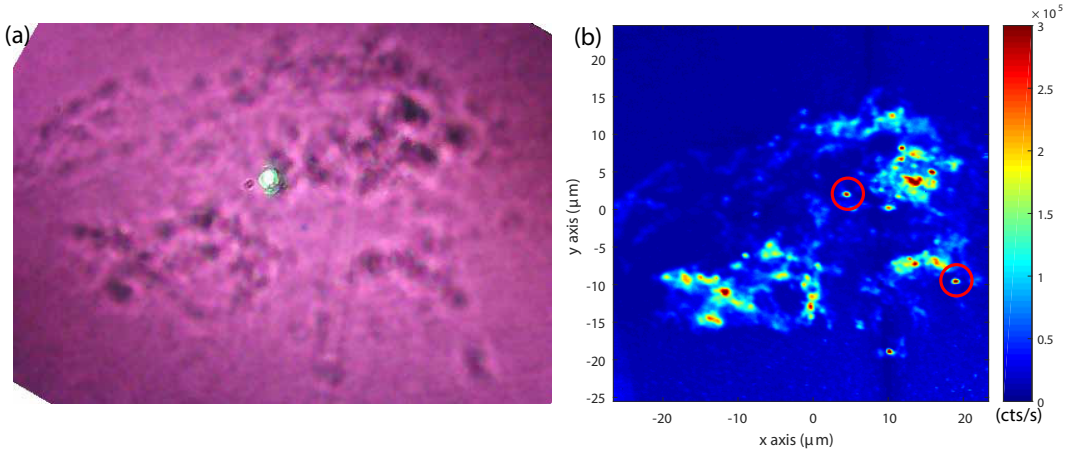


FIGURE 7.6: Webcam (a) and PL image (b) of the region where single hBN defects were found in Sample 2. The residue from the transfer process is clearly visible on both images. The positions of hBN38 and hBN86 are circled in red.

(Figure 7.7 (a) and (b)). It was assumed that there were two defects contributing to the emission spectra and CW HBT measurements showed $g^{(2)}(0)$ values of 0.75 and 0.67 respectively for the full emission spectrum (Figure 7.7 (c) and (d)). Pulsed HBT measurements recorded at an excitation rate of 20 MHz also showed single photon purities of 45% and 64% (Figure 7.7 (e) and (f)) for the full spectrum. Bandpass filters with a bandwidth of 10 nm were used to isolate the strongest ZPL transitions at 627 nm for hBN38 and 673 nm for hBN86, resulting in improved single photon characteristics. For this filtered emission, the CW HBTs showed decreases in the $g^{(2)}(0)$ values to 0.15 and 0.25. The single photon purities were also found to increase to 82% and 94%. As the filtered emission shows improved single photon purities under both CW and pulsed excitation, the weaker features in the emission spectrum of hBN38 and hBN86 originate other emitters within the same nanoflakes.

With single photon emission now confirmed, pulsed saturation measurements were performed for the filtered emission to estimate the QE of these defects. The excitation rate

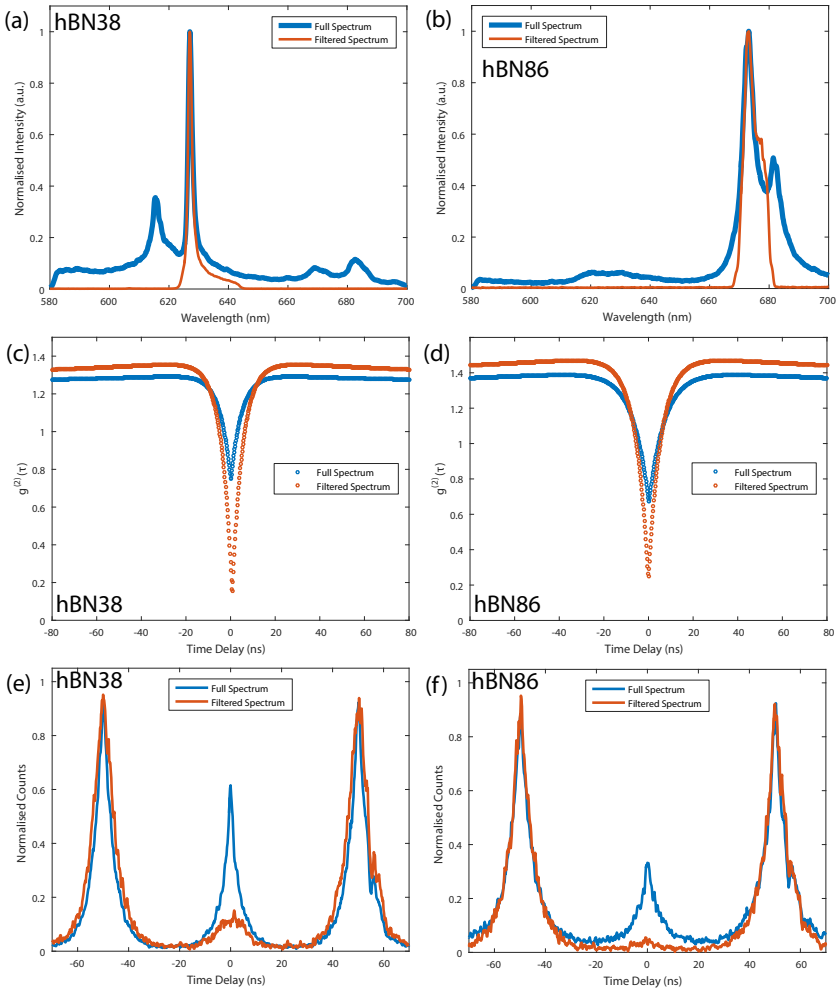


FIGURE 7.7: Emission spectra and HBT characterisation of hBN38 and hBN86. The results for hBN38 are on the left column (a,c,e) and hBN86 on the right (b,d,f). The filtered results were obtained using bandpass filters (640 nm and 690 nm) which were rotated to move the band to the peaks at 627 nm (hBN38) and 673 nm (hBN86).

used is 10MHz and the saturation behaviour displayed in Figure 7.8 is fit with Equation 4.6. For hBN38, $I_{sat}(10MHz) = 328 \pm 161$ kcts/s and for hBN86, $I_{sat}(10MHz) = 343 \pm 170$ kcts/s. Their single photon efficiencies at the detectors (Equation 5.1)are then 3.28% (hBN38) and 3.43% (hBN86). The collection efficiencies are calculated from the filtered emission spectra in Figure 7.7 (a) and (b) using Equation 3.28, with $\langle \eta_{coll} \rangle$(hBN38) = 0.78 and $\langle \eta_{coll} \rangle$(hBN86) = 0.50. The system efficiency was found to be $\eta_{sys} = 0.36 \pm$

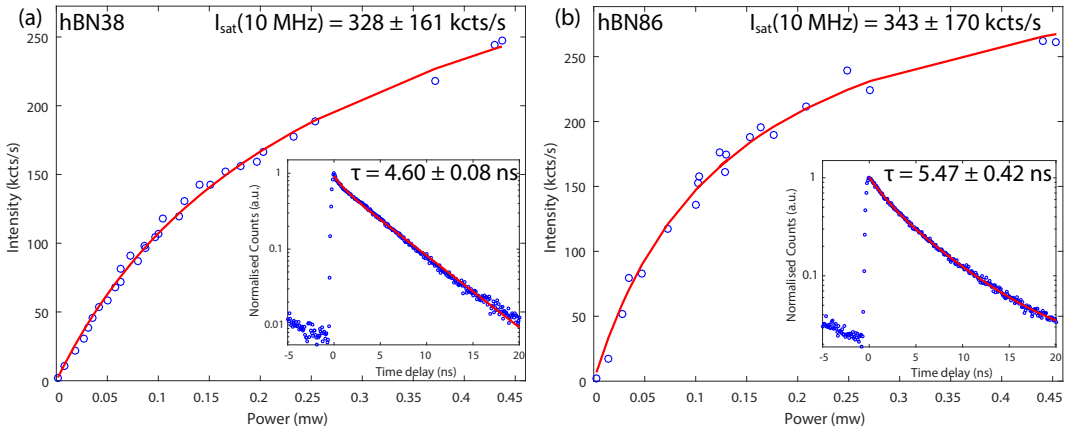


FIGURE 7.8: Pulsed saturation measurements for the filtered emission for hBN38 (a) and hBN86 (b). The insets show the TRPL measurement for each defect.

0.02. Using Equation 4.7, QE(hBN38) = 0.12 ± 0.06 and QE(hBN86) = 0.19 ± 0.09. These QE values are comparable to those for the brightest NV centres in nanodiamonds measured in Chapter 5. TRPL measurements showed excited state lifetimes of 4.60 ± 0.08 ns for hBN38 and 5.47 ± 0.42 for hBN86 (Figure 7.8 insets). Therefore, unlike NV centres, these defects can be excited at rates up to ∼50 MHz while maintaining the same single photon emission efficiency.

Despite the presence of the secondary ZPL on their emission spectra, the narrow linewidth of hBN38 and hBN86 will allow the cavity mode to enhance their specific ZPLs, while suppressing off-resonant emission. This will improve the single photon purities measured compared to the filtered half-space emission. The sample was inverted and these defects were relocated. Cavity coupling was attempted but unfortunately, stable cavity modes could not be formed, meaning no enhancement was observed. The presence of the transfer residue is likely to be the cause of scattering. The dark circular objects seen in Figure 7.6 (a) were thought to be made of either PMMA from the transfer process, or silicon from the original substrate where the nanoflakes were deposited on. The sample was

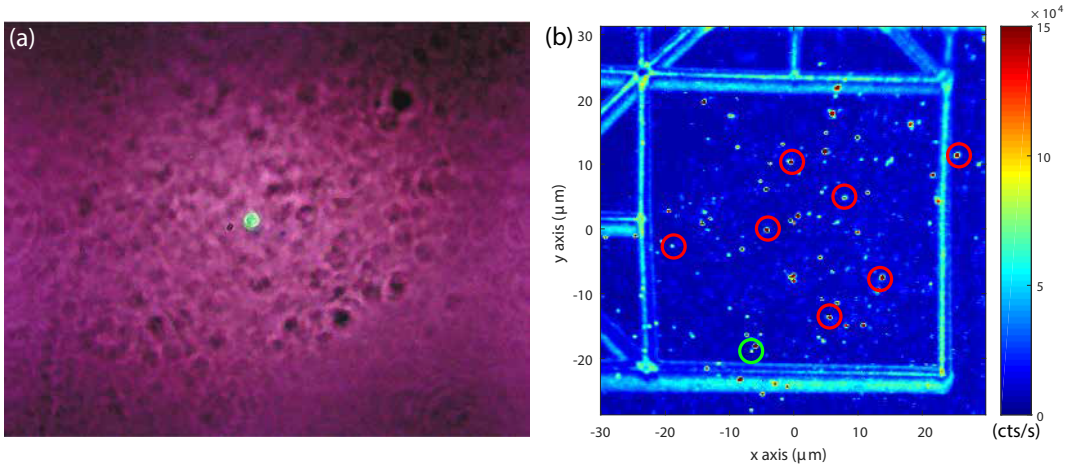


FIGURE 7.9: Webcam (a) and PL image (b) of the region in Sample 3 where single hBN defects were found. The PL image is taken with a ×100 0.8NA lens. The residue from the transfer process is clearly visible on the webcam image, but not on the PL image. The positions of defects with narrow emission spectra are circled in red. hBN40 is circled in green.

soaked in acetone for over 12 hours and no change in the webcam or PL image was observed. Therefore, the residue is likely to be formed from silicon islands which were not completely etched away in the first step of the process outlined in Figure 4.7.

7.2.3 Sample 3

The results from Section 7.2.2 were extremely promising due to the location of photo-stable emitters. However, improved sample processing was required such that cavity coupling could be achieved. The final sample to be discussed in this thesis (Sample 3) provided both bright narrow emitters with sufficient photo-stability for all measurements to be performed. Figure 7.9 shows the webcam (a) and PL image (b) of an area within the FIB marked grid where promising defects were found. The webcam image still shows dark spots from the transfer process. However, this material is not visible on the PL image, and may have less of an effect than in Sample 2. Figure 7.9 (b) shows the position of six promising single defects circled in red. These defects survived ∼160 hours of

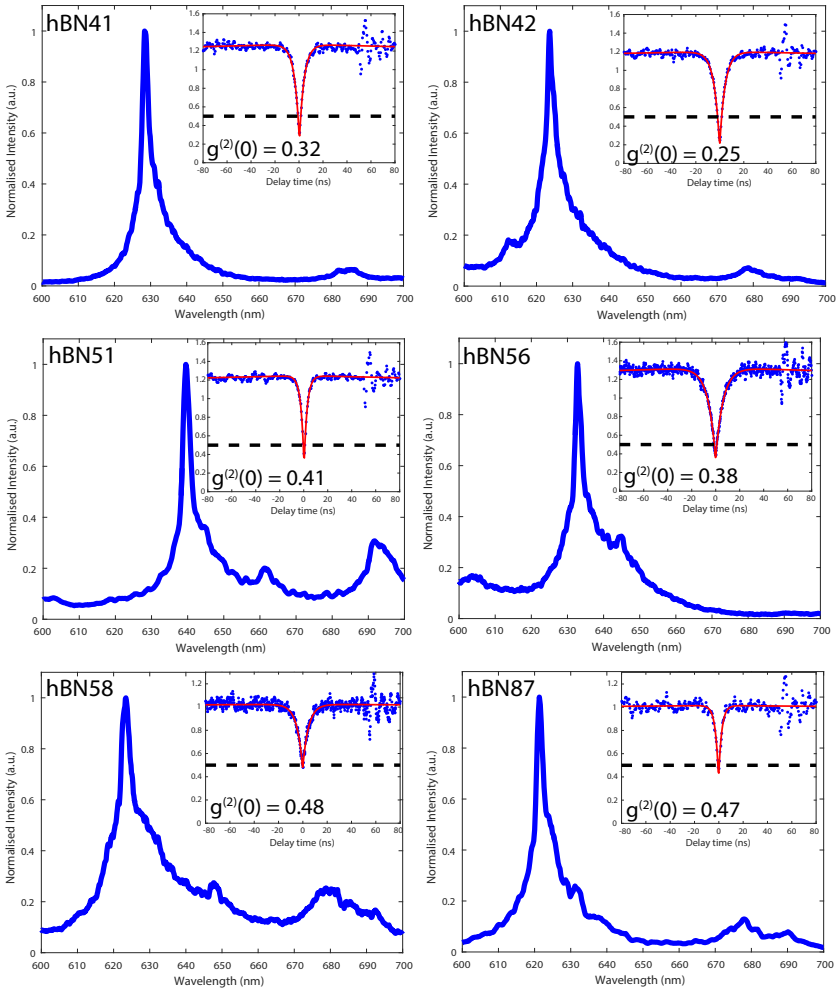


FIGURE 7.10: Emission spectra and HBT characterisation of six hBN defects in Sample 3. The emission spectra all show sharp ZPLs between 620–640 nm. The CW HBT measurements all show $g^{(2)}(0) < 0.5$, indicative of single photon emission.

photo-bleaching at a laser power of 1.4 mW without any degradation in photo-stability or emission properties. Figure 7.10 shows the spectral profile of these six emitters. All the defects display sharp ZPLs between 620 – 640 nm. The CW HBTs show mostly single photon emission with $g^{(2)}(0) < 0.5$. The emission spectra of hBN41 and hBN42 show the clearest ZPLs with no other discerning features. Subsequently, they also display the best $g^{(2)}(0)$ values. The best defect chosen for further characterisation is hBN40, which is

circled in green in Figure 7.9 (b).

7.3 hBN40 Single Photon Source

7.3.1 hBN40 Half-space Characterisation

The results of Section 7.2.3 show Sample 3 to provide the most ideal defects out of the three samples discussed so far. With all the defects circled in Figure 7.9 (b) displaying sufficient photo-stability, further characterisation was performed on hBN40. These results are displayed in Figure 7.11. The CW HBT measurement shows a dip at zero time delay with $g^{(2)}(0) = 0.21$ (Figure 7.11 (a)), the lowest $g^{(2)}(0)$ value out of all the emitters in Section 7.2.3. The emission spectrum shows a single ZPL transition at 651 nm with a FWHM of 3.8 nm (Figure 7.11 (b)). This linewidth corresponds to a Q-factor of $Q \sim 171$, much larger than the typical Q-factors for NV centres ($Q \sim 10$). The pulsed HBT measurement was performed at 10 MHz and shows a small peak at zero-time delay, yielding a single photon purity of 95% (Figure 7.11 (c)). Unlike for NV25 (Figure 6.12), the single photon purity under pulsed excitation is not analogous with the CW $g^{(2)}(0)$ value. As the electronic structure of the defect in hBN is unknown, continuous wave excitation may induce additional emission processes which limit the minimum of $g^{(2)}(0)$. However, under pulsed excitation, the short pulse length ($\sim$100 ps) and time delay between excitation events may favour the strongest transition leading to a high single photon purity.

Figure 7.11 (d) shows the TRPL measurement for hBN40. The excited state lifetime was found to be 2.70 ± 0.02 ns. With such a short excited state lifetime, hBN40 can be excited at up to 80 MHz (12.5 ns time delay) while still allowing the excited state population to fully decay. The CW saturation count is 2.1 ± 1.1 Mcts/s (Figure 7.11 (e)). This measurement was not taken to saturation in order to keep the emitter stable, resulting in

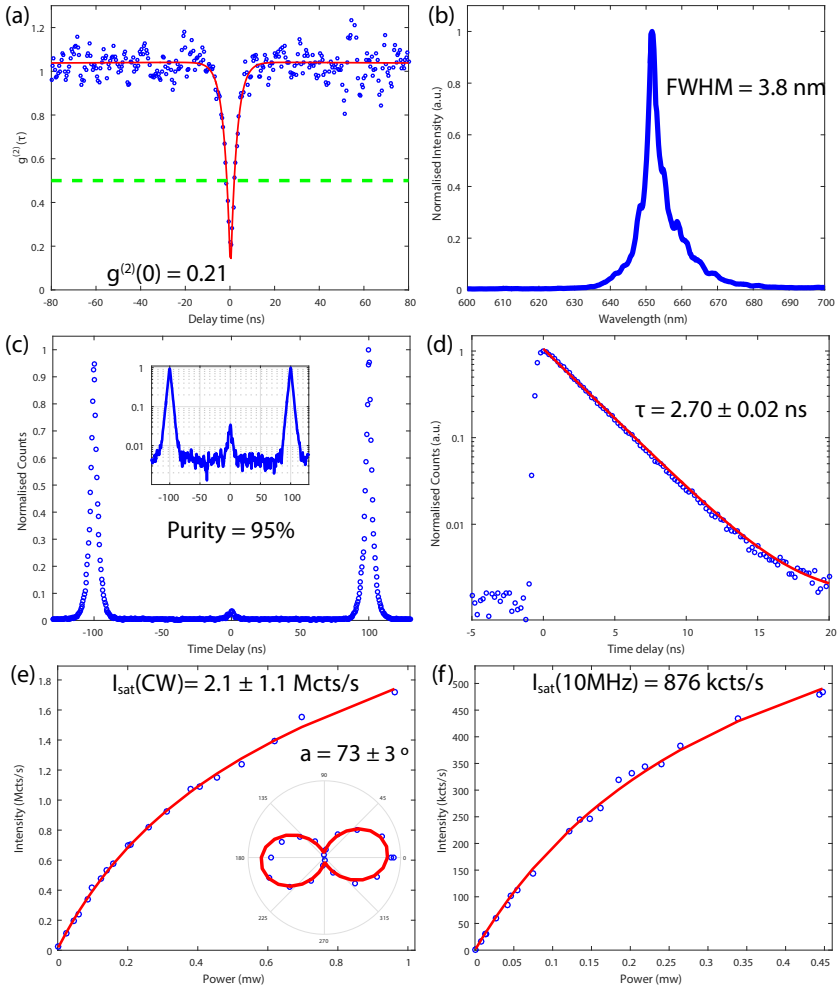


FIGURE 7.11: Characterisation of hBN40. (a) CW HBT measurement shows $g^{(2)}(0) = 0.21$. The green line represents $g^{(2)}(0) = 0.5$ (b) The emission spectrum shows the ZPL at 651 nm with a FWHM of 3.8 nm. (c) Pulsed HBT measurement performed at 10 MHz shows a single photon putirty of 95%. (d) TRPL measurement showing an excited state lifetime of 2.70 $\pm$ 0.02 ns. (e) CW saturation measurement showing $I_{sat} = 2.1 \pm 1.1$ Mcts/s. The inset shows the polarisation measurement, with the defect displaying strong polarisibility and an angle of 73 $\pm$ 3 $^\circ$ to the plane. (f) Pulsed saturation measurement at 10 MHz showing a saturation count of 878 kcts/s.

the large error bars. The inset of (Figure 7.11 (e)) shows the polarisation measurement of hBN40. hBN40 showed large polarisibility with the emission intensity reducing by $\sim$90% when the excitation laser polarisation is rotated perpendicularly to the defect axis. The

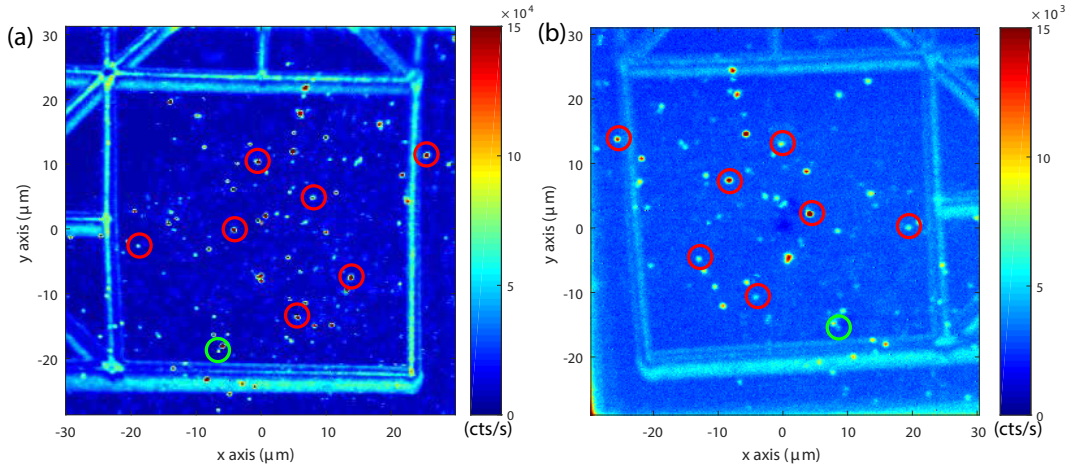


FIGURE 7.12: PL images of Sample 3 with the mirror facing towards (a) and away (b) from the objective lens. The previously circled defects are all visible with the mirror facing away from the objective.

defect angle was calculated by Equation 4.9 to be $a = 73 \pm 3\ ^\circ$. (Figure 7.11 (f)) shows the saturation measurement for hBN40 under pulsed excitation at 10 MHz. Although the pulsed laser power was not sufficient to reach saturation, Equation 4.6 gives $I_{sat} = 876$ ($\pm$ 819) kcts/s. The error bars are comparable to the I_{sat} value due to the insufficient power of the pulsed laser. For hBN40's half space emission, the single photon detection efficiency is $\langle \mathcal{N} \rangle = 8.76$ %, much larger than the values obtained for NV232 ($\langle \mathcal{N} \rangle = 2.58$ %) and NV25 ($\langle \mathcal{N} \rangle = 3.9$ %). Using Equation 3.28, the collection efficiency for hBN40's emission is $\langle \eta_{coll} \rangle = 0.60$, with the quantum efficiency approximated by Equation 4.7 to be $QE = 0.4$ ($\pm$ 0.37). Even though the error bar on the QE value is large, the observed count rate at the maximum laser power (485 kcts/s) is much greater than those of NV232 (135 kcts/s), NV25 (169 kcts/s), hBN38 (248 kcts/s) and hBN86 (262 kcts/s), even when accounting for the differing collections efficiencies. Therefore, hBN40 must possess a higher quantum efficiency justifying the calculated value of $QE = 0.4$.

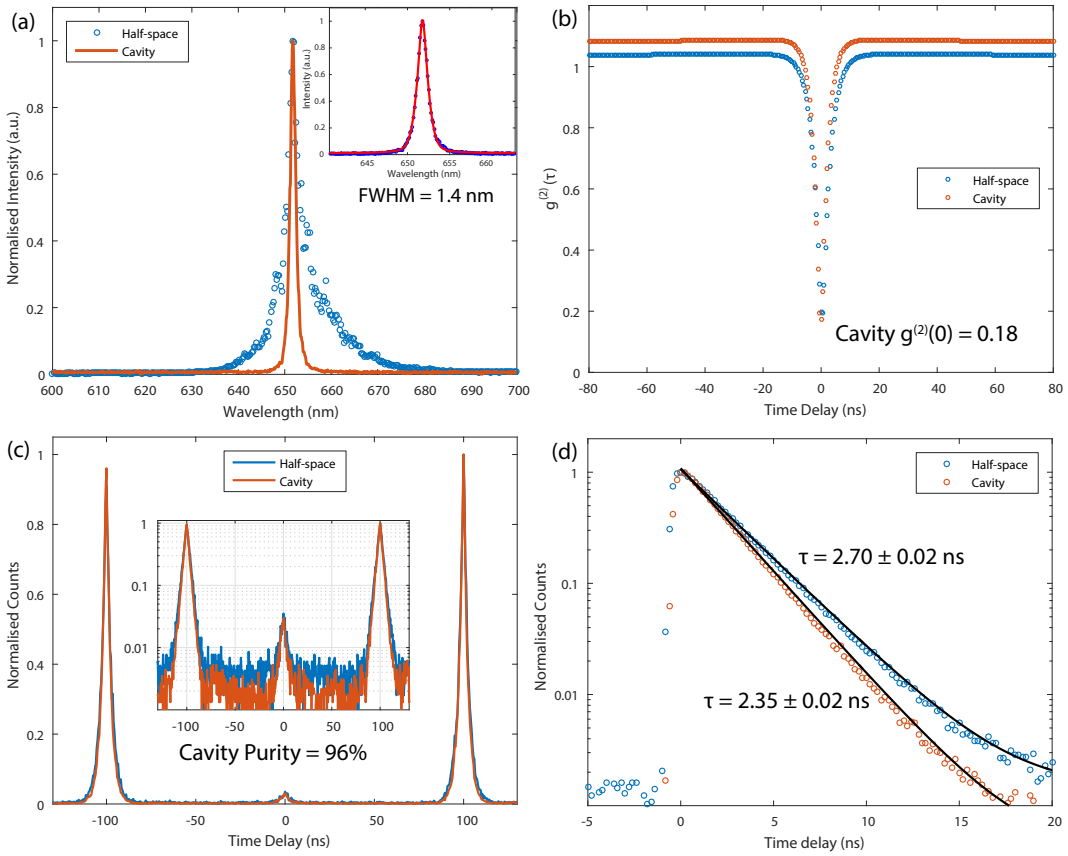


FIGURE 7.13: (a) PL spectra of the half-space and cavity coupled emission. The inset shows the TEM_{00} mode to possess a linewidth of 1.4 nm. (b) CW HBT measurement for the half-space and cavity-coupled emission. The cavity-coupled emission shows $g^{(2)}(0) = 0.18$. (c) Pulsed HBT measurement of hBN40's half-space and cavity-coupled emission, showing a slight increase in purity to 96% when coupled to the cavity. (d) TRPL measurement showing a 13% decrease in the excited state lifetime to 2.35 $\pm$ 0.02 ns when coupled to the cavity.

7.3.2 hBN40 Cavity Coupling

Following the characterisation of hBN40, the sample was inverted and hBN40 was relocated. Figure 7.12 shows the 60μm $\times$ 60μm PL images with the planar mirror facing towards and away from the objective lens. Both of these images were taken with a 100$\times$ 0.8 NA air objective lens. The sample was photo-bleached further for 60 hours at 2.8 mW to reduce the background on the back-side of the planar mirror. Despite the lack of

coverslip correction, all the previously circled defects are visible in the inverted image, including hBN40. The featured mirror (99.997% reflectivity at 640 nm) was then aligned behind hBN40, with the 8 μm feature from Figure 6.1 chosen for cavity coupling. The distance between the two mirrors was closed until the $q = 3$ mode index was reached. From here, the measurements in Figure 7.11 were repeated to determine the effect of the cavity on the emission properties of hBN40. Unfortunately, once cavity coupled, hBN40 did not remain photo-stable and a full characterisation could not be completed. The results obtained are presented in Figure 7.13.

Figure 7.13 (a) shows the cavity coupled spectra from the 8 μm cavity. Due to hBN40's already narrow emission spectrum, minimal PL intensity was observed unless the TEM_{00} mode was located at the ZPL (651 nm). The TEM_{00} linewidth was measured to be 1.4 nm. The CW HBT for the cavity coupled emission showed a slight decrease in $g^{(2)}(0)$ to 0.18. Due to the narrower TEM_{00} linewidth, a bandpass filter was not needed to isolate the single mode. With the use of a $\sim$8 nm bandpass filter, the $g^{(2)}(0)$ value is expected to drop further. The pulsed HBT measurement also showed a negligible increase in single photon purity to 96% for the cavity coupled emission. The inset of Figure 7.13 (c) is plotted on a log scale and shows the background baseline between $\tau = \pm$ 100 ns to decrease to a lower value for the cavity coupled emission compared to half-space emission. The TRPL measurement for hBN40's cavity coupled emission showed a 13% decrease in excited state lifetime from $\tau = 2.70 \pm 0.02$ ns to $\tau = 2.35 \pm 0.02$ ns.

Even though a saturation measurement could not be completed, a count rate of $I = 1$ Mcts/s was detected at an excitation power of 0.45 mW under continuous wave excitation. The count rate at this excitation power in half-space is taken from Figure 7.11 (e) to be 1.18 Mcts/s. The excitation power within the cavity is unknown as the transmission 532 nm light oscillates between $0.33 \leq P_{cav} \leq 1$ of the half-space power (Figure

4.17). As a first approximation, the 532 nm transmission into the cavity is assumed to be unity. The detected spectral density within the cavity is then 714 kcts/(s nm) compared to 308 kcts/(s nm) in half-space at this power. Unlike for NV232 (Section 6.3) and NV25 (Section 6.4), the results in Figure 7.13 were collected with an air-objective lens without cover slip correction. The use of a coverslip corrected lens was found to increase detected count rates by ∼12% due to improved aberration correction. With this correction, the detected count rate into the cavity mode (1.12 Mcts/s) is now comparable to the half-space value (1.18 Mcts/s). Although not at saturation, a count rate of 1.12 Mcts/s into the TEM_{00} mode corresponds to a spectral density of 800 kcts/(s nm), ∼8 times larger than the values measured for NV232 and NV25.

7.3.3 Discussion

As hBN40 is a relatively narrow emitter ($DW \sim 0.85$), with the cavity mode at the ZPL position, non-resonant emission is greatly suppressed. Equation 3.53 then provides a much more appropriate estimate of the Purcell factor compared to broad emitters such as the NV centre. From Equation 3.15, the Q-factor of hBN40 is $Q_{em} = 171$, while for the cavity, $Q_{cav} = 465$. Using Equation 3.54, the effective Q-factor is then $Q_{eff} = 125$. The TEM_{00} mode volume is given by Equation 3.23 to be $V = 3.85\lambda^3$. Therefore, Equation 3.53 gives $F_{P,eff} = 2.47$, much larger than the measured ratio of excited state lifetimes. FDTD simulations were used to gain a clearer understanding for this limited reduction. The hBN nanoflake was modelled as a cylinder with a diameter of 200 nm and thickness of 10 nm, with a refractive index of $n = 1.8$ [65]. The dipole was placed in the centre, 5 nm above the planar mirror surface. As described in Section 3.5.1, the Purcell factors for the nanoflake in free-space, on the planar mirror and within the cavity were determined. Equation 3.60 gives a free-space Purcell factor of $F_{P,fs} = 0.55$, $F_{P,hs} = 0.87$ and $F_{P,cav} = 1.82$. Relative to free-space, the half-space and cavity effective Purcell factors are then

$F'_{P,hs}$ = 1.58 and $F'_{P,cav}$ = 3.31. The simulated cavity Q-factor and mode volume are Q = 561, and V = 2.68λ^3. The experimentally measured value of Q_{cav} = 465 shows a broader cavity mode than expected, most likely due to scattering from the residue of the transfer process.

Using the simulated mode volume (V = 2.68λ^3) and experimentally measured Q-factor (Q_{cav} = 465), Equation 3.53 gives $F_{P,eff}$ = 2.96. This is only a ∼10% discrepancy from the value of $F'_{P,cav}$ calculated from Equation 3.61. As $F_{P,cav}/F_{P,hs}$ = 2.09, the excited state lifetime is expected to decrease by this value. However, Figure 7.13 (d) shows the excited state lifetime within the cavity decreased by only 13%. With the values of $F'_{P,i}$ for the half-space and cavity emission, Equation 3.63 gives γ_{rad} = 0.10·γ_{nr}, making QE = 0.09. From the saturation measurement in Figure 7.11 (f), the quantum efficiency of hBN40 on the planar mirror was estimated as QE = 0.4. As this value is features γ_{rad} enhanced by $F'_{P,hs}$ = 1.58, the true QE from this measurement is QE = 0.30 (± 0.28). The inconsistency between the value obtained from the change in excited state lifetime and saturation measurement may potentially be explained by features in hBN's electronic structure which remain unknown [32, 76].

For systems such as the NV centre, non-resonant excitation (532 nm) leads to an electronic transition to higher vibronic level of the electronic excited state, followed by rapid relaxation (∼ps) to the ground vibronic level of the electronic excited state (as seen in Figure 3.1). Therefore, the vibration-assisted relaxation does not affect the radiative decay. For hBN defects, the excitation wavelength has been shown to affect the quantum efficiency [76]. This infers the presence of at least one another electronic state which possesses its own individual lifetime, and may provide an alternative decay pathway to the ground excited state. Vogl *et al.* have also coupled single defects in hBN to open microcavities [85]. With an effective Q-factor of ∼93 and mode volume 1.76λ^3, $F_{P,eff}$

= 4.07 was calculated using Equation 3.53. A reduction of 2.83 in the excited state was observed, yielding a quantum efficiency of QE = 0.51. The key difference between the results for hBN40 and the work of Vogl *et al.* is the excitation wavelength. For hBN40, a 532 nm excitation source was used with the ZPL at 651 nm. While for Vogl *et al.*, excitation at 522 nm was used for a defect with a ZPL at 566 nm. For simplicity, these energies will be converted to eV. The energy difference between the ZPL and excitation sources are 0.42 eV for hBN40 and 0.18 eV for Vogl *et al*. Therefore, for hBN40, this increased detuning may be ample for excitation to alternative excited states, affecting the observed cavity dynamics of the system.

7.4 Conclusion

This chapter has characterised the properties of numerous defects in multi-layer hexagonal boron nitride. These defects were found to present several favourable properties for use as single photon source, including narrow emission spectrum, polarised excitation and emission, short excited state lifetimes and high single photon purities. However, they did not provide sufficient photo-stability for prolonged measurements, especially under pulsed excitation. The most stable defect was hBN40, allowing the full half-space characterisation to be performed. hBN40 displayed all the ideal characteristics often reported with hBN defects and was successfully coupled to a feature with β = 8 μm. The cavity coupled emission showed a $\sim$2.5 times increase in the spectral density of photons into a single cavity mode. Despite this system possessing a relatively high effective Q-factor (Q_{eff} = 125), only a 13% decrease in the excited state lifetime was observed. FDTD simulations were used to estimate the quantum efficiency, but with a disparity compared to the measured value obtained by the saturation measurement. As the exact electronic structure is unknown, this difference was attributed to the presence of other electronic states in the bandgap which can be reached by non-resonant excitation. Although further

work is required to elucidate first the presence, and then dynamics of the other electronic states within the hBN bandgap, these additional levels provide an explanation for the limited decrease in the excited state lifetime observed for hBN40. Ultimately, the poor photo-stability of these emitters will limit their functionality to laboratory experiments, and they are are yet to display sufficient robustness for use in a practical device. Novel fabrication methods or the use of a suitable encapsulating material are being studied further, and could yet provide a means to acheive photo-stable defects in hBN.

8 |

Conclusions and Outlook

This section will firstly summarise the main experimental results presented in the preceding chapters, before discussing the future prospects of this work. The room temperature cavity coupling of single defects in nanoscale diamond and hexagonal boron nitride has been demonstrated. The single photon emission properties of these defects, in combination with cavity enhanced emission, provides a means to create a triggered single photon source device, capable for use in non-laboratory environments. The experimental methods used to determine key device parameters such as the saturation count, excited state lifetime, quantum efficiency and emission spectrum were established, allowing a direct comparison between their half-space and cavity enhanced properties. The experimental configuration used to create this emitter-cavity system was shown, including the deterministic protocol used to optimise emission into the cavity modes. These defects were firstly characterised in the absence of the cavity to determine their emission properties.

Single NV centres were readily found within nanodiamonds, and a good supplier of high quality material has been sourced. The emission spectra showed the NV centres from this material did not display NV^0 character, maintaining the negatively charged state over prolonged high-power exposure. A small sample of NV centres within nanodiamonds from the 100 nm sample have been shown to provide the required robustness for a functioning device. These NV centres displayed photo-stability over the equivalent of 1000 hours of device operation. The device efficiency was found to decrease with increasing excitation

rate, with this relationship being described by the recovery lifetime τ_{rec} – where τ_{rec} was found to be similar to the excited state lifetime. As NV centres in nanodiamonds mostly showed excited state lifetimes between 30 – 36 ns, to maintain the highest efficiencies, the device excitation rate is limited to ∼10 MHz. The quantum efficiency of the brightest NV centres within this project were estimated as 0.25, contrary to previous reports showing quantum efficiencies of up to $QE = 0.9$ for single NV centres in nanodiamonds [49, 152, 153].

The cavity coupling of single NV centres to open-access micro cavities led to an enhancement in the spectral density of photons. Two sets of results were presented, using cavities with peak reflectivities at 640 nm (NV232) and 690 nm (NV25), both reaching the $q = 3$ mode index. The results for the $\beta = 8$ μm feature from both of these systems were similar, displaying a coupling efficiency of ∼47% into the TEM_{00} mode and a ∼2% decrease in the excited state lifetime. FDTD simulations of the cavity system were found to be in good agreement with the measured change in excited state lifetime, when considering the QE. In addition, the TEM_{00} linewidth showed little inhomegenous broadening, with a measured Q-factor of 485 compared to 505 from the FDTD simulation. For the 690 nm cavity, a $\beta = 4$ μm feature was also coupled to NV25 with improved results. The fraction of emission coupled into the TEM_{00} mode was 56%, with a detected single photon purity of 96%. The spectral density of photons after the first lens was measured to be 268 kcts/(s nm), the highest of any NV-based single photon source to date. Defects in hexagonal boron nitride were also studied, and found to provide even more favourable optical properties to be enhanced by the cavity. All the emitters surveyed eventually photo-bleached and did not show the required photo-stability for a robust device. The best hBN defect characterised in this project was hBN40, which displayed single photon emission into a narrow ZPL (3.8 nm) with DW factor of 0.9. The cavity coupled results showed a 13% decrease in the excited state lifetime and an observed spectral density of 800 kcts/(s nm). Further

work is required to stabilise the emission, especially under pulsed excitation. Therefore, at present, defects in hBN are not as suitable for a practical single photon source device compared to NV centres in nanodiamonds.

With further processing of the plinth, the mirror separation can be further reduced, allowing the $q = 2$ mode index to be reached. Conservative results for this geometry were estimated, with an expected device efficiency of $\langle \mathcal{N} \rangle$>5.3% and single photon flux of >531 kcts/s under triggered excitation at 10 MHz for NV25. The brightest NV centre characterised during this project provided a saturation count of 276 kcts/s at an excitation rate of 5 MHz, corresponding to an estimated quantum efficiency of 0.22 on the planar mirror. With such an emitter, the NV-cavity device at the $q = 2$ mode index is estimated to deliver single photon count rates approaching 1 Mcts/s at an excitation rate 10 MHz – a device efficiency of 10%. While these specifications are very distant from the sources described in Section 2.4.3, this NV-cavity system offers a relatively simple and robust means for the production of high purity single photons. This will provide a relatively cheap device which researchers may use for the development of more complex experiments and technologies.

The results of this project have led to the development of a prototype single photon source device, in collaboration with the Fraunhofer Centre for Applied Photonics. The device will comprise of a solid-state emitter embedded in a microcavity module, housed in a temperature stabilising unit. The NV centre has been chosen as the emitter and along with the cavity, it forms the key component of the device. The manufacturing process follows the process detailed in Section 4.7. The individual components which will form the module are shown in Figure 8.1 (a), with the complete module shown in Figure 8.1 (b). A new confocal microscope has being built for the construction of this module. Two 3-axis piezoelectric stages will be used to optimise the coupling to a chosen emitter as seen in Figure

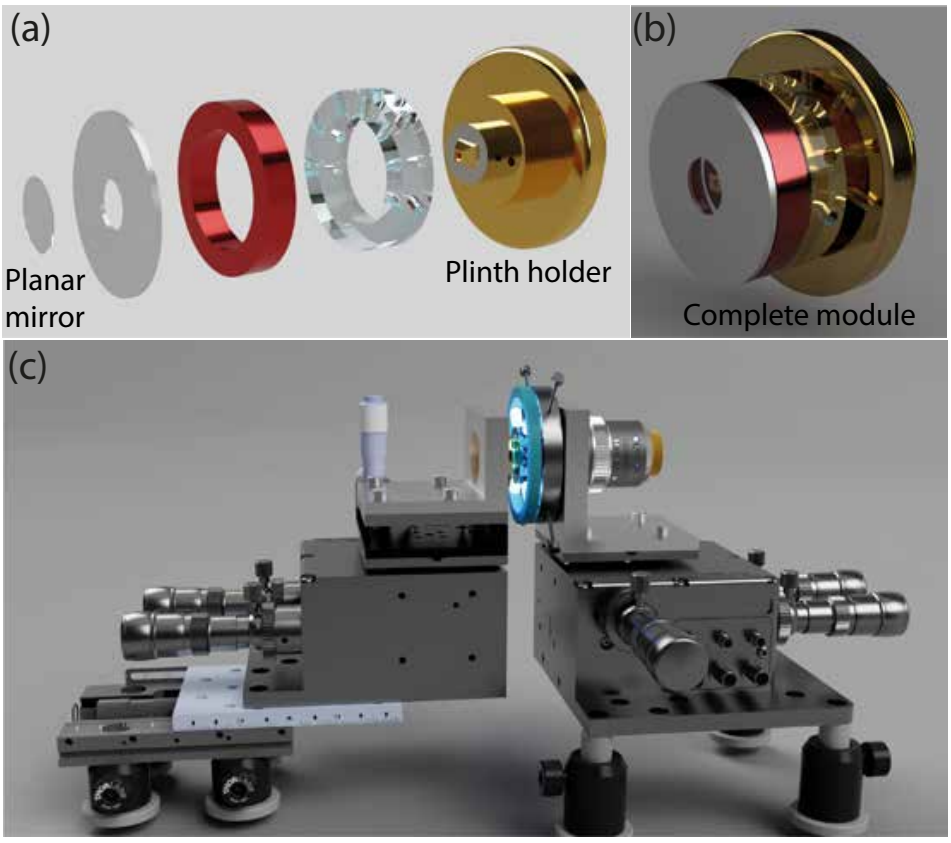


FIGURE 8.1: Schematics of the NV cavity module. (a) Exploded-view drawing of the individual components which form the module. The planar mirror and plinth holder are labelled. (b) The complete module where all the components are fixed together around a cavity coupled emitter. (c) The two 3-axis stages used to optimise coupling to a chosen emitter, and glue the module components together. The blue ring comprises of UV-LEDs to cure the adhesive once the desired cavity coupled configuration is acheived.

8.1 (c), before the components are all glued together by a UV-cured adhesive. Figure 8.2 presents the schematics of the full device. The pre-aligned module will be placed in a housing unit with minimal optics. A fiber coupled excitation is focused on the emitter (green path) resulting in the emission of cavity coupled photons (red path). This device is relatively simplistic compared to the larger apparatus involved with other cryogenic devices, proving an accessible tool for experiments which require a source of single photons.

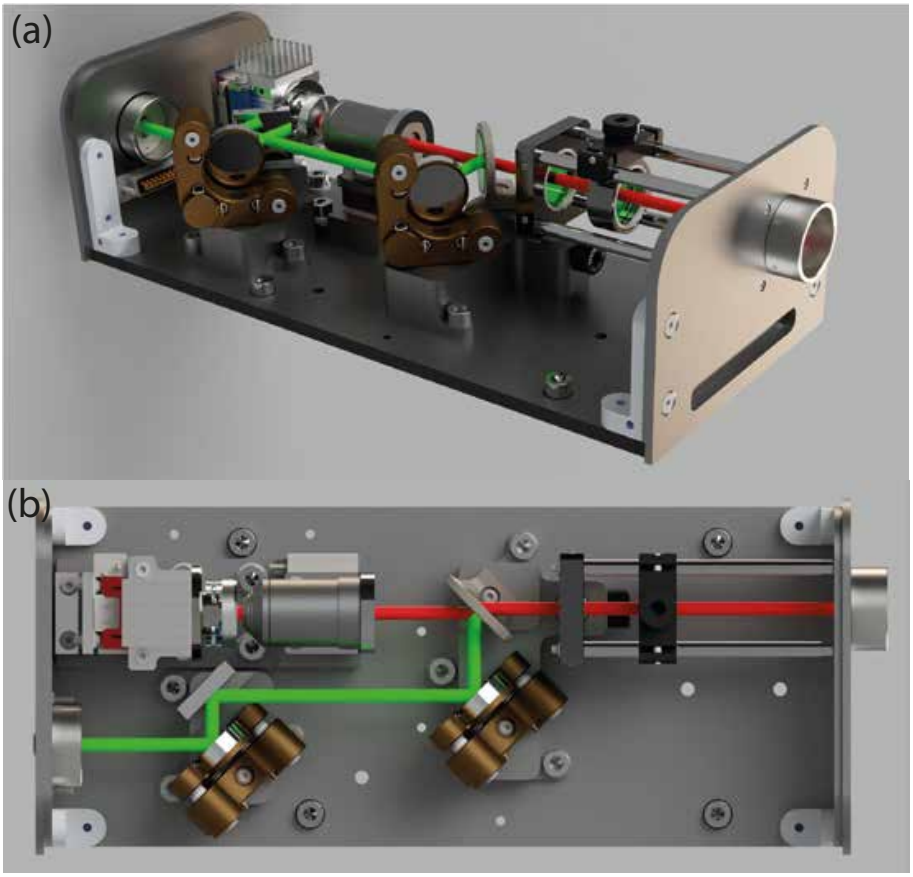


FIGURE 8.2: Schematics of the complete single photon source device from side (a) and aerial view (b).

To conclude, solid-state single photon sources provide a promising approach to develop future photonic quantum technologies. To deliver such technologies based on these systems, vast improvements in the emission and collection properties of are required. These improvements continue to occur through the use of optical microcavities, as well as the discovery of novel single photons sources. This thesis has demonstrated the open-access microcavity as an increasingly favourable platform for the realisation of a robust efficient room-temperature triggered single photon source.

Bibliography

(1) J. L. O'Brien, A. Furusawa and J. Vučković, *Nature Photonics*, 2009, **3**, 687–695.

(2) N. Gisin, G. Ribordy, W. Tittel and H. Zbinden, *Reviews of Modern Physics*, 2002, **74**, 145–195.

(3) V. Scarani, H. Bechmann-Pasquinucci, N. J. Cerf, M. Dušek, N. Lütkenhaus and M. Peev, *Reviews of Modern Physics*, 2009, **81**, 1301–1350.

(4) N. Gisin and R. Thew, *Nature Photonics*, 2007, **1**, 165–171.

(5) A. K. Ekert, *Physical Review Letters*, 1991, 1177–1180.

(6) C. H. Bennett and G Brassard, *IEEE International Conference on Computers, Systems, and Signal Processing*, 1984.

(7) Bennett C. H., Bessette F., Brassard G., Salvail L. and S. J., *Journal of Cryptology*, 1992, **5**, 3–28.

(8) C. Hong, Z. Ou and L Mandel, *Physical Review Letters*, 1987, **59**, 2044–2046.

(9) A. Gatti, M. Bache, D. Magatti, E. Brambilla, F. Ferri and L. A. Lugiato, *Journal of Modern Optics*, 2006, **53**, 739–760.

(10) V Giovannetti, S Lloyd and L Maccone, *Physical Review Letters*, 2006, **96**, 010401.

(11) M. Eisaman, J. Fan, A. Migdall and S. Polyakov, *Review of Scientific Instruments*, 2011, **82**, DOI: 10.1063/1.3610677.

(12) M. Dušek, O. Haderka and M. Hendrych, *Optics Communications*, 1999, **169**, 103–108.

(13) B. R. Johnson, M. D. Reed, A. A. Houck, D. I. Schuster, L. S. Bishop, E. Ginossar, J. M. Gambetta, L. Dicarlo, L. Frunzio, S. M. Girvin and R. J. Schoelkopf, *Nature Physics*, 2010, **6**, 663–667.

(14) L. Liang, G. W. Lin, Y. M. Hao, Y. P. Niu and S. Q. Gong, *Physical Review A*, 2014, **90**, 1–4.

(15) Z. L. Yuan, A. W. Sharpe and A. J. Shields, *Applied Physics Letters*, 2007, **90**, DOI: 10.1063/1.2430685.

(16) I. Aharonovich, D. Englund and M. Toth, *Nature Photonics*, 2016, **10**, 631–641.

(17) Q. Zhang, F. Xu, Y.-A. Chen, C.-Z. Peng and J.-W. Pan, *Optics Express*, 2018, **26**, 24260.

(18) E. Biham, B. Huttner and T. Mor, *Physical Review A - Atomic, Molecular, and Optical Physics*, 1996, **54**, 2651–2658.

(19) T. Jennewein, C. Simon, G. Weihs, H. Weinfurter and A. Zeilinger, *Physical Review Letters*, 2000, **84**, 4.

(20) N. Sangouard, C. Simon, J. Minář, H. Zbinden, H. De Riedmatten and N. Gisin, *Physical Review A*, 2007, **76**, 1–4.

(21) N. L. Piparo and M. Razavi, *IEEE Journal on Selected Topics in Quantum Electronics*, 2015, **21**, DOI: 10.1109/JSTQE.2014.2364129.

(22) A. V. Sergienko, M Atature, Z Walton, G Jaeger, B. E. A. Saleh and M. C. Teich, *Physical Review A*, 1999, **60**, 2622–2625.

(23) M. Bock, A. Lenhard, C. Chunnilall and C. Becher, *Optics Express*, 2016, **24**, 23992.

(24) P. Senellart, G. Solomon and A. White, *Nature Nanotechnology*, 2017, **12**, 1026–1039.

(25) I. Aharonovich, S. Castelletto, D. A. Simpson, C. H. Su, A. D. Greentree and S. Prawer, *Reports on Progress in Physics*, 2011, **74**, DOI: 10.1088/0034-4885/74/7/076501.

(26) M. Lounis, B; Orrit, *Reports on Progress in Physics*, 2005, **68**, 1129–1179.

(27) N. Somaschi, V. Giesz, L. De Santis, J. C. Loredo, M. P. Almeida, G. Hornecker, S. L. Portalupi, T. Grange, C. Antón, J. Demory, C. Gómez, I. Sagnes, N. D. Lanzillotti-Kimura, A. Lemaítre, A. Auffeves, A. G. White, L. Lanco and P. Senellart, *Nature Photonics*, 2016, **10**, 340–345.

(28) *Quandela*, http://quandela.com.

(29) *Sparrow Quantum*, http://sparrowquantum.com.

(30) H. P. Springbett, K. Gao, J. Jarman, T. Zhu, M. Holmes, Y. Arakawa and R. A. Oliver, *Applied Physics Letters*, 2018, **113**, 101107.

(31) I. Aharonovich and E. Neu, *Advanced Optical Materials*, 2014, **2**, 911–928.

(32) T. T. Tran, K. Bray, M. J. Ford, M. Toth and I. Aharonovich, *Nature Nanotechnology*, 2016, **11**, 37–41.

(33) *Quantum Communications Victoria*, qcvictoria.com/home/.

(34) K. J. Vahala, *Nature*, 2003, **424**, 839–846.

(35) S. Johnson, Ph.D. Thesis, University of Oxford, 2015.

(36) B Darquie, A Jones, M, P, J Dingjan, J Beugnon, S Bergamini, Y Sortais, G Messin, A Browaeys and P Grangier, *Science*, 2005, **309**, 454–456.

(37) B Lounis and W. E. Moerner, *Nature*, 2000, **407**, 491–493.

(38) X. Ma, N. F. Hartmann, J. K. Baldwin, S. K. Doorn and H. Htoon, *Nature Nanotechnology*, 2015, **10**, 671–675.

(39) H. Kurtseifer, Christian; Mayer, Sonja; Zarda, Patrick; Weinfurter, *Physical Review Letters*, 2000, **85**, 290–293.

(40) B. Hensen, H. Bernien, A. E. Dreaú, A. Reiserer, N. Kalb, M. S. Blok, J. Ruitenberg, R. F. Vermeulen, R. N. Schouten, C. Abellán, W. Amaya, V. Pruneri, M. W. Mitchell, M. Markham, D. J. Twitchen, D. Elkouss, S. Wehner, T. H. Taminiau and R. Hanson, *Nature*, 2015, **526**, 682–686.

(41) S. Johnson, P. R. Dolan, T. Grange, A. A. Trichet, G. Hornecker, Y. C. Chen, L. Weng, G. M. Hughes, A. A. Watt, A. Auffèves and J. M. Smith, *New Journal of Physics*, 2015, **17**, 122003.

(42) C.-H. Su, A. D. Greentree and L. C. L. Hollenberg, *Physical Review A - Atomic, Molecular, and Optical Physics*, 2009, **80**, 1–11.

(43) V. Acosta and P. Hemmer, *MRS Bulletin*, 2013, **38**, 127–130.

(44) F. Jelezko and J. Wrachtrup, *Physica Status Solidi (A) Applications and Materials Science*, 2006, **203**, 3207–3225.

(45) Y. R. Chang, H. Y. Lee, K. Chen, C. C. Chang, D. S. Tsai, C. C. Fu, T. S. Lim, Y. K. Tzeng, C. Y. Fang, C. C. Han, H. C. Chang and W. Fann, *Nature Nanotechnology*, 2008, **3**, 284–288.

(46) W. W. W. Hsiao, Y. Y. Hui, P. C. Tsai and H. C. Chang, *Accounts of Chemical Research*, 2016, **49**, 400–407.

(47) Y. C. Chen, P. S. Salter, S. Knauer, L. Weng, A. C. Frangeskou, C. J. Stephen, S. N. Ishmael, P. R. Dolan, S. Johnson, B. L. Green, G. W. Morley, M. E. Newton, J. G. Rarity, M. J. Booth and J. M. Smith, *Nature Photonics*, 2017, **11**, 77–80.

(48) H. Bernien, B. Hensen, W. Pfaff, G. Koolstra, M. S. Blok, L. Robledo, T. H. Taminiau, M. Markham, D. J. Twitchen, L. Childress and R. Hanson, *Nature*, 2013, **497**, 86–90.

(49) T. Plakhotnik and H. Aman, *Diamond and Related Materials*, 2018, **82**, 87–95.

(50) L. Rondin, G. Dantelle, A. Slablab, F. Grosshans, F. Treussart, P. Bergonzo, S. Perruchas, T. Gacoin, M. Chaigneau, H. C. Chang, V. Jacques and J. F. Roch, *Physical Review B - Condensed Matter and Materials Physics*, 2010, **82**, 1–5.

(51) V. V. Kononenko, I. I. Vlasov, V. M. Gololobov, T. V. Kononenko, T. A. Semenov, A. A. Khomich, V. A. Shershulin, V. S. Krivobok and V. I. Konov, *Applied Physics Letters*, 2017, **111**, 2–6.

(52) W. E. Moerner, *New Journal of Physics*, 2004, **6**, 1–21.

(53) C. Bradac, T. Gaebel, N. Naidoo, J. R. Rabeau and A. S. Barnard, *Nano Letters*, 2009, **9**, 3555–3564.

(54) Y. Dumeige, F. Treussart, R. Alléaume, T. Gacoin, J. F. Roch and P. Grangier, *Journal of Luminescence*, 2004, **109**, 61–67.

(55) B. Grotz, M. V. Hauf, M. Dankerl, B. Naydenov, S. Pezzagna, J. Meijer, F. Jelezko, J. Wrachtrup, M. Stutzmann, F. Reinhard and J. A. Garrido, *Nature Communications*, 2012, **3**, DOI: 10.1038/ncomms1729.

(56) E. Neu, D. Steinmetz, J. Riedrich-Möller, S. Gsell, M. Fischer, M. Schreck and C. Becher, *New Journal of Physics*, 2011, **13**, DOI: 10.1088/1367-2630/13/2/025012.

(57) E. Neu, M. Agio and C. Becher, 2012, **20**, 19956.

(58) I. I. Vlasov, A. S. Barnard, V. G. Ralchenko, O. I. Lebedev, M. V. Kanzyuba, A. V. Saveliev, V. I. Konov and E. Goovaerts, *Advanced Materials*, 2009, **21**, 808–812.

(59) A. A. Basov, M. Rähn, M. Pärs, I. I. Vlasov, I. Sildos, A. P. Bolshakov, V. G. Golubev and V. G. Ralchenko, *Physica Status Solidi (A) Applications and Materials Science*, 2009, **206**, 2009–2011.

(60) S. Lindner, A. Bommer, A. Muzha, A. Krueger, L. Gines, S. Mandal, O. Williams, E. Londero, A. Gali and C. Becher, *New Journal of Physics*, 2018, **20**, DOI: 10.1088/1367-2630/aae93f.

(61) S. Choi, V. Leong, V. A. Davydov, V. N. Agafonov, M. W. Cheong, D. A. Kalashnikov and L. A. Krivitsky, *Scientific Reports*, 2018, **8**, 1–7.

(62) U. Jantzen, U. L. Andersen, L. J. Rogers, D. S. Rudnicki, A. Kubanek, A. B. Kurz, C. Schäfermeier, V. N. Agafonov, K. D. Jahnke, F. Jelezko and V. A. Davydov, *New Journal of Physics*, 2016, **18**, 073036.

(63) M. Leifgen, T. Schröder, F. Gädeke, R. Riemann, V. Métillon, E. Neu, C. Hepp, C. Arend, C. Becher, K. Lauritsen and O. Benson, *New Journal of Physics*, 2014, **16**, DOI: 10.1088/1367-2630/16/2/023021.

(64) L. J. Martínez, T. Pelini, V. Waselowski, J. R. Maze, B. Gil, G. Cassabois and V. Jacques, *Physical Review B*, 2016, **94**, 121405.

(65) J. D. Caldwell, I. Aharonovich, G. Cassabois, J. H. Edgar, B. Gil and D. N. Basov, *Nature Reviews Materials*, 2019, **4**, 552–567.

(66) J. D. Caldwell, A. V. Kretinin, Y. Chen, V. Giannini, M. M. Fogler, Y. Francescato, C. T. Ellis, J. G. Tischler, C. R. Woods, A. J. Giles, M. Hong, K. Watanabe, T.

Taniguchi, S. A. Maier and K. S. Novoselov, *Nature Communications*, 2014, **5**, 1–9.

(67) S Dai, Z Fei, Q Ma, S Rondin, A, M Wagner, S Mcleod, A, K Liu, M, W Gannet, W Regan, K Watanabe, T Taniguchi, M Thiemens, G Dominquez, H Castro Neto, A, A Zettl, F Keilmann, P Jarillo-Herrero, M Fogler, M and N Basov, D, *Science*, 2014, **343**, 1125–1130.

(68) Y. M. He, G. Clark, J. R. Schaibley, Y. He, M. C. Chen, Y. J. Wei, X. Ding, Q. Zhang, W. Yao, X. Xu, C. Y. Lu and J. W. Pan, *Nature Nanotechnology*, 2015, **10**, 497–502.

(69) G. Cassabois, P. Valvin and B. Gil, *Nature Photonics*, 2016, **10**, 262–266.

(70) S. A. Tawfik, S. Ali, M. Fronzi, M. Kianinia, T. T. Tran, C. Stampfl, I. Aharonovich, M. Toth and M. J. Ford, *Nanoscale*, 2017, **9**, 13575–13582.

(71) T. T. Tran, C. Elbadawi, D. Totonjian, C. J. Lobo, G. Grosso, H. Moon, D. R. Englund, M. J. Ford, I. Aharonovich and M. Toth, *ACS Nano*, 2016, **10**, 7331–7338.

(72) S. Choi, T. T. Tran, C. Elbadawi, C. Lobo, X. Wang, S. Juodkazis, G. Seniutinas, M. Toth and I. Aharonovich, *ACS Applied Materials and Interfaces*, 2016, **8**, 29642–29648.

(73) T. Vogl, G. Campbell, B. C. Buchler, Y. Lu and P. K. Lam, *ACS Photonics*, 2018, **5**, 2305–2312.

(74) N. Chejanovsky, M. Rezai, F. Paolucci, Y. Kim, T. Rendler, W. Rouabeh, F. Fávaro De Oliveira, P. Herlinger, A. Denisenko, S. Yang, I. Gerhardt, A. Finkler, J. H. Smet and J. Wrachtrup, *Nano Letters*, 2016, **16**, 7037–7045.

(75) S. Hou, M. D. Birowosuto, S. Umar, M. A. Anicet, R. Y. Tay, P. Coquet, B. K. Tay, H. Wang and E. H. T. Teo, *2D Materials*, 2018, **5**, aa8e61.

(76) A. W. Schell, M. Svedendahl and R. Quidant, *Advanced Materials*, 2018, **30**, 1–5.

(77) R. Bourrellier, S. Meuret, A. Tararan, O. Stéphan, M. Kociak, L. H. Tizei and A. Zobelli, *Nano Letters*, 2016, **16**, 4317–4321.

(78) G. Grosso, H. Moon, B. Lienhard, S. Ali, D. K. Efetov, M. M. Furchi, P. Jarillo-Herrero, M. J. Ford, I. Aharonovich and D. Englund, *Nature Communications*, 2017, **8**, 1–8.

(79) A. Dietrich, M. Bürk, E. S. Steiger, L. Antoniuk, T. T. Tran, M. Nguyen, I. Aharonovich, F. Jelezko and A. Kubanek, *Physical Review B*, 2018, **98**, 2–6.

(80) R Geick and H Perry, C, *Physical Review*, 1966, **146**, 543–547.

(81) S. Reich, A. C. Ferrari, R. Arenal, A. Loiseau, I. Bello and J. Robertson, *Physical Review B*, 2005, **71**, 1–12.

(82) X. Li, G. D. Shepard, A. Cupo, N. Camporeale, K. Shayan, Y. Luo, V. Meunier and S. Strauf, *ACS Nano*, 2017, **11**, 6652–6660.

(83) A. Bommer and C. Becher, *Nanophotonics*, 2019, 1–8.

(84) A. L. Exarhos, D. A. Hopper, R. R. Grote, A. Alkauskas and L. C. Bassett, *ACS Nano*, 2017, **11**, 3328–3336.

(85) T. Vogl, R. Lecamwasam, B. C. Buchler, Y. Lu and P. K. Lam, *ACS Photonics*, 2019, DOI: 10.1021/acsphotonics.9b00314.

(86) W. L. Barnes, G. Björk, J. M. Gérard, P. Jonsson, J. A. E. Wasey, P. T. Worthing and V. Zwiller, *European Physical Journal D*, 2002, **18**, 197–210.

(87) J. P. Hadden, J. P. Harrison, A. C. Stanley-Clarke, L. Marseglia, Y. L. D. Ho, B. R. Patton, J. L. O'Brien and J. G. Rarity, *Applied Physics Letters*, 2010, **97**, DOI: 10.1063/1.3519847.

(88) L. Li, E. H. Chen, J. Zheng, S. L. Mouradian, F. Dolde, T. Schröder, S. Karaveli, M. L. Markham, D. J. Twitchen and D. Englund, *Nano Letters*, 2015, **15**, 1493–1497.

(89) S. Johnson, P. R. Dolan and J. M. Smith, *Progress in Quantum Electronics*, 2017, **55**, 129–165.

(90) R. Alléaume, F. Treussart, G. Messin, Y. Dumeige, J. F. Roch, A. Beveratos, R. Brouri-Tualle, J. P. Poizat and P. Grangier, *New Journal of Physics*, 2004, **6**, 1–14.

(91) E. M. Purcell, *Physical Review*, **69**(11), (1946).

(92) P. R. Dolan, G. M. Hughes, F. Grazioso, B. R. Patton and J. M. Smith, *Optics Letters*, 2010, **35**, 3556.

(93) A. A. P. Trichet, P. R. Dolan, D. M. Coles, G. M. Hughes and J. M. Smith, *Optics Express*, 2015, **23**, 17205.

(94) A. Kuhn and D. Ljunggren, *Contemporary Physics*, 2010, **51**, 289–313.

(95) T. Noda, Susumu; Fujita, Masayuki; Asano, *Nature Photonics*, 2007, **1**, 449–458.

(96) S. Tomljenovic-Hanic, M. J. Steel, C. M. de Sterke and J. Salzman, *Optics Express*, 2006, **14**, 3556.

(97) J. Riedrich-Möller, L. Kipfstuhl, C. Hepp, E. Neu, C. Pauly, F. Mücklich, A. Baur, M. Wandt, S. Wolff, M. Fischer, S. Gsell, M. Schreck and C. Becher, *Nature Nanotechnology*, 2012, **7**, 69–74.

(98) A. Faraon, C. Santori, Z. Huang, V. M. Acosta and R. G. Beausoleil, *Physical Review Letters*, 2012, **109**, 2–6.

(99) B. J. Hausmann, B. J. Shields, Q. Quan, Y. Chu, N. P. De Leon, R. Evans, M. J. Burek, A. S. Zibrov, M. Markham, D. J. Twitchen, H. Park, M. D. Lukin and M. Loncăr, *Nano Letters*, 2013, **13**, 5791–5796.

(100) Y. Dumeige, R. Alléaume, P. Grangier, F. Treussart and J. F. Roch, *New Journal of Physics*, 2011, **13**, DOI: 10.1088/1367-2630/13/2/025015.

(101) A. E. Siegman, *Lasers*, Oxford University Press, University Science Books, 1990.

(102) G. V. Prakash, L. Besombes, T. Kelf, J. J. Baumberg, P. N. Bartlett and M. E. Abdelsalam, *Optics Letters*, 2004, **29**, 1500.

(103) G. Cui, J. M. Hannigan, R Loeckenhoff, F. M. Matinaga and M. G. Raymer, 2006, **14**, 2289–2299.

(104) M. Trupke, E. A. Hinds, S. Eriksson, E. A. Curtis, Z. Moktadir, E. Kukharenka and M. Kraft, *Applied Physics Letters*, 2005, **87**, 1–3.

(105) D. Hunger, T. Steinmetz, Y. Colombe, C. Deutsch, T. W. Hänsch and J. Reichel, *New Journal of Physics*, 2010, **12**, 0–23.

(106) L. Greuter, S. Starosielec, D. Najer, A. Ludwig, L. Duempelmann, D. Rohner and R. J. Warburton, *Applied Physics Letters*, 2014, **105**, DOI: 10.1063/1.4896415.

(107) D. Hunger, C. Deutsch, R. J. Barbour, R. J. Warburton and J. Reichel, *AIP Advances*, 2012, **2**, DOI: 10.1063/1.3679721.

(108) Z. Di, H. V. Jones, P. R. Dolan, S. M. Fairclough, M. B. Wincott, J. Fill, G. M. Hughes and J. M. Smith, *New Journal of Physics*, 2012, **14**, DOI: 10.1088/1367-2630/14/10/103048.

(109) R. Albrecht, A. Bommer, C. Deutsch, J. Reichel and C. Becher, *Physical Review Letters*, 2013, **110**, 1–5.

(110) A. Auffèves, J. M. Gérard and J. P. Poizat, *Physical Review A - Atomic, Molecular, and Optical Physics*, 2009, **79**, 1–5.

(111) A. Auffèves, D. Gerace, J. M. Gérard, M. F. Santos, L. C. Andreani and J. P. Poizat, *Physical Review B - Condensed Matter and Materials Physics*, 2010, **81**, 245419.

(112) J. Benedikter, H. Kaupp, T. Hümmer, Y. Liang, A. Bommer, C. Becher, A. Krueger, J. M. Smith, T. W. Hänsch and D. Hunger, *Physical Review Applied*, 2017, **7**, 024031.

(113) S. Kim, J. E. Fröch, J. Christian, M. Straw, J. Bishop, D. Totonjian, K. Watanabe, T. Taniguchi, M. Toth and I. Aharonovich, *Nature Communications*, 2018, **9**, 1–8.

(114) P. Lodahl, *Quantum Science and Technology*, 2018, **3**.

(115) S. Buckley, K. Rivoire and J. Vučković, *Reports on Progress in Physics*, 2012, **75**, DOI: 10.1088/0034-4885/75/12/126503.

(116) L Goldstein, F Glas, Y Marzin, J, N Charasse, M and G Le Roux, *Applied Physics Letters*, 1985, **47**, 1099 –1101.

(117) S Solomon, G, A Trezza, J and S Harris, J, *Applied Physics Letters*, 1995, **66**, 3161–3163.

(118) C. Santori, M. Pelton, G. Solomon, Y. Dale and Y. Yamamoto, *Physical Review Letters*, 2001, **86**, DOI: 10.1109/QELS.2001.962045.

(119) Z. Yuan, B. E. Kardynal, R. M. Stevenson, A. J. Shields, C. J. Lobo, K. Cooper, N. S. Beattie, D. A. Ritchie and M. Pepper, *Science*, 2002, **295**.

(120) A. J. Bennett, D. C. Unitt, P. See, A. J. Shields, P. Atkinson, K. Cooper and D. A. Ritchie, *Physical Review B*, 2005, **72**, DOI: 10.1103/PhysRevB.72.033316.

(121) A. J. Bennett, D. C. Unitt, P. See, A. J. Shields, P. Atkinson, K. Cooper and D. A. Ritchie, *Applied Physics Letters*, 2005, **86**, 1–3.

(122) M. Pelton, J. Vučković, G. Solomon, C. Santori, B. Zhang, J. Plant and Y. Yamamoto, *Physical Review Letters*, 2002, **89**, DOI: 10.1016/S1386-9477(02)00872-X.

(123) A. J. Bennett, D. C. Unitt, P. Atkinson, D. A. Ritchie and A. J. Shields, *Optics Express*, 2005, **13**, 50–55.

(124) A. J. Shields, *Nature Photonics*, 2007, **1**, 215–223.

(125) D. J. P. Ellis, A. J. Bennett, S. J. Dewhurst, C. A. Nicoll, D. A. Ritchie and A. J. Shields, *New Journal of Physics*, 2008, **10**, 0–8.

(126) J. C. Loredo, M. A. Broome, P. Hilaire, O. Gazzano, I. Sagnes, A. Lemaitre, M. P. Almeida, P. Senellart and A. G. White, *Physical Review Letters*, 2017, **118**, DOI: 10.1103/PhysRevLett.118.130503.

(127) A. Beveratos, R. Brouri, T. Gacoin, A. Villing, J. P. Poizat and P. Grangier, *Physical Review Letters*, 2002, **89**, 4–7.

(128) T. Schröder, F. Gädeke, M. J. Banholzer and O. Benson, *New Journal of Physics*, 2011, **13**, DOI: 10.1088/1367-2630/13/5/055017.

(129) P. R. Dolan, S. Adekanye, A. A. P. Trichet, S. Johnson, L. C. Flatten, Y. C. Chen, L. Weng, D. Hunger, H.-C. Chang, S. Castelletto and J. M. Smith., *Optics Express*, 2018, **26**, 7056.

(130) H. Kaupp, T. Hümmer, M. Mader, B. Schlederer, J. Benedikter, P. Haeusser, H. C. Chang, H. Fedder, T. W. Hänsch and D. Hunger, *Physical Review Applied*, 2016, **6**, 1–10.

(131) G. Kiršanske, H. Thyrrestrup, R. S. Daveau, C. L. Dreeßen, T. Pregnolato, L. Midolo, P. Tighineanu, A. Javadi, S. Stobbe, R. Schott, A. Ludwig, A. D. Wieck, S. I. Park, J. D. Song, A. V. Kuhlmann, I. Söllner, M. C. Löbl, R. J. Warburton and P. Lodahl, *Physical Review B*, 2017, **96**, 1–11.

(132) W. Z. Heisenberg, *Physik*, 1927, **43**, 172–198.

(133) E. H. Kennard, *Physik*, 1927, **44**, 326–352.

(134) M. Born and J. R. Oppenheimer, *Annalen der Physik*, 1927, **389**, 457–484.

(135) E. Hecht, *Optics 4th edition*, Addison-Wesley, New York, USA, 2001.

(136) G. Brooker, *Modern Classical Optics*, Oxford University Press, Oxford, United Kingdom, 2002.

(137) W. Lukosz, *Journal of the Optical Society of America*, 1979, **69**, 1495.

(138) L. R. Brovelli and U. Keller, *Optics Communications*, 1995, **116**, 343–350.

(139) *Python Transfer Matrix tmm 0.1.7*, https://pypi.org/project/tmm/.

(140) M. Fox, *Quantum Optics: An Introduction*, Oxford University Press, Oxford, United Kingdom, 2006.

(141) *Lumerical Solutions, Inc.* https://www.lumerical.com/products/fdtd-solutions/.

(142) H Chew, *Physical Review A*, 1988, **38**, 3410–3416.

(143) C. Santori, P. E. Barclay, K. M. Fu, R. G. Beausoleil, S. Spillane and M. Fisch, *Nanotechnology*, 2010, **21**, DOI: 10.1088/0957-4484/21/27/274008.

(144) L. C. Flatten, Ph.D. Thesis, University of Oxford, 2017.

(145) L. J. Su, C. Y. Fang, Y. T. Chang, K. M. Chen, Y. C. Yu, J. H. Hsu and H. C. Chang, *Nanotechnology*, 2013, **24**, DOI: 10.1088/0957-4484/24/31/315702.

(146) H.-C. Chang, W. W.-W. Hsiao and M.-C. Su, *Fluorescent Nanodiamonds, First Edition*, Wiley, 2018.

(147) K. M. C. Fu, C. Santori, P. E. Barclay and R. G. Beausoleil, *Applied Physics Letters*, 2010, **96**, 1–4.

(148) M. V. Hauf, B. Grotz, B. Naydenov, M. Dankerl, S. Pezzagna, J. Meijer, F. Jelezko, J. Wrachtrup, M. Stutzmann, F. Reinhard and J. A. Garrido, *Physical Review B - Condensed Matter and Materials Physics*, 2011, **83**, 1–4.

(149) R Hanbury-Brown and Q Twiss, R, *Nature*, 1956, 27–29.

(150) M. W. Doherty, N. B. Manson, P. Delaney, F. Jelezko, J. Wrachtrup and L. C. Hollenberg, *Physics Reports*, 2013, **528**, 1–45.

(151) F. A. Inam, T. Gaebel, C. Bradac, L. Stewart, M. J. Withford, J. M. Dawes, J. R. Rabeau and M. J. Steel, *New Journal of Physics*, 2011, **13**, DOI: 10.1088/1367-2630/13/7/073012.

(152) A. Mohtashami and A. Femius Koenderink, *New Journal of Physics*, 2013, **15**, DOI: 10.1088/1367-2630/15/4/043017.

(153) F. A. Inam, M. J. Steel and S. Castelletto, *Diamond and Related Materials*, 2014, **45**, 64–69.

(154) F. A. Inam, A. M. Edmonds, M. J. Steel and S. Castelletto, *Applied Physics Letters*, 2013, **102**, DOI: 10.1063/1.4812711.

(155) R. Albrecht, A. Bommer, C. Deutsch, J. Reichel and C. Becher, *Physical Review Letters*, 2013, **83**, 1–12.

(156) N. B. Manson and J. P. Harrison, *Diamond and Related Materials*, 2005, **14**, 1705–1710.

(157) N. Aslam, G. Waldherr, P. Neumann, F. Jelezko and J. Wrachtrup, *New Journal of Physics*, 2013, **15**, DOI: 10.1088/1367-2630/15/1/013064.

(158) J. Jeske, D. W. Lau, X. Vidal, L. P. McGuinness, P. Reineck, B. C. Johnson, M. W. Doherty, J. C. McCallum, S. Onoda, F. Jelezko, T. Ohshima, T. Volz, J. H. Cole, B. C. Gibson and A. D. Greentree, *Nature Communications*, 2017, **8**, 1–8.

(159) P. Siyushev, H. Pinto, M. Vörös, A. Gali, F. Jelezko and J. Wrachtrup, *Physical Review Letters*, 2013, **110**, 1–5.

(160) H. Kaupp, C. Deutsch, H. C. Chang, J. Reichel, T. W. Hänsch and D. Hunger, *Physical Review A - Atomic, Molecular, and Optical Physics*, 2013, **88**, 1–8.

(161) R. Albrecht, A. Bommer, C. Pauly, F. Mücklich, A. W. Schell, P. Engel, T. Schröder, O. Benson, J. Reichel and C. Becher, *Applied Physics Letters*, 2014, **105**, DOI: 10.1063/1.4893612.